Uniwersytet Warszawski
Wydział Fizyki
Instytut Fizyki Doświadczalnej
Zakład Cząstek i Oddziaływań Fundamentalnych

Michał Drągowski

Polarization Effects in Scattering of Relativistic Electrons

ROZPRAWA DOKTORSKA

Promotor:
prof. dr hab. Aleksander Filip Żarnecki
Uniwersytet Warszawski

Promotor pomocniczy:
dr Marek Adamus
Narodowe Centrum Badań Jądrowych

Warszawa, 2022

Streszczenie

Przedmiotem badań były efekty polaryzacyjne w rozpraszaniu Møllera, to jest w elastycznym rozpraszaniu dwóch elektronów. Celem pracy była weryfikacja przewidywań relatywistycznej mechaniki kwantowej w odniesieniu do przekazu polaryzacji (zależności między polaryzacją wiązki i polaryzacją elektronów po rozproszeniu) oraz korelacji spinowych pomiędzy dwoma cząstkami w stanie końcowym. Motywacją przeprowadzonych badań był fakt, iż w eksperymentach korelacyjnych przeprowadzonych dotychczas nie było możliwe zaobserwowanie efektów relatywistycznych, z powodu zbyt małej energii cząstek.

Złożony charakter pomiaru, polegającego na dwóch następujących po sobie oddziaływaniach elektronu w dwóch różnych tarczach, wymagał zaprojektowania i zbudowania dedykowanego układu pomiarowego. Do przeprowadzenia eksperymentu wykorzystana została wiązka elektronów z akceleratora Mainzer Mikrotron o energii 3 MeV. W trakcie zderzenia spolaryzowany elektron wiązki przekazywał część swojej polaryzacji niespolaryzowanemu elektronowi wybijanemu z tarczy wykonanej z berylu. Następnie pomiar polaryzacji elektronów pochodzących z rozpraszania Møllera wykonywany był metodą polarymetrii Motta, która polega na rozproszeniu elektronu na jądrze ciężkiego pierwiastka, w tym przypadku złota. Dodatkowo, do optymalizacji układu doświadczalnego, a także do wyznaczenia końcowego wyniku, konieczne było przeprowadzenie symulacji komputerowej, w tym stworzenie dedykowanego modelu rozpraszania Motta.

Analiza danych zebranych w roku 2020 pozwoliła po raz pierwszy wyznaczyć przekaz polaryzacji w rozpraszaniu Møllera. Wyniki eksperymentu zostały porównane z przewidywaniami relatywistycznej mechaniki kwantowej. Zmierzony stosunek polaryzacji elektronów przed i po rozproszeniu okazał się zgodny z przewidywaniami teoretycznymi. Średnia polaryzacja elektronów w stanie końcowym rozpraszania Møllera została wykorzystana do obliczenia eksperymentalnych ograniczeń wartości funkcji korelacji. Przewidywania oparte o rachunki nierelatywistyczne zostały wykluczone przez wynik doświadczalny na wysokim poziomie znaczoności.

Abstract

Considered in the presented study were polarization effects in Møller (elastic electron–electron) scattering. The primary aim of this work was to verify the predictions of relativistic quantum mechanics regarding polarization transfer (relation between primary-beam polarization and electron polarization after the scattering) and spin correlations between two particles in the final state. This study was motivated by the fact that in all of the spin-correlation experiments performed until now the energy of the particles was too low to observe relativistic effects.

Taking into account the complex nature of the measurement, which consisted of subsequent electron interactions in two different targets, a dedicated experimental setup had to be designed and constructed. A 3 MeV electron beam from the Mainzer Mikrotron accelerator was used in the experiment. In the scattering off a target made of beryllium, a polarized beam electron transferred part of its polarization to an unpolarized target electron. Subsequently, the polarization of the electron originating from Møller scattering was measured using the Mott polarimetry method, by electron scattering off gold nuclei. The use of computer simulation methods, including implementation of a dedicated Mott scattering model, was necessary to optimize the experimental setup and to determine the final result.

Analysis of the data collected in 2020 resulted in the first determination of the polarization transfer in Møller scattering. The results of the experiment were compared to the predictions of relativistic quantum mechanics. The ratio of electron polarizations before and after the scattering was found to be in agreement with the theoretical predictions. The average polarization of electrons in the final state was used to calculate the experimental limits on the correlation function. Results of the nonrelativistic calculations were excluded by the experimental result with high significance.

Acknowledgements

I would like to express my deepest gratitude to my supervisors, Prof. A. F. Żarnecki and Dr. M. Adamus. I am indebted to all colleagues, who participated in this project, and shared their knowledge and expertise with me. I would also like to acknowledge the work of the mechanical and electronics workshops. I am convinced, I would not have undertaken this journey without the inspiration from my teachers, in particular Ms. J. Ratyńska and Ms. B. Parciak. Finally, I would like to thank my family, especially my wife, for their constant support.

Contents

Chapter 1

Introduction

1.1. Historical background

In 1924, W. Pauli formulated a requirement that there needs to be an additional quantum number, allowing to double the number of electrons occupying a given energy level in an atom. The interpretation assuming the existence of another form of angular momentum, in addition to the orbital angular momentum, was proposed by G. Uhlenbeck and S. Goudsmit, as well as slightly earlier by R. Kronig, who did not, however, decide to publish his idea. This quantity, spin, was found to be fundamental for the description of elementary particles, in particular in the framework of relativistic quantum mechanics, derived soon afterwards.

At the same time, the correctness of quantum mechanics was frequently questioned, due to the fact that some of its predictions, such as the nonlocality of entangled systems, were considered counter-intuitive. These concerns were formalized by A. Einstein, B. Podolsky and N. Rosen (EPR) in their 1935 paper [1]. Subsequently, the general argument of EPR was illustrated by D. Bohm [2] with a thought experiment, referring to the spin-projection correlations of two particles in an entangled state.

J. Bell, in order to prove that quantum mechanics is a nonlocal theory, proposed an inequality involving correlation functions, defined as the average product of the results of spin-projection measurements performed on two particles, which must hold for any theory preserving local realism [3]. It turns out that, according to the predictions of quantum mechanics, the Bell inequality is violated. This fact was experimentally verified at the turn of the 70s and 80s (some less conclusive experiments were also performed earlier). A. Aspect et al. conducted experiments, which showed that Bell inequalities are, without any doubt, violated [4, 5]. The 2022 Nobel Prize in Physics was awarded to A. Aspect, J. F. Clauser, and A. Zeilinger, *for experiments with entangled photons, establishing the violation of Bell inequalities and pioneering quantum information science.*

Even though the original example of Bohm referred to a pair of spin-1/2 particles, photons in singlet state were used in the experiments – for technical reasons it is easier to perform such measurement with photons rather than massive particles. The relativistic effects in EPR correlations of massive particles were also investigated in several theoretical works (e.g., [6–15]); selected results are described in the next section.

1.2. Relativistic quantum spin correlations

Quantum correlation was defined by Bell as the average value of the product of two observables. The quantum correlation function $\mathcal{C}$ can be written, in general, as

$$\mathcal{C}(A,B) = \sum_{\alpha\beta} \alpha\beta \mathcal{P}_{\alpha\beta}, \tag{1.1}$$

where $\mathcal{P}_{\alpha\beta}$ denotes the probability of obtaining α and β as a result of measurement of observables A and B, respectively.

Usually, observables A and B are chosen to be the spin projections on some particular directions (denoted $\vec{a}$ and $\vec{b}$), measured by two observers. For spin-1/2 particles the possible outcomes of each measurement are $\pm\hbar/2$. Let us assume for simplicity that spin projections are measured in units of $\hbar/2$. Then the corresponding spin correlation function $C(\vec{a},\vec{b})$ yields

$$C(\vec{a},\vec{b}) = P_{++}(\vec{a},\vec{b}) - P_{+-}(\vec{a},\vec{b}) - P_{-+}(\vec{a},\vec{b}) + P_{--}(\vec{a},\vec{b}), \tag{1.2}$$

where P with proper indices denote the probability of obtaining a positive $(+)$ or negative $(-)$ spin projection on direction $\vec{a}$ and $\vec{b}$, for the first and second particle, respectively (e.g., P_{+-} represents the probability of obtaining positive spin projection for the first particle and negative for the second particle).

In the relativistic case, relativistic corrections to the correlation function, dependent on particle momenta, are to be expected. As an example, a pair of massive spin-1/2 fermions in singlet state may be considered. It is straightforward to show that the correlation function of this system, calculated within nonrelativistic quantum mechanics, has the following form

$$C(\vec{a},\vec{b}) = -\vec{a}\cdot\vec{b}. \tag{1.3}$$

Caban et al. calculated the relativistic correlation function for a pair of spin-1/2 fermions in singlet and triplet state [6, 7]. The relativistic correlation function corresponding to the singlet state is

$$C(\vec{a},\vec{b}) = -\vec{a}\cdot\vec{b} + \frac{\vec{k_1}\times\vec{k_2}}{m^2+k_1k_2}\left(\vec{a}\times\vec{b} + \frac{(\vec{a}\cdot\vec{k_1})(\vec{b}\times\vec{k_2}) - (\vec{b}\cdot\vec{k_2})(\vec{a}\times\vec{k_1})}{(k_1^0+m)(k_2^0+m)}\right), \tag{1.4}$$

where k_1 and k_2 denote particle four momenta, and m their mass. The function consists of a nonrelativistic part identical with equation (1.3) and a relativistic correction dependent on momenta.

Further analysis of the relativistic correlation functions by Caban et al. [8] revealed their unexpected behavior — for certain configurations, the correlation function dependence on particle momenta may be non-monotonic. They later found local extrema of the correlation functions in many systems, including a pair of spin-1/2 and spin-1 particles [9, 10], a hybrid system of a photon and a spin-1/2 fermion [11], and helicity correlations of relativistic bosons [12].

The authors of some earlier works [13–15] predicted that the degree of Bell-type inequalities violation should be a decreasing function of momentum. It was, however, shown [8,9] that in some cases it is a non-monotonic function of the momentum. There

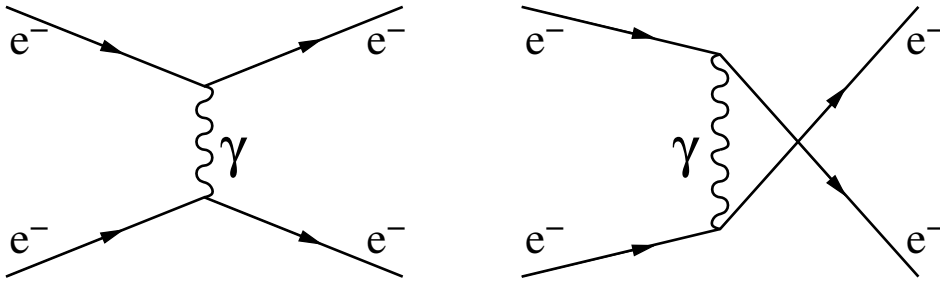

Figure 1.1: Leading order QED Feynman diagrams representing Møller scattering.

exist configurations for which the degree of the inequality violation increases with the particle momenta and reaches its maximal value in the ultrarelativistic limit.

A few experiments were also carried out with massive particles. The quantum spin correlations and the violation of Bell–type inequalities were measured for spin-1/2 particles with mass by Lamehi–Rachti and Mittig [16] in 1976, as well as more recently by Hamieh et al. [17] and Sakai et al. [18], in 2004 and 2006, respectively. In all three cases protons originating from low-energy nuclear reactions were used for this purpose. In all of the experiments [16–18] the particle energies were insufficient to observe the relativistic correction – their results turned out to be in agreement with the predictions of nonrelativistic quantum mechanics.

Experiments with massive particles in the relativistic regime offer a promising opportunity to observe quantum entanglement in the range of relativistic energies and to test the relativistic spin observables [19]. No experimental studies of this kind have been performed until now. Due to the experimental difficulties with preparing a maximally entangle state in the range of relativistic energies, the measurement of quantum spin correlations in relativistic electron–electron scattering was considered [20, 21] as an alternative approach.

1.3. Møller scattering

The first relativistic description of elastic electron–electron scattering, $e^-e^- \to e^-e^-$, has been given by Møller [22]. The leading order quantum electrodynamics (QED) Feynman diagrams representing Møller scattering are shown in Fig. 1.1.

Møller scattering has been extensively studied in several experiments. This included, in particular, precise studies of electroweak interactions. Parity violation can be tested by measuring the cross section asymmetry in Møller scattering of longitudinally polarized electron beams [23]. The resulting precision of the weak mixing angle measurement is comparable to the best results from colliders. Such measurement was performed by E158 Collaboration at SLAC [24], and further work in this field is ongoing, in particular, by the MOLLER Collaboration at JLab [25].

Another application is the Møller polarimetry method, which has become the standard tool for beam polarization measurement in high-energy spin physics [26–28]. The application of Mott polarimetry [29], based on spin–orbit interaction in electron–nucleus scattering, is impractical for energies exceeding about 10 MeV due to quickly

decreasing cross section and analyzing power, while Møller polarimetry is successfully applied in the GeV energy range.

Even though Møller scattering has been studied in great detail over its almost 100 year history, it still offers unexplored research opportunities. Given the availability of polarized electron beams and the good understanding of electron polarimetry, it was found to be a suitable process for the study of polarization transfer effects from a polarized electron to electrons in the final state of Møller scattering, including the creation of entanglement between both particles, manifesting itself through quantum spin correlations. The quantum spin correlation function and the corresponding probabilities for electrons in the final state of Møller scattering have recently been calculated in a special case of polarized electron beam scattering off an unpolarized target [20], as well as the scattering of two polarized electrons [21], assuming the Mott polarimetry technique for spin projection measurement. These calculations show that the studies of the final spin state in Møller scattering of polarized electron beams open new research perspectives and become a unique tool for testing relativistic spin observables and quantum entanglement in the range of relativistic energies. A measurement of this kind was first proposed in [30].

1.4. Aims of this work

Described in this thesis is the study aimed at the measurement of polarization transfer in Møller scattering. The average polarization of the electrons in the final state of near-symmetric Møller scattering was measured [31] using the Mott polarimetry method [29]. The measurements were performed with a 3 MeV polarized electron beam from the injector linac of Mainzer Mikrotron (MAMI) [32]. The result (ratio of the transverse polarization in the final state to the incoming-beam polarization) was compared to the predictions of relativistic quantum mechanics [21]. It was, to our knowledge, the first such measurement.

The main experimental challenge of this measurement was related to the low interaction probability leading to a signal-to-background ratio many orders of magnitude lower than in the case of a standard polarization measurement performed on a beam. The signal events are rare due to the low combined probability of coincident Møller and Mott scattering processes, of the order of 10^{-11} per incident beam electron with kinetic energy of 3 MeV. Additionally, the Mott polarimeter has to operate, in contrast to the conventional applications, on a divergent stream of secondary Møller electrons, which further increases the background contribution.

The theoretical aim was to find the relation between quantum spin correlations and the average polarization of the particles in the final state. We showed that the range of allowed values of the correlation function might be strongly limited, if the average polarization of the particles in the final state is large. In the case of Møller scattering, the non-monotonic dependence of the correlation function on energy can be partly explained by the limits calculated from the average polarization.

Finally, the theoretical result combined with the experimental result regarding polarization transfer in Møller scattering, were used to derive the experimental limits on the correlation function. This allowed us to observe, for the first time, the relativistic

contribution to the final spin state, as the measured values of average polarization in the final state of Møller scattering exclude the nonrelativistic predictions.

The additional aims of this work were to test a standard Mott polarimeter as a tool for the measurement of quantum spin correlations in Møller scattering, based on a simultaneous determination of the spin projections for both electrons in the final state, and to obtain guidelines for the design of a two-polarimeter device for such an experiment. The polarization transfer measurement is a prerequisite for measuring spin correlations, as it demonstrates the feasibility of the measurement of the spin projection for one final-state Møller electron. Our results demonstrate that a standard Mott polarimeter is a suitable tool for measuring polarization with a divergent stream of Møller electrons despite the high-background environment.

1.5. Outline of the dissertation

The dissertation consists of nine chapters (including this introduction) and two appendices.

In Chapter 2, *Theoretical predictions*, the main interactions of electrons in the MeV energy range, Mott scattering (electron – nucleus) and Møller scattering (electron – electron), are described. The theoretical predictions for the polarization transfer and spin correlations in Møller scattering are reviewed based on literature [20, 21]. New results, regarding the relation between the average polarization in the final state and the allowed range of the spin correlation function values, are also shown.

In Chapter 3, *Experimental setup*, the principle of the measurement is explained. The design of a dedicated Mott polarimeter for the study of polarization transfer in Møller scattering is discussed.

In Chapter 4, *Electronics and data acquisition*, the complete data acquisition system is presented. Results of the detector (SiPM sensors with dedicated front-end) tests are discussed. Trigger and readout electronics prepared for the experiment are also described.

In Chapter 5, *Simulation of the analyzing power*, a dedicated Monte Carlo simulation of polarized-electron interaction with matter [33], taking into account polarization transfer in Mott scattering, is presented. The simulation results, used to optimize the polarimeter design with regard to the effective Sherman function dependence on energy, target thickness and scattering angle [34], are discussed. Finally, predictions for the effective analyzing power of the Mott polarimeter are shown.

In Chapter 6, *Simulation of the experimental setup*, the results of the simulations of the complete detector, performed with the Geant4 toolkit, are presented. The first aim of the simulation was to identify the main sources of background. Results concerning beam dispersion and depolarization during the passage through target material are also discussed. The simulation results are then used to estimate some of the systematic uncertainties.

In Chapter 7, *Polarization transfer measurement*, all steps of the complete data analysis procedure used in the polarization transfer experiment are presented.

In Chapter 8, *Analysis of uncertainties*, the measurement uncertainties are estimated using the experimental and simulated data.

In Chapter 9, *Final results and conclusions*, the main experimental results [31], regarding the polarization transfer in Møller scattering, obtained in two experimental configurations, are presented. The experimental results are compared to the theoretical predictions. Finally, the conclusions of the thesis are summarized.

In Appendix A, *Measurement of spin correlations*, guidelines for future spin correlation experiments are discussed. The theoretical predictions are reviewed with the focus on a possible measurement of the relativistic correction to the correlation function. The design of the experimental setup, using two Mott polarimeters for spin correlation measurement, is presented. The feasibility of such experiment is discussed. Predictions for the signal and background rates are shown, and methods of improving the signal to background ratio are proposed. Finally, the possibility to observe the violation of Bell-type inequalities in scattering of two polarized electrons is demonstrated.

In Appending B, more detailed drawings of the experimental setup designed as part of this work are appended.

Chapter 2

Theoretical predictions

Reviewed in the chapter are the theoretical predictions for the cross section and polarization transfer in Møller and Mott scattering of relativistic electrons, and quantum spin correlations in Møller scattering. A new result, regarding the relation between the average polarization in the final state and spin correlations, is shown.

2.1. Møller scattering

2.1.1. Cross section

Let p_1, p_2 and k_1, k_2 represent four-momenta in the two-electron initial and final state, respectively. The cross section is conveniently expressed in terms of Mandelstam variables s, t, u:

$$s = (p_1 + p_2)^2 = (k_1 + k_2)^2 \,, \tag{2.1a}$$
$$t = (p_1 - k_1)^2 = (p_2 - k_2)^2 \,, \tag{2.1b}$$
$$u = (p_1 - k_2)^2 = (p_2 - k_1)^2 \,. \tag{2.1c}$$

The differential cross section for $e^-e^- \to e^-e^-$ scattering is given by [20]

$$\mathrm{d}\sigma_{\text{Møller}} = \frac{4\pi e^4 m^4}{s(s-4m^2)} \, |F|^2 \, \mathrm{d}t \, \frac{\mathrm{d}\phi}{2\pi}, \tag{2.2}$$

where e is the elementary charge and $|F|^2$ is defined (for scattering off an unpolarized target) by the following relation:

$$\begin{aligned} |F|^2 = \frac{1}{4m^4} \Bigg[& \frac{1}{t^2} \left(\frac{s^2+u^2}{2} + 4m^2(t-m^2) \right) \\ & + \frac{1}{u^2} \left(\frac{s^2+t^2}{2} + 4m^2(u-m^2) \right) \\ & + \frac{4}{tu} \left(\frac{s}{2} - m^2 \right) \left(\frac{s}{2} - 3m^2 \right) \Bigg] \,. \end{aligned} \tag{2.3}$$

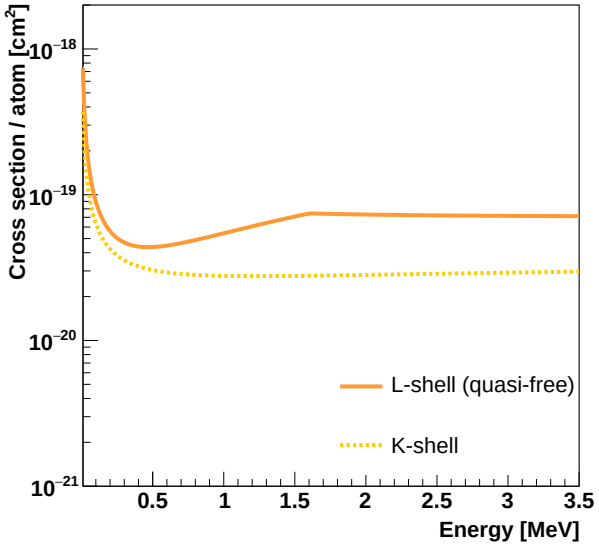

Figure 2.1: Total cross sections for electron–electron scattering in a stationary target made of beryllium, plotted as a function of beam kinetic energy. Dashed line: ionization cross section for the K-shell, calculated using [36]. Solid line: Møller scattering cross section for the L-shell (neglecting binding energy) integrated with a low-energy cutoff of 9 eV.

The differential cross section is divergent in the limit of 0° or 90° scattering angle (in the target reference frame, corresponding to $t \to 0$ and $u \to 0$, respectively). Nevertheless, if scattering off atomic electrons is considered, the binding energy of electrons in an atom can be used as a natural cutoff.

The total cross section for scattering off atomic electrons in a beryllium foil is shown in Fig. 2.1. Two different cases can be distinguished, since four electrons occupy two electron shells with different binding energies. The K-shell binding energy is approx. 112 eV [35]. The code of Bote et al. [36] was used to calculate the total ionization cross sections corresponding to scattering off K-shell electrons. The L-shell binding energy is much lower, approx. 9 eV [37], and the aforementioned code does not provide data for this case. It is, however, clear that given the low binding energy these electrons can be considered free to a good approximation. Therefore, in this case the theoretical Møller scattering cross section was integrated using the binding energy as an energy-transfer cutoff. For the probability of Møller scattering in the angular range corresponding to the polarization transfer experiment, see Section 6.3.2.

2.1.2. Polarization transfer

The initial state of two electrons (before the interaction) can be described by a density matrix $\hat{\rho}^{\text{in}}$, which is a product of density matrices of individual particles, as the states of colliding electrons are prepared separately. The elements of $\hat{\rho}^{\text{in}}$ can be written as

$$\rho^{\text{in}}_{(\tau_1,\tau_2),(\tau_1',\tau_2')}(q_1, q_2, q_1', q_2') = \rho^{1\,\text{in}}_{\tau_1\tau_1'}(q_1, q_1')\ \rho^{2\,\text{in}}_{\tau_2,\tau_2'}(q_2, q_2'), \tag{2.4}$$

where τ_i, τ_i', $i = 1, 2$, are the indices related to the spin part of the matrix and can take values $\pm 1/2$, while q_i, q_i' denote the four-momenta of the interacting electrons. If scattering of particles with well determined momenta is considered, matrix elements $\rho^{i\,\mathrm{in}}$ take the following form:

$$\rho^{i\,\mathrm{in}}_{\tau_i \tau_i'}(q_i, q_i') = \frac{2p_i^0}{\delta^3(\vec{0})}\, \delta^3(\vec{q_i} - \vec{p_i})\, \delta^3(\vec{q'}_i - \vec{p_i})\, \frac{1}{2}(\mathbf{1} + \vec{P_i} \cdot \vec{\sigma})_{\tau_i \tau_i'}, \tag{2.5}$$

where $\vec{P_i}$ and p_i denote the polarization vector and the four-momentum of the i-th electron, respectively; $\vec{\sigma} = (\sigma_1, \sigma_2, \sigma_3)$ and σ_k are the Pauli matrices.

The density matrix of the final state (after the interaction) of two electrons originating from Møller scattering, $\hat{\rho}^{\mathrm{out}}$, is obtained from

$$\hat{\rho}^{\mathrm{out}} = \frac{\hat{M}\hat{\rho}^{\mathrm{in}}\hat{M}^\dagger}{\mathrm{Tr}(\hat{M}\hat{\rho}^{\mathrm{in}}\hat{M}^\dagger)}, \tag{2.6}$$

where $\hat{M}$ is the scattering amplitude. The scattering amplitude matrix element can be found in literature [38] and the explicit form of $\hat{\rho}^{\mathrm{out}}$ in the paper by Caban et al. [20].

The outgoing electrons may be entangled in consequence of the scattering, so neither of them is found in a well-defined polarization state separately. Therefore, it is, in general, impossible to assign polarization vectors to the electrons after the scattering, because only their joint polarization state is well defined by the density matrix $\hat{\rho}^{\mathrm{out}}$. Nevertheless, one can use the reduced density matrices of the final state electrons to assign mean polarization vectors to both of them [21].

In order to calculate the mean polarization vector of the i-th secondary electron, a partial trace operation over the other one, j-th, was performed, yielding a reduced density matrix

$$\hat{\rho}_i^{\mathrm{out}} = \mathrm{Tr}_j \left(\hat{\rho}^{\mathrm{out}} \right). \tag{2.7}$$

Next, the mean polarization vector of the i-th electron, $\vec{P_i}$, was calculated as

$$\vec{P_i} = \mathrm{Tr} \left(\hat{\rho}_i^{\mathrm{out}} \cdot \vec{\sigma} \right). \tag{2.8}$$

When a 100% polarized beam is scattered off an unpolarized stationary electron, both electrons in the final state are partially polarized, which is illustrated in Fig. 2.2 for a transversely polarized 3 MeV beam. Shown is the polarization transfer defined as the length of the transverse polarization vector component of the scattered electron divided by the initial beam polarization. In the symmetric scattering configuration (90° scattering angle in the center-of-mass frame, corresponding to the laboratory scattering angle $\theta = 26.75°$ for an incident electron with kinetic energy of 3 MeV), both outgoing electrons have the same polarization due to the indistinguishability of the particles. The transverse polarization is equal to approx. 0.399 of the beam polarization, if the beam polarization vector lies in the Møller scattering plane, and approx. 0.382, if the beam polarization is perpendicular to the Møller scattering plane. However, in an asymmetric configuration, in particular, for very small scattering angles, the electron with higher energy inherits the majority of the incoming electron polarization.

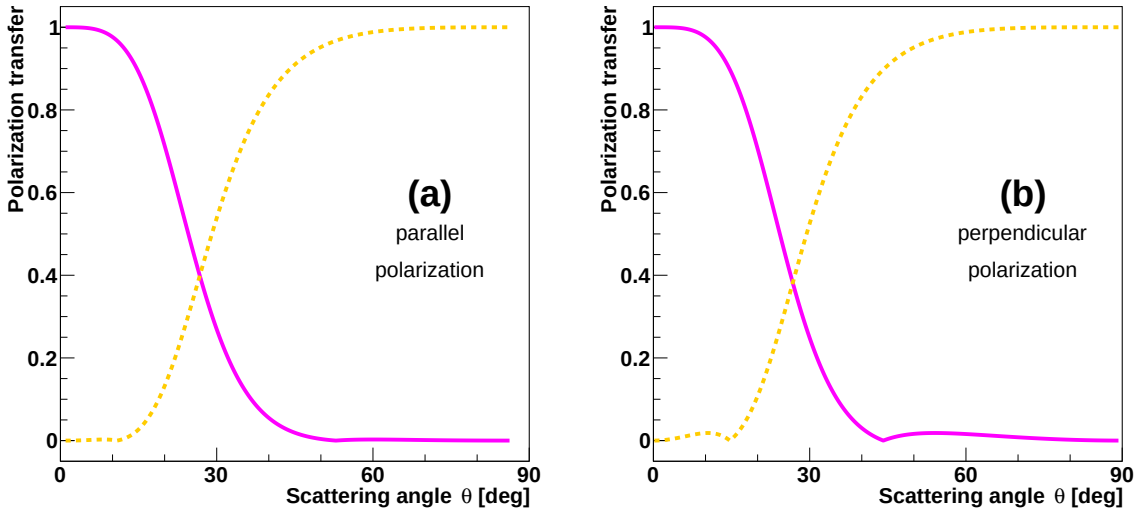

Figure 2.2: Polarization transfer from a transversely polarized 3 MeV beam electron to the secondary Møller electrons, (a) beam polarization in the Møller scattering plane, (b) beam polarization perpendicular to the Møller scattering plane. The polarization transfer (length of the transverse polarization vector component divided by the initial beam polarization) dependence on the scattering angle θ (measured in the laboratory frame of reference) is plotted with the solid line. The corresponding polarization of the second electron is plotted with a dashed line. Equal polarization sharing occurs for the symmetric scattering configuration ($\theta = 26.75°$ for incident electrons with 3 MeV kinetic energy, which corresponds to scattering at 90° in the center-of-mass frame).

In Fig. 2.3 one can also see that the joint polarization vector (the sum of the mean polarization vectors of both electrons) is not a unit vector, which indicates a certain degree of entanglement. The maximum of entanglement (minimum of joint polarization) corresponds to the symmetric scattering. It has been shown in [20] that negativity, which is a proper entanglement measure, reaches its maximum for the symmetric scattering angle independent of the beam energy. On the other hand, in case of symmetric scattering, the degree of entanglement increases with the decrease of the beam kinetic energy. In the zero-energy limit, the final state becomes a pure singlet state, which is demonstrated in the next section.

2.1.3. Spin correlations

While the measurement of the mean polarization allows the average spin state of individual electrons to be investigated, the measurement of spin correlations can give insight into the phenomenon of entanglement in relativistic Møller scattering.

For a state described by a density matrix $\hat{\rho}^{\text{out}}$, the correlation function can be calculated according to

$$\mathcal{C}(A,B) = \text{Tr}\left(\hat{A} \otimes \hat{B}\, \hat{\rho}^{\text{out}}\right), \tag{2.9}$$

and the $\mathcal{P}_{\alpha\beta}$ probabilities can be calculated according to

$$\mathcal{P}_{\alpha\beta} = \mathrm{Tr}\left(\hat{\Pi}_\alpha \otimes \hat{\Pi}_\beta \, \hat{\rho}^{\mathrm{out}}\right), \tag{2.10}$$

where $\hat{\Pi}_\alpha$ and $\hat{\Pi}_\beta$ are the projectors from the spectral decomposition of the $\hat{A}$ and $\hat{B}$ operators, corresponding to the eigenvalues α and β, respectively.

The spin-projection operators $2\vec{a}\hat{S}$ and $2\vec{b}\hat{S}$ have to be substituted for $\hat{A}$ and $\hat{B}$ in Eq. (2.9), in order to calculate the spin correlation function $C(\vec{a},\vec{b}) = \mathcal{C}(2\vec{a}\hat{S}, 2\vec{b}\hat{S})$. The Newton–Wigner form of the relativistic spin operator $\hat{S}$ is most commonly used. In one-particle subspace, in the special case when the Mott polarimetry method, sensitive only to the spin-projection on the direction perpendicular to the Mott scattering plane, is used for spin-projection measurement (cf. Section 2.2), the projection of the Newton-Wigner operator on a direction $\vec{n}$ takes the following form

$$\vec{S}(k,\vec{n}) = \frac{1}{2m}\left[m\vec{n}\cdot\vec{\gamma}\gamma^5 + i((\vec{n}\times\vec{k})\vec{\gamma})\gamma^0 - k^0\vec{n}\cdot\vec{\gamma}\gamma^0\gamma^5\right], \tag{2.11}$$

where m is the mass and k is the four momentum of the particle, $\gamma = (\gamma^0, \vec{\gamma})$ are the Dirac matrices and $\gamma^5 = i\gamma^0\gamma^1\gamma^2\gamma^3$.

The correlation function in case of Møller scattering of an electron beam off an unpolarized target(assuming the Mott polariemetry method for spin-projection measurement) is given by [20]

$$\begin{aligned} C(\vec{a},\vec{b}) = &\left[k_1^0 - m\right]\left[k_1^0 - p_1^0\right] \\ &\left[2\left(\vec{a}\cdot\vec{b}\right)\left(k_1^{0^2} - k_1^0\left(m + p_1^0\right) - m\left(m - 3p_1^0\right)\right) + \left(\vec{a}\cdot\vec{p_1}\right)\left(\vec{b}\cdot\vec{p_1}\right)\right] \\ &\Bigg[2\Big(k_1^0\left(m^3 - 3m^2p_1^0 - 6mp_1^{0^2} - 2p_1^{0^3}\right) - 2k_1^{0^3}\left(m + p_1^0\right) + \\ &+ 3k_1^{0^2}p_1^0\left(2m + p_1^0\right) + k_1^{0^4} + p_1^0\left(-m^3 + 4m^2p_1^0 + p_1^{0^3}\right)\Big)\Bigg]^{-1}, \end{aligned} \tag{2.12}$$

where p_1 denotes the four momentum of the beam electron, k_1 and k_2 are the four momenta of particles in the final state, m is the electron mass. The nonrelativisitic limit, obtained by expanding (2.12) around zero-energy, is

$$C(\vec{a},\vec{b}) = \left(3 - \frac{p_1^0 - m}{k_1^0 - m}\,\frac{p_1^0 - m}{p_1^0 - k_1^0}\right)^{-1}\vec{a}\cdot\vec{b}. \tag{2.13}$$

In the symmetric scattering configuration, $(k_1^0 - m) = (p_1^0 - m)/2$, it reduces to

$$C(\vec{a},\vec{b}) = -\vec{a}\cdot\vec{b}, \tag{2.14}$$

which depends only on the spin projection directions, and shows that in the zero-energy limit the electrons are in a pure singlet state.

The correlation function in case of Møller scattering of an electron beam off an unpolarized target, which is the simplest sufficient case that can be realized experimentally, is shown in Fig. 2.4 as a function of beam energy in the symmetric scattering

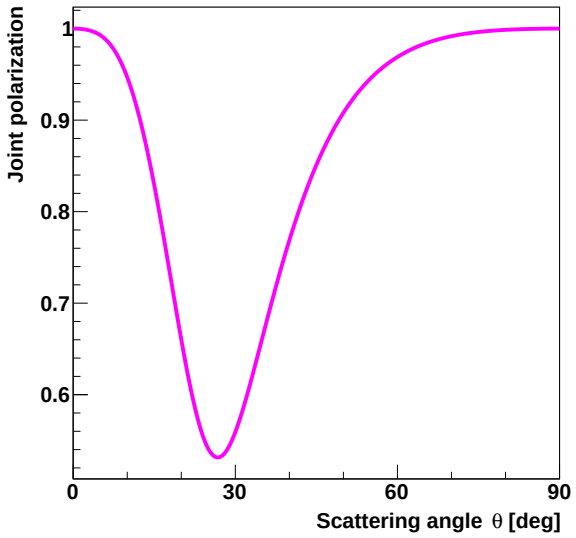

Figure 2.3: Polarization transfer from a transversely polarized 3 MeV beam electron to the secondary Møller electrons, with beam polarization in the Møller scattering plane. The length of the joint polarization vector of both electrons in the final state is shown as a function of the scattering angle θ. The minimum is observed for the symmetric scattering configuration ($\theta = 26.75°$ for incident electrons with 3 MeV kinetic energy).

configuration. The proposed experimental setup (to be discussed it details in Chapter 3) allows to perform the measurement for two different configurations of the $\vec{a}$ and $\vec{b}$ vectors: (A) both in the Møller scattering plane, and (B) at angles equal to 45° to the Møller scattering plane. The angle to the Møller scattering plane is sufficient to describe the orientations of the $\vec{a}$ and $\vec{b}$ vectors, since in both configurations they are assumed to be perpendicular to particle momenta due to the use of the Mott polarimetry method. In configuration A (both $\vec{a}$ and $\vec{b}$ vectors, on which the spins are projected, lie in the Møller scattering plane, and Møller scattering is symmetric with respect to the beam direction), the correlation function exhibits a strongly non–monotonic dependence on beam energy.

There are no experimental data on the spin correlations for relativistic particles with mass. The studies of the final spin state in Møller scattering of polarized electrons could allow for the first observation of the relativistic correction to the quantum spin correlation function, and for the verification of the unexpected, non–monotonic dependence on energy.

Even though the correlation function itself does not depend on beam polarization, the $P_{\pm\pm}$ probabilities do. The correlation probabilities in configuration A are shown in Fig. 2.5 as a function of beam energy. It can be seen that without primary beam polarization, the probabilities of obtaining the same spin projection results for both electrons (P_{++} and P_{--}) are equal. Beam polarization in the Møller scattering plane (with a nonzero component in the direction of the spin projection measurement) distinguishes between the two cases. The P_{++} probability with 85% beam polarization reaches approx. 0.43 compared to approx. 0.26 without beam polarization. The probabilities

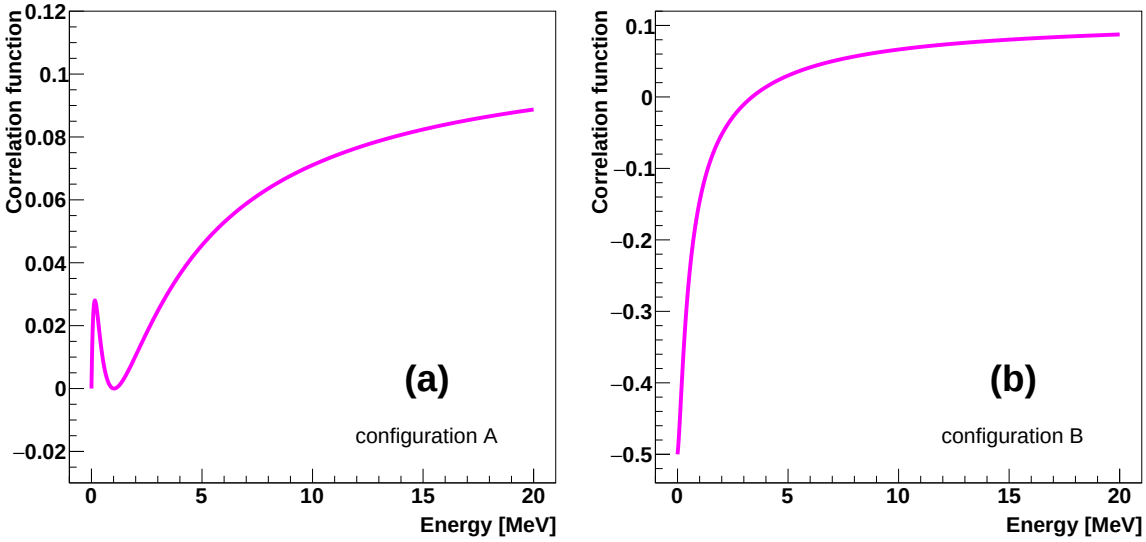

Figure 2.4: Dependence of the correlation function on beam energy for a pair of electrons originating from Møller scattering (theoretical predictions [20]) with (a) the $\vec{a}$ and $\vec{b}$ vectors (on which the spins are projected) in the Møller scattering plane, (b) $\vec{a}$ and $\vec{b}$ vectors at angles equal to 45° to the Møller scattering plane. The scattering is symmetric with respect to the beam direction.

of obtaining opposite spin projection results for both electrons (P_{+-} and P_{-+}) remain equal in both considered scenarios (they can be distinguished with a longitudinally polarized beam).

The same effects are observed in configuration B, which can be seen in Fig. 2.6. Without primary beam polarization, the same pairs of probabilities are equal. Beam polarization perpendicular to the Møller scattering plane (with a nonzero component in the direction of the spin projection measurement) distinguishes between P_{++} and P_{--}. The P_{++} probability with 85% beam polarization reaches approx. 0.36 compared to approx. 0.25 without beam polarization.

2.1.4. Relation between polarization transfer and spin correlations

The dependence of correlation probabilities on beam polarization is closely related to the polarization transfer discussed in Section 2.1.2.

The average spin projection of a single electron (polarization in the direction of the $\vec{a}$ or $\vec{b}$ vector) can be calculated from the probabilities by summing over the other electron,

$$P_1(\vec{a}) = \left(P_{++}(\vec{a},\vec{b}) + P_{+-}(\vec{a},\vec{b})\right) - \left(P_{-+}(\vec{a},\vec{b}) + P_{--}(\vec{a},\vec{b})\right), \tag{2.15a}$$

$$P_2(\vec{b}) = \left(P_{++}(\vec{a},\vec{b}) + P_{-+}(\vec{a},\vec{b})\right) - \left(P_{+-}(\vec{a},\vec{b}) + P_{--}(\vec{a},\vec{b})\right). \tag{2.15b}$$

This method gives identical results to the direct polarization transfer calculation, which confirms the consistency of the calculations.

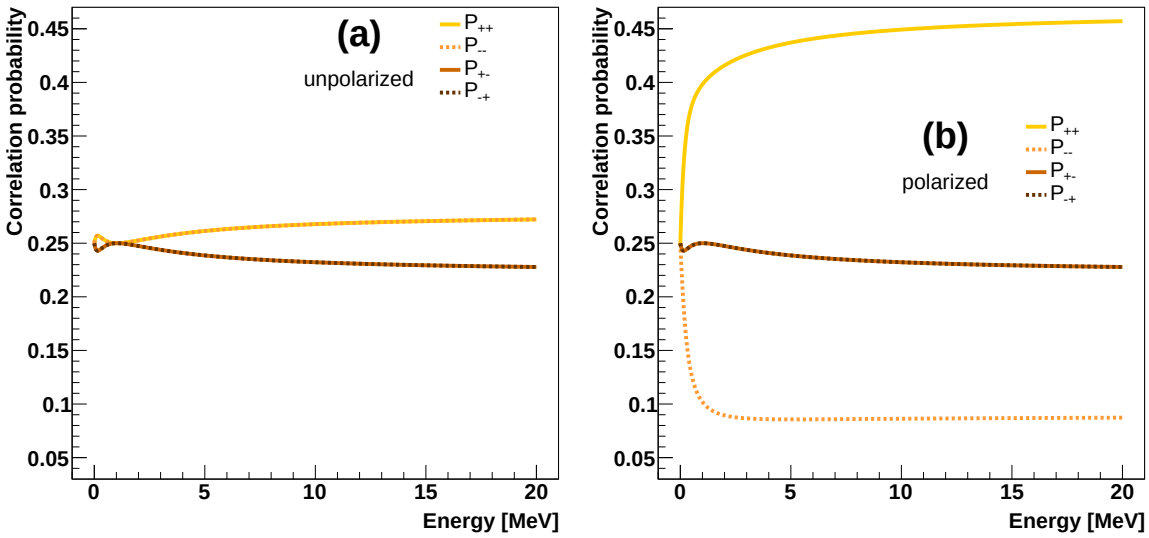

Figure 2.5: Dependence of the correlation probabilities on beam energy for a pair of electrons originating from Møller scattering (theoretical predictions [20]) with (a) unpolarized beam, (b) beam transversely polarized in 85% in the Møller scattering plane. Configuration A: the scattering is symmetric with respect to the beam direction, and the $\vec{a}$ and $\vec{b}$ vectors (on which the spins are projected) in the Møller scattering plane.

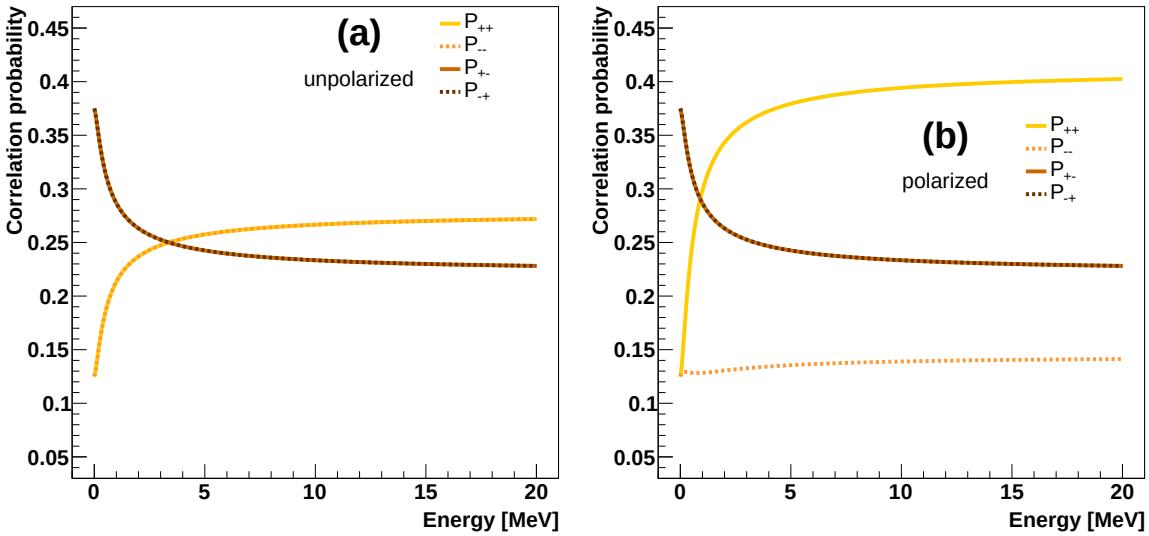

Figure 2.6: Dependence of the correlation probabilities on beam energy for a pair of electrons originating from Møller scattering (theoretical predictions [20]) with (a) unpolarized beam, (b) beam polarized in 85% perpendicular to the Møller scattering plane. Configuration B: the scattering is symmetric with respect to the beam direction, and the $\vec{a}$ and $\vec{b}$ vectors (on which the spins are projected) at angles equal to 45° to the Møller scattering plane.

The above equations, together with the correlation function definition (1.2) and the normalization condition (sum of probabilities must be equal to 1), form a set of four linear equations, which can be inverted to express the correlation probabilities in terms of the correlation function and polarization transfer,

$$P_{++}(\vec{a},\vec{b}) = \frac{1}{4}\left(C(\vec{a},\vec{b}) + P_1(\vec{a}) + P_2(\vec{b}) + 1\right), \tag{2.16a}$$

$$P_{+-}(\vec{a},\vec{b}) = \frac{1}{4}\left(-C(\vec{a},\vec{b}) + P_1(\vec{a}) - P_2(\vec{b}) + 1\right), \tag{2.16b}$$

$$P_{-+}(\vec{a},\vec{b}) = \frac{1}{4}\left(-C(\vec{a},\vec{b}) - P_1(\vec{a}) + P_2(\vec{b}) + 1\right), \tag{2.16c}$$

$$P_{--}(\vec{a},\vec{b}) = \frac{1}{4}\left(C(\vec{a},\vec{b}) - P_1(\vec{a}) - P_2(\vec{b}) + 1\right). \tag{2.16d}$$

The correlation probabilities depend both on the spin correlation function and the average polarization. If only one probability is measured, the contributions from both effects cannot be distinguished.

It is now clear from Eqs. (2.16) why the P_{+-} and P_{-+} probabilities are equal in both considered experimental configurations. Due to the symmetry of the arrangement of the $\vec{a}$ and $\vec{b}$ vectors, and electron polarizations, the difference of average polarizations cancels out in both probabilities.

Let us analyze the limit of zero scattering angle in case when the beam electron is 100% transversely polarized. It was shown in Fig. 2.2 that one of the electrons in the final state remains 100% transversely polarized and the other one is unpolarized. In such case, setting the $\vec{a}$ vector along the primary-beam polarization, only the P_{++} and P_{+-} probabilities take nonzero values and the correlation function is equal to zero, since there is no possibility for correlations if at least one polarization is known with certainty. This simple example demonstrates that some predictions regarding spin correlations can be made with just the knowledge of the polarization transfer itself.

The above reasoning can be easily generalized to the case of arbitrary polarizations. Taking into account the normalization conditions (the probabilities take values between 0 and 1), one finds by simple algebraic transformations of Eqs. (2.16) that the correlation function must fulfill the relation

$$-1 + \left|P_1(\vec{a}) + P_2(\vec{b})\right| \leq C(\vec{a},\vec{b}) \leq 1 - \left|P_1(\vec{a}) - P_2(\vec{b})\right|. \tag{2.17}$$

The polarization sum and difference dependence on the scattering angle is shown in Fig. 2.7(a) in the configuration corresponding to Fig. 2.2(a) (transverse beam polarization, $\vec{a}$ and $\vec{b}$ vectors in the Møller scattering plane). The corresponding limits on the correlation function, calculated from Eq. (2.17), are shown in Fig. 2.7(b). It can be seen that the range of allowed correlation function values is strongly restricted when the scattering angle approaches 0 or $\pi/2$, due to the large mean polarization. The symmetric scattering angle corresponds to a minimum of the polarization sum, which results in the weakest constraints on the correlation function.

The correlation function [20] exhibits a strongly nonmonotonic dependence on the scattering angle, which is shown in Fig. 2.8 for beam kinetic energy $T = 2m$ (corresponding to the minimum of the correlation function for symmetric scattering, cf.

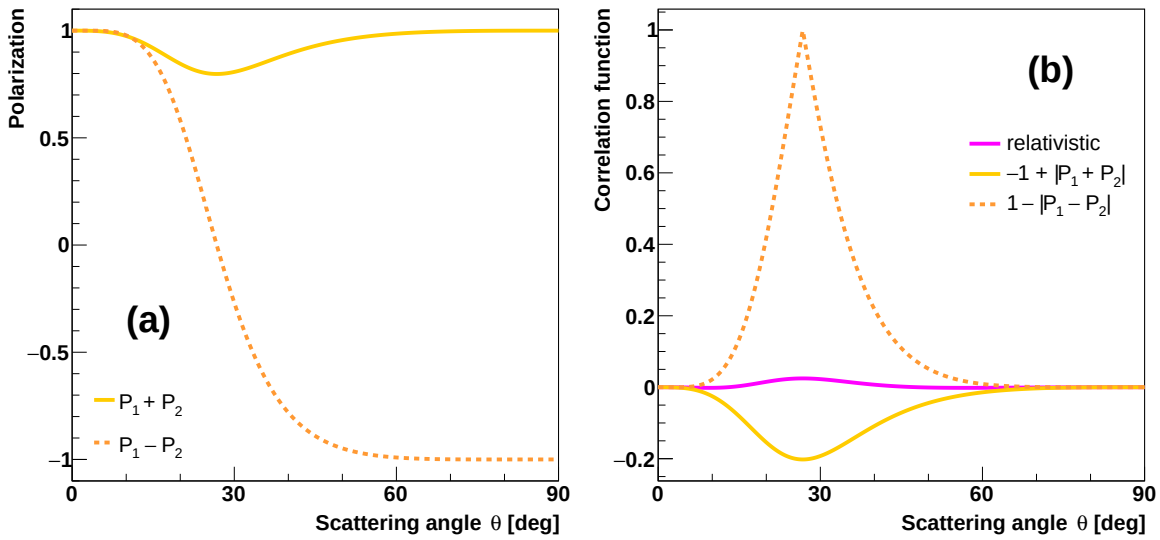

Figure 2.7: Dependence of the sum and difference of mean polarizations (a), correlation function (theoretical predictions [20]) and limits from polarization transfer, Eq. (2.17), (b) on scattering angle for a pair of electrons originating from Møller scattering of a 3 MeV beam, 100% transversely polarized in the Møller scattering plane. The $\vec{a}$ and $\vec{b}$ vectors (on which the spins are projected) lie in the Møller scattering plane.

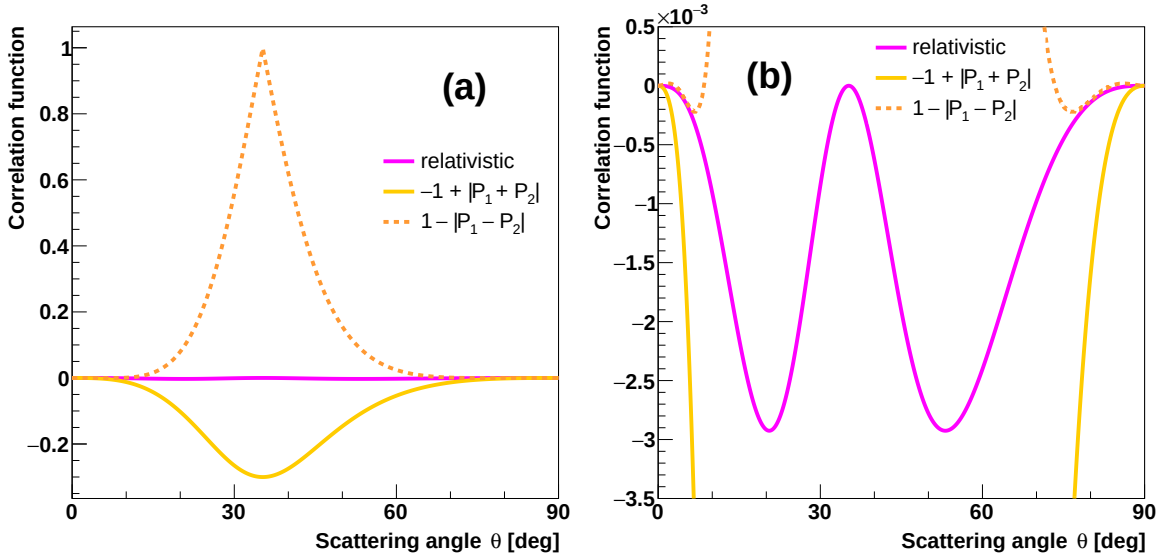

Figure 2.8: Dependence of the correlation function (theoretical predictions [20]) and limits from polarization transfer, Eq. (2.17), on scattering angle for a pair of electrons originating from Møller scattering, with a 100% transverse primary-beam polarization in the Møller scattering plane and beam kinetic energy $T = 2m$. The $\vec{a}$ and $\vec{b}$ vectors (on which the spins are projected) lie in the Møller scattering plane. Shown in the right panel is the same dependence with the extended vertical scale.

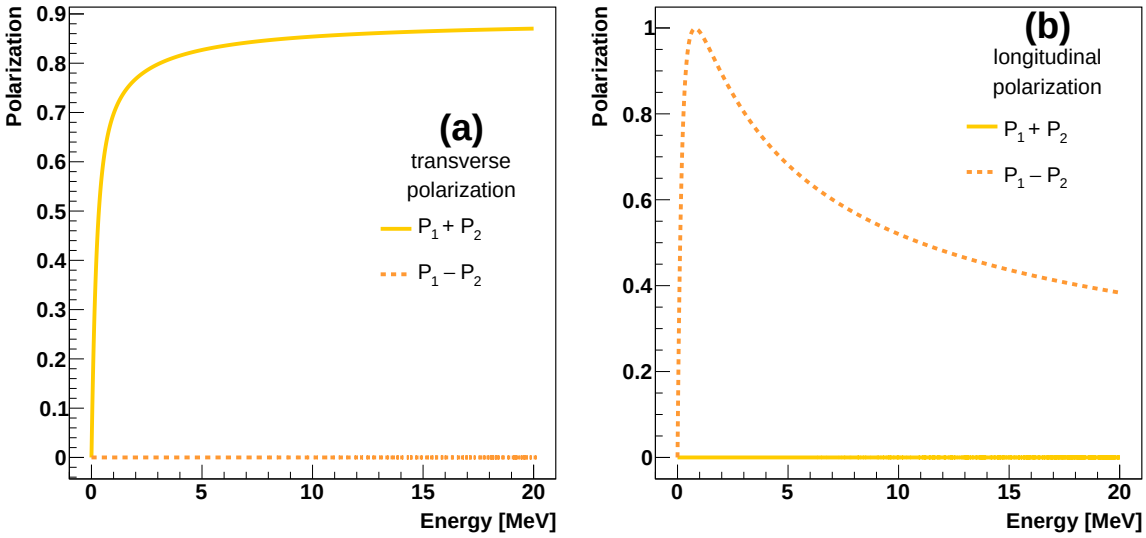

Figure 2.9: Dependence of the sum and difference of mean polarizations on beam energy for a pair of electrons originating from Møller scattering with (a) 100% transverse primary-beam polarization in the Møller scattering plane, (b) 100% longitudinal primary-beam polarization. Configuration A: the scattering is symmetric with respect to the beam direction, and the $\vec{a}$ and $\vec{b}$ vectors (on which the spins are projected) in the Møller scattering plane.

Fig. 2.4(a)) and the same arrangement of polarization and spin projection directions as in the previous example. The value for 0 and $\pi/2$ scattering angle is zero, as discussed above. It can be seen that the correlation function has a maximum in the symmetric scattering angle (approx. 35°) and two minima for intermediate angles. The limits calculated according to Eq. (2.17) show that the correlation function must decrease below zero for scattering angles above 0 and below $\pi/2$ due to the large difference of polarizations $|P_1(\vec{a}) - P_2(\vec{b})|$.

A similar analysis can be performed to explain the non-monotonic dependence of the correlation function on energy, which has a local minimum in configuration A for beam kinetic energy $T = 2m$. It is interesting to note that, since the correlation function does not depend on beam polarization, the limits established with all possible polarizations must be fulfilled simultaneously.

The polarization transfer dependence on beam energy is shown in Fig. 2.9 for two primary-beam polarizations, longitudinal and transverse in the Møller scattering plane, and the $\vec{a}$ and $\vec{b}$ vectors in the Møller scattering plane. The sum and difference of polarizations reaches the largest values for the former and the latter beam polarization, respectively. Therefore, it is sufficient to analyze these two scenarios.

The correlation function dependence on beam energy is shown in Fig. 2.10 together with the upper limit calculated according to Eq. (2.17). It can be seen that the decrease of the correlation function in configuration A for energies around approx. 800 keV is related to the low upper limit due to the large difference of polarizations $|P_1(\vec{a}) - P_2(\vec{b})|$ (see expanded view in Fig. 2.10(c)).

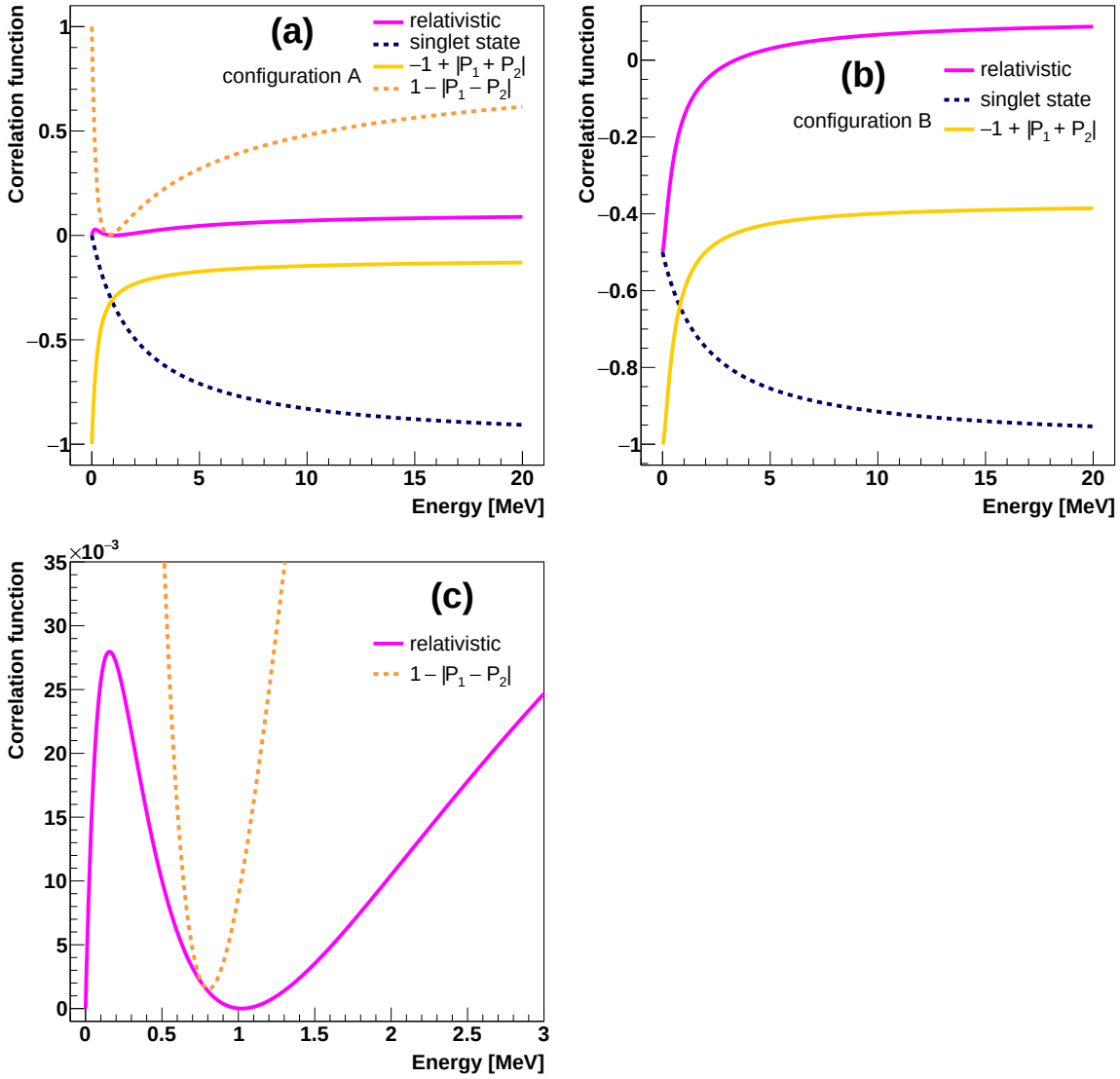

Figure 2.10: Dependence of the correlation function (theoretical predictions [20]) and limits from polarization transfer, Eq. (2.17), on beam energy for a pair of electrons originating from Møller scattering with (a) the $\vec{a}$ and $\vec{b}$ vectors (on which the spins are projected) in the Møller scattering plane, (b) $\vec{a}$ and $\vec{b}$ vectors at angles equal to 45° to the Møller scattering plane; (c) is an enlarged fragment of panel (a). Predictions for the singlet state (nonrelativistic limit) are shown for comparison. The scattering is symmetric with respect to the beam direction.

The predictions corresponding to the singlet state (nonrelativistic limit), which also depend on energy due to the different configuration of the $\vec{a}$ and $\vec{b}$ vectors (perpendicular to particle momenta), are also shown for comparison in Fig. 2.10. It can be seen that the singlet state is excluded by the lower limit on correlation function for energies above approx. 1 MeV. It should also be noted that the beam energy of 3 MeV, used in the proposed experiment, is appropriate to distinguish between the classical and relativistic approaches.

In conclusion, even though the full measurement of the correlation function is necessary to ultimately confirm the theoretical predictions, the measurement of the average polarization of electrons in the final state can as well give valuable insight in the correlation phenomena by constraining the range of allowed correlation-function values.

2.2. Mott scattering

2.2.1. Cross section

The study of the polarization transfer in Møller scattering of a polarized electron beam comes down to the measurement of the electron spin projection on a given direction in space. As already mentioned above, Mott polarimetry is the standard method in the MeV energy range. It is based on measuring the azimuthal asymmetry, arising from the spin–orbit interaction, in scattering of a polarized electron beam off thin targets made of heavy elements [39]. An exhaustive overview of the theoretical formalism can be found in the work of Kessler [40]. The differential cross section for Mott scattering off a single nucleus is given by

$$\left(\frac{d\sigma}{d\Omega}\right)_{\text{Mott}} = \left(\frac{d\sigma}{d\Omega}\right)_0 \left(1 + S(E,\theta)\vec{P}\cdot\vec{n}\right), \tag{2.18}$$

where the cross section $(d\sigma/d\Omega)_0$ corresponds to the scattering of unpolarized electrons, $S(E,\theta)$ is the Sherman function describing the analyzing power of Mott scattering, E is the kinetic energy of the incoming electron, θ is the polar scattering angle, $\vec{P}$ is the incident-electron polarization vector and $\vec{n}$ is the unit vector normal to the scattering plane,

$$\vec{n} = \frac{\vec{p}\times\vec{p}'}{|\vec{p}\times\vec{p}'|}, \tag{2.19}$$

where $\vec{p}$ and $\vec{p}'$ denote the momenta of the incoming and scattered electron, respectively.

The unpolarized cross section is determined by two scattering amplitudes f and g,

$$\left(\frac{\mathrm{d}\sigma_{\text{Mott}}}{\mathrm{d}\Omega}\right)_0 = |f(E,\theta)|^2 + |g(E,\theta)|^2, \tag{2.20}$$

where $f(E,\theta)$ is the spin–conserving amplitude and $g(E,\theta)$ is the spin–flip amplitude. They can be calculated theoretically under assumptions regarding details of atomic and nuclear structure; the formalism was first given by Sherman [41].

2.2.2. Polarization transfer

The change of the electron polarization in a single Mott scattering event is described by a relatively simple equation,

$$\vec{P}' = \frac{(\vec{P}\cdot\vec{n} + S(E,\theta))\vec{n} + T(E,\theta)\vec{n}\times(\vec{n}\times\vec{P}) + U(E,\theta)(\vec{n}\times\vec{P})}{1 + S(E,\theta)\vec{P}\cdot\vec{n}}, \tag{2.21}$$

where $\vec{P}'$ is the polarization vector after the scattering. It can be expressed in terms of the same scattering amplitudes, according to the following relations [40]:

$$S(E,\theta) = i\frac{fg^* - f^*g}{|f|^2 + |g|^2}, \tag{2.22a}$$

$$T(E,\theta) = \frac{|f|^2 - |g|^2}{|f|^2 + |g|^2}, \tag{2.22b}$$

$$U(E,\theta) = \frac{fg^* + f^*g}{|f|^2 + |g|^2}. \tag{2.22c}$$

Note that the quantities S, T and U are not independent ($S^2 + T^2 + U^2 = 1$).

2.2.3. Computation of the scattering amplitudes

As has been shown in the previous sections, the two scattering amplitudes are the only quantities necessary to calculate the final state of the electron after Mott scattering, since they determine the Sherman function (azimuthal asymmetry) and the change of the polarization vector, as well as the cross section for unpolarized electron–nucleus scattering. They are obtained from the Dirac equation with the appropriate nuclear potential.

In this work the ELSEPA package [42] – a numerical implementation of the formalism originally proposed by Sherman [41] – that is also a source of data for a NIST reference database [43], was used to calculate the scattering amplitudes. The numerical solution is obtained by a relativistic (Dirac) partial–wave analysis in a central potential, according to the following formulae [44]:

$$f(\theta) = \frac{1}{2ik}\sum_{l=0}^{\infty}\left((l+1)\left(\exp(2i\delta_{\kappa=-l-1}) - 1\right) + l\left(\exp(2i\delta_{\kappa=l}) - 1\right)\right)P_l(\cos\theta), \tag{2.23a}$$

$$g(\theta) = \frac{1}{2ik}\sum_{l=0}^{\infty}\left(\exp(2i\delta_{\kappa=l}) - \exp(2i\delta_{\kappa=-l-1})\right)P_l^1(\cos\theta), \tag{2.23b}$$

where k is the wave number corresponding to a given momentum, P_l and P_l^1 are Legendre polynomials and associated Legendre functions, respectively, and δ_κ are phase shifts representing the large–r behavior of the Dirac spherical waves.

The potential assumed by default in the calculations corresponds to the Fermi distribution of nuclear charge density [45]. The nuclear potential is modified by the presence of atomic electrons, which shield the nucleus. The atomic-electron density is obtained from numerical results of relativistic Dirac–Fock calculations [46]. Another

contribution comes from approximate exchange correction. The effect is commonly known from non–relativistic bound state calculations; here it represents the case when the scattered electron exchanges places with an atomic electron, which gives a minor contribution to the potential. The last correction arises from the presence of neighboring atoms in a macroscopic target material, which modifies the scattering potential with respect to the value for a single atom (in particular for large impact parameters). In ELSEPA this effect is described according to the muffin–tin model [47], which can be switched on if desired (for details of the implementation see [42]). In this model the electron cloud is assumed to be confined in a sphere of a diameter equal to the average distance between atoms, and the presence of the nearest neighboring atom is taken into account in the potential. This way the potential is continuous in the whole target volume.

Details on the simulation of the Mott polarimeter analyzing power, based on the scattering amplitudes calculated with the ELSEPA package [42], are given in Chapter 5.

Chapter 3

Experimental setup

The general concept of the polarization transfer measurement, using the Mott polarimetry method, is presented in this chapter. The design of the experimental setup is discussed.

3.1. Experimental method

Using the Mott polarimetry method, the polarization measurement can be performed with two detectors, denoted L and R, placed symmetrically at an angle θ with respect to the beam axis (i.e., with opposite directions of the $\vec{n}$ vector in Eq. (2.18)). The count-rate asymmetry A is defined as

$$A = \frac{N_L - N_R}{N_L + N_R}, \tag{3.1}$$

where N_L and N_R are the count rates of electrons Mott-scattered off the target, recorded in the L and R detectors.

Alternatively, the measurement can be done with a single detector by reversing the beam polarization direction; the asymmetry A is then defined as

$$A = \frac{N^{\uparrow} - N^{\downarrow}}{N^{\uparrow} + N^{\downarrow}}, \tag{3.2}$$

where $N^{\uparrow}$ and $N^{\downarrow}$ are the count rates for opposite beam polarizations.

If the measurement is performed using two detectors, placed symmetrically with respect to the beam axis, and the beam polarization direction is being reversed, the combined asymmetry can be calculated using the formula [48]

$$A = \frac{1 - \sqrt{Q}}{1 + \sqrt{Q}}, \tag{3.3a}$$

with

$$Q = \frac{N_L^{\uparrow} N_R^{\downarrow}}{N_L^{\downarrow} N_R^{\uparrow}}. \tag{3.3b}$$

The advantage of this approach is that, when the polarization direction is reversed periodically, the detector efficiencies do not contribute to the uncertainty, since they cancel out in Eqs. (3.2) and (3.3).

The polarization-vector component perpendicular to the scattering plane can be related to the count-rate asymmetry A, arising from the polarization-dependent term in Eq. (2.18), as follows:

$$\vec{P} \cdot \vec{n} = \frac{A}{S_{\text{eff}}(E, \theta)}, \tag{3.4}$$

where the theoretical value of the Sherman function S, cf. Eq. (2.18), appropriate for scattering off a single atom, was replaced with its effective value S_{eff}, in which multiple interactions of the electron in the target material are taken into account.

While the theoretical Sherman function can be calculated numerically, for example, with the ELSEPA package [42], the calculation of the effective Sherman function requires a full Monte Carlo simulation with particle tracking and polarization transfer calculations. Large differences between the theoretical and effective Sherman function are to be expected, in particular, when thick targets are used, resulting in a large contribution of multiple scattering. For the results presented in this thesis, the effective Sherman function was obtained with a simulation performed with the Geant4 toolkit [49] supplied with a dedicated Mott scattering model [33] (cf. Chapter 5).

3.2. Polarization transfer experiment

The experimental setup used in the presented study is shown schematically in Fig. 3.1 in the single-polarimeter configuration of the polarization transfer experiment. Møller scattering was realized by scattering a polarized electron beam off atomic electrons in a target made of beryllium, 100 μm thick. The Møller target thickness was chosen based on the Monte Carlo simulation results, which is discussed in Section 6.3.2.

In order to eliminate scattering off air atoms, a vacuum of approx. 10^{-7} mbar was maintained inside the setup. The beryllium foil was provided by the manufacturer as a vacuum-tight assembly in form of a standard CF40 flange. The target thickness was sufficient to withstand the pressure difference between accelerator vacuum and atmospheric pressure, so that the accelerator would not be affected even in case of a vacuum failure in the experiment.

The electrons scattered off the beryllium target passed through two pipes (below called legs), positioned at an angle of 26.75° with respect to the primary beam direction, corresponding to the symmetric Møller scattering at 3 MeV beam energy. One leg was equipped with a Mott polarimeter, see Fig. 3.1, 336 mm downstream from the beryllium target (for more details refer to Fig. B.1). The other leg was terminated with a detector pointing directly at the beryllium target, below referred to as the tagging counter. Copper collimators placed in the legs accepted Møller scattering events close to the symmetric configuration only (in the range 26.75° ± 1.5°, corresponding to a solid angle of 8.6×10^{-3} sr, cf. Fig. B.2).

The scattering angle range of Møller scattering and the distance between the Møller and Mott targets are not independent of each other. Both the increase of the angular range, and of the distance between the targets, lead to an increase of the diameter

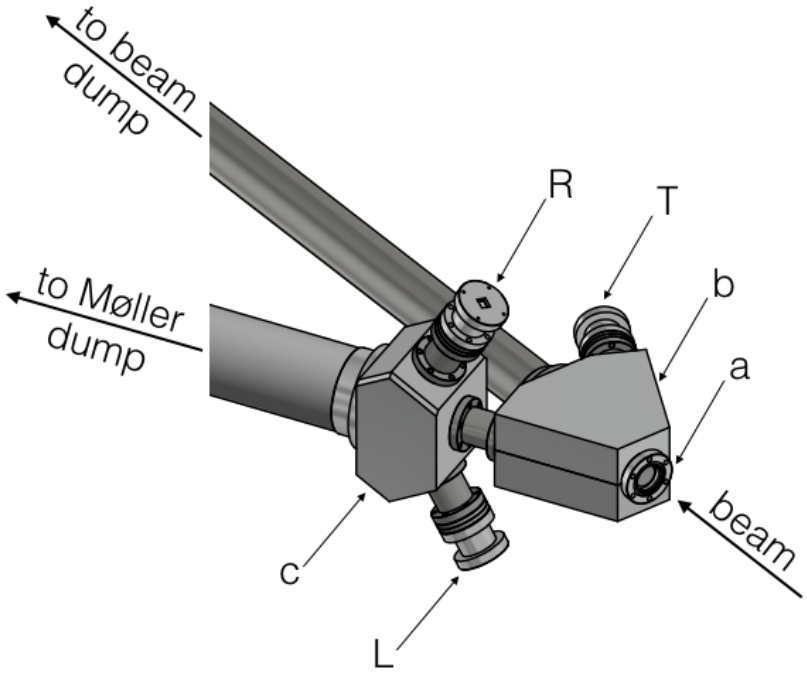

Figure 3.1: Drawing of the experimental setup in configuration A (vertical Mott scattering plane, see text for details); a – Møller (Be) target, b – Møller scattering chamber, c – Mott scattering chamber, T – tagging counter, L and R – detectors in the Mott polarimeter. The shielding and the full length of the dump pipes are not shown.

of the secondary beam spot on the Mott target. The smallest distance between the targets providing sufficient space for the Mott scattering chamber was used. The gold targets at our disposal were of 30 mm diameter. The largest scattering angle range providing that all electrons passing through the collimators fit on the Mott target was chosen.

Beam electrons passing through the beryllium target (scattered at small angles) were absorbed in a beam-dump material (graphite and aluminum) approx. 2 m downstream. The diameter of the pipe leading to the beam dump was 66 mm. The largest possible value (taking into account geometrical limitations) was chosen intentionally, to minimize background due to electron scattering off the beam pipe. The divergence of the electron beam after passing through the beryllium target was modeled with a Monte Carlo simulation (cf. Section 6.3.1).

The polarization of one of the electrons in the final state of Møller scattering, as well as the polarization of beam electrons (Mott-scattered off the beryllium target), could be measured in the Mott polarimeter (for technical details refer to Figs. B.3 and B.4 in Appendix B). Collimators in the Mott polarimeter restricted the measurement to electrons backscattered off a 9.9 μm thick gold target at an angle of $120^\circ \pm 5^\circ$ (corresponding to the solid angle of 9.5×10^{-2} sr). The target thickness, scattering angle, and angular range of Mott scattering was optimized using a dedicated Monte Carlo simulation taking into account polarization transfer, which is discussed in Section 5.3.

An aluminum frame holding the gold target was mounted in one slot of an aluminum

Figure 3.2: Photograph of the beam spot image on the beryllium oxide window.

ladder, which could be moved remotely between two positions (cf. Fig. B.5). The other slot contained an empty target frame identical to that holding the gold foil. The position of the ladder was changed periodically, allowing us to measure the empty-target background, which was then subtracted from the data acquired with the gold foil. The target ladder was controlled using compressed air. The target ladder mechanism was provided by TU Darmstadt (used previously in another experiment).

The same mechanism was used to move the target ladder holding the beam viewer screen, placed upstream from the beryllium target. The beam viewer screen was made of beryllium oxide, which produces light when hit by electrons. The screen was observed with a camera through a glass window; an example image is shown in Fig. 3.2. The marks on the screen were used to move the beam spot to the geometrical center at the beginning of the experiment, and to periodically monitor the beam position. The false asymmetry arising when the beam spot is not placed in the geometrical center of the beryllium target was modeled with a Monte Carlo simulation (cf. Section 6.4.3).

When the electrovalve was disconnected, or when there was no air pressure in the system, springs held the target ladders in the positions corresponding to the gold target in place and beam viewer out of the beamline (this way, the experiment could be, in principle, continued in case of a failure). When the valve was powered on, the compressed air moved the target ladder (compressing the spring), allowing us to replace the gold target with an empty target frame, or to move the beam viewer in.

Electrons passing through the gold target (scattered at small angles) were absorbed in a Møller dump material (plastic). The diameter of the pipe leading to the Møller dump was 100 mm. Again, the large diameter was chosen due to the divergence of the electron beam after passing through two targets (a similar effect was also discussed in [50]).

The inside walls of the Mott scattering chamber, as well as the pipes leading to the

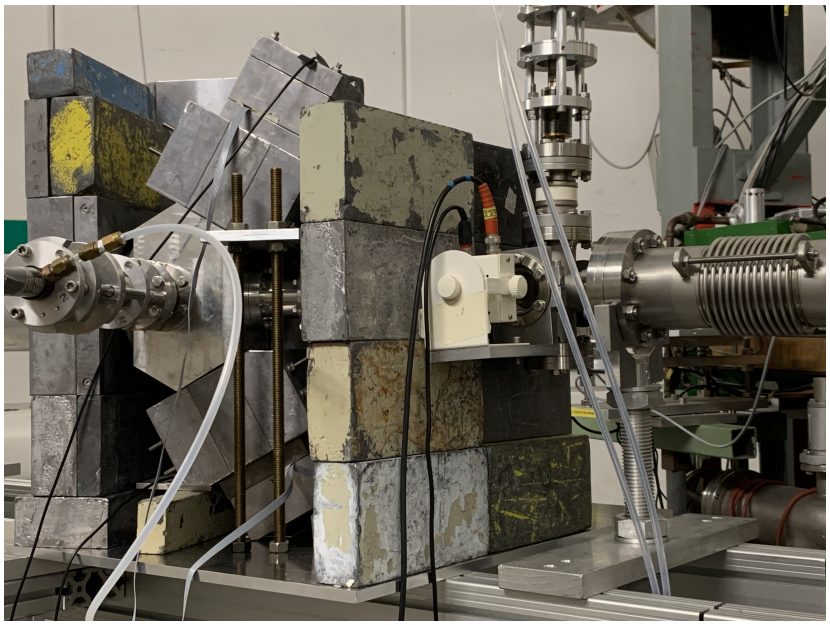

Figure 3.3: A photograph of the experiment installed in the beamline of the Mainzer Mikrotron accelerator.

dumps, were covered with graphite in order to reduce backscattering. For practical reasons, the scattering chambers were made of PA6 (AW-2017A) aluminum alloy. It is well suited for machining, but contains, among other elements, $0.6\% - 0.8\%$ Fe, $3.5\% - 4.5\%$ Cu, $0.4\% - 1.0\%$ Mn. In the standard Mott polarimeter operating at MAMI [50], the Mott scattering chamber made of very pure aluminum was compared to one made of a standard aluminum alloy containing a few per cent of heavier elements (copper, lead, iron). It was found that the use of the latter material substantially increased background [V. Tioukine, private communication]. The background conditions could be improved in the future with the use of an alloy with a reduced content of heavy elements.

The surroundings of the Mott polarimeter, the whole space between the detectors and the beam pipe in particular, were packed with lead bricks to shield against the external background. Some of the bricks were machined to match the shapes of polarimeter elements (cf. Figs. B.1, B.6, and B.7). The shielding was made of approx. 40 standard lead bricks (50 mm $\times$ 100 mm $\times$ 200 mm). The total weight was of the order of 450 kg. The experimental setup and the shielding were placed on two aluminum plates, 10 mm thick, attached to the aluminum profiles of the main beamline support of the accelerator. A photograph of the experimental setup with the shielding, installed on beam, is shown in Fig. 3.3.

The measurements were performed in two configurations of the Mott polarimeter, corresponding to different beam polarization orientations: (A) horizontal beam polarization (in the Møller scattering plane) and vertical Mott scattering plane and (B) vertical beam polarization (perpendicular to the Møller scattering plane) and Mott scattering plane at an angle of 45° to the Møller scattering plane. Both configurations are shown schematically in Fig. 3.4. The asymmetry reaches its maximum when the

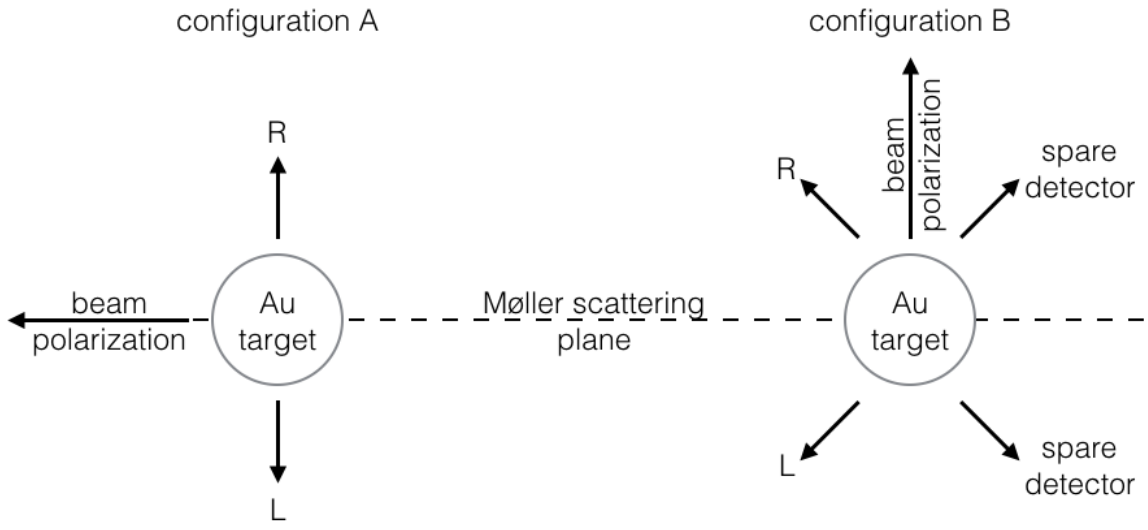

Figure 3.4: Schematic illustration of both experimental configurations (cross section in the gold-target plane, perpendicular to the direction of the Møller-electrons stream); L and R denote the locations of the detectors in the Mott polarimeter.

polarization vector is perpendicular to the Mott scattering plane, cf. Eq. (3.4). Thus, the best resolution in configuration B would be achieved with a horizontal Mott scattering plane, but this was not possible in the present polarimeter design for geometrical reasons (one of the detectors would coincide with the beam pipe).

In configuration B, owing to the 45° angle between the Mott and Møller scattering planes, and the symmetry with respect to the polarization vector direction, there are four equivalent directions of measurement in the Mott polarimeter. The background originating from electrons scattered off the beryllium target towards the beam pipe and other parts of the setup resulted in significantly different background conditions in detectors placed close to and far from the beam axis, despite thick shielding. The additional symmetry allowed us to place the detectors in the pair of locations subject to the lowest level of background, more distant from the beam pipe.

The scattered electrons were detected using scintillation counters. The light from the scintillator (Nuclear Enterprises NE200) was collected with a plexiglass lightguide. A silicon photomultiplier (SiPM) sensor was used to detect the scintillation light. In case of standard photomultiplier tubes (PMT), whose entrance window (and photocathode) is typically round, a simple conical lightguide could be used. In case of the SiPMs, which was of a square shape, a dedicated lightguide, which provided a smooth transition between the round shape of the scintillator and the square shape of the detector, was designed (cf. Fig. B.8). The lightguide assembly was placed in an aluminum housing, matching its complicated shape, to which the PCB holding the SiPM sensor was attached. A CF40 flange with a glass window (commercially available from LewVac) was placed between the scintillator and the lightguide, thus the vacuum was closed at that point, allowing us to replace the SiMP in case of a failure without breaking the vacuum.

Short response time and pulse width ensured precise timing required for a coinci-

dence trigger of one of the polarimeter detectors and the tagging counter, used to record Møller scattering events. The pulse height analysis allowed for an approximate energy calibration, sufficient to distinguish the electrons originating from Møller scattering from scattered beam electrons, whose energy is on average twice as high.

Chapter 4

Electronics and data acquisition

The detectors, trigger and readout electronics, as well as the data acquisition concept, are described in this chapter. Results of detector tests are also shown.

4.1. Detectors

4.1.1. Preliminary research

Photomultiplier tubes (PMT) have been widely used to convert light (for example generated in a scintillation process) into an electric signal. The principle of operation is based on the photoelectric effect, by means of which electrons are ejected from the photocathode hit by photons. Subsequently, electrons are multiplied thanks to secondary emissions from several electrodes (dynodes), between which the electrons are accelerated.

Initially, the polarimeter was tested on beam with ET Enterprises 9108B PMTs (with HV3020AN base). However, the PMTs exhibited a serious degradation effects after a few days of beam time, resulting in the drift of the signals towards lower amplitudes and a cutoff of the low-energy part of the spectrum. The tagging counter signal amplitude spectrum is shown in Fig. 4.1 for the first and last test run, separated by approx. 60 hours of data acquisition with the detector exposed to the flux of particles scattered off the beryllium target at approx. 27 nA beam current. The positions of both peaks (1.5 MeV Møller electrons and 3 MeV electrons from Mott scattering of beam electrons in the beryllium target, called *beam peak* in the following), obtained from the fits to the signal amplitude spectra, are plotted as a function of time in Fig. 4.2. It can be seen that the Møller peak position decreased by approx. 20% over a relatively short period of time, below 60 hours.

In conclusion, it was found that the initially considered detector technology is not suitable for regular data acquisition in the experiment. Due to the rapid degradation of the PMTs, a decision was made to investigate the suitability of available SiPM dectectors for a replacement. An additional benefit would be much reduced detector size, which would allow for experimental configurations impossible with PMTs due to geometrical reasons.

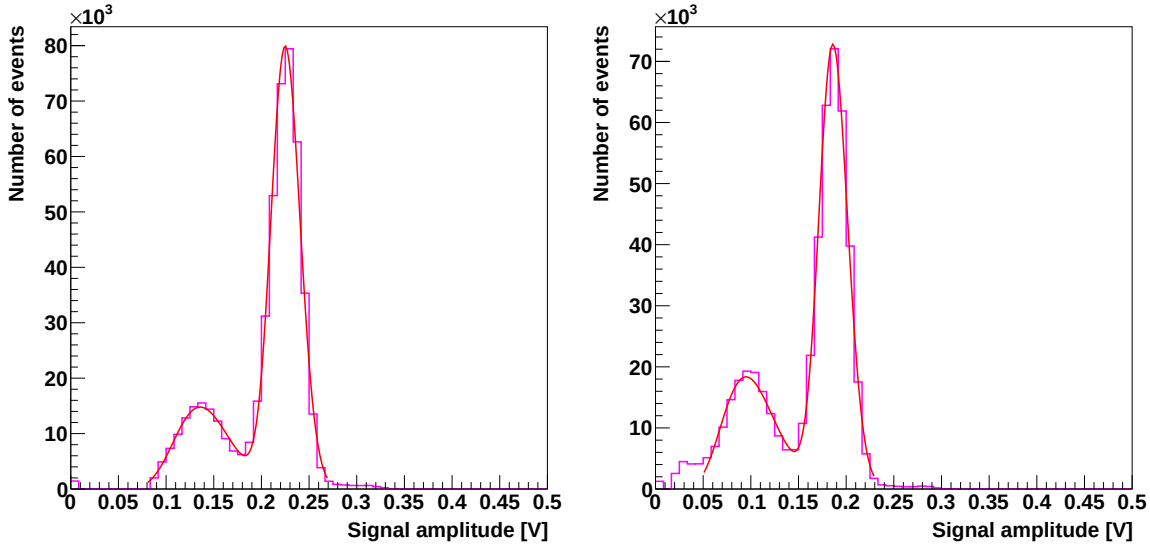

Figure 4.1: Signal amplitude spectrum in the tagging counter equipped with a PMT, from the first (left) and last (right) run of a 2.5-day test period. The smaller peak at lower amplitudes corresponds to Møller electrons of 1.5 MeV energy on average, and the larger peak corresponds to Mott-scattered beam electrons of 3 MeV energy.

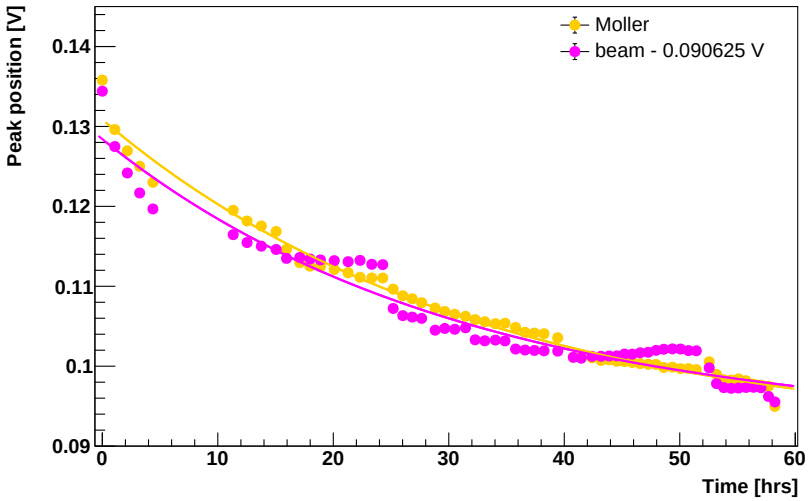

Figure 4.2: Dependence of the peak position on time in the tagging counter equipped with a PMT. Yellow – Møller peak (1.5 MeV). Magenta – beam peak (3 MeV, values are shifted by the average distance between peaks for comparison). The lines represent exponential fits.

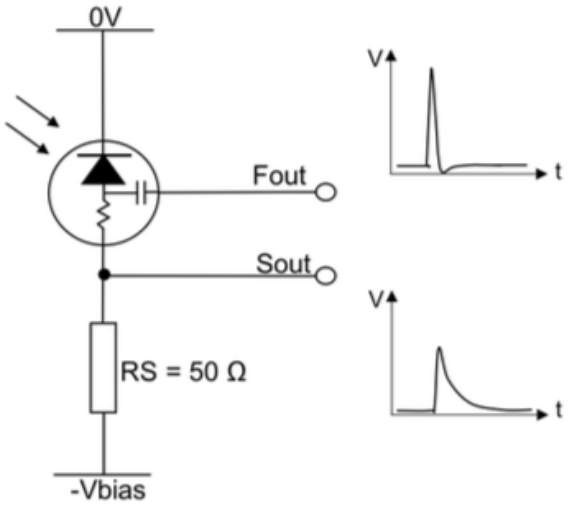

Figure 4.3: Application circuit of the SiPM sensor. Sout denotes the standard output from the biasing circuit and Fout denotes the fast signal output. If the slow output is not used, the sensing resistor RS can be removed. Source: [51].

4.1.2. SiPM detectors

With the advance of semiconductor technology a new detector type, silicon photomultiplier (SiPM), appeared on the market as an alternative to the vacuum tubes. In this case, the principle of operation is based on the creation of electron–hole pairs in silicon by incident photons. In order to achieve a multiplication of charge carriers, a photodiode needs to be reversely biased at a voltage sufficiently high that the accelerated charge carriers can cause secondary ionization (a diode operated in this regime is referred to as a single photon avalanche diode). A single SiPM detector consists of a large number (order of 10k) of avalanche photodiodes, implemented in a single silicon structure. The photocurrents from all diodes are combined together to form a common signal, so the detector response is to a good approximation proportional to the number of incident photons.

The detector chosen for evaluation was a J-Series SiPM sensor manufactured by ON Semiconductor (ARRAYJ–30035–16P–PCB). The main reason for this choice was an exceptionally good timing performance. In a typical SiPM, the current signal through the biasing circuit of the sensor is integrated to obtain a measure of the number of detected photons. The time width of this signal is of the order of the recharge time of the sensor, which is significantly longer than the pulse from the PMT. Whereas, in the chosen SiPM model the photodiodes are additionally equipped with a fast output capacitively coupled to the biasing terminal. The fast signals from all of the diodes are summed together to form a voltage pulse with amplitude proportional to the number of detected photons, as shown in Fig. 4.3. The width of this pulse claimed by the manufacturer is of 1.5 ns, which would be a significant improvement over the previous detector, resulting in a reduced number of false coincidences recorded in the experiment. Additionally, if only the fast output is used, the sensing resistor in the biasing circuit can be removed, resulting in an improved recharge time of the sensor.

Table 4.1: Selected characteristics of the PMT and SiPM detectors used in this work.

	PMT **ET Enterprises 9108B**	**SiPM** **ARRAYJ–30035–16P–PCB**
photosensitive area	4.9 cm^2 (ϕ 25 mm)	1.4 cm^2 (12 mm x 12 mm)
pulse width (fwhm)	5 ns	1.5 ns
recharge time constant	—	45 ns
gain	2×10^6	6.3×10^6 (slow output)

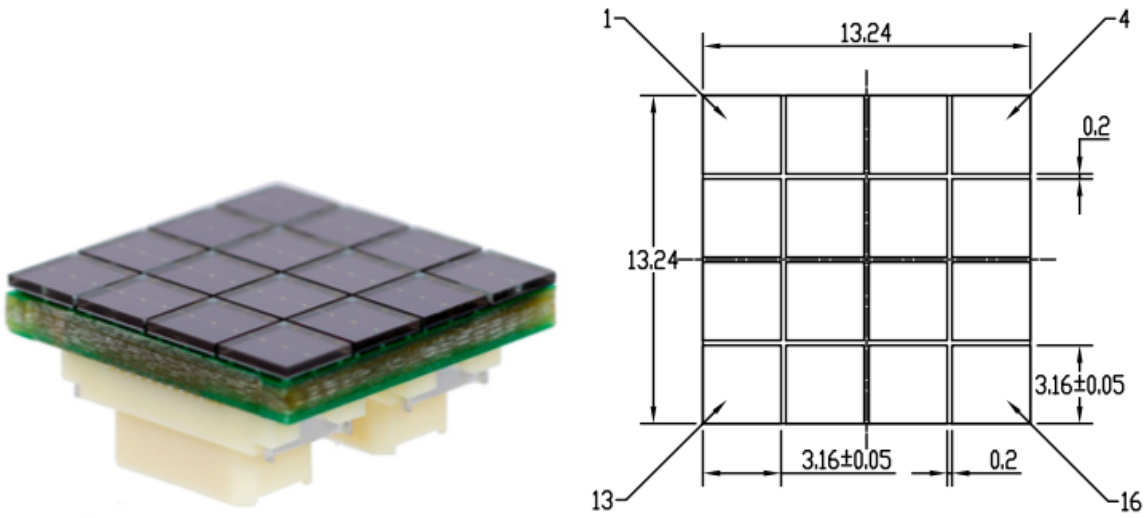

Figure 4.4: Layout of a SiPM array. The divisions between 16 individual pixels are visible. Source: [52].

The key parameters of both detectors are compared in Table 4.1.

4.1.3. Single pixel tests

For the initial tests, the SiPM array was mounted on a test board provided by the manufacturer of the sensor (ARRAYJ–BOB3–16P). The array surface is divided into 16 independent pixels, which can be read out separately in position-sensitive applications, or summed together if detection position is not relevant (cf. Fig. 4.4). The test board allows to connect one of the pixels of an array to SMA connectors for the connection to the bias source and readout.

In the first test, scintillation light created by the passage of cosmic radiation was observed with a scintillator crystal placed directly above the sensor. One of such events (slow and fast signal), observed with one of the pixels in the center of the array, can be seen in an oscilloscope shot in Fig. 4.5. Note that in order to observe the slow signal, a 50 Ω sensing resistor was placed in the biasing circuit, so the timing is worse than optimal.

A significant amount of signal distortion is visible especially in the fast output. Its origin is not related to signal reflections (the line was correctly terminated, and anyway

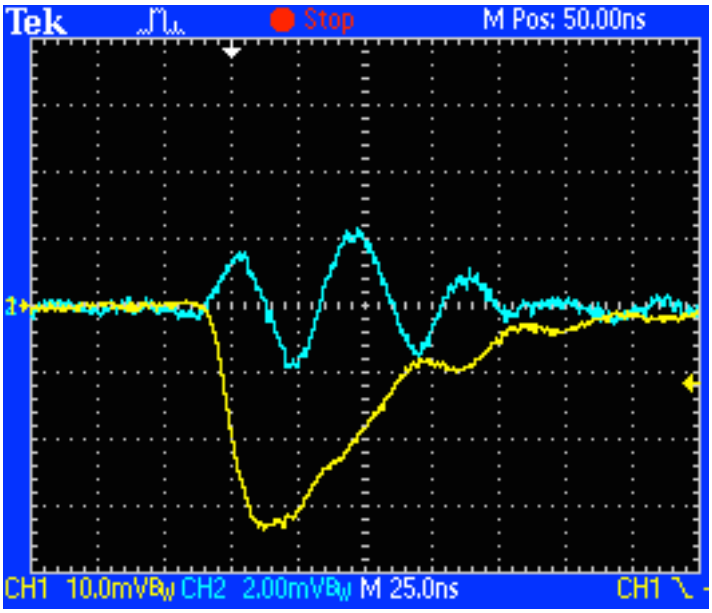

Figure 4.5: Scintillation signal from cosmic radiation recorded with a SiPM sensor connected to an evaluation board available from the manufacturer. Yellow – slow signal. Blue – fast signal.

the anticipated distance between subsequent pulses, assuming a delay of around 5 ns per 1 m of cable, would be much shorter than observed). This result demonstrates that the design of the test board is not suitable for the readout of such fast signals, in particular due to the fact that the ground of the sensor, power supply and readout had to be connected by means of jumper wires connected on top of the board.

The test board was modified by adding fixed connections to the ground plane, which to some extent improved the performance as can be seen in further plots. Additionally, the fast output signal was amplified with an external preamplifier with a gain of 20 dB, since the raw pulse amplitudes were of the order of a few mV only. A typical fast pulse after these modifications is compared to a typical signal from the PMT in Fig. 4.6.

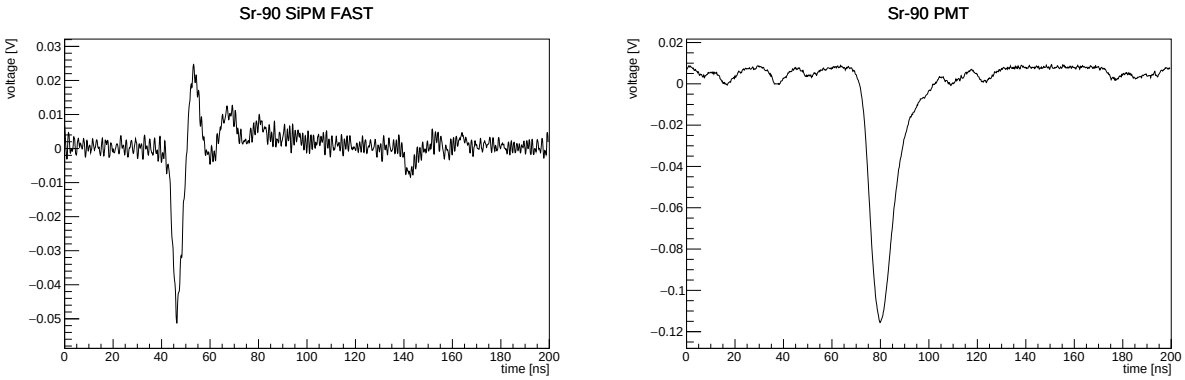

Figure 4.6: Scintillation signal from Sr-90/Y-90 β source recorded with a SiPM sensor (fast signal, left), and a PMT (right).

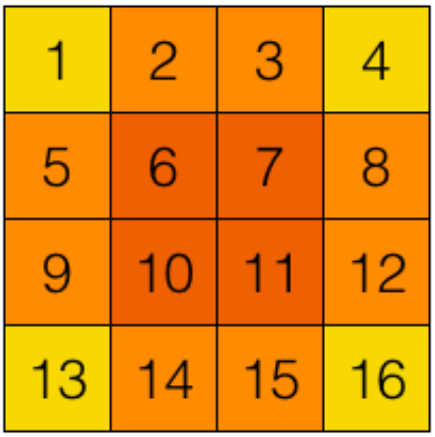

Figure 4.7: Positions of the pixels with indicated channel numbers within an array. Pixels belonging to different groups according to the distance from the center (center, side and corner) are marked with different colors.

The Sr-90/Y-90 β source spectra taken with each pixel within an SiPM array were compared in order to investigate any correlation with the position of the pixel in the array, see Fig. 4.7. A comparison of the signal-amplitude distributions recorded with a few selected pixels is shown in Fig. 4.8.

A comparison between pixels placed at the same distance to the center of the matrix allows to estimate the random differences between the pixels within one array. Additionally, the measurements were performed with two arrays, in order to investigate possible differences between two detectors of the same type, which might appear due to random differences in the manufacturing process. The signal-amplitude distributions are shown in Fig. 4.9 and a good agreement is found, with no significant differences between pixels in the two arrays.

It is worth noting that the differences between pixels placed at different positions within an array, shown in Fig. 4.8, are larger than the differences between different pixels placed at similar positions with respect to the center of the array (including pixels of two different arrays), shown in Fig. 4.9. This supports the hypothesis that the amount of light reaching a particular pixel depends weakly on the position within the array. An additional anisotropy might arise due to the imperfect positioning of the source with respect to the geometrical center of the detector or the asymmetry of the source itself.

In summary, a satisfactory uniformity of the pixels within a matrix was observed and no significant differences between two matrices of the same type were found. The observed differences between pixels placed at different positions are small and should not affect the experiment significantly.

4.1.4. Complete detector tests

Since the SiPM sensor is sold without a power supply and signal readout, a custom frontend board had to be developed. A dedicated readout board, equipped with a

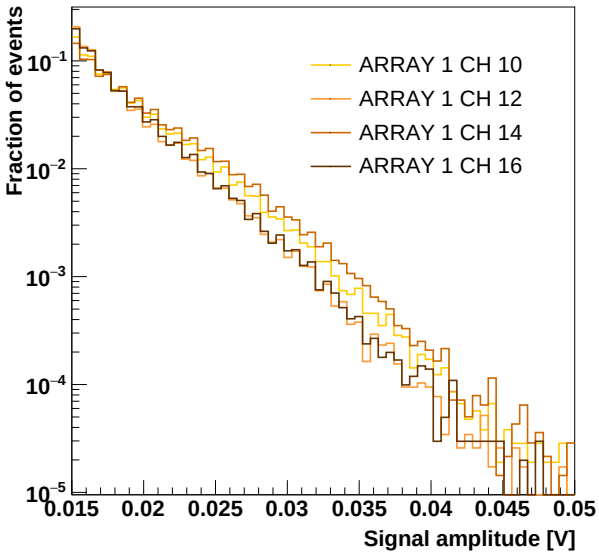

Figure 4.8: Normalized Sr-90/Y-90 β source spectra recorded with 4 pixels of an SiPM array placed at different positions: CH10 – center, CH12 – right side, CH14 – bottom side, CH16 – corner (fast signals, +20 dB).

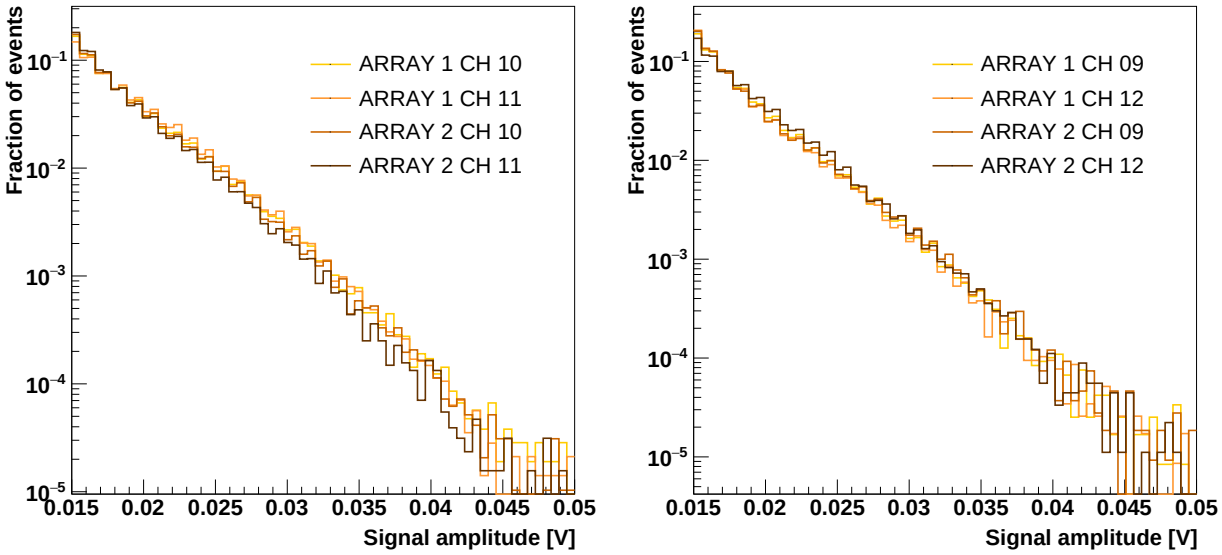

Figure 4.9: Normalized Sr-90/Y-90 β source spectra recorded with pixels of two SiPM arrays placed at the same distances from the center: left – central pixels, right – side pixels (fast signals, +20 dB).

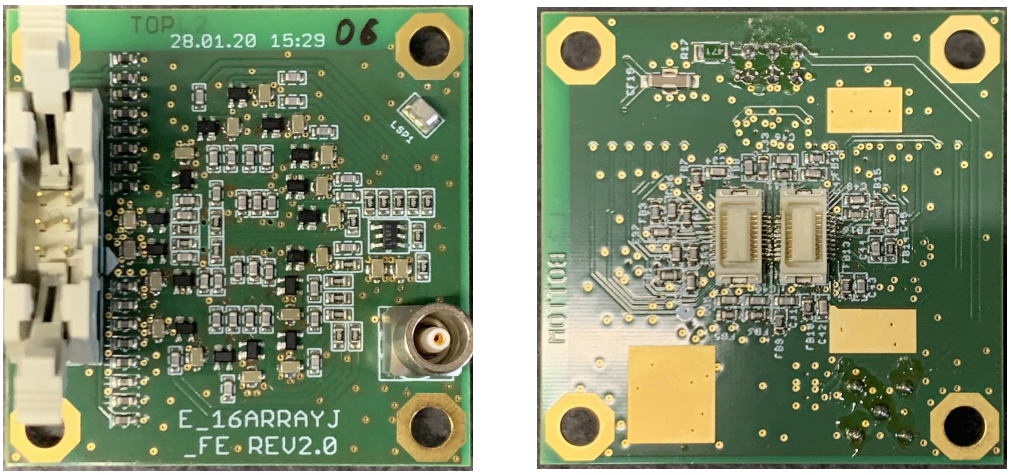

Figure 4.10: Front end board of the SiPM detector. Left: connector side. Right: sensor side.

summed fast output from all 16 pixels within an array, as well as an integrated amplifier, was manufactured. The custom design of the readout board, thanks to much shorter signal lines between the sensor and the preamplifier, allowed to reduce the noise observed in the fast signal. Additionally, the new readout board allowed for a fixed mechanical connection between the light guide and the sensor, which was not possible with the test board, removing the uncertainty regarding the light guide positioning on the array.

The cathodes of all pixels were connected to ground, and the anodes of all pixels were connected to a common power supply channel, via decoupling capacitors to stabilize bias. The fast outputs of all channels were summed together to form one output signal per array, via Schottky diodes to reduce noise. The summed signal was amplified by a factor of 10. A LEMO connector for the fast signal output, and a ribbon cable for power supply, were provided. The board is shown in Fig. 4.10.

The summed signals from entire arrays were compared by measuring cosmic ray spectra with six different sensors. The signal amplitude spectra are shown in Fig. 4.11. It can be seen that only one array deviates significantly from the other spectra; it was rejected from the measurements, since only three detectors at a time were needed for the polarization transfer experiment.

The dependence between the output pulse amplitude and the bias voltage is one of the key characteristics of the sensor. According to the manufacturer, the sensor has to be operated at an overvoltage (i.e., above the breakdown voltage of the diode) between 1 and 6 V, in order to achieve the charge multiplication. This corresponds to the operating voltage range from -25.5 to -30.5 V. Both the photon detection efficiency and gain are approximately linearly proportional to the bias voltage (see Fig. 4.12), at a price of increased number of dark counts and crosstalk. The signal amplitude spectra in the tagging counter, recorded with bias voltages of -29 and -29.5 V are compared in Fig. 4.13. During the experiment, the detectors were operated at -29 V, which is sufficient to record the entire Møller electrons peak. Nevertheless, one should note that the level of low-energy noise is similar also at -29.5 V, since the small dark count signals are not detected in applications involving a large flux of light. The difference

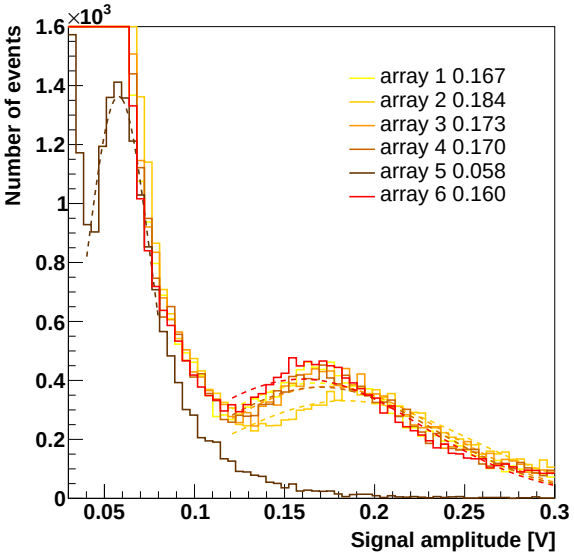

Figure 4.11: Cosmic spectra recorded with six arrays over the same data acquisition time. The single particle peak positions from the fits are shown for comparison in the plot legend.

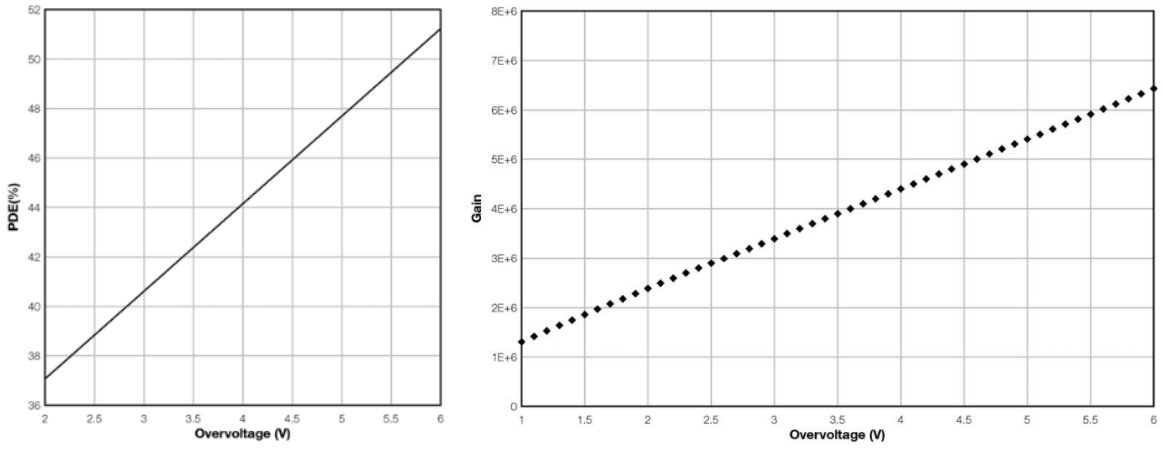

Figure 4.12: Performance of the SiPM detector claimed by the manufacturer. Left: photon detection efficiency dependence on overvoltage. Right: gain dependence on overvoltage. Source: [53].

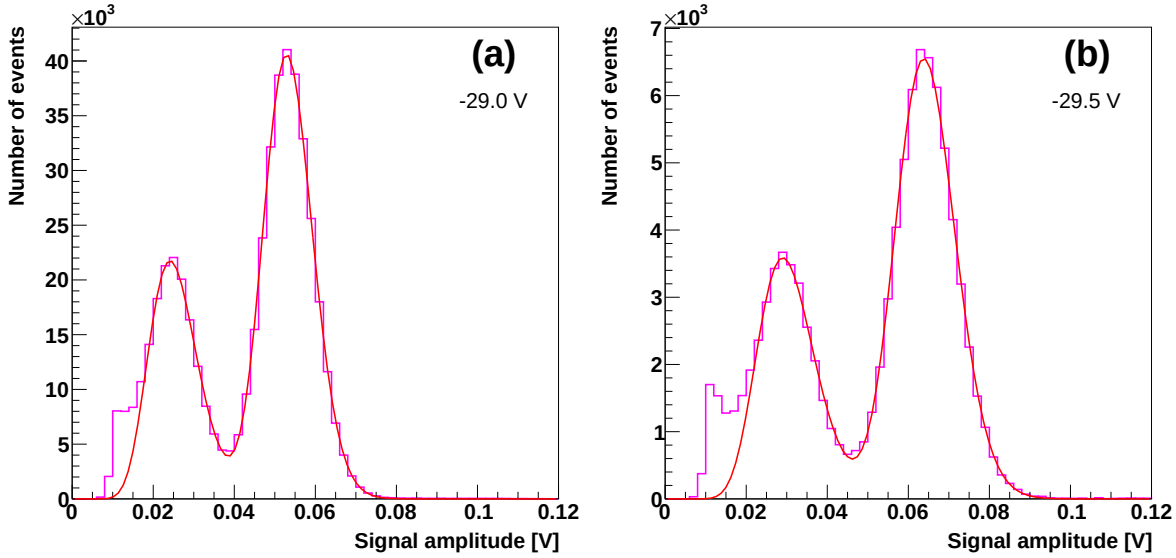

Figure 4.13: Signal amplitude spectrum in the tagging counter with a SiPM operated at (a) −29 V and (b) −29.5 V bias voltage. The smaller peak at lower amplitudes corresponds to Møller electrons of 1.5 MeV average energy (Møller peak), and the larger peak corresponds to beam energy of 3 MeV (beam peak).

between various overvoltage settings would become much more apparent in photon counting applications, which require exceptionally low noise.

4.2. Readout

4.2.1. Signal digitization

The signals from the SiPMs were digitized with a DRS4 Evaluation Board equipped with a DRS4 switched capacitor array chip [54]. The board can sample four input channels at 5 GHz rate, and 1024 samples can be stored from each input channel. The signals stored in the DRS4 chip are digitized with an ADC. The board is also equipped with a FPGA (Xilinx Spartan 3) for the readout of the ADC output and data acquisition control, including trigger logic. A microcontroller allows to read the data out via USB 2.0 interface. The schematic block diagram of the digitizer board is shown in Fig. 4.14.

4.2.2. Trigger

The board contains a built-in trigger logic. Each of the input channels is connected to a comparator, whose output is read out by the FPGA. A basic trigger logic similar to that available in digital oscilloscopes was implemented in the firmware provided by the manufacturer. The fact that the operation of the board is controlled by a FPGA allowed us to implement certain modification to the basic functionality.

In case of the polarization transfer experiment it was necessary to take into account the information about beam polarization. The beam polarization was controlled with

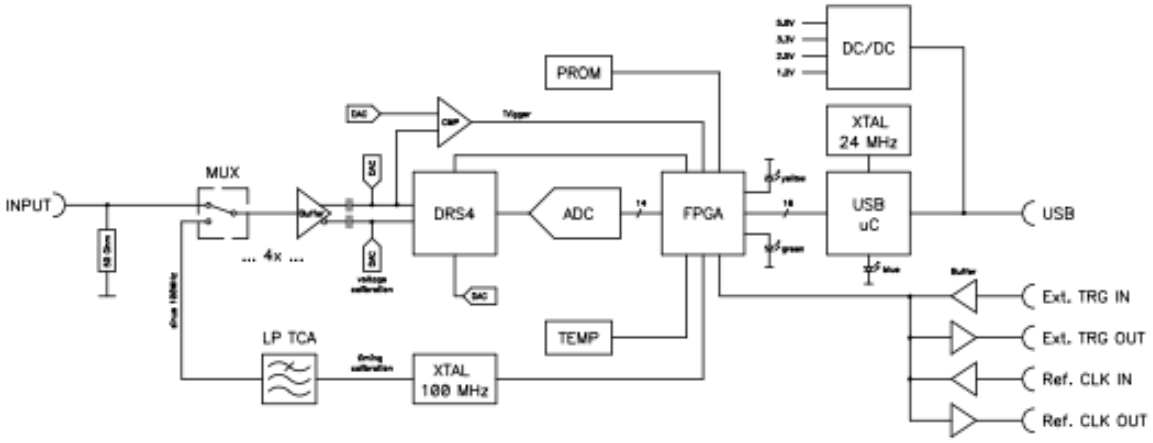

Figure 4.14: Schematic block diagram of the DRS4 Evaluation Board. Source: [55].

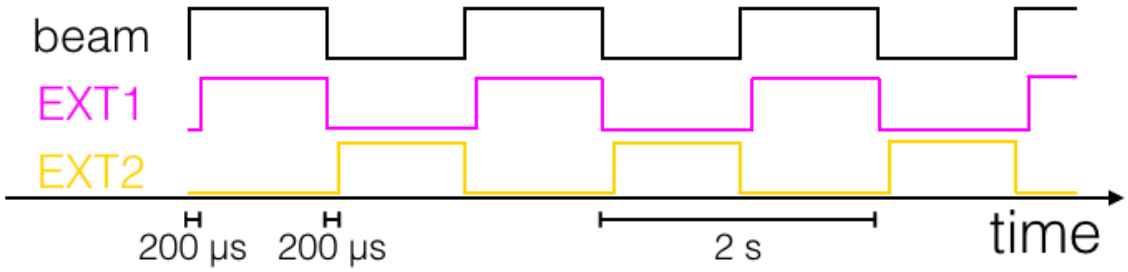

Figure 4.15: Illustration of the external trigger signals dependence on time (not to scale). Beam denotes the Pockels cell switching signal (2 s square wave), EXT1 is the trigger signal corresponding to high voltage state of the beam signal (start delayed by 200 μs), and EXT2 is the trigger signal corresponding to low voltage state of the beam signal (also delayed by 200 μs).

a multi-channel signal generator. Three synchronized outputs of the generator were used. One of them was connected to the Pockels cell in the laser system of the polarized electron source. Due to the finite switching times and possible signal delays, the data acquisition should be stopped for a short period of time around the switching moment. Therefore, two additional trigger signals, delayed with respect to the cell control signal, were generated, as shown in Fig. 4.15. The trigger condition in the polarization transfer experiment reads

$$(L \vee R) \wedge T \wedge (EXT1 \vee EXT2), \tag{4.1}$$

where L and R denote the polarimeter detectors, T is the tagging counter, $EXT1$ and $EXT2$ are the external trigger signals from the generator, corresponding to opposite beam polarization orientations. There were two digitizer boards at our disposal, therefore, the L and R detectors were read out with separate boards, allowing us to reduce the dead time. Thus in reality each digitizer board realized the trigger condition (4.1) with one of the detectors from the first alternative.

It can be seen in Fig. 4.14 that the board has two auxiliary inputs, described in

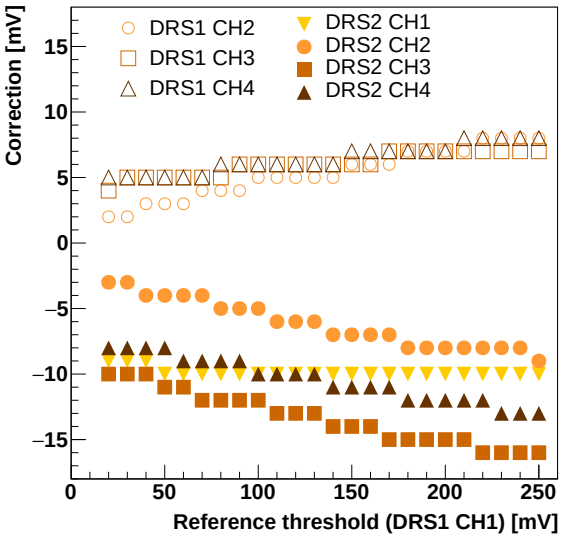

Figure 4.16: Calibration curves of the trigger thresholds of all input channels of the DRS evaluation boards (trigger threshold correction defined as the difference between the trigger threshold of a given channel and the reference threshold of channel 1, DRS board 1).

the schematics as external trigger input and reference clock input. Further analysis of schematics reveals that the electronic paths of both signals are identical, their names reflect only the difference in the use of both signals in the standard firmware. Therefore, the firmware was modified in such a way that an alternative of both inputs was included in the trigger logic, in coincidence with the input signals from the detectors. This way, the data acquisition was stopped when the beam polarization was uncertain.

In order to be able to assign the beam polarization to the recorded events, it was necessary to save the information on which of the two external trigger signals was active. Two additional latches were implemented, in order to store the external trigger input states when the trigger condition was met. In order to be able to use the data acquisition software provided by the board manufacturer, the readout format was left unchanged. Instead, the information on the external trigger was encoded in the last bins of the digitized waveforms. 1024 points of each waveform are read out, which is much more than the typical duration of a signal from a PMT or SiPM, thus the loss of a few last data points is not a problem.

In case of the spin correlation experiment, a more complex trigger condition has to be implemented, namely a coincidence of any detectors from two polarimeters and the external trigger signal,

$$(L_1 \vee R_1) \wedge (L_2 \vee R_2) \wedge (EXT1 \vee EXT2), \tag{4.2}$$

where the subscripts 1 and 2 denote the first and second polarimeter, respectively. Thanks to the use of an FPGA, it is straightforward to implement such trigger condition, therefore, the evaluation board is also suitable for the use in a future correlation experiment.

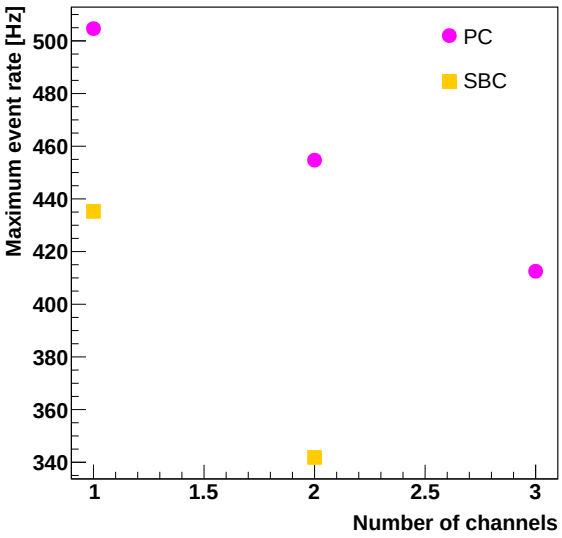

Figure 4.17: Maximum rate of events that can be saved to the file plotted as a function of the number of readout channels. Magenta: PC with Intel Core i7-3770, yellow: SBC with Samsung Exynos 5422.

While the DRS evaluation board has built in circuits for timing and voltage calibration of the signal digitizer, there is no automatic trigger calibration. A test was performed with a signal generator connected to each signal input of both boards. The measured trigger threshold corrections are shown in Fig. 4.16, with one of the channels used as a reference (trigger levels of all channels were compared to the trigger level of channel 1 of DRS board 1 corresponding to the same input voltage). It can be seen that there is a significant difference between two boards, but the channels within one board are also not identical. A table with data from Fig. 4.16 was used during the experiment to achieve similar trigger thresholds for all detectors.

4.2.3. Dead time

When the trigger condition is met, input signal sampling is stopped to allow the samples already stored in the DRS board memory to be readout by the data acquisition control program running on the connected computer. This results in a considerable dead time, which needs to be taken into account when analysing data. In order to experimentally determine the dead time of the readout electronics, the DRS software was modified to record the event time stamp with a microsecond precision (instead of the standard millisecond accuracy).

The test was performed with a large event rate saturating the readout (the time between consecutive pulses was negligible compared to the dead time). The maximum event rate that can be written to the disk is shown as a function of the number of channels in Fig. 4.17. It was found that the dead time depends not only on the DRS digitizer board, but also on the configuration of the readout computer. The effective (average) dead time values (inverse of the maximum event rate) are listed in Table 4.2. For single channel readout, the maximum event rate of 500 Hz corresponds

Table 4.2: Average dead time values of the DRS board corresponding to the maximum event rate. The results were determined in a test with a signal generator, with different numbers of active channels in the digitizer board and two different readout computers (see text for details).

CPU	1 channel	2 channels	3 channels
Samsung	2.3 ms	2.9 ms	
Intel	2.0 ms	2.2 ms	2.4 ms

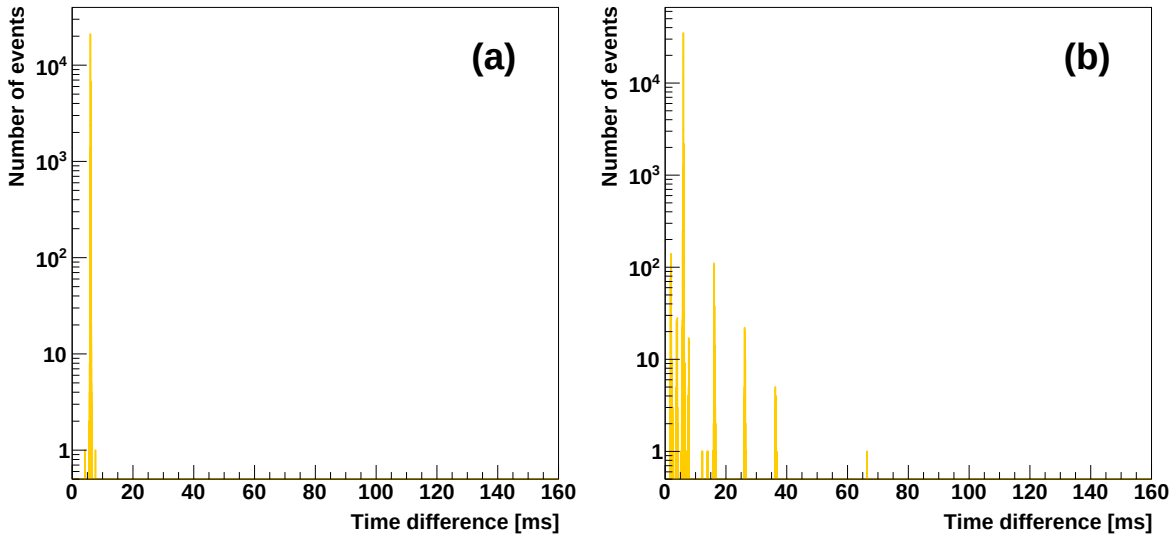

Figure 4.18: Histogram of the time between consecutive events from the test with pulse generator; (a) data not written to file, (b) data written to file. The event rate from the generator was about 165 Hz (6 ms time between pulses).

to the average dead time value of 2 ms. It can be seen that the effective dead time is about 0.3 ms longer for the single board computer (SBC) with Samsung Exynos 5422 processor (2 GHz clock) than for the PC with Intel Core i7-3770 (3.4 GHz).

These observations were also confirmed in a subsequent test with a lower event rate from the pulse generator. The distributions of time between consecutive events with and without writing the data to the file can be compared in Fig. 4.18. It can be seen that, when the data are not stored, the distribution consists of a single peak corresponding to the constant time distance between the pulses from the generator (in this case the dead time is shorter than this time). However, when the data are written to the disk, additional peaks, corresponding to different delay times, appear in the spectrum due to the latency of the computer and hard drive. It shows that the dead time might be larger than 6 ms (time between test pulses) at least for some events.

The procedure of the experimental-data correction for the presence of dead time is described in Section 7.2.

4.2.4. Data acquisition

The general scheme of the data acquisition setup, which was used in the polarization transfer experiment, is shown in Fig. 4.19. The readout of the spin correlation experiment could be very similar, except that instead of the tagging counter there would be additional polarimeter detectors.

In order to avoid signal attenuation in exceptionally long cables, it was desirable to place the digitizer boards as close to the detectors as possible. Since the DRS boards are read out via USB connection, also the readout computers had to be placed nearby. Therefore, small single board computers (SBC) were used instead of standard PCs. Both the SBCs and the DRS boards were placed in a lead house located directly under the polarimeter. An additional SBC was used to control the power supply of the SiPMs and a relay board.

The SiPM power supply board was equipped with a microcontroller, which communicated with the SBC via a serial interface. The remotely controlled power supply allowed us to change the bias voltage (only for testing) and to switch individual detectors on and off (the tagging counter was switched off during the beam polarization measurement).

The relay board was used to switch two compressed air electrovalves controlling the target ladders. The relay board was connected directly to the digital output pins of the third SBC. The relay controlling the gold target was switched by an application receiving commands from the main data acquisition program, which automatically moved the gold target in and out between runs. The relay controlling the beam monitor had to be switched from the operator's console.

The coordination between the four computers involved in the data acquisition was achieved using socket programming. Socket programming offers a convenient way of establishing data transmission between programs running on two computers in the same network (the connection is made using the IP addresses and port numbers). The remote computers sent the received commands back to the control computer. If the sent and received messages were different, an error would be displayed.

The PC placed in the counting room was used only to control the process, while the data acquisition itself took place on the computers placed in the experimental hall. Raw data were stored on fast SSD drives connected directly to the SBCs in the experimental hall, thus the data were not transmitted over the ethernet. The main control program ran in terminal on the control PC, a sample output is shown in Fig. 4.20. The output visible in the terminal was stored to a file for future reference.

The data from the program were also automatically stored in a more user-friendly form in the electronic logbook of the experiment, based on the ELOG software. A new logbook entry was created automatically at the end of each run and when the operator changed. A sample logbook page is shown in Fig. 4.21. Manual logbook entries could also be added in case of non-standard events.

At the beginning of a new run, the control PC issued commands to the software running on SBCs, first to change the target position, and then to start the data acquisition. When the run duration time requested by the operator elapsed, commands to stop the data acquisition, and to provide the number of recorded events, were sent. The remote computers replied with the number of recorded events, saved signal-amplitude

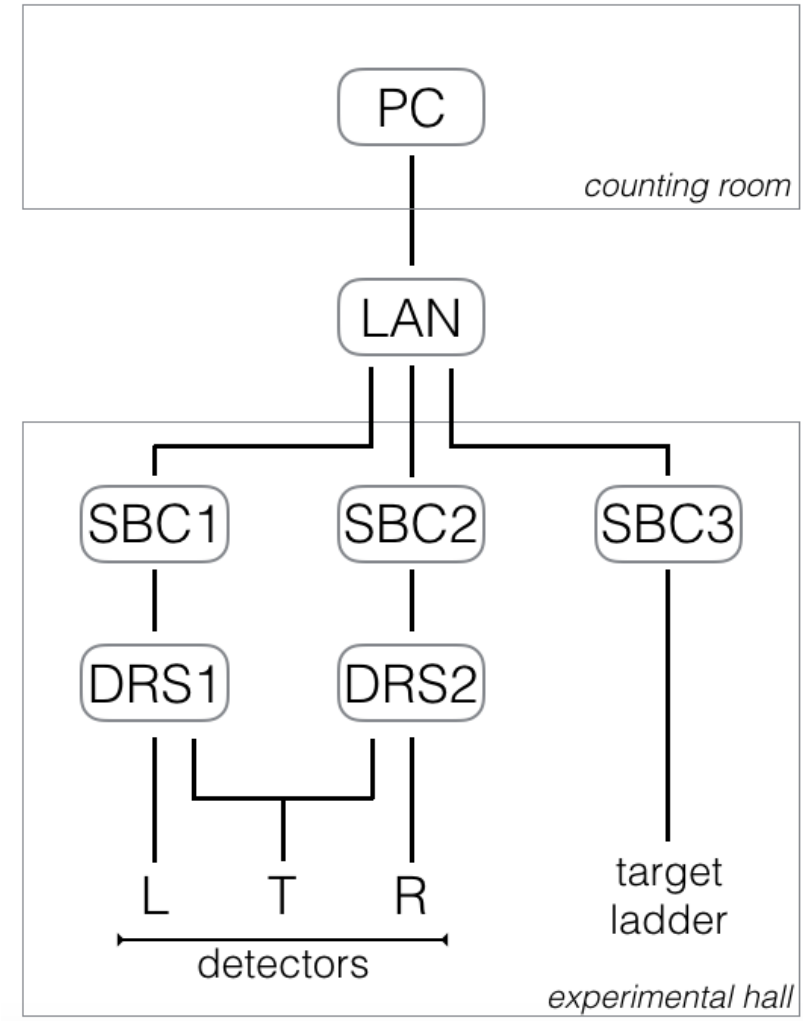

Figure 4.19: Schematic illustration of the data acquisition and slow control system in the polarization transfer experiment. PC is the main control computer, LAN is the ethernet switch, SBC are the single board computers, DRS denote the digitizer boards. L and R are the SiPMs in the Mott polarimeter, and T is the SiPM of the tagging counter.

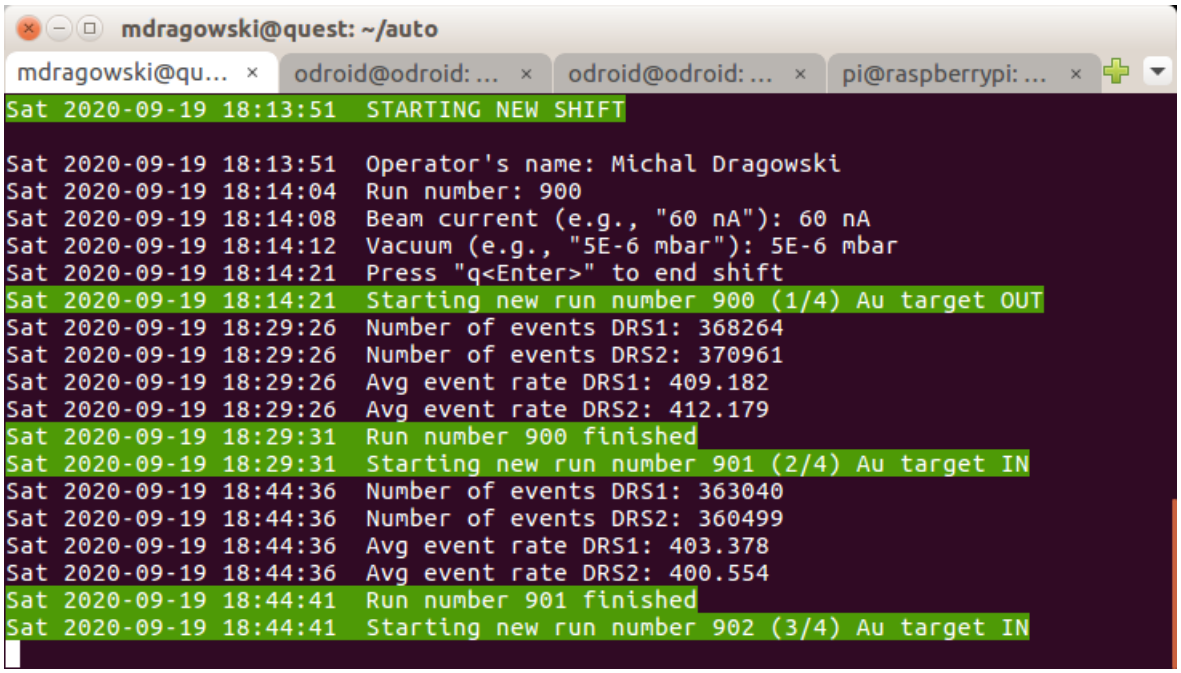

Figure 4.20: Terminal window with the data acquisition software running.

histograms, which were appended to the electronic logbook, and created a backup of the data on spare hard drives. The control program analyzed the average event rates during the experiment and displayed warnings in case they differed significantly from previous values. This way, large changes of the beam current could be detected.

Since all the data acquisition software was controlled from the PC located in the counting room, it was possible to control the experiment remotely by logging in to that computer over ssh. This way, some of the shifts at the experiment during the coronavirus epidemic were done remotely from Warsaw.

The software running on the SBCs controlling the DRS boards was modified from the DRS Oscilloscope program provided by the board manufacturer. As the name suggests, the original program resembled the interface of a digital oscilloscope, with the main window showing the acquired waveforms. Additionally, the software could measure several parameters of the waveform and histogram the results. The signal amplitude was found useful for the experiment, as it allowed to quickly preview the approximate spectrum in the tagging counter, which allowed the operator to check if the data is acquired correctly (the spectrum in the polarimeter detectors was not useful without further offline analysis due to the high rate of low-energy background).

The interactive controls of the graphical interface were disabled (the operator observed a static display instead of an interactive interface). Instead, the setting were either fixed or controlled automatically according to the instructions from the main control program. A typical window is shown in Fig. 4.22. The waveforms are shown in the top half of the window, and the signal amplitude histograms are shown in the bottom. Two channels are read out, the data from a polarimeter detector are shown in yellow, and from the tagging counter in red.

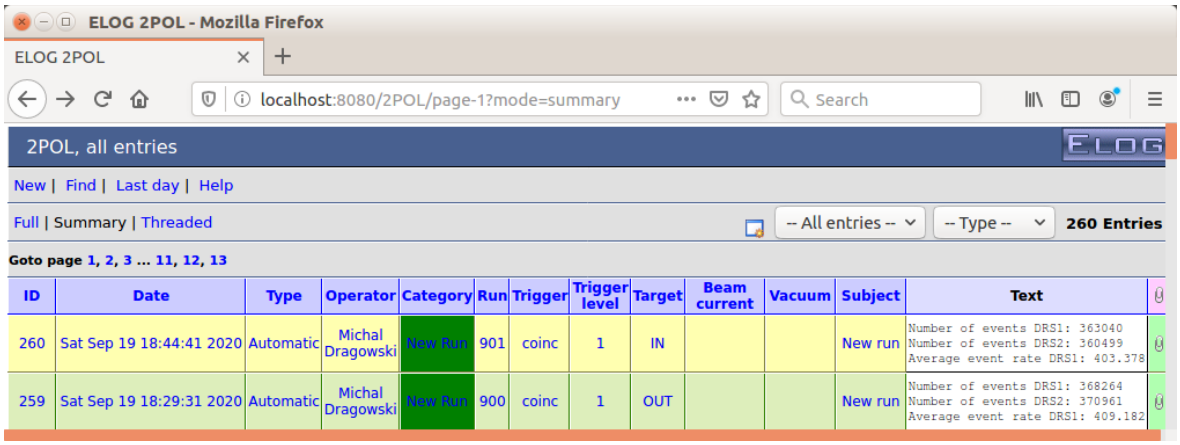

Figure 4.21: Electronic logbook window with two entries made automatically by the data acquisition software.

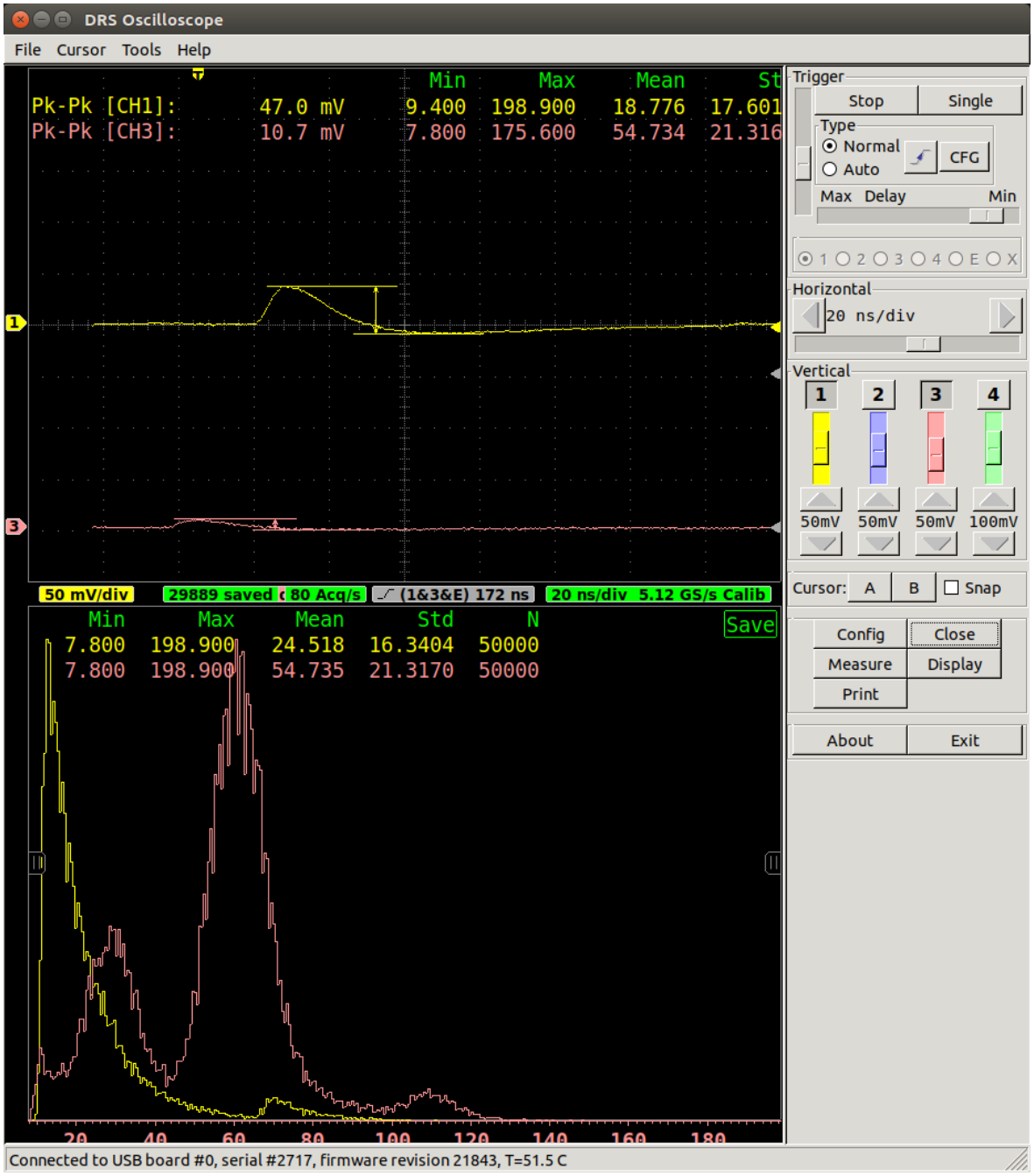

Figure 4.22: Graphical interface of the DRS Oscilloscope application. During the automatic data acquisition the buttons visible on the right hand side were displayed, but inactive (controlled remotely by the main data acquisition program).

Chapter 5

Simulation of the analyzing power

For the simulation of Mott scattering of polarized electrons, a dedicated model for the Geant4 toolkit was created. The results of the validation of the model, and the predictions for the polarization transfer experiment, are presented in this chapter. Parts of this chapter related to the model were published in [33] and its predictions for electron polarimetry in the MeV energy range in [34].

5.1. Mott scattering model

The simulation taking into account polarization effects in Mott scattering is beyond the scope of general purpose Monte Carlo codes, such as the commonly used Geant4 toolkit [49]. The Geant4 package includes models of Møller scattering (ionization) and bremsstrahlung, that take into account electron polarization. However, polarization effects are not accounted for in the description of Mott scattering. There are multiple implementations of electron–nucleus scattering in Geant4 (for a comparison of different models see, e.g., [56]), but neither of these takes into account polarization effects in this interaction. Thus, Geant4 is unsuitable for simulation of processes involving electron polarization in the MeV and sub–MeV energy range, due to the large cross section for Mott scattering in the discussed case. There were dedicated simulations written for the study of polarized electron elastic scattering (e.g., [57, 58]), however, we do not know of any such code available to the public.

A custom description of a given interaction process in Geant4 can be achieved by implementing a so–called interaction model, to be used instead of the standard ones available in the toolkit. The implementation details of a custom interaction are left to the user, the only requirement is to use the common interface recognized by Geant4. The Geant4 core takes care of propagating the particle through the simulation in the same way regardless if standard or custom interaction models are used. Therefore, a new model of Mott scattering for electrons, that can be used with Geant4 instead of the default electron Coulomb scattering model, has been created. The scattering amplitudes determining the cross section and polarization transfer have to be provided as an input; as already mentioned in Section 2.2, they can be reliably calculated for instance with the ELSEPA package [42].

The implementation is based on our earlier standalone simulation code PEBSI

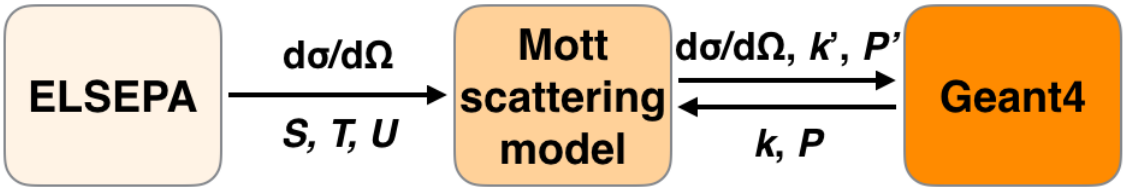

Figure 5.1: Block diagram illustrating the implementation strategy of the new interaction model in Geant4; $d\sigma/d\Omega$ is the cross section, S, T, U are the functions determining the polarization transfer, k is the momentum, P is the polarization.

(Polarised Electron Bremsstrahlung SImulator) [59, 60] written in FORTRAN. The applications of the original code extended much beyond its original aims, but were limited because of its lack of flexibility. It was decided that in order to overcome this issue it would be favorable to merge the Mott scattering model from PEBSI with Geant4.

The main advantage of the new implementation is that it can be easily used in any Geant4 simulation by replacing the standard Coulomb scattering model. Compared to PEBSI, the extremely wide capabilities of the Geant4 framework offer many additional improvements, such as the possibility to describe more complex geometries, multi–threaded computation, and many others. It has also been observed that the computation time is shorter in Geant4.

The modular (object oriented) architecture of the Geant4 toolkit allows for adding new interaction models without any changes to the core simulation code, which can be seen in the diagram illustrating the implementation idea, shown in Figure 5.1. The theoretical data, obtained from the ELSEPA code, are then used in the Mott scattering model (based on the PEBSI simulation), which is interfaced to Geant4.

A custom interaction model has to overwrite predefined functions, inherited from a base interaction class, responsible for calculating cross sections, sampling the scattering parameters (momentum and polarization after the scattering) and producing secondary particles (also with appropriate momentum and polarization vectors). This way, only the part of the code responsible for performing the Mott scattering in PEBSI had to be rewritten from FORTRAN to C++. After adapting the implementation to the Geant4 interface, the new polarized electron Mott scattering model, used in place of the default Coulomb scattering model, works out of the box as a part of the simulation.

For simplicity, the cross section generator is used as a standalone program. The differential cross section (and S, T, U functions) tables are generated with ELSEPA and stored in data files. These data are then imported to our Mott scattering model at the initialization of the simulation. The cross section generator could be, in principle, compiled together with the simulation code, but in most cases the data tables need to be generated only once and there is no need to repeat this calculation each time the simulation is started.

We provide a sample program running the ELSEPA code to generate the data tables in the appropriate format. For certain conditions (energies) the ELSEPA code issues a warning that the calculation might not have converged successfully, and indeed it has

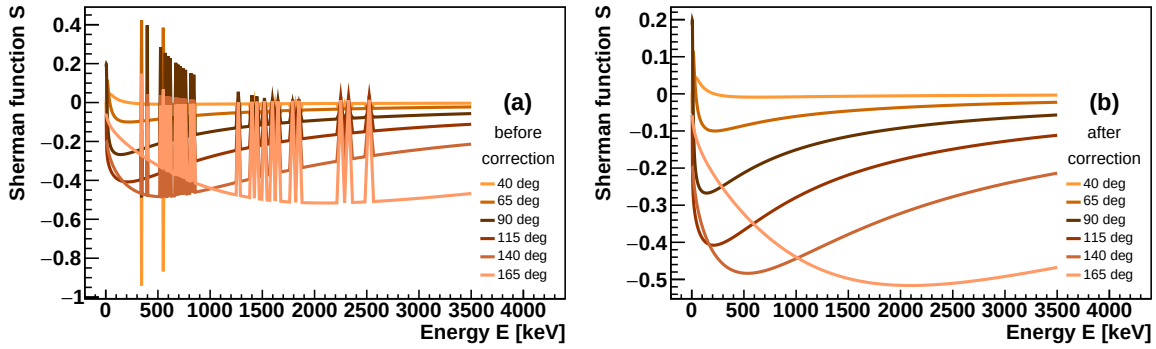

Figure 5.2: Dependence of the theoretical Sherman function S on electron energy E for electron scattering off gold atoms, generated with ELSEPA [42], before (a) and after corrections (b).

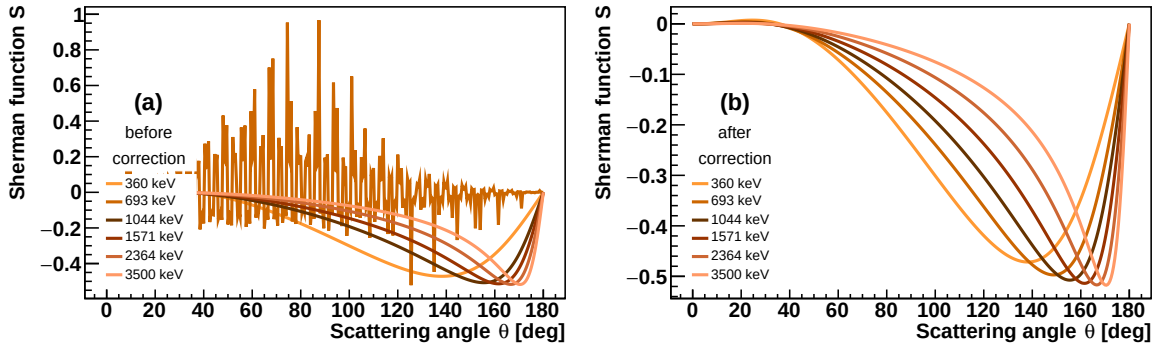

Figure 5.3: Dependence of the theoretical Sherman function S on the scattering angle θ for electron scattering off gold atoms, generated with ELSEPA [42], before (a) and after corrections (b).

been noticed that some data points are incorrect (by inspecting the cross section and Sherman function dependence on energy one can observe that some data points do not fit the general dependence). A simple data correction algorithm, which interpolates the value from the neighboring points if an inconsistency is found in the ELSEPA output, has been included in the generator and can be switched on if desired. If the interpolation is unsuccessful in a few iterations, then extrapolation from previous points is performed. The control plots corresponding to uncorrected and corrected data are shown in Figs. 5.2 and 5.3. The errors in uncorrected data are clearly visible. After correction there are no inconsistencies noticeable in the plots. In any case it is advisable to always verify the consistency of the input data by means of, for example, control plots similar to those in Figs. 5.2 and 5.3.

The implementation of the Geant4 extension has been divided in two classes. The first one, `MottScatteringModel`, inheriting from a native Geant4 virtual class `G4VEmModel`, provides an interface to Geant4 and follows the structure of the corresponding classes of other Geant4 interaction models. This way, the Geant4 core functions responsible for managing the simulation and calling the interaction processes are able to interact with the custom model. The actual extension can be found in

the `MottCrossSection` class, containing functions practically identical to those found in the original PEBSI code, whose methods are called by the `MottScatteringModel`. This part of the code is responsible for providing the total cross section (for a given beam energy and target material) and performing the scattering (i.e., calculating the energy, momentum and polarization change for a particle of a given primary energy, momentum and polarization, scattered off a target atom). The cross section and S, T, U values for intermediate energies and scattering angles are interpolated from the data tables imported during initialization.

5.2. Validation of the model

Reliability of the simulation has been proven by comparison with experimental data regarding the azimuthal asymmetry (effective Sherman function) in Mott scattering of polarized electron beams. The comparison has been performed for 100 keV, in the 1 – 3.5 MeV range, and for 14 MeV, which is the highest energy for which applicability of the Mott polarimetry method has so far been demonstrated.

5.2.1. Parametrization of the effective Sherman function

Dependence on target thickness

The parametrization of the asymmetry dependence on target thickness is commonly used for the calibration of Mott polarimeters (i.e., determining the effective Sherman function for targets of finite thicknesses). In our earlier work [60] we have shown that at lower energies (100 keV) different parametrizations are more appropriate, depending on the scattering angle. The Monte Carlo simulation can be useful to determine which parametrization should be used under given experimental conditions.

It is difficult to predict the effective Sherman function dependence on target thickness, as the scattering probability differs with the position in the target due to multiple scattering and energy loss, which in general cannot be modeled analytically. This problem can be illustrated with the distributions of the target penetration depth (i.e., the largest value of the electron-track coordinate along the primary beam direction), which are shown in Fig. 5.4 for 1.5 MeV electrons scattered off a 40 μm thick gold target. It can be seen that the shape of the distribution depends on the scattering angle. In general, the backscattering probability increases with target thickness, however, when energy selection is applied, a maximum of the distribution is observed around a few μm, as the passage through the target is associated with energy loss. This result also demonstrates that a nonzero value of the effective Sherman function can be expected even for an infinitely thick target, since most of the electrons recorded in the detectors are scattered at a relatively small depth.

The effective Sherman function dependence on target thickness is typically parametrized either with an exponential [61]

$$S_{\text{eff}}(d) = S_\infty + (S_0 - S_\infty)\exp(-\alpha\, d), \tag{5.1}$$

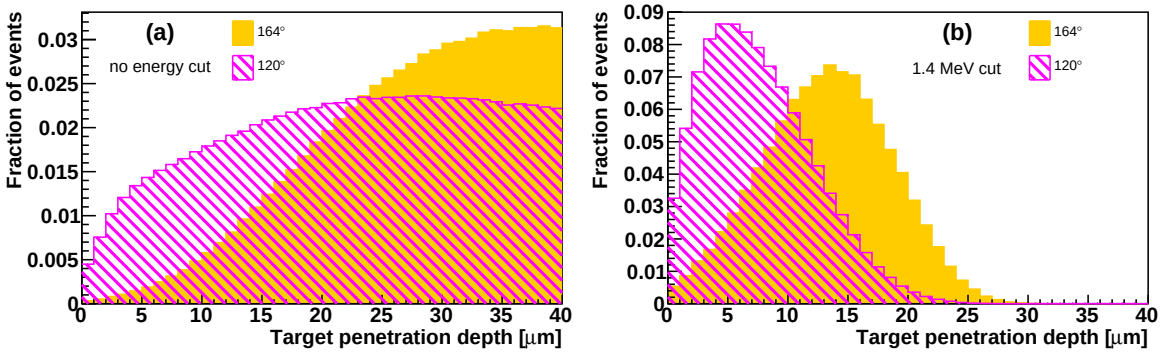

Figure 5.4: Distributions of the target penetration depth for 1.5 MeV electrons scattered off a 40 μm thick gold target, for detectors placed at two angles, 120° and 164°, with respect to the beam axis, without energy selection (a) and with a 1.4 MeV low-energy cut (cf. Section 5.2.3) (b).

or hyperbolic

$$S_{\text{eff}}(d) = S_\infty + \frac{S_0 - S_\infty}{1 + \alpha\, d} \tag{5.2}$$

function. In this convention the S_0 and S_∞ parameters denote the effective Sherman function value for zero and infinite target thickness, respectively, and α describes the attenuation of the effective Sherman function with increasing target thickness.

The hyperbolic dependence of the effective Sherman function on target thickness can be derived analytically under certain approximations, namely neglecting the existence of trajectories with three or more scattering events. The double-scattering approximation was originally studied by Wegener [62], and later was used by several authors to obtain predictions for the effective Sherman function decrease with target thickness [63–66].

The assumption that, in the case of thin targets, which are typically used in Mott polarimetry, one can restrict the description of multiple scattering to double scattering only, can be easily verified with a Monte Carlo simulation. This way the validity range of Wegener's approximation can be defined, in order to assess the usefulness of analytical calculations for the computation of the effective Sherman function. The distributions of the number of scattering events at an angle larger than 10° along each electron track are shown in Fig. 5.5 for 1.5 MeV electrons scattered off gold foils of various thicknesses. The first observation is that there is no substantial difference between the two scattering angles, the average number of scattering events being no more than a few per cent larger at 164° than at 120°. In case of thin targets, of the order of 1 μm, the double-scattering approximation seems to be reasonable, given that the majority of events consist of a single scattering at an angle larger than 10° and that the mean number of scattering events is approx. 1.5. Nevertheless, even for thin targets there is a noticeable number of triple-scattered electrons. Most importantly, the double-scattering approximation is not adequate for thicker targets, of the order of 10 μm, for which the maximum of the distribution is observed at much higher values.

Some authors [65,66] included higher order terms in order to account for the multiple scattering. Let us expand the number of detected electrons to the third power in target

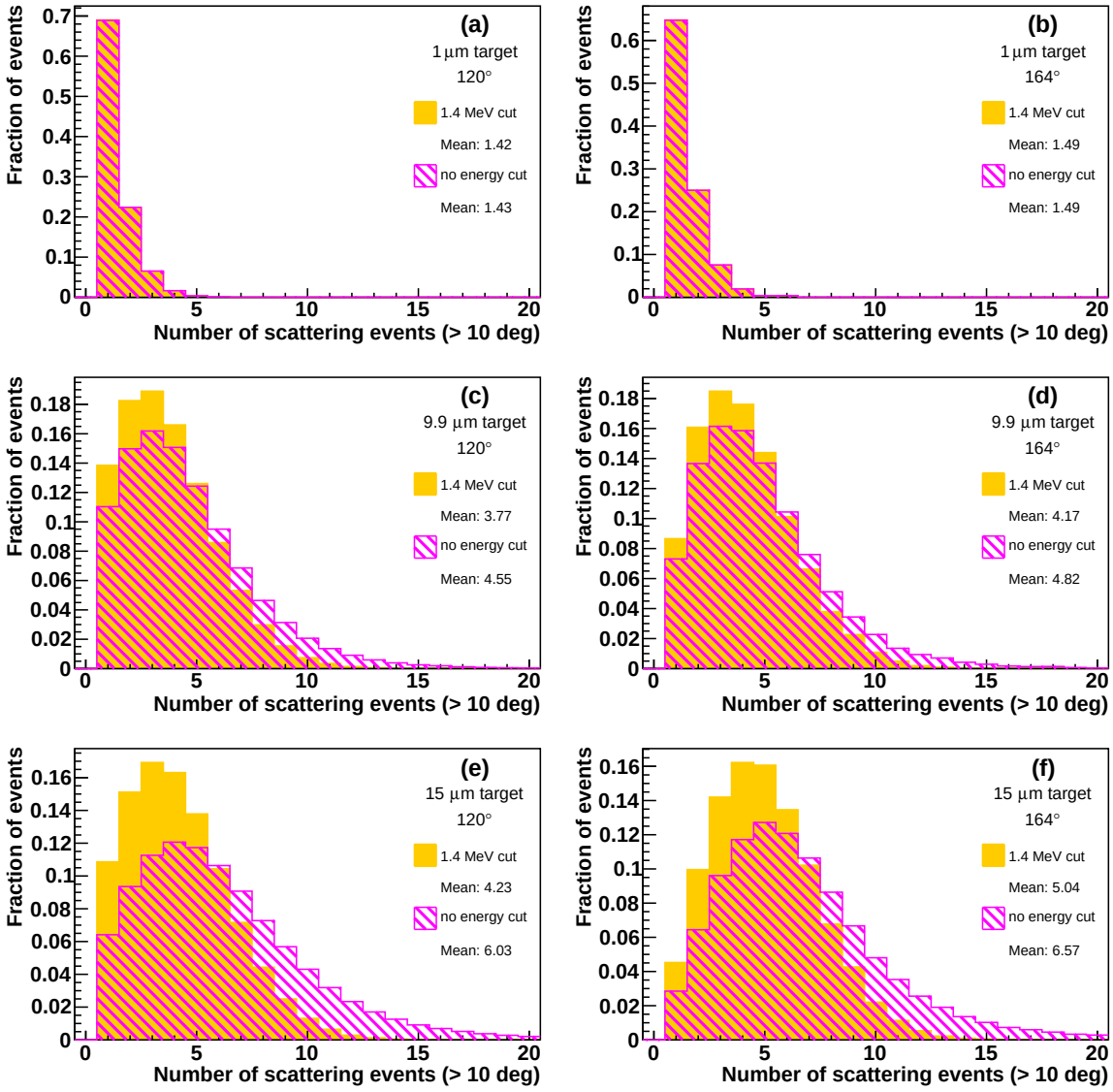

Figure 5.5: Distributions of the number of scattering events at an angle larger than 10° during the passage of a 1.5 MeV electron through gold targets of various thicknesses d (1, 9.9 and 15 μm), for detectors placed at two angles, 120° and 164°, with respect to the beam axis, without energy selection and with a 1.4 MeV low-energy cut (cf. Section 5.2.3).

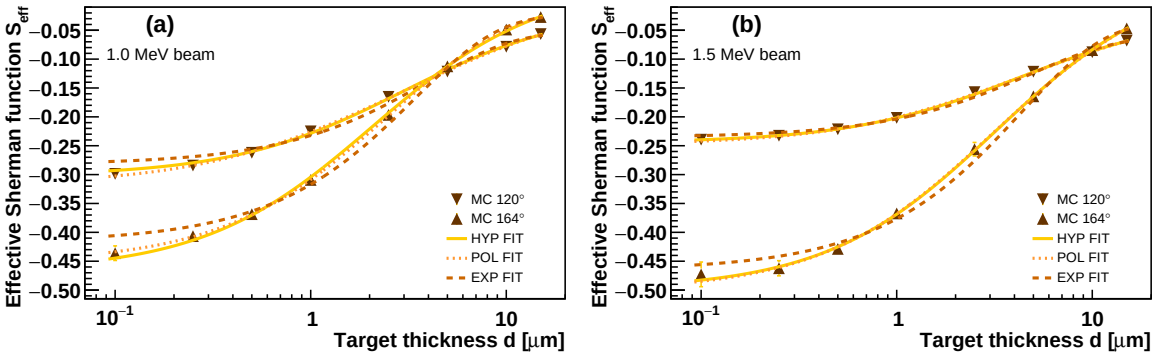

Figure 5.6: Dependence of the simulated effective Sherman function S_{eff} (points) on the target thickness d for detectors placed at two angles, 120° and 164°, with respect to the beam axis (scattering angle ranges $115° < \theta < 125°$ and $163.5° < \theta < 164.5°$), and two beam energies: 1.0 MeV (a) and 1.5 MeV (b). The lines represent three different fits to the data: hyperbolic (solid lines), polynomial (dotted lines) and exponential (dashed lines), defined with Eqs. (5.2), (5.8) and (5.1), respectively.

thickness d (corresponding to triple scattering)

$$N_{\substack{L\\R}} = N_0 \left[(1 \pm S_0)d + \alpha(1 \pm S_0)d^2 + \beta d^2 + \gamma(1 \pm S_0)d^3 + \delta d^3 \right], \tag{5.3}$$

where the upper and lower signs correspond to N_L and N_R, respectively. Coefficients α and γ describe the double and triple scattering with analyzing power. Coefficients β and δ describe the double and triple scattering without analyzing power. For the difference and sum one gets

$$N_L - N_R = 2N_0 \left[S_0 d + \alpha S_0 d^2 + \gamma S_0 d^3 \right], \tag{5.4}$$

$$N_L + N_R = 2N_0 \left[d + \alpha d^2 + \beta d^2 + \gamma d^3 + \delta d^3 \right]. \tag{5.5}$$

The polynomial parametrization can be obtained from the asymmetry

$$S_{\text{eff}}(d) = \frac{N_L - N_R}{N_L + N_R} = \frac{S_0 + \alpha S_0 d + \gamma S_0 d^2}{1 + (\alpha + \beta)d + (\gamma + \delta)d^2}. \tag{5.6}$$

If β is the only parameter different from 0, one gets the standard hyperbolic dependence

$$S_{\text{eff}}(d) = \frac{S_0}{1 + \beta d}. \tag{5.7}$$

Eq. (5.6) can be rewritten in the form

$$S_{\text{eff}}(d) = \frac{S_0 + \beta_1\, d + \beta_2\, d^2}{1 + \alpha_1\, d + \alpha_2\, d^2}, \tag{5.8}$$

where the fitted constants β_1, β_2, and α_1, α_2 describe the scattering with and without analyzing power, respectively.

A comparison of the three proposed parametrizations is shown in Fig. 5.6 for two energies. It can be seen that the exponential parametrization does not describe the data

Table 5.1: Comparison of the theoretical Sherman function S, corresponding to the scattering off a single atom, obtained with the ELSEPA [42] code to the extrapolated zero-thickness values S_0 obtained from fitting the hyperbolic (5.2) and polynomial (5.8) target-thickness parametrizations to the simulated data for detectors placed at an angle of 164° with respect to the beam axis (scattering angle range $163.5° < \theta < 164.5°$).

beam energy	**ELSEPA**	**HYP**	**POL**
1.0 MeV	-0.454	-0.468 ± 0.005	-0.454 ± 0.007
1.5 MeV	-0.505	-0.501 ± 0.007	-0.502 ± 0.005

Table 5.2: Comparison of the reduced χ^2 values obtained with the hyperbolic (5.2) and polynomial (5.8) target-thickness parametrizations of the simulated effective Sherman function data for detectors placed at an angle of 164° with respect to the beam axis (scattering angle range $163.5° < \theta < 164.5°$).

beam energy	**HYP**	**POL**
1.0 MeV	7.83	0.56
1.5 MeV	0.40	0.46

well. In general a good fit to the experimental data was achieved with the hyperbolic parametrization, in agreement with the analysis done at 14 MeV [33]. However, for the lowest energy of 1.0 MeV there is a noticeable difference between the polynomial and hyperbolic parametrization.

In order to determine which of the parametrizations is more adequate, the extrapolated zero-target-thickness value S_0 can be compared to the theoretical predictions for scattering off a single atom. The extrapolation results are compared to the values obtained with ELSEPA in Table 5.1. A better agreement at 1.0 MeV is achieved with the polynomial extrapolation. At higher energies both parametrizations are in agreement within the uncertainties.

The χ^2 test results, listed in Table 5.2, confirm that a much better description of 1.0 MeV data is obtained with the polynomial fit, while the results at 1.5 MeV are similar for both parametrizations. In all tested cases except hyperbolic parametrization at 1.0 MeV, values in agreement with the χ^2 distribution were obtained (results of the order of 0.5 have a relatively large probability for a low number of degrees of freedom, due to the asymmetry of the χ^2 distribution).

Dependence on energy

The Monte Carlo simulation is performed in the full range of scattering angles, but at a fixed beam energy. The parametrization of the effective Sherman function dependence on energy can thus be used to interpolate the data for intermediate energies. Additionally, it will be used in the polarization transfer experiment, which requires the measurements to be performed at two different energies.

Our results (cf. Section 5.2.3) indicate that in the case of thick targets, the effective Sherman function dependence on energy is approximately linear. However, the theo-

retical Sherman function typically exhibits a minimum around a few MeV (for a fixed scattering angle), which is reflected in the data for thin targets. A satisfactory description of the data can be achieved with a linear function modified with an exponential term,

$$S_{\text{eff}}(E) = a + bE \exp(cE), \tag{5.9}$$

where a, b, and c are fitted constants. For thin targets the value of the c parameter is negative and approaches zero with increasing target thickness.

5.2.2. Comparison to the experimental data at 100 keV

The reliability of the original PEBSI simulation code was verified by comparing the simulated effective Sherman function with experimental data for 100 keV electrons scattered off gold targets of varying thicknesses measured by Kohashi et al. [67] in the full range of scattering angles. The results from Geant4 are in perfect agreement with the former code and reproduce the experimental data reasonably well, as shown in Figure 5.7. A detailed discussion of the simulation results and a possible explanation of the discrepancies between the simulations and the measurements can be found in the original paper [60].

5.2.3. Comparison to the experimental data at 1 – 3.5 MeV

The simulation results were compared to the measurements performed with the Mott polarimeter at the Mainzer Mikrotron (MAMI) electron accelerator, at the scattering angle of 164°, with several beam energies and target thicknesses [50].

The MAMI Mott polarimeter is shown schematically in Fig. 5.8. It consists of a vacuum scattering chamber made of very pure aluminum, containing the gold targets of various thicknesses, which can be changed on demand. It is operated with the beam polarization vector in the horizontal plane, therefore, electrons Mott-scattered in the vertical plane at an angle of 164° with respect to the beam axis are detected in two identical counters. The angular acceptance of approx. ±0.5° (corresponding to the solid angle of 0.21 msr) is defined by cylindrical collimators made of aluminum. The electrons passing through the collimators are deflected at an angle of approx. 90° in double focusing spectrometer magnets imaging the beam spot from the target to the scintillator surface. This arrangement reduces the gamma-ray background originating from electron scattering off the collimators, chamber walls, and beam dump. The vacuum is closed with aluminum windows, 0.5 mm thick, placed in front of the scintillators and the scintillation light is detected with photomultipliers. The beam polarization orientation is reversed periodically, which reduces the systematic errors.

The asymmetry was determined from the count rates measured in two detectors at five energies (1.0, 2.0, 2.5, 3.0, and 3.5 MeV) with five gold targets (0.1, 0.25, 0.5, 1, and 15 μm thick) [50]. The experimental data were analyzed in the following way: (*i*) the measured dependence of the count rate asymmetry on the target thickness was extrapolated to zero target thickness, (*ii*) the beam polarization was calculated from the extrapolated zero-thickness asymmetry and the theoretical value of the Sherman

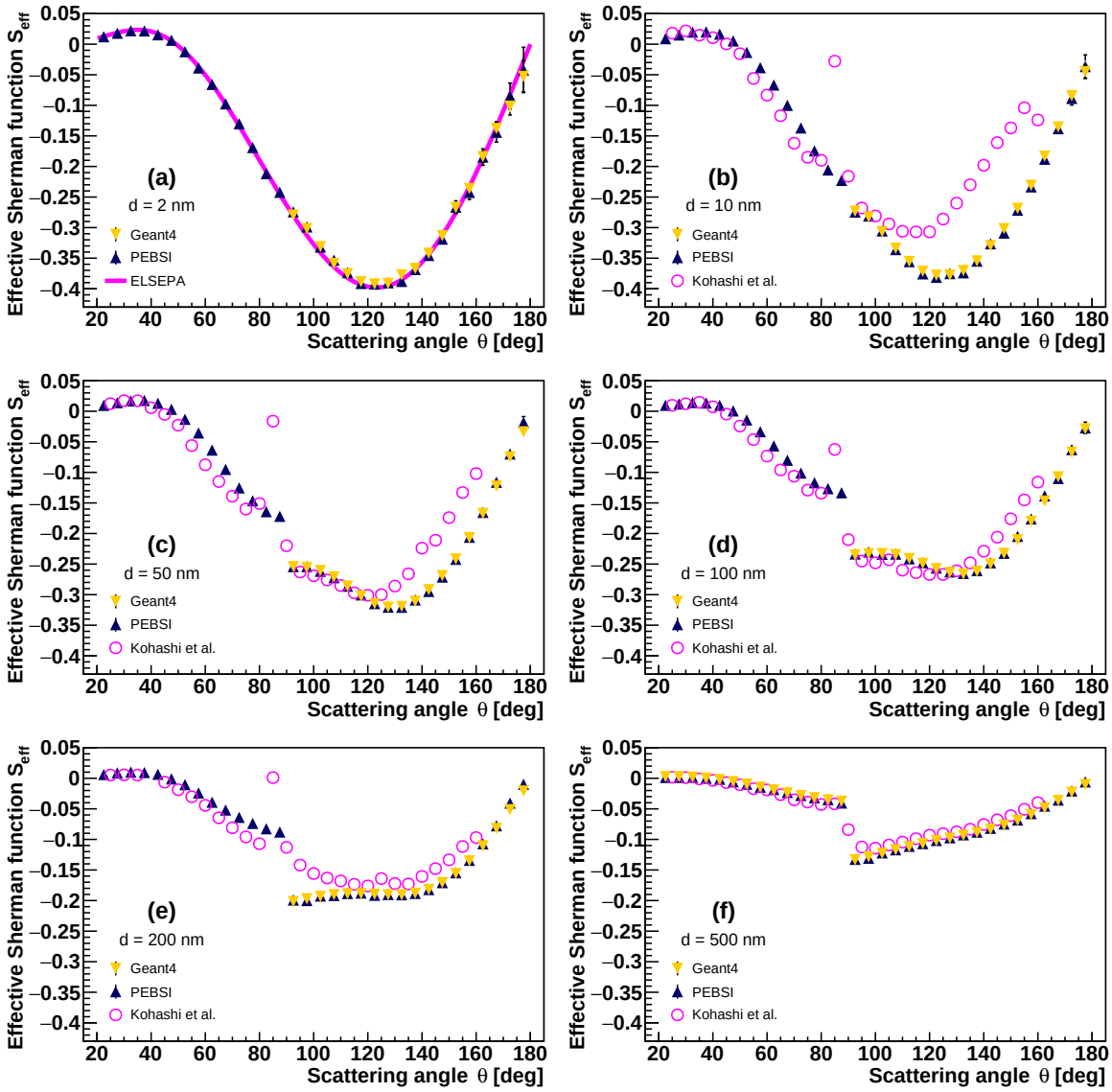

Figure 5.7: Dependence of the effective Sherman function on the scattering angle θ for 100 keV beam and 6 gold target thicknesses: (a – f) 2, 10, 50, 100, 200, 500 nm (50 keV low–energy cut on simulation and experimental data). Full points – simulation: yellow triangle down – Geant4, dark blue triangle up – PEBSI. Solid line (a) – theoretical value for a single atom from ELSEPA [42]. Open points (b – f) – measurements of Kohashi et al. [67].

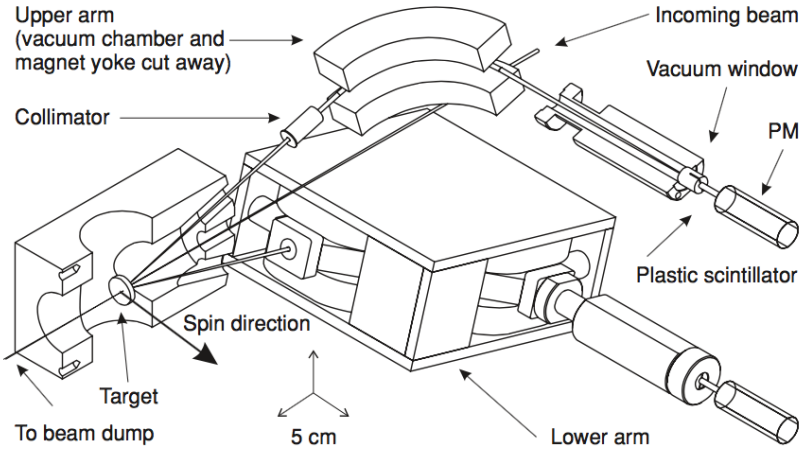

Figure 5.8: Schematic illustration of the Mott polarimeter at MAMI. Electrons backscattered at 164° in the vertical plane, after passing through collimators, are deflected in a magnetic field and detected in scintillation counters. Source: [50].

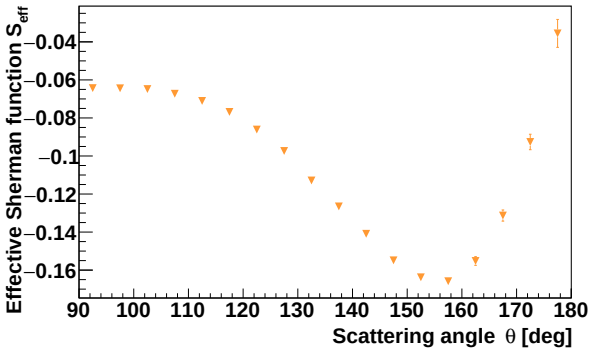

Figure 5.9: Dependence of the simulated effective Sherman function S_{eff} on the scattering angle θ, for a 3.0 MeV beam scattered off a 9.9 μm Au target.

function for a single atom, (*iii*) the effective Sherman function for finite target thicknesses was calculated from the measured asymmetry values and the beam polarization according to Eq. (3.4).

Impact of data selection

Scattering angle

The effective Sherman function depends significantly on the scattering angle; an example is shown in Fig. 5.9. It is, therefore, necessary to understand how the simulation and extrapolation results are sensitive to the accepted scattering angle range (aperture of the collimators).

The dependence of the theoretical Sherman function on beam energy is shown in Fig. 5.10 for three scattering angles around 120° and five scattering angles around 164°. Around 120°, there is a good agreement between the nominal ELSEPA predictions and

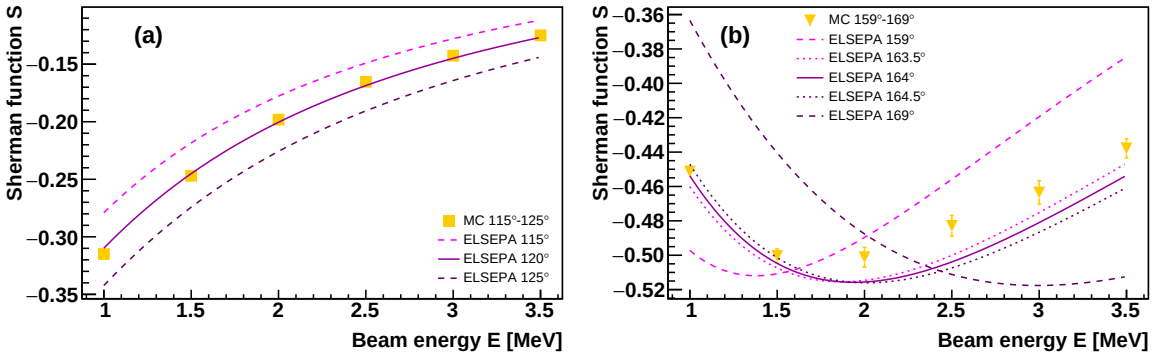

Figure 5.10: Dependence of the Sherman function S on beam energy E in two scattering angle ranges: around 120° (a) and around 164° (b). Extrapolations of the simulated data (points) are compared to the theoretical predictions from the ELSEPA [42] code (curves).

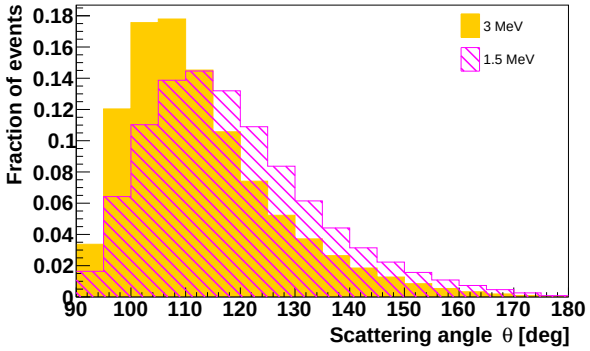

Figure 5.11: Distributions of the scattering angle θ for 1.5 MeV and 3.0 MeV electron beams backscattered off a 5 μm thick gold target.

the zero-thickness extrapolation of the simulation results. However, around 164°, extending the scattering angle range (increasing the collimator aperture) increases the extrapolated value in comparison to the theoretical predictions for energies above approx. 1.5 MeV.

Monte Carlo simulations may be useful to explain this effect. The angular distribution of electrons scattered off a 5 μm thick gold foil is shown in Fig. 5.11. It can be seen that locally, both around 120° and 164°, the number of scattered electrons decreases with the scattering angle. Therefore, an event sample recorded with a finite collimator aperture will contain more events scattered at the lower end of the accepted angular range, which is reflected in the extrapolation results shown in Fig. 5.10. Around 120°, the Sherman function decreases approximately linearly with the scattering angle. As a result, the extrapolation result converges to the central value even for wide collimators accepting electron tracks in the range 115° — 125°. Meanwhile, at 2.0 MeV there is a local minimum of the Sherman function around 164°, which explains the increase of the extrapolated Sherman function obtained in the range 159° — 169° with respect to the theoretical value at 164°. A similar increase is also observed at higher energies due

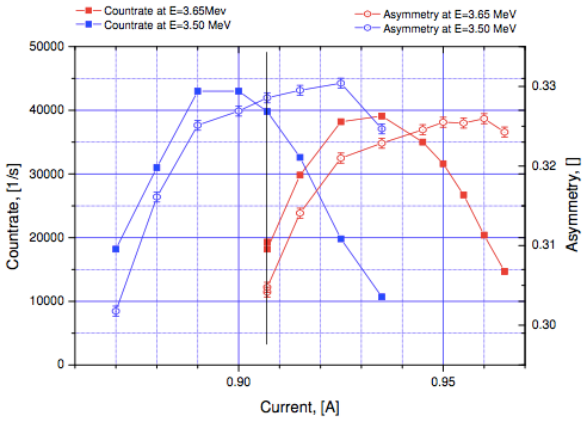

Figure 5.12: Dependence of the measured asymmetry and count rate on the bending magnet current in the MAMI polarimeter. The black vertical line corresponds to the magnet current of 907 mA used at 3.5 MeV. Source: V. Tioukine, private communication.

to the nonlinear dependence on the scattering angle.

Energy

The MAMI polarimeter design using a magnetic spectrometer introduces an implicit energy selection due to the finite collimator and scintillator sizes. The trajectory radius R is

$$R = \frac{\sqrt{T^2 + 2mT}}{eB}, \tag{5.10}$$

where B is the magnetic field, m and e are the electron mass and charge, and T is the kinetic energy. Therefore, the maximum energy loss of electrons passing through the collimators in the MAMI spectrometer is expected to change with beam energy due to the different bending of electron tracks in the magnetic field.

The low-energy limit of recorded electrons was estimated by performing measurements with various magnet currents, as shown in Fig. 5.12. The count rate maximum at 3.5 MeV is observed for the current of approx. 895 mA and the count rate maximum at 3.65 MeV is observed for the current of approx. 935 mA. These two values allow for the calibration of the relation between central energy and magnet current. The magnet current of 907 mA used at 3.5 MeV corresponds to a slightly higher energy than 3.5 MeV. The central energy calculated from the linear interpolation is approx. 3.55 MeV.

From the intersection of the 907 mA line with the count rate dependences at 3.5 and 3.65 MeV, one can tell that the count rate decreases by approx. 50% with the energy change of 0.15 MeV. Therefore, the low-energy cut corresponding to 50% count rate decrease is equal to approx. 3.4 MeV. Alternatively, the same result can be obtained from the 3.5 MeV count rate dependence. The count rate decreases by 50% for the magnet current of approx. 870 mA. Using the linear extrapolation, one obtains again 3.4 MeV. Since such measurements were performed only at 3.5 MeV, we assumed, to

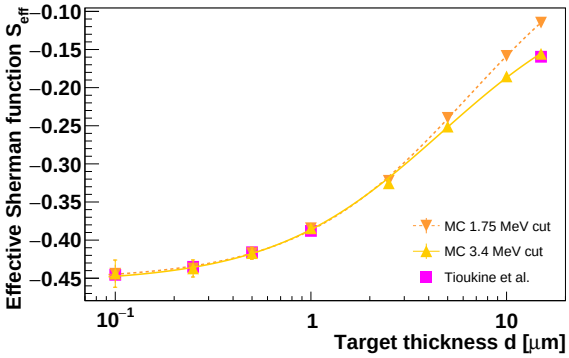

Figure 5.13: Dependence of the effective Sherman function S_{eff} on the target thickness d, for a 3.5 MeV beam with detectors placed at an angle of 164° with respect to the beam axis. The measurements of Tioukine et al. [50] (square magenta points) are compared to the simulation results (scattering angle range $162° < \theta < 166°$) with two low-energy cuts: 1.75 MeV (orange triangles down) and 3.4 MeV (yellow triangles up); the latter cut corresponds to the approximate low-energy cut in the experiment (see text for details). The lines represent the polynomial fit to the simulated data.

a first approximation, the same upper limit on energy loss of 0.1 MeV for all beam energies.

The difference between the simulated effective Sherman function with the measured low-energy cut and with a much lower cut of half the beam energy is shown in Fig. 5.13. It can be seen that the difference is negligible for targets thinner than a few μm, due to the low energy loss, but significant in case of thicker targets.

Comparison to the experimental data

The experimental and simulated data are compared in Fig. 5.14 for 5 target thicknesses and 5 energies. It can be seen that the simulated and measured data agree reasonably well.

The simulation was also performed for the intermediate energy of 1.5 MeV, which was not used during the measurements with the MAMI Mott polarimeter, but is used in the polarization transfer experiment [31]. The predictions for the polarization transfer experiment, performed at the 120° scattering angle, are also shown in the figures.

The dependence of the effective Sherman function on energy is shown in Fig. 5.15. Comparison of the fits to the experimental and simulated data confirms that in general the results are in good agreement, although for the thick target the fitted curves depart from each other below approx. 2 MeV, due to the discrepancy observed at the lowest beam energy of 1.0 MeV.

5.2.4. Comparison to the experimental data at 14 MeV

The use of the Geant4 toolkit vastly improved the computation performance, allowing for the simulation of electron beams of higher energy, which was impractical with the PEBSI code due to the long computation time. One of the main reasons is a faster

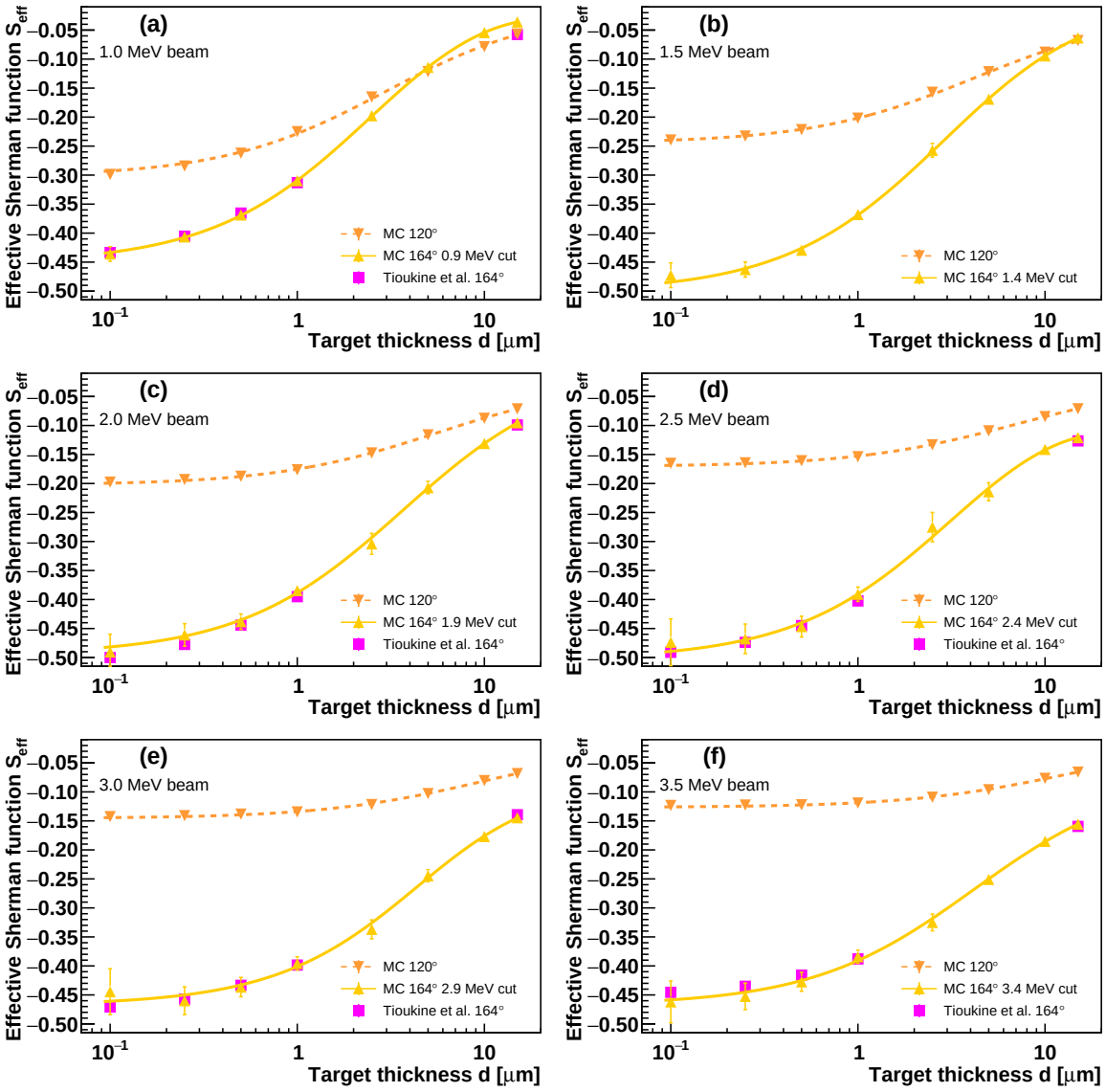

Figure 5.14: Dependence of the effective Sherman function S_{eff} on the target thickness d for detectors placed at two angles, 120° and 164°, with respect to the beam axis (scattering angle ranges $115° < \theta < 125°$ and $163.5° < \theta < 164.5°$), and six beam energies (a – f): 1.0, 1.5, 2.0, 2.5, 3.0, 3.5 MeV. Triangular points – simulation, square points – measurements of Tioukine et al. [50] at 164°. The lines represent the polynomial fit to the simulated data.

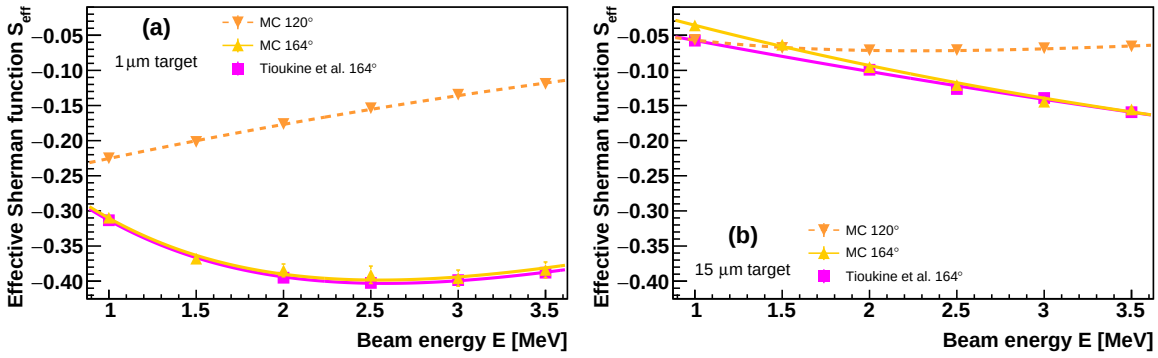

Figure 5.15: Dependence of the effective Sherman function S_{eff} on beam energy E for detectors placed at two angles, 120° and 164°, with respect to the beam axis (scattering angle ranges $115° < \theta < 125°$ and $163.5° < \theta < 164.5°$), and two target thicknesses: 1 μm (a) and 15 μm (b). Triangular points – simulation, square points – measurements of Tioukine et al. [50] at 164°. The lines represent the fits to the data, Eq. (5.9).

random number generator, and probably also a better optimization achieved in the Geant4 code, which has been broadly used and continuously developed over many years. An important practical improvement is also the automation of multi–threaded computations. Generation of 10^9 events of a 100 keV beam scattered off a 500 nm gold foil takes around 4 hours on a decent computer[1]. Simulations at 14 MeV are much more time consuming and can be effectively performed only on a cluster.

In Figure 5.16 one can see the comparison of the simulated effective Sherman function and the experimental data for 14 MeV electrons scattered off lead foils of varying thicknesses measured by Sromicki et al. [64][2]. The availability of experimental data in this energy range is very limited; the advantages of the measurements of Sromicki et al. are both the high energy and the fact that they were performed for a few different scattering angles.

One can see that a good agreement is found for the lowest scattering angle. For higher scattering angles, the agreement is promising for target thicknesses up to about 135 μm, but decreases with target thickness. Despite this fact, the simulation can be useful also in this energy range, since the thickest targets under consideration do not seem practically applicable in Mott polarimetry due to the low value of the effective analyzing power, below 5%, and a large amount of background.

A possible source of discrepancy between the simulated and measured data might arise from applied event selection. A low–energy cut of 7 MeV (half of the beam energy) was applied to the simulated data. A comparison of the results obtained with this cut and with a much higher cut of 13 MeV is shown in Fig. 5.17. It can be seen that the results for thick targets depend significantly on energy selection, contrary to the case of thin targets. The events from the simulation were selected in the ±5° range of the azimuthal angle. Unfortunately, no information about event selection applied to the experimental data was provided in the work of Sromicki et al. [64].

Another possible explanation of the differences observed at the high energy of

[1] tested on 2 × Intel Xeon E5-2680 V3

[2] the experimental values were read out from the plots in the original paper

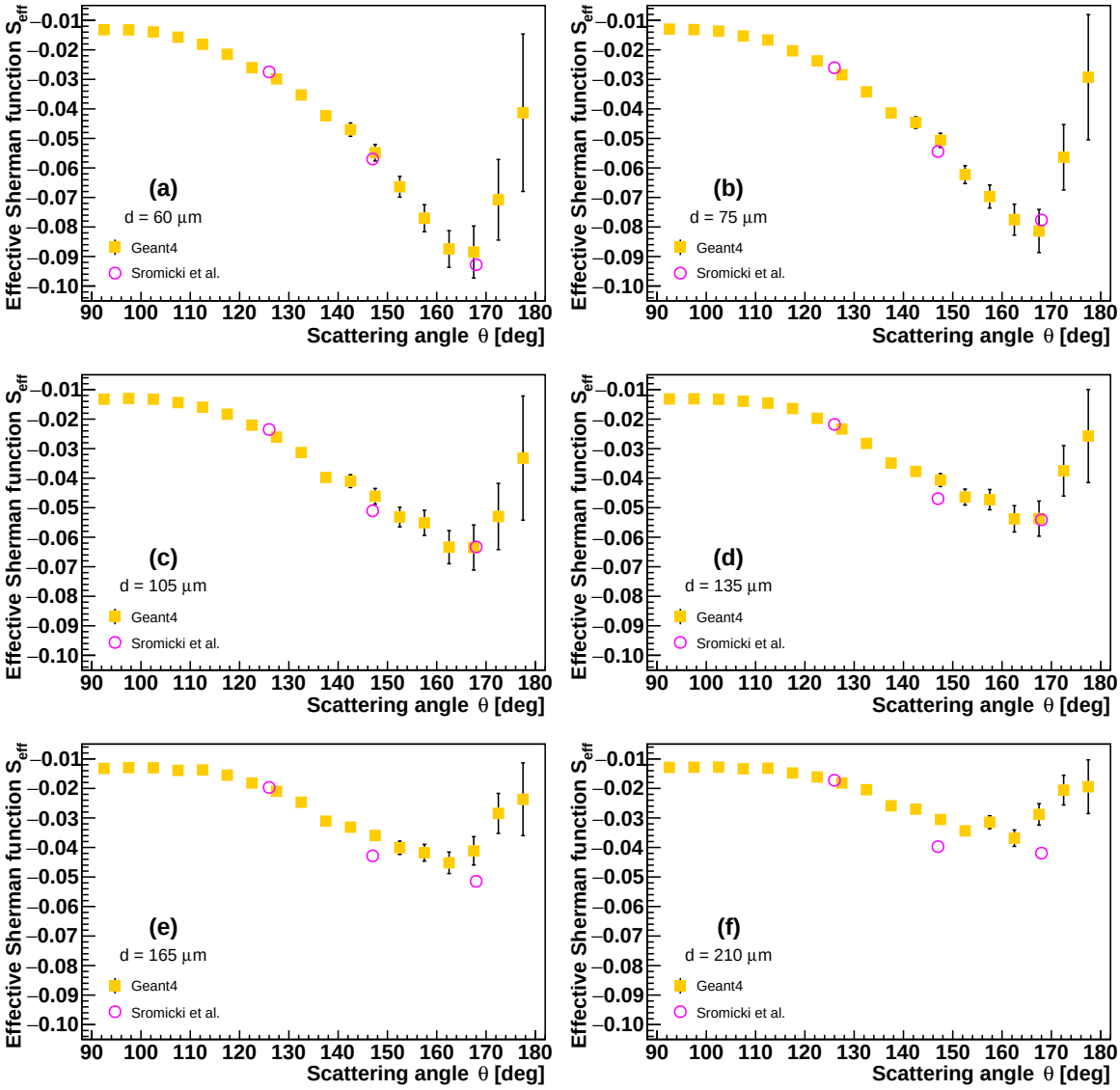

Figure 5.16: Dependence of the effective Sherman function on the scattering angle θ for 14 MeV beam and 6 lead target thicknesses: (a – f) 60, 75, 105, 135, 165, 210 μm. Full points – simulation (7 MeV low–energy cut on simulation data). Open points – measurements of Sromicki et al. [64].

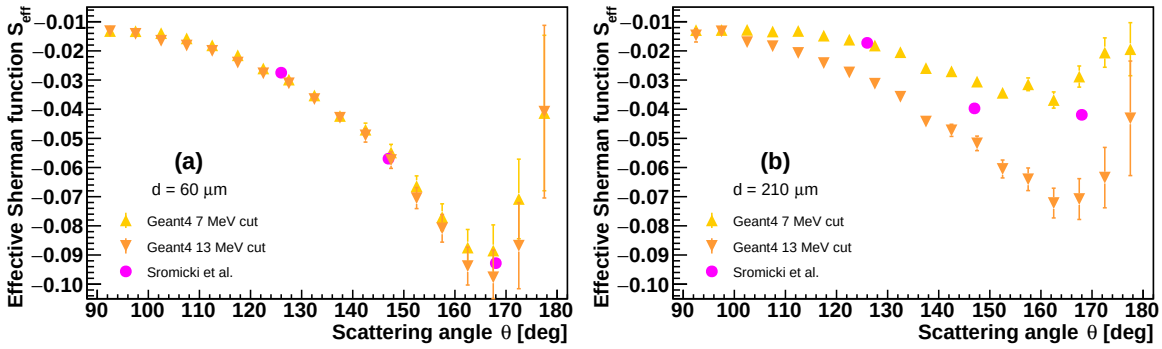

Figure 5.17: Dependence of the effective Sherman function on the scattering angle θ for 14 MeV beam and 2 lead target thicknesses: 60 μm (a), and 210 μm (b). Triangles oriented up and down correpond to the simulation results with 7 MeV and 13 MeV low–energy cut on simulation data, respectively. Circles – measurements of Sromicki et al. [64].

14 MeV might follow from a few effects relevant for the calculation of the Sherman function, pointed out in [68], which were not accounted for in the simulations. We are not aware of an exact calculation of the first-order radiative corrections to Mott scattering. Nevertheless, their magnitude is expected to be increasing with energy and at 14 MeV might produce a significant contribution to the Sherman function with respect to the value generated with ELSEPA.

Production of secondary particles in ionization and bremsstrahlung emission was not taken into account in order to speed up the computations. According to the simulations at 100 keV [60], Møller scattering does not significantly contribute to the effective Sherman function, if an energy cut above half of the beam energy is applied. This is also in agreement with the theoretical predictions for polarization transfer in Møller scattering (cf. Fig. 2.2), according to which the polarization of electrons scattered at angles up to more than half of the symmetric scattering angle (up to about 15° at 3 MeV) remains practically unchanged. Thus to a first approximation one may simulate only the change of polarization caused by Mott scattering.

We have not encountered any data for energies higher than 14 MeV. The comparisons presented above demonstrate the usefulness of our code in the whole range of the practical applicability of Mott polarimetry.

5.3. Optimization of the experiment

5.3.1. Scattering angle and target thickness

The Monte Carlo simulation allowed us to make predictions for the new polarization transfer experiment [31]. Here we report the results of the study performed before the actual measurement, in order to optimize the design with regard to the effective Sherman function dependence on energy, target thickness and scattering angle.

The aim of the experiment is to measure the ratio of the transverse polarization

vector component length of the electrons in the final state of Møller scattering to the incoming-beam polarization, using the Mott polarimetry method. In this case, the interaction probability is many orders of magnitude lower than in the case of a standard polarization measurement performed on a beam, due to the low combined probability of coincident Møller and Mott scattering.

In order to reduce the background rate, Mott polarimetry measurements are typically performed with the thinnest possible target that provides acceptable event rates. Additionally, the largest value of the Sherman function at MeV energies is achieved at a large angle (almost complete backscattering). These experimental conditions are far from those optimal from the statistics point of view, due to the rapid decrease of the Mott-scattering cross section with the scattering angle. In this section we present the method of statistical optimization of the polarimeter. We obtain the scattering angle and target thickness ranges minimizing the measurement time under the assumption of no background.

An optimal experimental configuration should minimize the statistical uncertainty of the measured polarization value. The uncertainty of the asymmetry calculated from Eq. (3.1) is

$$\Delta A = \sqrt{\frac{4N_L N_R}{(N_L + N_R)^3}}. \tag{5.11}$$

At the same time, from Eqs. (3.1) and (3.4) one can find that

$$\frac{4N_L N_R}{(N_L + N_R)^2} = 1 - (\vec{P} \cdot \vec{n})^2 S_{\text{eff}}^2. \tag{5.12}$$

Neglecting the uncertainty of the effective Sherman function, the uncertainty of the measured polarization value is

$$\Delta P = \sqrt{\frac{1}{N_L + N_R}\left(\frac{1}{S_{\text{eff}}^2} - (\vec{P} \cdot \vec{n})^2\right)}. \tag{5.13}$$

The effective Sherman function in the polarization transfer experiment is of the order of 0.1, thus the term $1/S_{\text{eff}}^2$ dominates and the uncertainty is to a good approximation

$$\Delta P \approx \sqrt{\frac{1}{S_{\text{eff}}^2 (N_L + N_R)}}. \tag{5.14}$$

Therefore, minimizing the uncertainty is equivalent to maximizing the figure of merit, defined as [40]

$$F = S_{\text{eff}}^2 (N_L + N_R) = S_{\text{eff}}^2 \frac{N}{N_0}, \tag{5.15}$$

where N is the number of electrons recorded in the detectors and N_0 is the total number of incoming beam electrons (N_L and N_R denoted the normalized count rates).

The figure-of-merit dependence on the scattering angle is shown in Fig. 5.18. It can be seen that, regardless of target thickness, the maximum is attained for intermediate scattering angles, much lower than those typically used. Both at 1.5 and 3.0 MeV the optimal scattering angle values are between 110° and 125°, with a slight increase with

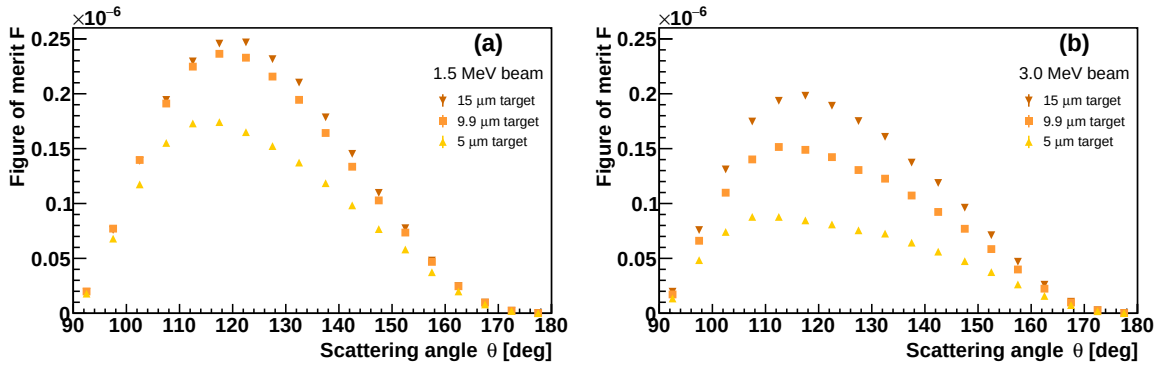

Figure 5.18: Dependence of the figure of merit F on the scattering angle θ for three target thicknesses d (5, 9.9, 15 μm) and two beam energies: 1.5 MeV (a) and 3.0 MeV (b).

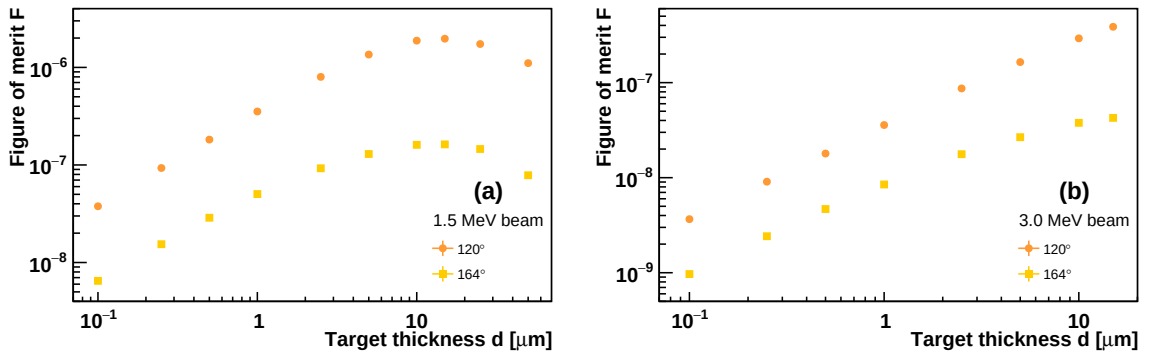

Figure 5.19: Dependence of the figure of merit F on the target thicknesses d for detectors placed at two angles, 120° and 164°, with respect to the beam axis (scattering angle ranges $115° < \theta < 125°$ and $159° < \theta < 169°$), and two beam energies: 1.5 MeV (a) and 3.0 MeV (b).

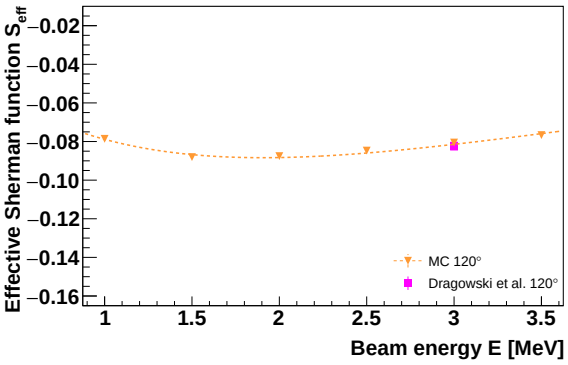

Figure 5.20: Dependence of the effective Sherman function S_{eff} on beam energy E, for detectors placed at an angle of 120° with respect to the beam axis (scattering angle range $115° < \theta < 125°$) and 10 μm target thickness. Triangular points – simulation, square point – value measured in the polarization transfer experiment [31]. The line represents the fit to the simulated data, Eq. (5.9).

the target thickness. A similar angular range was found to be optimal also at 100 keV energy [60].

By analyzing the figure-of-merit dependence on the target thickness one can find the thickness value that is optimal from the statistics point of view. It can be seen in Fig. 5.19 that the figure of merit at 1.5 MeV is rapidly increasing up to about 5 μm (note the logarithmic scale in the plot). The change is much smaller when going to even thicker targets; in particular for the 120° scattering angle there is very little difference between the values at 10 and 15 μm (see also Fig. 5.18(a)). Since the use of thicker targets is associated with a higher rate of target-related background events, one can conclude that it is not desirable to use targets thicker than about 10 μm at 1.5 MeV. The thickest targets at our disposal, 9.9 μm and 10.1 μm thick, were found to be quite close to the optimal thickness.

5.3.2. Dependence on energy

The final result in the polarization transfer experiment is derived as the ratio of polarizations before and after Møller scattering. Under the experimental conditions assuming symmetric Møller scattering, the two polarization values are measured at energies different by a factor of 2. It is, therefore, useful to parametrize the effective Sherman function dependence on the beam energy for a given target thickness and scattering angle. Such a parametrization is convenient for determining the effective Sherman function ratio at two energies, which can be used in the data analysis instead of the absolute values.

The predictions for the dependence of the effective Sherman function on energy in the polarization transfer experiment are shown in Fig. 5.20. The experimental result obtained at 3.0 MeV, which is also shown for comparison, is found in good agreement with the simulations. A very small dependence of the effective Sherman function on beam energy is found under the proposed conditions of the experiment. This way the effective Sherman function ratio at two energies, which is used for the determination

of the measurement results, is less sensitive to the systematic uncertainty of the Monte Carlo predictions, as long as the predicted dependence shape (near constant) is correct.

The effective Sherman function dependence on the low-energy cut has been discussed in Section 5.2.3 in case of the MAMI polarimeter (Fig. 5.13). A similar effect can be important for the polarization transfer experiment, given the relatively large thickness of the optimal targets chosen at the beginning of this section. Therefore, a similar study was performed using the simulation results, which is discussed in Section 8.3.

Chapter 6

Simulation of the experimental setup

A simulation of the complete experimental setup was performed with the Geant4 toolkit. It allowed us to study possible background processes and the influence of finite target thickness on interaction probabilities.

6.1. Geant4 model of the experimental setup

During the simulation, the positions and momenta of particles entering the targets and scintillators were saved. In case of the gold target, the target penetration depth and exit position and momentum was stored as well. The real energy deposit in the scintillator, which in general might be lower than particle energy, was recorded. Finally, all particle trajectories were stored in form of a list of detector parts traversed by the particle (e.g., the expected signal electron trajectory corresponds to the following sequence of volumes: beryllium target, gold target, scintillator). The charge of particles was stored as well, in order to distinguish between signals created by electrons and by gammas. The model of the experimental setup, visualized with Geant4, is shown in Fig. 6.1.

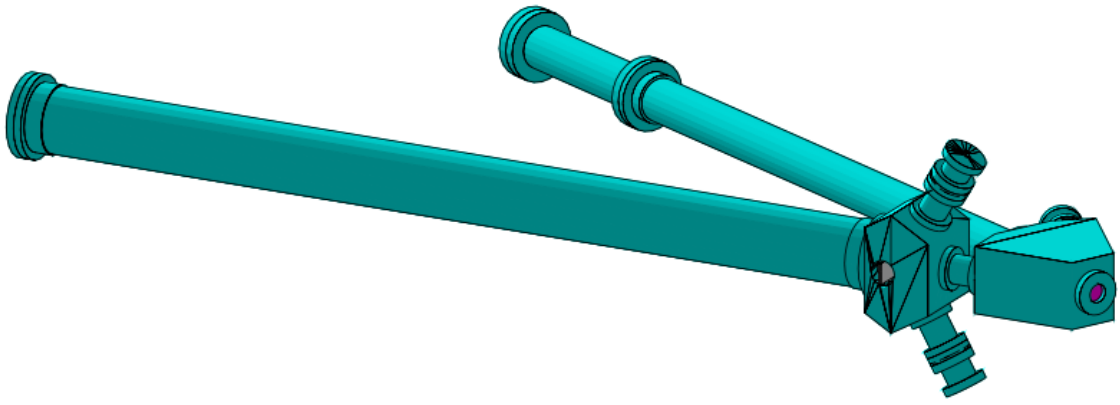

Figure 6.1: Model of the experimental setup in configuration *A* visualized in Geant4.

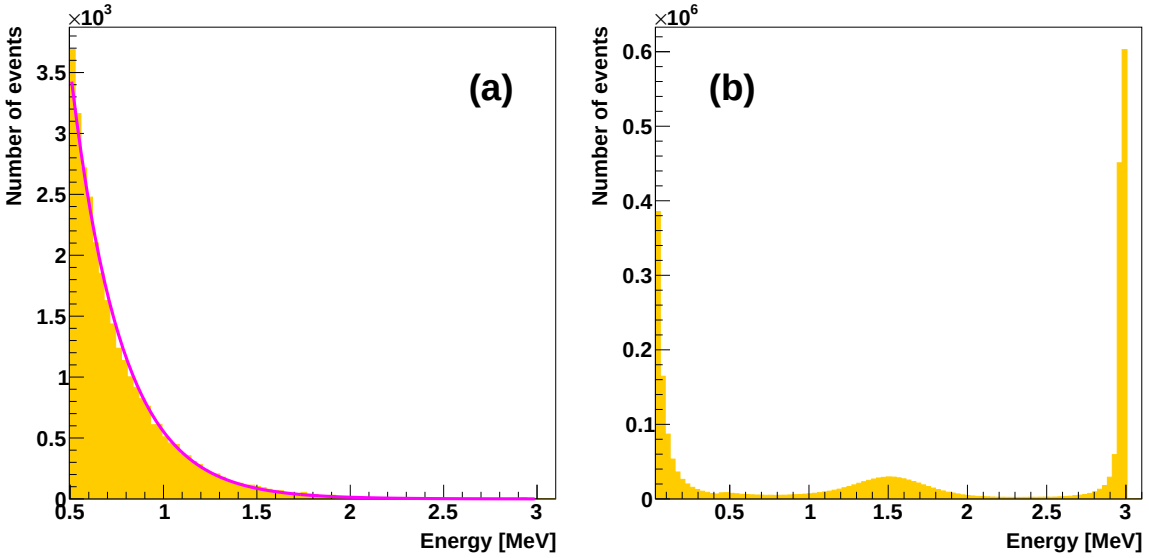

Figure 6.2: Simulated energy spectra in the polarimeter detectors (a) and tagging counter (b). The magenta line in the left plot represents an exponential fit.

Table 6.1: Sources of background events (scattering elements of the background electrons) with energy above 0.5 MeV recorded in polarimeter detectors.

source	fraction of events
beam pipe	61.5%
Møller scattering chamber	24.6%
both	12.4%
other	1.5%

6.2. Background energy spectrum

The distributions of single-counter energy deposit are shown in Fig. 6.2. It can be seen that they differ quite significantly between the polarimeter detector and the tagging counter. In the latter case, a contribution of Mott-scattered beam electrons (3 MeV) and Møller electrons (1.5 MeV) is clearly visible. In the polarimeter, the spectrum consists mostly of low-energy background, which can be modeled as exponential.

The simulation allowed us to investigate the origin of background. Visualizations of example signal and background events are shown in Figs. 6.3 and 6.4, respectively. In order to quantitatively analyze the origins of background events, particle trajectories were studied. As can be seen in Table 6.1, the majority of background events originated from beam electrons scattered off the beryllium target at low angles, subsequently hitting the beam pipe. This result demonstrated the importance of the shielding of the polarimeter. On the other hand, the background created in the polarimeter itself, produced a much lower contribution.

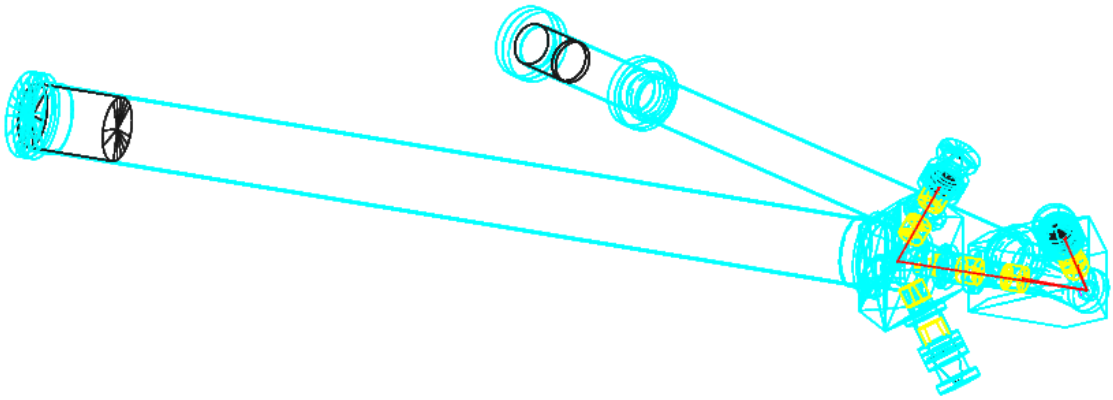

Figure 6.3: Geant4 visualization of a signal event. Trajectories of two electrons in the final state of Møller scattering are shown with red lines.

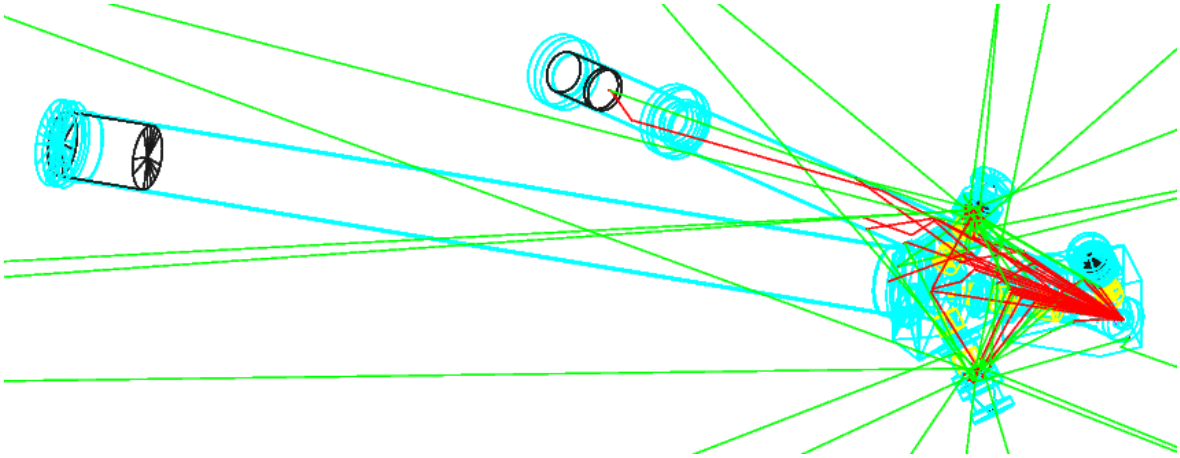

Figure 6.4: Geant4 visualization of 30 events with energy deposit in any of the polarimeter detectors above 0.5 MeV. Electron trajectories are shown in red and gamma trajectories are shown in green.

6.3. Passage through the beryllium target

6.3.1. Beam dispersion

When the beam passes through the beryllium target, electrons are Mott-scattered off beryllium nuclei, making the beam divergent downstream from the target. Electrons scattered at a sufficiently large angle hit the beam pipe, leading to the change of their direction or production of secondary radiation, which might reach the detectors, creating background events in the experiment. While it is not possible to eliminate this effect completely, it might be reduced with the use of a sufficiently large diameter of the beam pipe.

The beam profile after passing through a 100 μm thick beryllium target was modeled with the Monte Carlo simulation. The initial beam spot (before entering the beryllium target) was modeled as a symmetrical two-dimensional Gaussian distribution with a standard deviation of 1 mm. The secondary beam spot (after passing through the target), observed on a virtual plane 300 mm downstream from the target, which is the position corresponding to the projection of the gold target position on the primary beam direction, is shown in Fig. 6.5. A good description of the secondary beam profile was achieved with a Gaussian fit and the standard deviation was found to be of approx. 12 mm.

Given the limited space between the Mott polarimeter and the beam pipe, the choice of the beam pipe diameter has to balance the number of electrons scattered off the pipe (increasing the background) and the thickness of the lead shielding around the pipe (reducing the background). A standard CF63 flange matches a pipe with an inside diameter of 61 mm, which corresponds to approx. 2.5 σ coverage of the beam spot. At the same time, there was not enough space for a larger CF100 flange. Custom flanges, which could be connected to a CF63 flange on the beam-dump side, but allowing us to use a pipe of a slightly larger diameter, were manufactured. The inner diameter of 66 mm was finally achieved, which corresponds to approx. 2.7 σ coverage.

6.3.2. Interaction probability

In theory, the Møller scattering probability increases with beryllium target thickness. However, electrons in the final state of Møller scattering (in the angular range corresponding to the collimators acceptance), which are the candidates for signal events, are also subject to Mott scattering off beryllium nuclei. As a result, not all of them reach the Mott polarimeter (gold target) or the tagging counter. The simulation allowed us to obtain the dependence of the expected number of signal events on beryllium target thickness.

It can be seen in Fig. 6.6 that the single-scattering approximation (linear increase of the scattering probability with target thickness) might be valid for targets up to at most a few μm. For higher thicknesses the increase is not as fast, and for thicknesses above approx. 50 μm the rate of signal events is practically constant, with a slight increase in the background contribution. Given the fact that the 100 μm thick beryllium target provides sufficient mechanical stability, there is no point in increasing the thickness above this value.

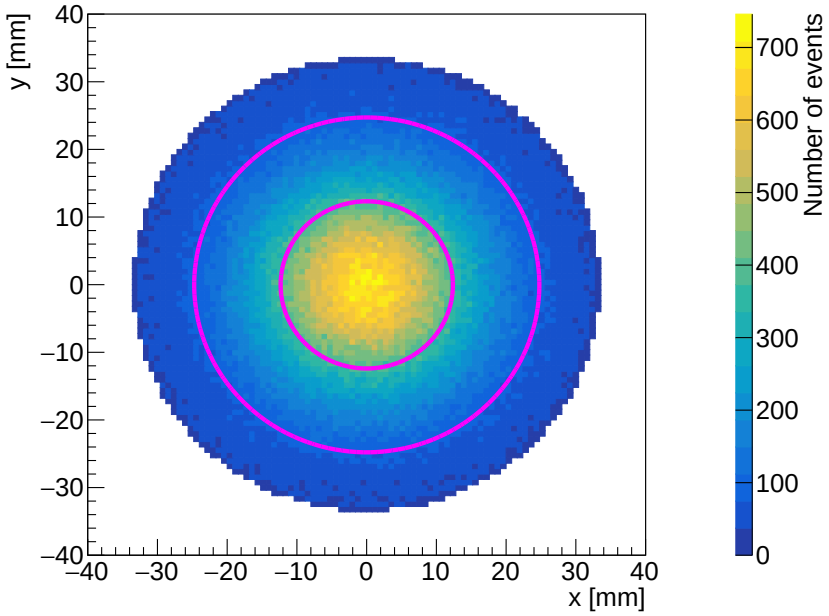

Figure 6.5: Simulated histogram of electron positions in a beam spot observed 300 mm downstream from a 100 μm thick beryllium target. The magenta contours correspond to the 1 σ and 2 σ levels of the one-dimensional projections. The histogram range corresponds to the dimensions of the beam pipe used in the experiment (66 mm in diameter).

With the 100 μm thick beryllium target used in the experiment, the probability of recording a signal event (one electron scattered directly from the beryllium target to the gold target in the polarimeter, and another electrons scattered directly to the tagging counter) is approx. 1.4×10^{-7}. The total probability including electrons subsequently scattered off other elements of the experimental setup is approx. 1.6×10^{-7}.

6.3.3. Beam depolarization

Møller polarization measurement

The simulation was also used to check whether the change of beam electrons and Møller electrons polarization during the passage through the beryllium target might affect the polarization measurement. Beam depolarization during the passage through the beryllium target was modeled with the same polarized electron Mott scattering model that was used to simulate the effective Sherman function. A 3 MeV electron beam passing through a 100 μm thick beryllium foil was simulated. The primary beam was assumed to be 100% transversely polarized.

The first analysis was restricted to electrons scattered at angles below 1.5° with

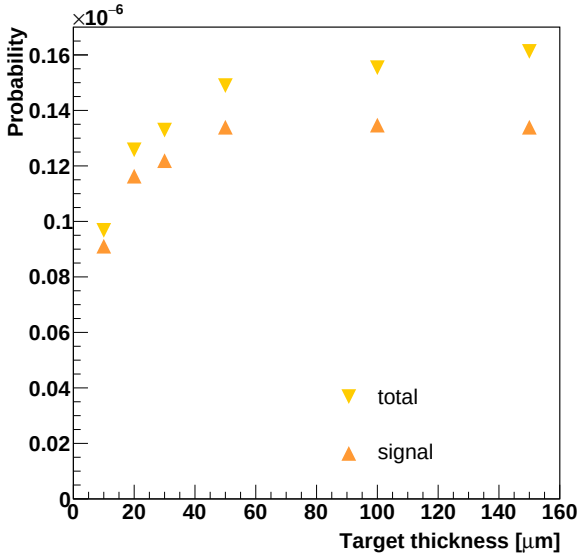

Figure 6.6: Dependence of the Møller scattering probability, as obtained from the Geant4 simulation of the experiment, on the beryllium target thickness. Total probability corresponds to all Møller electron pairs detected on the gold target and in the tagging counter, including background electrons scattered off the collimators or other parts of the experimental setup. Signal refers to the subsample of events, in which both electrons were scattered directly from the beryllium target to the gold target and the tagging counter.

respect to the primary beam direction, which corresponds to the angular acceptance of the leg collimators (between the beryllium and gold targets). In an average signal event, the beam electron passes through a half of the beryllium target thickness, then Møller scattering takes place, and the Møller electron passes through the remaining half. The maximum allowed deflection of Møller electrons is equal to the collimator acceptance (even though the scattered electron moves at an angle of 26.75° with respect to the primary beam direction, it is equivalent to analyze depolarization of electrons deflected not more than 1.5° around the initial beam direction).

In the case of beam deflection before Møller scattering, a larger angular range might be allowed (resulting in a broader energy distribution of Møller electrons). Therefore, a second analysis was done for comparison, with a wider range of scattering angles, up to 5° with respect to the primary beam direction.

The remaining polarization of the electrons exiting the foil was analyzed. The histograms of the remaining polarization in the direction of primary beam polarization are shown in Fig. 6.7. The depolarization effect is visible, since the average polarization is below 1. Nevertheless, even with unrealistically-high deflection angles up to 5°, the degree of depolarization is below 0.5%, and is much lower in the majority of events (note the logarithmic scale in the plot). It is, therefore, negligible in comparison to the other effects decreasing the measured asymmetry, such as the scattering off the collimators.

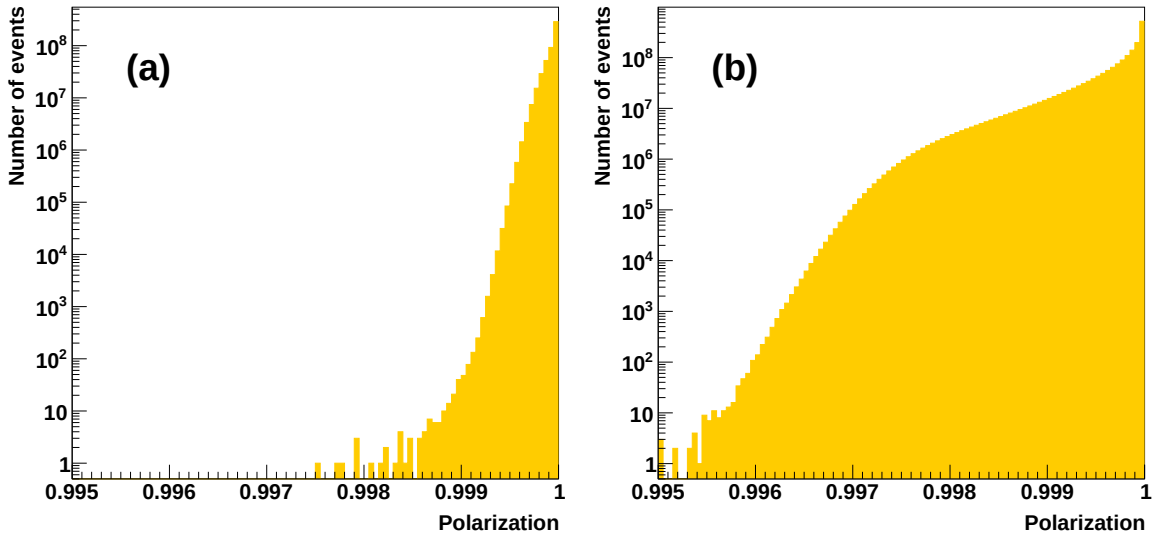

Figure 6.7: Remaining polarization in the direction of primary-beam polarization after scattering off a 100 μm thick beryllium target at 3 MeV at angles below 1.5° (a) and 5° (b).

Beam polarization measurement

The same simulation is also useful to check how the beam polarization is changed when beam electrons are scattered off the beryllium target during the beam polarization measurement. In this case, electrons scattered at a much larger angle are detected.

The histograms of polarization in the direction of polarization measurement in the Mott polarimeter for electrons Mott-scattered at 26.75° are shown in Fig. 6.8 in both experimental configurations. In configuration B (beam polarization perpendicular to the Mott scattering plane in the beryllium target), the polarization remains almost unchanged, similar to the scattering at small angles (Fig. 6.7). In configuration A, however, the beam polarization lies in the Mott scattering plane in the beryllium target, and the electron polarization direction is changed during the scattering. Except for the small depolarization, the polarization vector after the scattering remains horizontal and is perpendicular to the new momentum vector of the electron after the scattering. Even though in this case the polarization does not reach as high values as in configuration B, the depolarization is still below 0.3%. Therefore, the polarization measured with a polarimeter placed at an angle of 26.75° with respect to the primary beam direction is to a good approximation equal to the beam polarization (no correction is required).

6.4. Scattering off the collimators

6.4.1. Event generator

In order to speed up the computations, all other parts of the experimental setup except of the collimators were removed from the simulation. The interactions in the Møller target material were not simulated; the Møller event generator was used instead. An

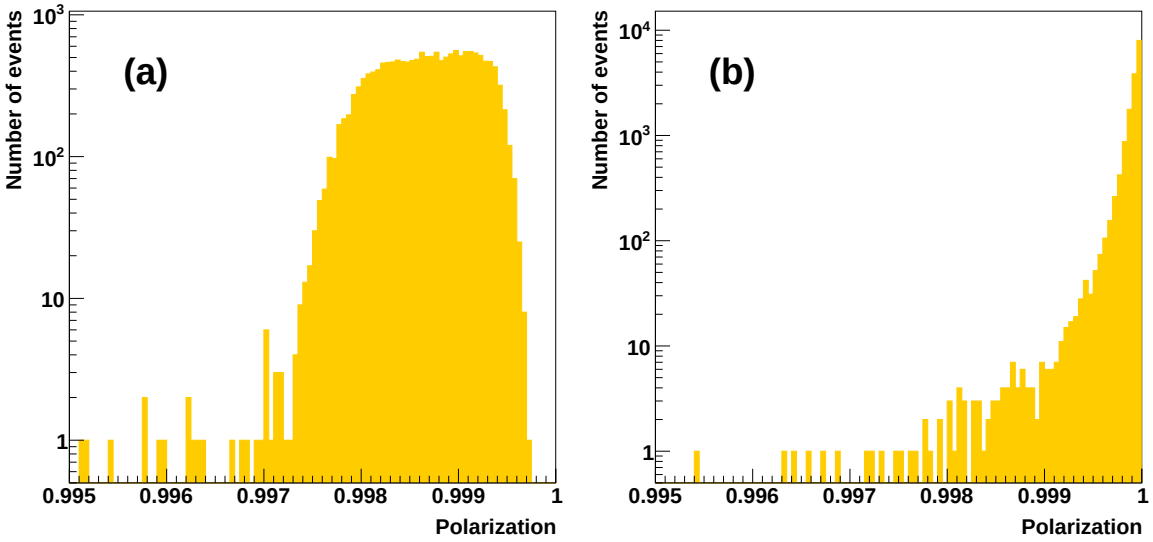

Figure 6.8: Remaining polarization after Mott scattering of a transversely polarized 3 MeV electron beam off a 100 μm thick beryllium target at an angle of 26.75°; (a) configuration A, beam polarization in the scattering plane (polarization measurement direction at 26.75° with respect to primary-beam polarization), (b) configuration B, beam polarization perpendicular to the scattering plane.

event generator simulated Møller electron pairs distributed according to the theoretical cross section and with the mean polarization vectors assigned according to the theoretical predictions. The Møller electrons were generated in the ±5° range around the symmetric scattering angle.

6.4.2. Beam spot diameter

A simulation using the Møller generator as an input and then performing particle tracking with Geant4 can be used to determine the corrections to the theoretical energy spectrum of Møller electrons due to the scattering off the collimators.

If the beam was perfectly focused in the geometrical center of the target, all electrons outside the ±1.5° would be stopped on the front surface of the collimator. In reality the energy range of recorded Møller electrons is wider than the collimator acceptance, due to the electrons scattered off the collimator surface in the direction of the Mott target. As a result of such scattering the electrons are at least partly depolarized and, therefore, decrease the measured asymmetry value.

The first parameter to be considered is the diameter of the beam spot, depending on how well the beam is focused. The beam position was sampled from a Gaussian distribution with the mean value in the center of the target and standard deviation of 1 mm and 1.5 mm. The resulting energy spectra are shown in Fig. 6.9. The tails of the distribution extend outside the theoretical energy range (between 1.4 and 1.6 MeV). One can also see a decrease of the number of events recorded close to the boundaries of the theoretical acceptance of the collimators. This again is the result of the beam being off center, therefore, the effect is higher for the larger beam spot. The distribution is

Table 6.2: Fraction of electrons scattered off the collimators reaching the polarimeter, simulated assuming different parameters of the beam spot.

beam position	**beam diameter**	**% collimator hits**
0	0	0.1%
0	1 mm	2.4%
0	1.5 mm	3.4%
+1 mm	1.5 mm	4.2%
−1 mm	1.5 mm	3.8%

slightly asymmetric due to the energy loss in the collimator material.

6.4.3. Beam position

The second parameter to be considered is the position of the beam spot, depending on how well the beam is positioned with respect to the geometrical center of the target. The more the beam electron is off the center, the wider the energy range that gets into the collimator. An additional asymmetry of the distribution is visible in the resulting energy spectra shown in Fig. 6.10.

The main result of the simulation is the fraction of electrons reaching the Mott target that were scattered off the collimators, which is listed in Table 6.2. The difference between the results obtained with opposite directions of the beam shift, 4.2% and 3.8%, is due to the different geometry of the scattering. At +1 mm shift, electrons scattered at lower-than-nominal angles, with larger cross section and energy, enter the collimator. At −1 mm shift, electrons scattered at larger angles, with lower cross section and energy, are detected.

6.4.4. False asymmetry

The different fraction of electrons scattered off the collimators for opposite beam shift directions might produce a false asymmetry in the number of counts, if the beam spot position is different for opposite beam polarization orientations.

The asymmetry of the fractions of collimator hits listed in Table 6.2 is approx. 0.05. However, in order to calculate the asymmetry observed in the experiment, the total numbers of counts have to be compared, as shown in Table 6.3. In case of the ±1 mm beam position asymmetry, the asymmetry calculated using all events recorded in the polarimeter, is more than a factor of 4 lower than the asymmetry of the numbers of electrons hitting the collimators. A similar result is obtained for a smaller, more realistic, beam position difference of ±0.1 mm. In this case the difference is more than a factor of 5.

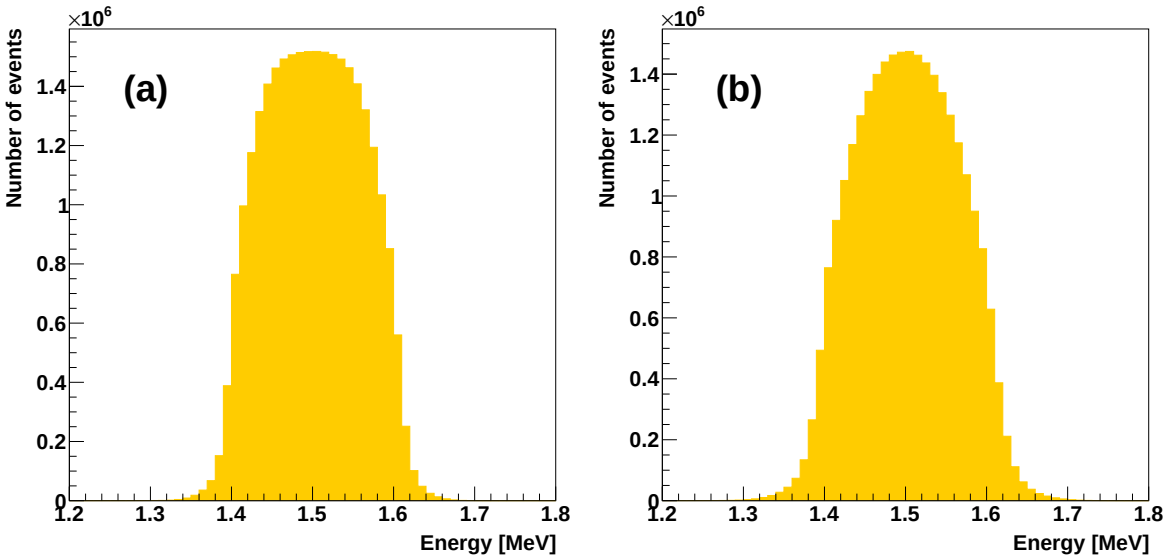

Figure 6.9: Simulated energy distribution of Møller electrons reaching the Mott target for a 3 MeV incident beam, for two beam spot diameters: (a) 1 mm and (b) 1.5 mm.

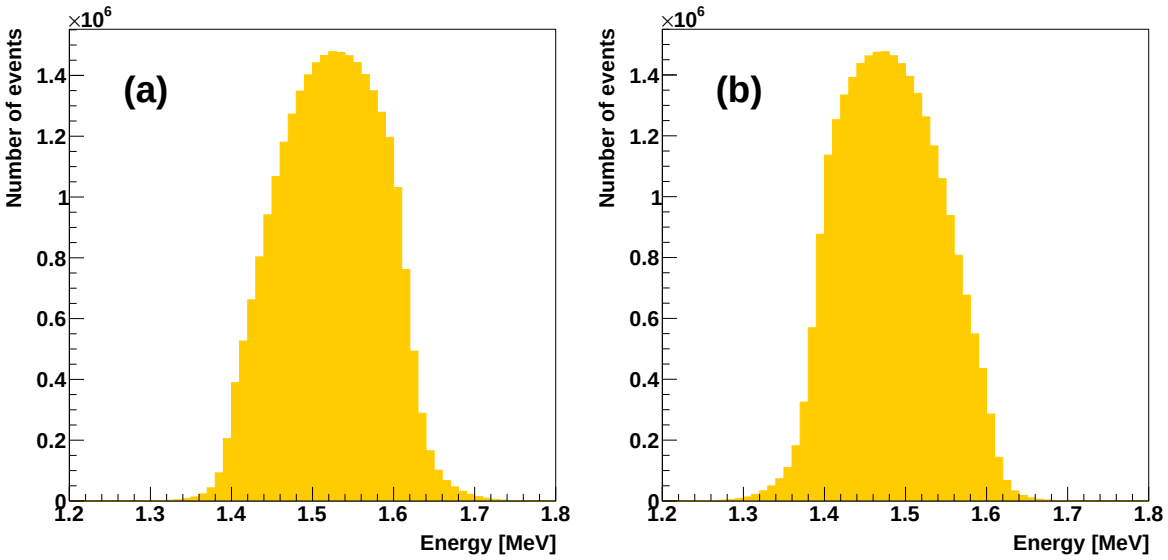

Figure 6.10: Simulated energy distribution of Møller electrons reaching the Mott target for a 3 MeV incident beam, with 1.5 mm beam spot diameter, for two beam positions off center in the horizontal plane: (a) +1 mm and (b) −1 mm.

Table 6.3: Asymmetry of the number of electrons reaching the polarimeter for opposite beam shifts (1.5 mm in diameter).

beam positions	**collimator hits asymmetry**	**all events asymmetry**
±1 mm	0.057	0.013
±0.1 mm	0.0063	0.0012

Chapter 7

Polarization transfer measurement

Described in this chapter are measurements of the polarization of the beam electrons (Mott-scattered off the beryllium target), as well as the mean polarization of electrons in the final state of Møller scattering. The measurements were performed with a one-polarimeter setup, in two configurations corresponding to different beam polarization orientations: (A) horizontal beam polarization (in the Møller scattering plane) and vertical Mott scattering plane, (B) vertical beam polarization (perpendicular to the Møller scattering plane) and Mott scattering plane at an angle of 45° to the Møller scattering plane (cf. Chapter 3, Fig. 3.4).

Data from the polarimeter were collected with two different triggers: (i) Møller trigger (coincidence of any of the polarimeter detectors with the tagging counter) and (ii) beam trigger (detectors in the polarimeter read out without coincidence). Data in configuration A were collected for 86 hours with Møller and 8 hours with beam trigger and in configuration B for 114 hours with Møller and 14 hours with beam trigger.

The beam polarization measurement was repeated every day; this way the polarization obtained after combining data from all runs should correspond to the mean value over the whole data taking period of the Møller scattering experiment. Additionally, in half of the runs, the Mott target was replaced with an empty target frame in order to record the background, which was then subtracted from the data collected with the target.

Furthermore, half of the runs were taken with a half-wave plate in the laser system of the polarized electron source yielding a 180° flip of the electron spin orientation, allowing us to reduce part of the systematic errors arising from a possible polarization-correlated asymmetry of electronics (such as unequal duration of opposite beam-polarization periods or different delays of trigger-signal paths corresponding to opposite beam-polarization orientations).

The analysis of experimental data consisted of the following steps, described in detail in the following sections:

1. File preparation:
   (a) Events from a previous run that were left in the buffer were removed from the beginning of each data file.
   (b) The first (incomplete) bunch of events was removed (until the first beam polarization change).

(c) The last bunches of events were removed (an even number of complete bunches was used for analysis).

(d) For each pair of runs (with the Mott target and with an empty target frame) the minimum number of bunches was found and the longer run was shortened.

(e) The length of one of the runs with the half-wave plate was adjusted to make the total acquisition time with and without the half-wave plate equal.

2. Dead time correction: an effective correction was calculated from the distribution of time between consecutive events for each run.

3. Pile–up removal: events containing signals with overlapping pulses were removed from the analysis.

4. Event analysis:

   (a) For each event in a data file the signal amplitudes were calculated.

   (b) Signal amplitude dependence on energy was calibrated using the beam (3 MeV) and Møller (1.5 MeV) peak positions in the amplitude spectra.

   (c) Only with the Møller trigger: the time distance between the rising edge positions of the tagging counter signal and the polarimeter-detector signal was calculated.

   (d) The selection criteria (signal amplitude and timing) were applied and events passing the selections were counted.

5. Calculation of the asymmetry and generation of control plots:

   (a) Dead time correction was applied to the histograms and the recorded numbers of events.

   (b) The distributions obtained with an empty target frame were subtracted from the distributions obtained with the gold foil.

   (c) Histograms of signal amplitude and time difference from all data files were merged.

   (d) Only with the Møller trigger: the number of background events was estimated by interpolating the time difference distribution under the signal peak. The interpolation result was subtracted from the number of recorded events.

   (e) The asymmetry was calculated using the data collected with two detectors and opposite beam polarization orientations.

The uncertainties of the results were calculated using the experimental data and the results of the Monte Carlo simulations, which is discussed in the next chapter. Finally, the polarization values were calculated by dividing the measured asymmetry by the simulated effective Sherman function and the polarization transfer was calculated by dividing the average polarization of the electrons in the final state of Møller scattering by the incoming-beam polarization.

Selected results of this chapter were included in publication [31].

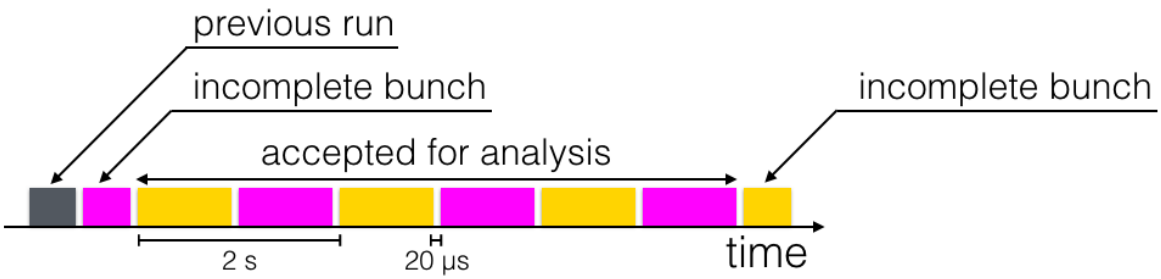

Figure 7.1: Typical time structure of a data file from a single run. The boxes illustrate the bunches of events recorded between the polarization switching moments (not to scale). The two colors correspond to two beam polarization orientations.

7.1. File preparation

A structure of a typical file containing data from one run is illustrated schematically in Fig. 7.1. The beam polarization orientation was changed periodically at 1 s intervals and the event bunches are separated by 20 μs gaps corresponding to the polarization switching moment, when the polarization is uncertain and the data are not recorded.

The file can contain spill-over data remaining in the buffer from a previous run, which are removed based on the time stamp. Then the first beam polarization flip is found and the preceding data are removed, since they might form an incomplete event bunch. An even number of bunches is used for the analysis to obtain an equal data acquisition period with both polarization orientations, which is necessary for the correct calculation of the count-rate asymmetry.

7.2. Dead time correction

The signals from the detectors were digitized with the DRS switched capacitor array circuit [54]. When the trigger condition was met, the data acquisition was stopped until the readout was finished. As a result, a dead time of about 2 ms was introduced, when no events could be recorded, which was confirmed in laboratory tests (see Section 4.2.3).

The distributions of time between consecutive events recorded during the experiment are shown in Fig. 7.2 for typical runs with the beam trigger. The shape of the histogram for times up to about 20 ms agrees well with the exponential distribution. The lack of events in the first bins is expected due to the standard dead time of the electronics. However, for time differences larger than about 25 ms, distributions shown in Fig. 7.2 deviate significantly from the extrapolation of the exponential distributions fitted to the lower time differences. There also exists a separate fraction of events with much larger delays, which suggests that there are two components with two different dead time values. It can be explained by the fact, that the dead time observed in the experiment also included the latency introduced by the computer which read the data from the digitizer board and stored them to a hard drive.

We found during the data analysis that after a certain period of inactivity, of the order of 40 ms, the CPU scheduler of the linux operating system suspended the threads

responsible for storing the data, allocating the CPU resources to other processes. The events at the end of the distribution (above 100 ms) were, therefore, delayed in the process of storing the data to the hard drive. In Fig. 7.2, the plot on the left hand side shows the distribution with the gold target (higher rate and less delayed events), and the plot on the right hand side with an empty target frame (lower rate and, as a result, more delayed events). Nevertheless, the number of events with large delays is small, note the logarithmic scale in the plots.

The effective correction (ratio of the true and measured event rate), taking into account both sources of dead time, was determined from the exponential fit to the time distribution,

$$N(t) = C \exp(-Rt), \tag{7.1}$$

where t is the time between consecutive events, R is the true event rate (larger than the measured event rate), and C is constant. The recorded number of events was multiplied by the ratio of the fitted (dead time free) event rate to the event rate recorded in the experiment. The fit was performed in the time range from 4 to 20 ms, where the distribution is exponential. Since the dead time correction depends on the count rate, which was different for the data acquired with opposite beam polarizations, as well as for the data acquired with the gold target and with an empty target frame, it had to be properly taken into account when calculating the asymmetry. The numbers of recorded events were corrected, and the histograms were reweighed, on a run-by-run basis.

The histograms of the dead time corrections determined from the fit are shown in Fig. 7.3. In case of the runs with the Møller trigger, the event rate, determined mostly by the low–energy background, was similar with and without target, leading to similar dead time corrections determined from the time distribution. On the other hand, the event rate in the empty–target runs with the beam trigger was much lower than with the target, leading to significantly different dead time corrections with and without target.

The dead time correction to the count rate was between 50% and 70% with the beam trigger (count rate approx. 190 evt./s) and approx. 50% with the Møller trigger (count rate approx. 150 evt./s). The dead time correction to the asymmetry was approx. +10% of the measured asymmetry value with the beam trigger (cf. Section 7.5.1) and approx. +2% with the Møller trigger. For the dead time contribution to the uncertainty, see Section 8.1.

7.3. Pile–up removal

A typical signal recorded in the tagging counter, with an amplitude corresponding to a 3 MeV beam electron, is shown in Fig. 7.4. There is only a single peak, beginning around 40 ns, and the voltage before the peak is close to zero. The histograms of the average voltage from the first and last 20 ns of the measured time window are shown in Fig. 7.5 for a polarimeter detector. The distribution for the end of the signal is shifted to negative values as a result of the negative signal reflection following the falling edge (cf. Fig. 7.4).

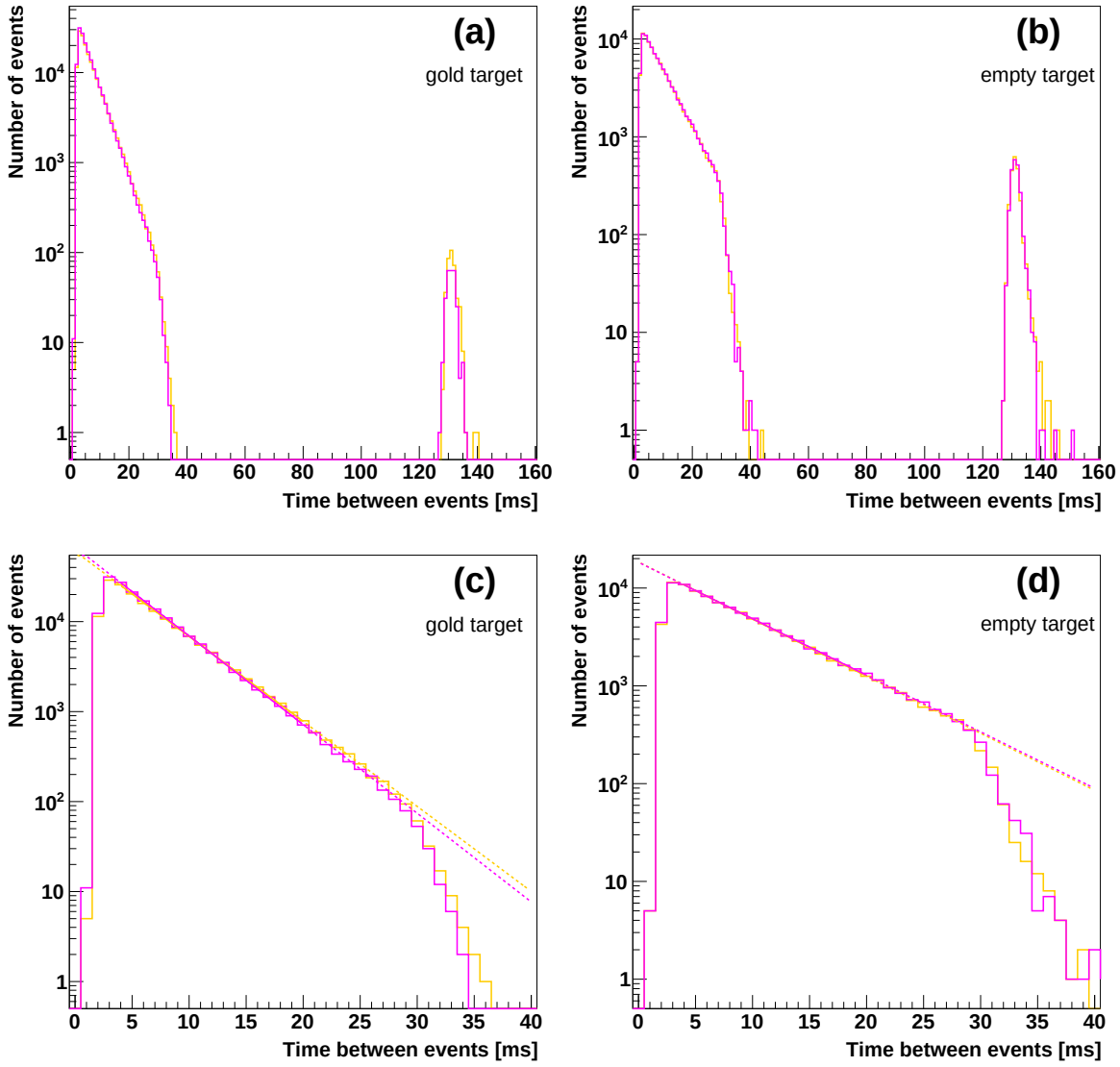

Figure 7.2: Example distributions of the time between consecutive events recorded with the beam trigger, for runs with the gold target (left) and for runs with an empty target frame (right). Histograms for opposite beam polarizations are plotted with different colors. Distributions restricted to times below 40 ms are shown in the bottom panels, with the exponential fit in the range from 4 to 20 ms shown with a solid line and its extrapolation with a dotted line.

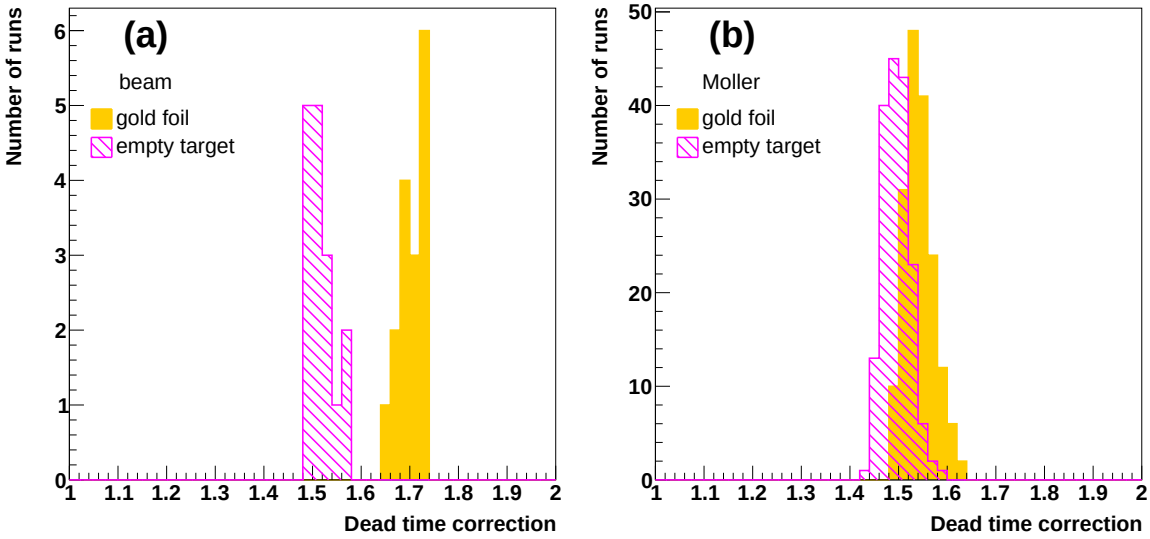

Figure 7.3: Histograms of the dead time correction calculated from the exponential fit for time differences between 4 and 20 ms, with (a) beam trigger, (b) Møller trigger.

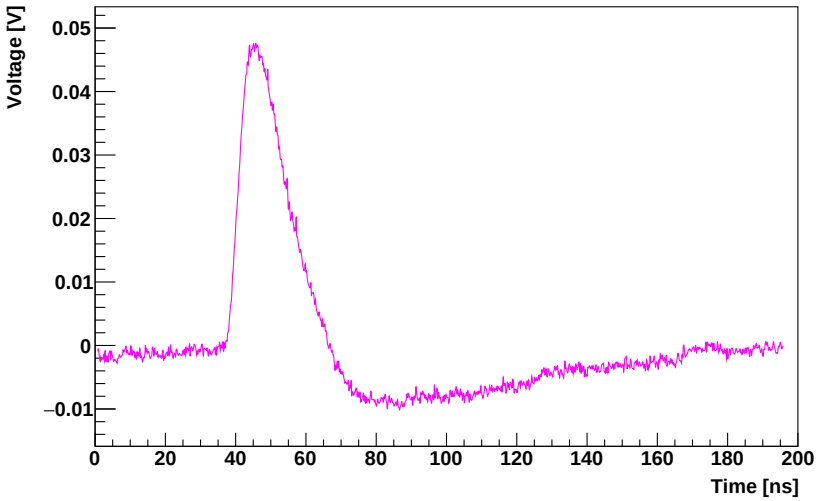

Figure 7.4: A typical signal recorded in the tagging counter, with an amplitude corresponding to a 3 MeV beam electron.

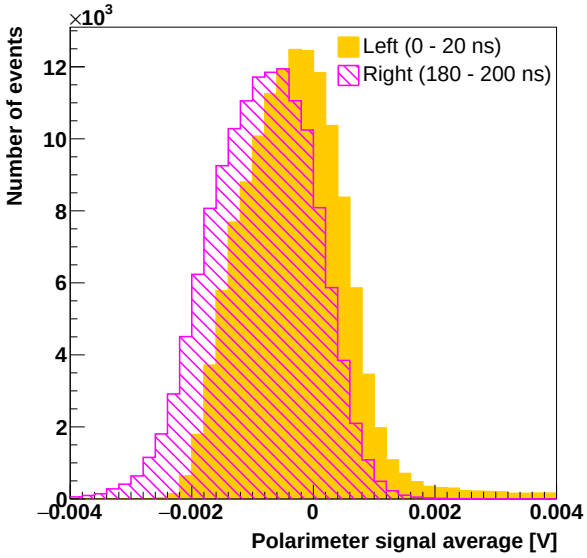

Figure 7.5: Histogram of the average signal voltage in a polarimeter detector from the first and last 20 ns of the time window.

Since the average voltage before the peak is close to zero (in the range ±2 mV) in case of single-peak events, the signal maximum value is a correct estimate of the amplitude, which is assumed to be proportional to the energy deposited in the scintillator. However, there exist events with two overlapping pulses, in particular in the tagging counter. They can be found by, for example, searching for signals, for which the voltage in the first 20 ns (i.e., before the signal that triggered the coincidence) deviates significantly from zero.

As an example, pile-up signals with an additional falling edge in the first 20 ns in the tagging counter are shown in Fig. 7.6. A clear similarity to the falling edge of the coincidence signal, starting around 40 ns, is visible. No such events were found in the polarimeter detectors, with a much smaller particle rate, which confirms that the the additional signal at the beginning originates from another particle that hit the detector slightly before.

It is clear that the signal maximum can no longer be regarded as a correct estimate of the pulse amplitude in case of events with overlapping signals. Due to the large number of events, an automatic selection of single-peak signals is necessary for the analysis. The properties of variables suitable for such selection are analyzed in the subsections below.

Number of peaks

The peaks in the signal were found automatically using the one–dimensional high–resolution peak search function [70] from the ROOT package. The results of the algorithm depend on several input parameters, in particular the expected width and the minimum height of the peak. The latter variable balances the efficiency of the algorithm (number of peaks correctly found) and the sensitivity to noise fluctuations (number of false peaks found). Reasonably good results were achieved by setting it to

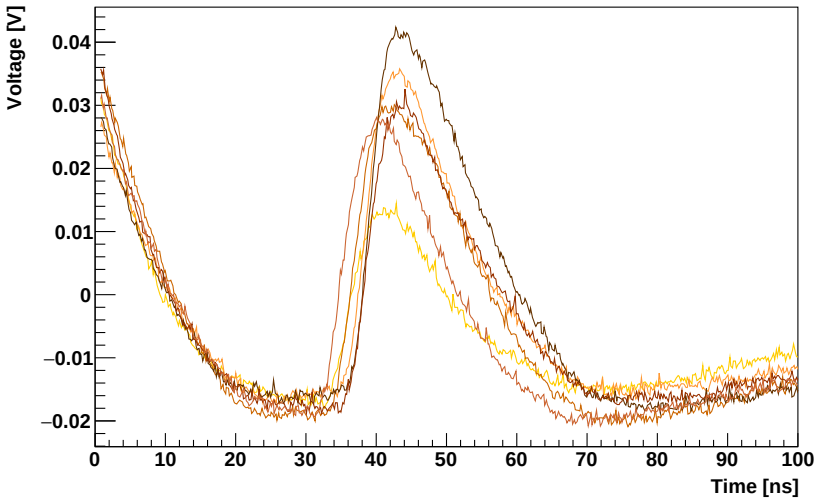

Figure 7.6: Examples of pile-up signals (tagging counter) with a falling edge of an earlier pulse in the first 20 ns.

5 mV, which is around the trigger threshold in the tagging counter, and slightly above the random noise. With a lower peak-height threshold, the random noise might be misinterpreted as a false peak.

The correct operation of the peak finding algorithm was tested by visual inspection of selected events. As an example, tagging counter signals with the highest number of peaks, i.e. 6, are shown in Fig. 7.7. By comparing the original curves and the points corresponding to peaks, it can be seen that all peaks have been correctly identified. The signal feature shown in Fig. 7.6, a falling edge at the beginning of the signal, is also identified as a peak even though the maximum is not recorded.

The distributions of the number of peaks found in the polarimeter and tagging counter signals are shown in Fig. 7.8. A clear difference due to the different rate of interacting particles is visible. In case of the polarimeter detector the problem of overlapping signals is practically non–existent (less than 0.2% events with more than one peak). On the other hand, the problem is definitely not negligible in case of the tagging counter, where around 30% of events contain more than one peak.

Further analysis reveals that the additional peaks are more likely to be found after the peak that triggered the coincidence. It is reasonable to assume that the signals which were produced later cannot affect the earlier signal that is used in the analysis. Therefore, only the events containing an additional peak before the coincidence signal maximum, which is used to determine amplitude (energy), cannot be analyzed as single-peak signals. The maximum number of peaks found before the coincidence signal was 2. Around 5% of tagging counter signals have such additional peak at the beginning and only these events were removed from analysis.

Signal minimum

Histograms of the minimum value of the signal from the first 20 ns of the time window are shown in Fig. 7.9 for both the polarimeter and tagging counter. The observation

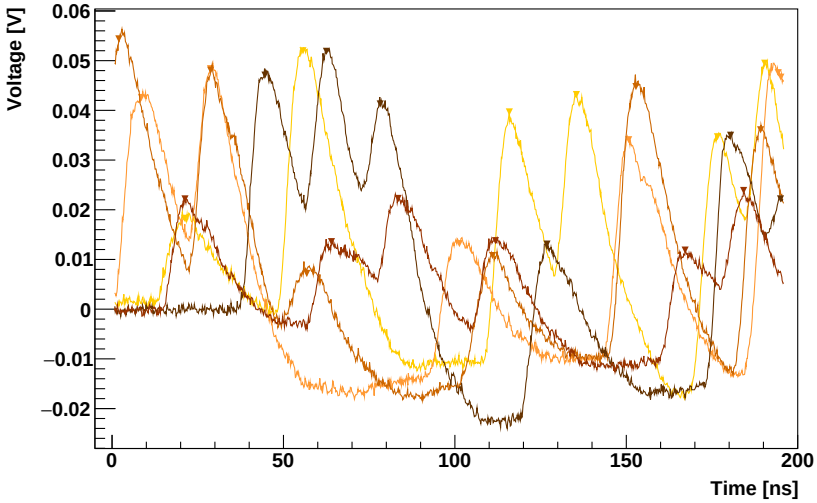

Figure 7.7: Events with 6 peaks (the maximum number found) in the tagging counter. Automatically found peaks are marked with a triangular symbol.

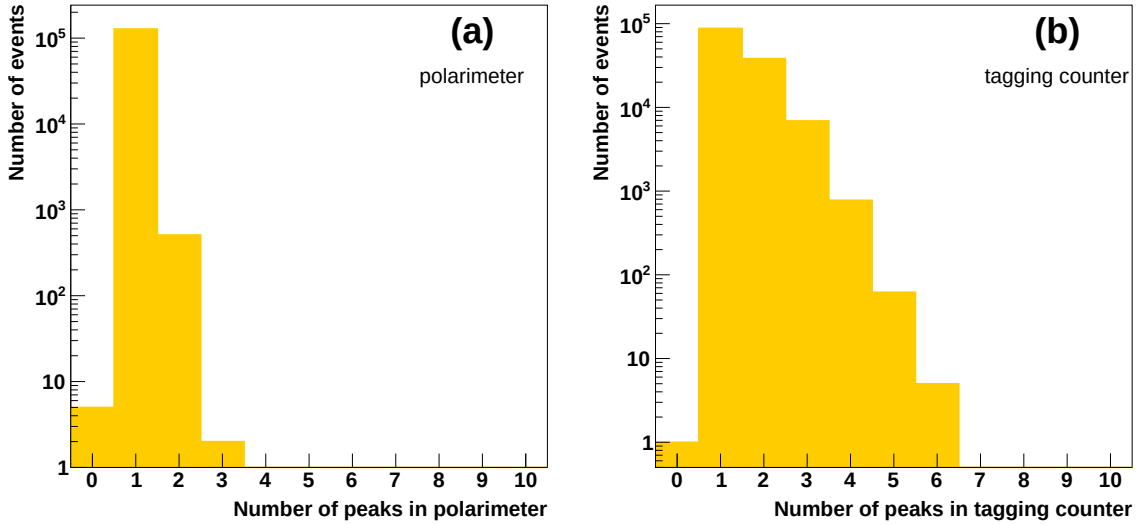

Figure 7.8: Histograms of the number of peaks found in the polarimeter (a) and tagging counter signals (b). A difference due to the particle rate is clearly visible.

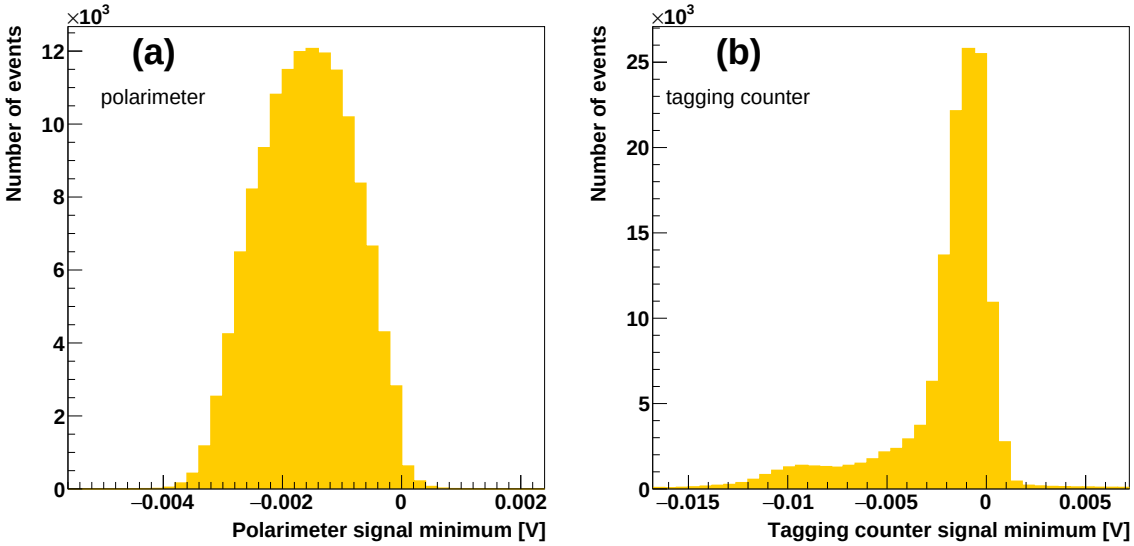

Figure 7.9: Histograms of the signal minimum value in the polarimeter (a) and tagging counter (b) from the first 20 ns of the time window.

that the overlapping signals practically do not occur in the polarimeter detector is also confirmed in this analysis. The polarimeter-detector histogram contains a single peak around −1.5 mV, which shall be interpreted as the average value of the random noise minimum. On the other hand, the tagging counter distribution contains two overlapping peaks, a larger one around −1 mV, in close agreement with the polarimeter-detector spectrum, and a smaller one around −9 mV. Taking into account that the tagging counter data contain a significant fraction of events with an additional peak at the beginning of the time window, which is not observed in the polarimeter detector, the additional peak around −9 mV seems to be resulting from the negative signal reflection following the falling edge.

The histogram of the global signal minimum, which typically corresponds to the negative signal reflection following the falling edge (cf. Fig. 7.4), is shown in Fig. 7.10 for comparison. A peak around −10 mV approximately agrees with the results from Fig. 7.9. The other, smaller peak around −5 mV is not visible in Fig. 7.9, which might, however, be explained by the fact that it is positioned in the overlap region of the two larger peaks.

Signal maximum

In analogy to signal minimum, the maximum voltage at the beginning of the signal could be used to eliminate pile-up events with additional peaks extending above the random noise range. Examples of events with the largest maximum value in the first 20 ns are shown in Fig. 7.11. One has to conclude that the signal maximum is not a suitable variable for selection of single–peak events. Restricting its value to the random noise range corresponding to typical single-peak events (i.e., with a rising edge around 40 ns) would reject also valid single–peak events such as those shown in Fig. 7.11. This way, an implicit timing selection would be introduced instead of only removing the

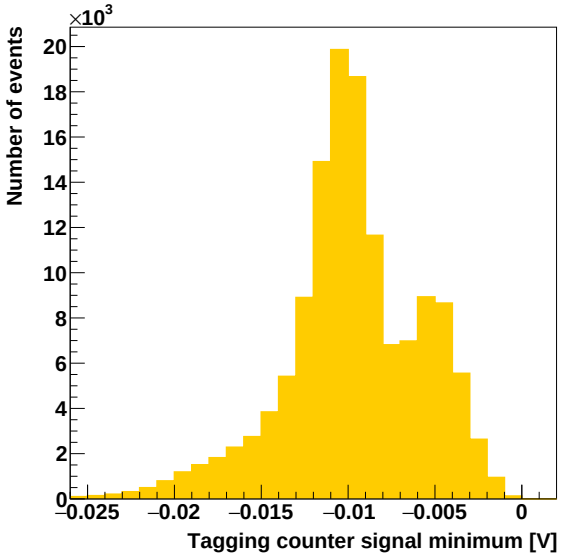

Figure 7.10: Histogram of the global signal minimum for the pulses measured in the tagging counter.

pile–up events.

The cut on the number of reconstructed peaks should rather be used, if the timing bias needs to be avoided. It allows to remove events with additional signal peaks preceding the coincidence signal, while leaving the single–peak events, including those out of time, in the data sample. Such events might be useful for the analysis as they carry information about the false–coincidence background rate (cf. Section 7.4.3).

Peak width

Taking into account that overlapping signals can contribute to single measurement, another interesting variable to be considered is the peak width. Firstly, it might also be used to remove the events with overlapping signals. Alternatively, it could be useful to cross–check the efficiency of the peak finding algorithm, when the number of peaks is used for event selection.

The histograms of the reconstructed peak width, for the polarimeter and the tagging counter, are shown in Fig. 7.12. Both distributions consist of a single, symmetric peak. There is no significant difference between the polarimeter detector response and that of the tagging counter. No separation between the single-peak and pile-up events can be obtained with this variable. Additionally, a possible correlation between the signal amplitude and width could introduce an unwanted amplitude bias, if such selection was applied.

Summary

In the analysis of the tagging counter signals, significant contribution from the pile-up events was identified, when two electrons are observed in a detector within a time shorter than the signal width. Since the number of such events is low, the easiest solu-

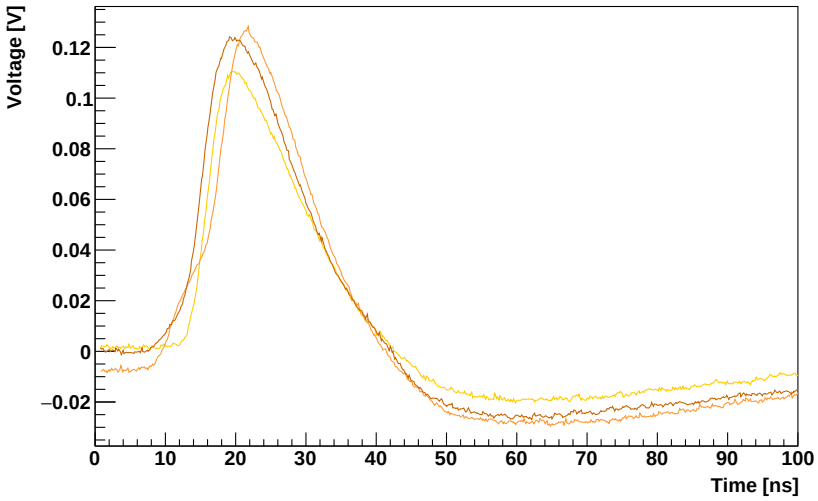

Figure 7.11: Signals with the largest maximum voltage in the tagging counter from the first 20 ns of the time window.

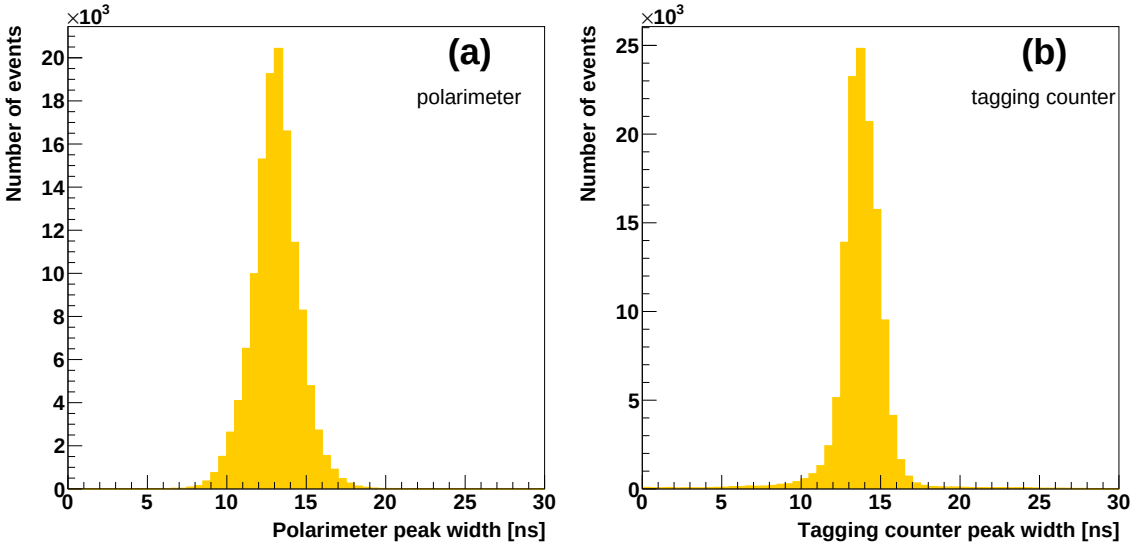

Figure 7.12: Histograms of the peak width in the polarimeter (a) and tagging counter (b).

Table 7.1: Results of the pile-up analysis in configuration A. The fractions of events with more than one peak and with negative values before the peak, as well as the fraction of events passing the selections, are shown.

detector	**0—20 ns signal minimum < -5 mV**	**> 1 peak**	**Accepted as single-peak events**
polarimeter	0.002%	0.2%	99.8%
tagging counter	12%	5%	84%

tion is to remove such events from the analysis. A two–stage event selection procedure was used:

1. Events with negative pulse values before the peak were removed based on the measured signal minimum (voltage in the first 20 ns of the time window below -5 mV).

2. Events with more than one peak were removed using the automatic peak search function (more than one peak found between the beginning of the time window and the middle of the falling edge, typically around 60 ns from the beginning, depending on the amplitude).

The statistics of pile-up events can be found in Table 7.1. The number of such events is negligible in the polarimeter detectors and around 16% in the tagging counter.

7.4. Event analysis

7.4.1. Tagging counter amplitude distribution

The tagging counter recorded electrons scattered off the beryllium target. These included Mott-scattered beam electrons (of approx. 3 MeV energy) as well as Møller electrons (of 1.5 MeV on average). Together with one of the detectors in the polarimeter, it produced a coincidence trigger used to record symmetric Møller scattering events. It also allowed us to infer the energy spectrum of particles reaching the Mott polarimeter. A typical raw signal amplitude spectrum is shown in Fig. 7.13, and an approximate energy calibration is also shown for reference. The peak at higher energies corresponds to the beam electrons Mott-scattered off the beryllium target, while the peak at lower energies to the Møller electrons.

Pointing directly to the beryllium target, the tagging counter was exposed to a large flux of particles. As a result, a significant fraction of events, around 16%, contains overlapping signals (cf. Section 7.3). The amplitude of the overlapping signals typically does not correspond to the energy of any of the particles that hit the detector during such event. If the number of events with a wrong amplitude is large, it might lead to the broadening of the 1.5 and 3 MeV peaks in the tagging counter amplitude spectrum.

The experimental distribution, shown in Fig. 7.13, was fitted with a sum of two

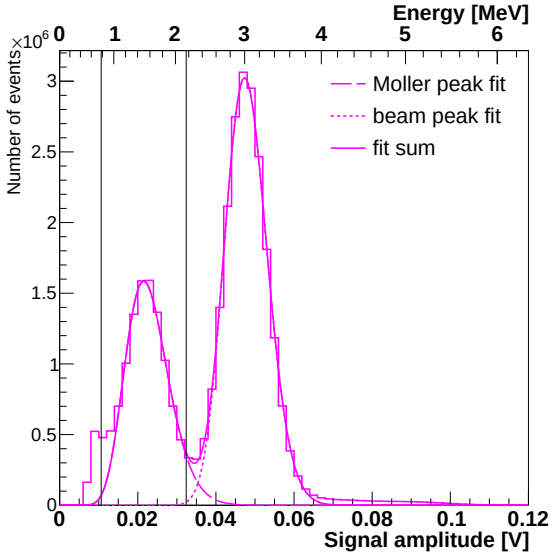

Figure 7.13: Signal amplitude spectrum in the tagging counter pointing directly at the beryllium target. The higher peak corresponds to the Mott-scattered beam electrons, and the lower peak to Møller electrons. Solid line – sum of two gamma distributions fitted to the spectrum; dashed line – gamma fit to the Møller peak; dotted line – gamma fit to the beam peak. The black vertical lines indicate the cuts applied to select the Møller scattering events.

gamma distributions,

$$\Gamma(x) = C \exp\left(-\left(\frac{x_0}{\sigma}\right)^2 \left(\frac{x - x_0}{x_0} - \log\frac{x}{x_0}\right)\right), \tag{7.2}$$

and the results are listed in Table 7.2. While the effect of the peak broadening is not significant enough to be easily noticeable in the histogram, the fit results seem to confirm it. This demonstrates also the usefulness of the pile-up removal procedure discussed in the previous section.

Energy calibration

Thanks to the large number of events recorded in the tagging counter, the peak positions can be determined with a high precision using the data from a single run. This

Table 7.2: Results of the tagging counter amplitude analysis in configuration A. The widths σ of the 1.5 and 3 MeV peaks in the amplitude spectrum were determined from gamma fits to the experimental distribution. The results were obtained without selections and for single-peak events; the broadening of the peaks demonstrates the usefulness of pile-up removal.

event selection	**1.5 MeV peak σ**	**3 MeV peak σ**
all events	7.9 mV	6.1 mV
single peak	7.7 mV	5.7 mV

way even peak position variation smaller than 1 mV can be detected. The reconstructed 1.5 MeV peak position for the tagging counter is plotted as a function of time in Fig. 7.14. The 3 MeV peak position, shifted by the average distance between the two peaks, is also shown for comparison.

Fit results indicate clearly that the peak position is not stable. The general trend is similar in both DRS boards except that the last part of results, after about 75 hours from the beginning of the data taking, is shifted to lower amplitudes in DRS board 2. The fact that a similar pattern is observed in both digitizer boards and that the largest differences occur after longer breaks in data acquisition, suggest that a possible reason of this effect might be the change of temperature. Furthermore, the difference between two digitizer boards suggests that it is more likely the variation of the DRS chip temperature and not of the SiPM sensor (in the latter case one would expect similar patterns in both DRS boards). The DRS chip is calibrated at a typical working temperature, thus the measurements performed shortly after the board is powered on (i.e., before it warms up) might be less precise.

The observed changes of peak position are most likely not caused by the fit procedure itself. In order to verify this possibility the tagging counter signal amplitude spectrum from DRS board 2 was plotted for the run with highest (run 446, 0.021987 ± 0.000021 mV) and lowest (run 774, 0.021040 ± 0.000022 mV) peak position in Fig. 7.15. The two-component fit matches the data well in both cases. It can be seen that that the whole distribution is visibly shifted to lower amplitudes (between run 446 and run 774), even though the difference is small (less than 1 mV).

As can be seen in Fig. 7.14, the positions of both peaks follow a very similar pattern. The data from different runs can therefore give some more information about the energy calibration of the counter. Taking into account that there are only two data points, there are two reasonable calibration functions: a quadratic dependence $aE^2 + bE$ (assuming that the calibration curve should pass through zero) and a linear function $aE + b$ (assuming that there is a constant detection threshold). Comparison of the linear and quadratic fit to the data from different runs can give some hint on which of the two calibration curves is more appropriate.

The calibration curves are shown in Fig. 7.16 again for the run with highest and lowest peak positions. If one assumes that the calibration is linear and that it does not pass through zero due to a non–zero detection threshold, one would expect this detection threshold (a physical effect) to be independent of calibration. The detection threshold (intersection of the calibration curve and the energy axis) is (0.2348 ± 0.0026) MeV for run 446 and (0.2743 ± 0.0026) MeV for run 774. The difference is more than 10 σ, which is one of the arguments in favor of the quadratic calibration. Nevertheless, the energy calibration is shown only for reference, as it has no impact on presented results. The analysis is performed in terms of signal amplitude (voltage) and only the signal amplitude is used for event selection (distinguishing between events belonging to the two peaks). Therefore, the result depends only on the peak position and width (detector resolution) and not on the exact calibration.

As the peak positions in the tagging counter can be determined with very good precision even using the data from a single run only, the tagging counter amplitude cuts were evaluated individually for each run, in order to account for the changes of the peak position in time.

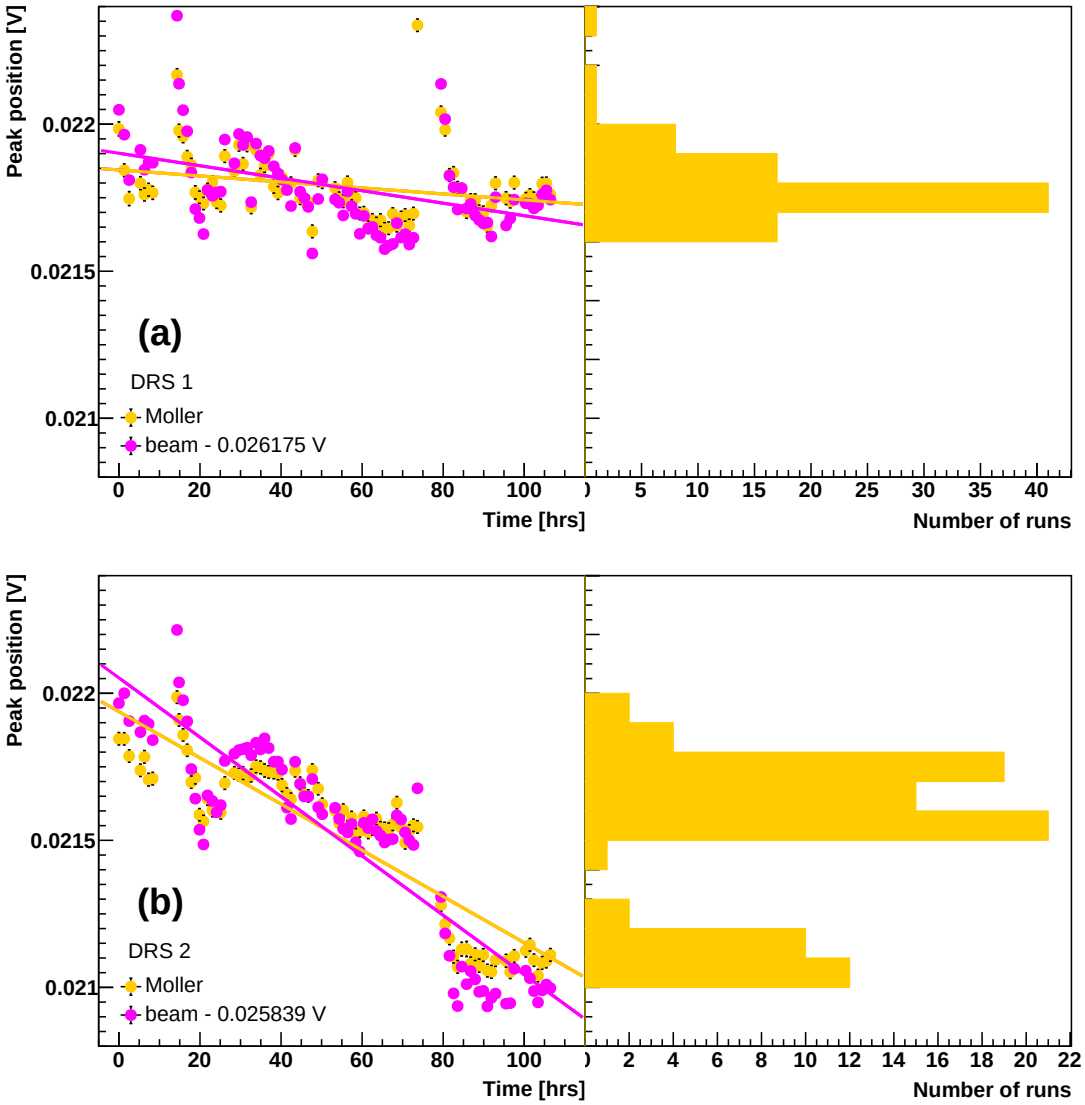

Figure 7.14: Dependence of the Møller and beam peak positions on time in the tagging counter from DRS board 1 (a) and 2 (b). Beam peak values are shifted by the average distance between peaks for comparison. The lines represent the linear fit.

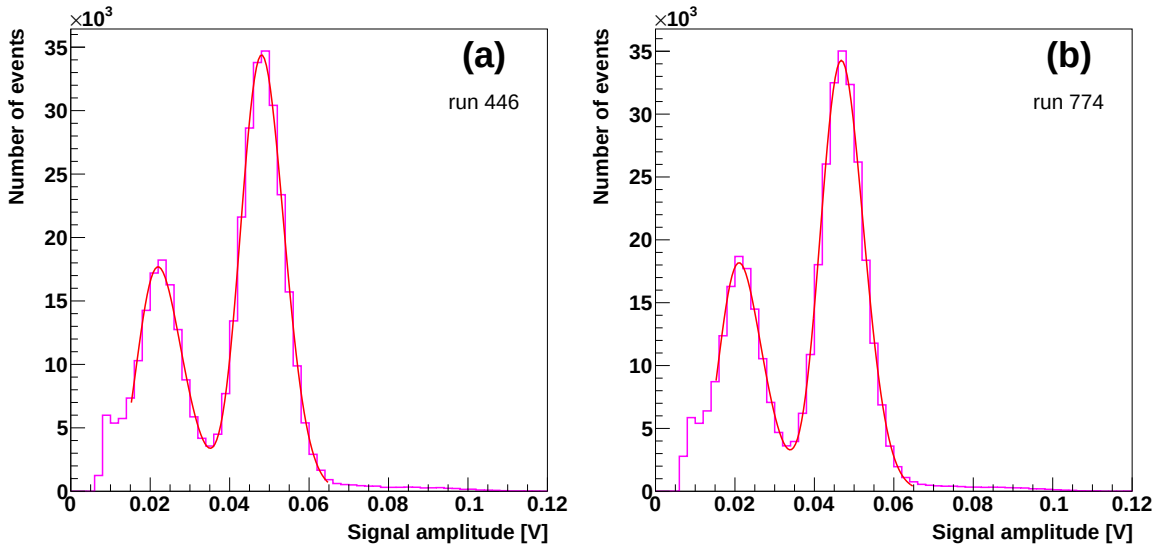

Figure 7.15: Signal amplitude spectrum in the tagging counter (DRS board 2) with (a) the largest 1.5 MeV peak position (run 446) and (b) the smallest 1.5 MeV peak position (run 774).

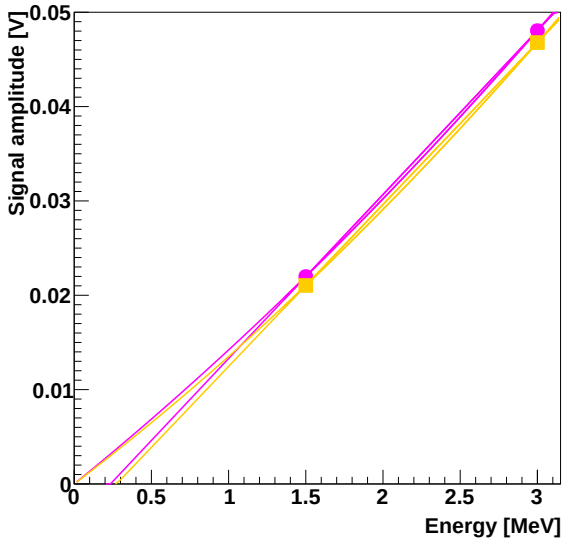

Figure 7.16: Dependence of the signal amplitude (peak position) on energy in the polarimeter detector for runs with the largest and the smallest peak positions (run 446 and 774, respectively). The lines represent the linear and quadratic fit.

7.4.2. Polarimeter-detectors amplitude distribution

The signal amplitude spectrum recorded in the polarimeter detectors with the Møller trigger, after dead time correction, is shown before and after offline background subtraction in Fig. 7.17. The data sample recorded with the Møller trigger is dominated by background events, which has to be corrected for using data collected with an empty target frame. After background subtraction, two peaks become clearly visible. The one around 1.5 MeV corresponds to Møller electrons, which give the coincidence signal, while the smaller peak around 3 MeV results from false coincidences of Mott-scattered beam electrons. The signal amplitudes are slightly higher than in the tagging counter, due to the tagging counter signal being split to two digitizer boards.

Energy calibration

Similarly to the tagging counter calibration, an approximate energy calibration for the polarimeter detectors was performed using the 1.5 and 3 MeV peak positions from the fits to the amplitude spectrum. The two data points were fitted with a quadratic equation $aE^2 + bE$. The fitted calibration curves are shown in Fig. 7.18.

In order to check if the calibration is stable, the positions of the 1.5 MeV peak were determined independently for each run. The peak position is plotted as a function of time in Fig. 7.19. The points appear to be distributed randomly, without any trend, which is confirmed with a linear fit. The slope is in agreement with zero: $(3.4 \pm 4.6)10^{-6}$ V/h (spin up), $(3.5 \pm 4.5)10^{-6}$ V/h (spin down), for the L polarimeter detector, and $(1.9 \pm 2.9)10^{-6}$ V/h (spin up), $(-1.6 \pm 2.7)10^{-6}$ V/h (spin down), for the R polarimeter detector.

The distribution of the peak positions is significantly wider for one of the polarimeter detectors than for the other. The ratio of the distribution widths is about 1.66. This is in an approximate agreement with the ratio of the relative count rate uncertainties, which is about 1.64 (cf. Section 7.5.2, results for selection 2 in Table 7.7).

7.4.3. Time distribution

The histogram of the rising edge position (time corresponding to 50% of the signal amplitude) for the single–peak events in the tagging counter is shown in Fig. 7.20. A clear maximum around 40 ns is visible on top of a uniform spectrum extending down to around 10 ns. Assuming that the position of the large peak corresponds to the expected timing of physical coincidences, the flat part of the distribution can be interpreted as originating from the false coincidences.

The histograms of the time distance between the rising edge position in the polarimeter and tagging counter without event selections are shown in Fig. 7.21 for the runs with an empty target frame and with the gold target. The analysis was performed for all events and for single–peak events only, in order to verify if removing the pile–up events might affect the timing distribution. It can be seen that the distribution shapes are very similar in both cases except that the pile–up events add an approximately uniform contribution extending outside the ± 30 ns time difference range covered by the single–peak events. This result again illustrates the usefulness of pile-up removal

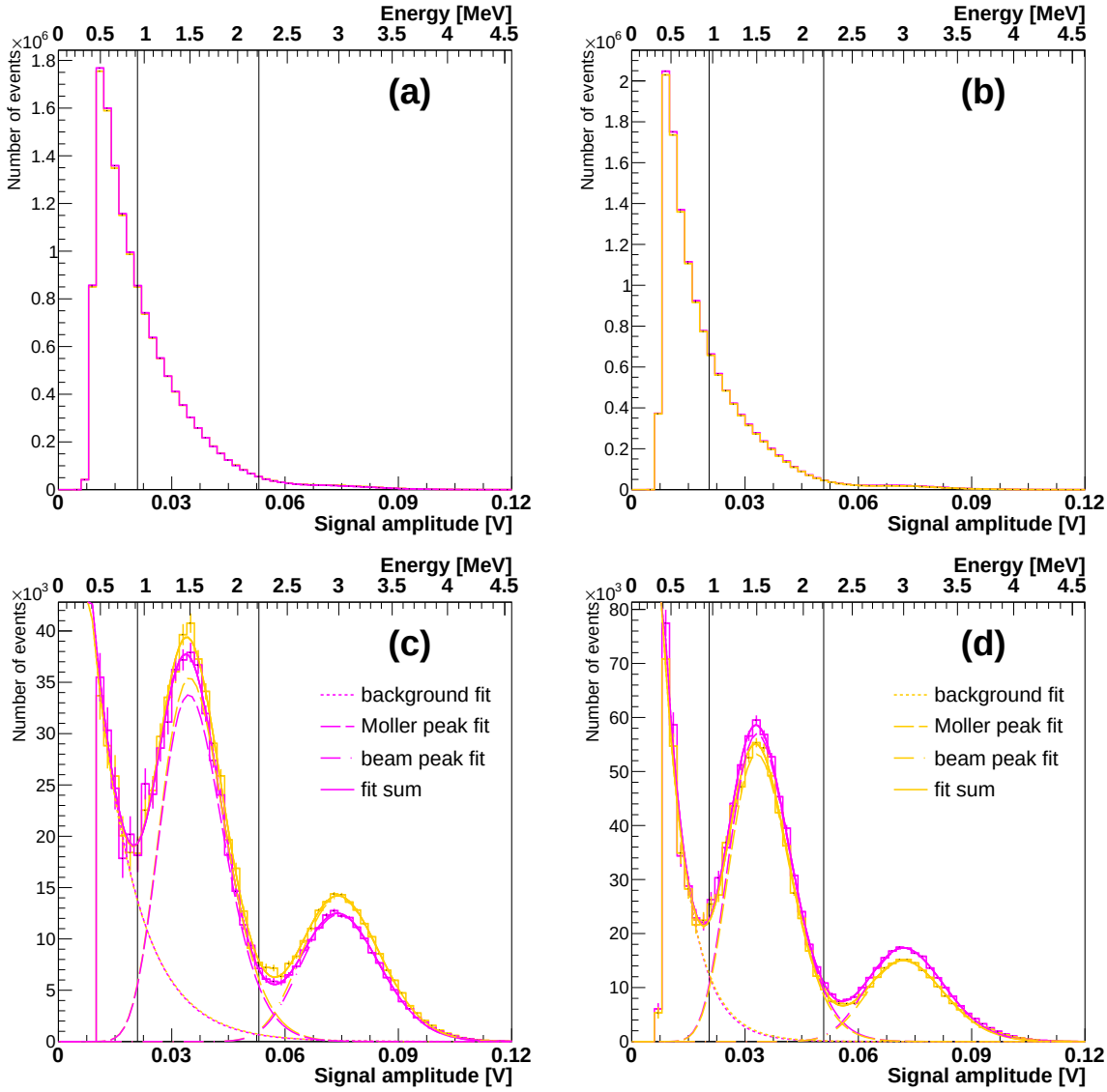

Figure 7.17: Signal amplitude spectrum, recorded in the L (left) and R (right) polarimeter detectors with the Møller (coincidence) trigger, before (top) and after (bottom) empty-target background subtraction. The peak around 1.5 MeV corresponds to Møller electrons backscattered off the gold target and the peak at higher energies to doubly Mott-scattered beam electrons (false coincidences). Solid line – sum of an exponential and two gamma functions fitted to the spectrum; dashed line – gamma fit to the (Møller or beam) peak; dotted line – exponential fit to the background tail. The black vertical lines indicate the cuts applied to select the Møller scattering events. Histograms for opposite beam polarizations are plotted with different colors.

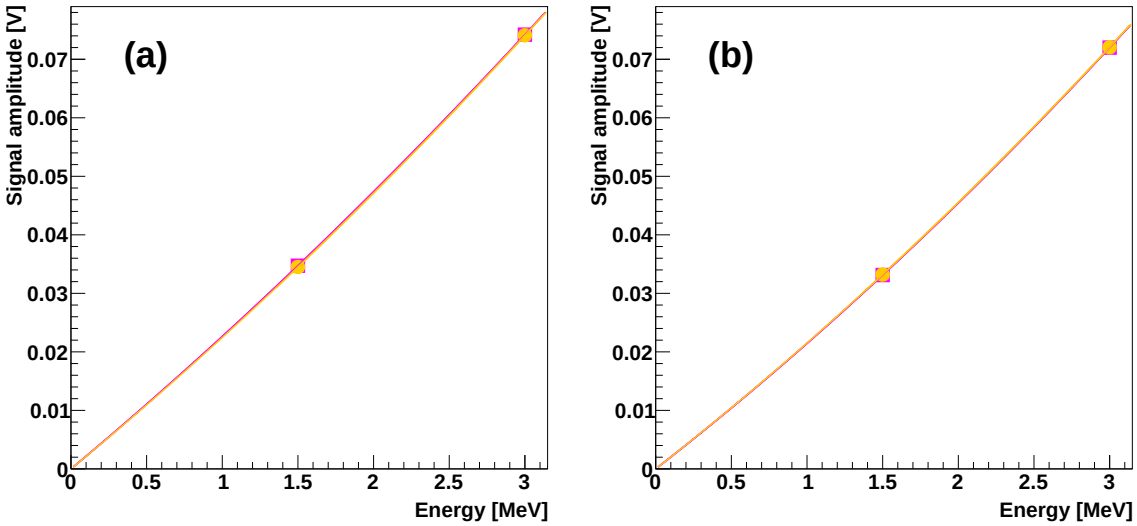

Figure 7.18: Dependence of the signal amplitude (peak position) on energy in the L (a) and R (b) polarimeter detectors. The line represents the quadratic fit. Data for opposite beam polarizations are plotted with different colors.

discussed in Section 7.3. Therefore, the further analysis was performed on single–peak events only, in order to avoid the ambiguity regarding the rising edge identification.

In general, there is a sharp signal peak around zero in the runs with the gold target, which is much smaller in case of the empty–target runs. The small peak remaining without the gold target is probably due to the electrons back–scattered of the target frame or the chamber walls.

The histograms of the time distance between the rising edge position in the polarimeter and tagging counter are shown in Fig. 7.22 for events which pass the amplitude selection in both channels: polarimeter-detector amplitude in the right half of the Møller peak and tagging counter amplitude in the full Møller peak. According to the amplitude analysis, these events consist in large part of the exponential empty–target background, but after removing the background there should be more than 95% Møller electrons in the data sample.

Contrary to the spectrum without selections (Fig. 7.21), the time difference distribution with amplitude selection (Fig. 7.22) is practically uniform in case of the empty–target data. The same histogram for the runs with the gold target consists of a sharp peak on top of a slightly higher flat background.

The distribution can be fitted with a sum of a constant and a Gaussian curve, the fit result is shown in Fig. 7.23. The fit results are listed in Table 7.3.

Due to the finite sampling rate of the signal digitizer, the analysis can be improved by interpolating the signals between the recorded data points. The time-difference distribution peak width obtained with a linear interpolation on the rising edge is slightly smaller than without interpolation, which is in agreement with the expectations. Anyway, the difference between the two methods is very small, which suggests that the main source of the observed distribution width is the natural variation of the signal timing, originating from the detector, and not the sampling frequency of the digitizer

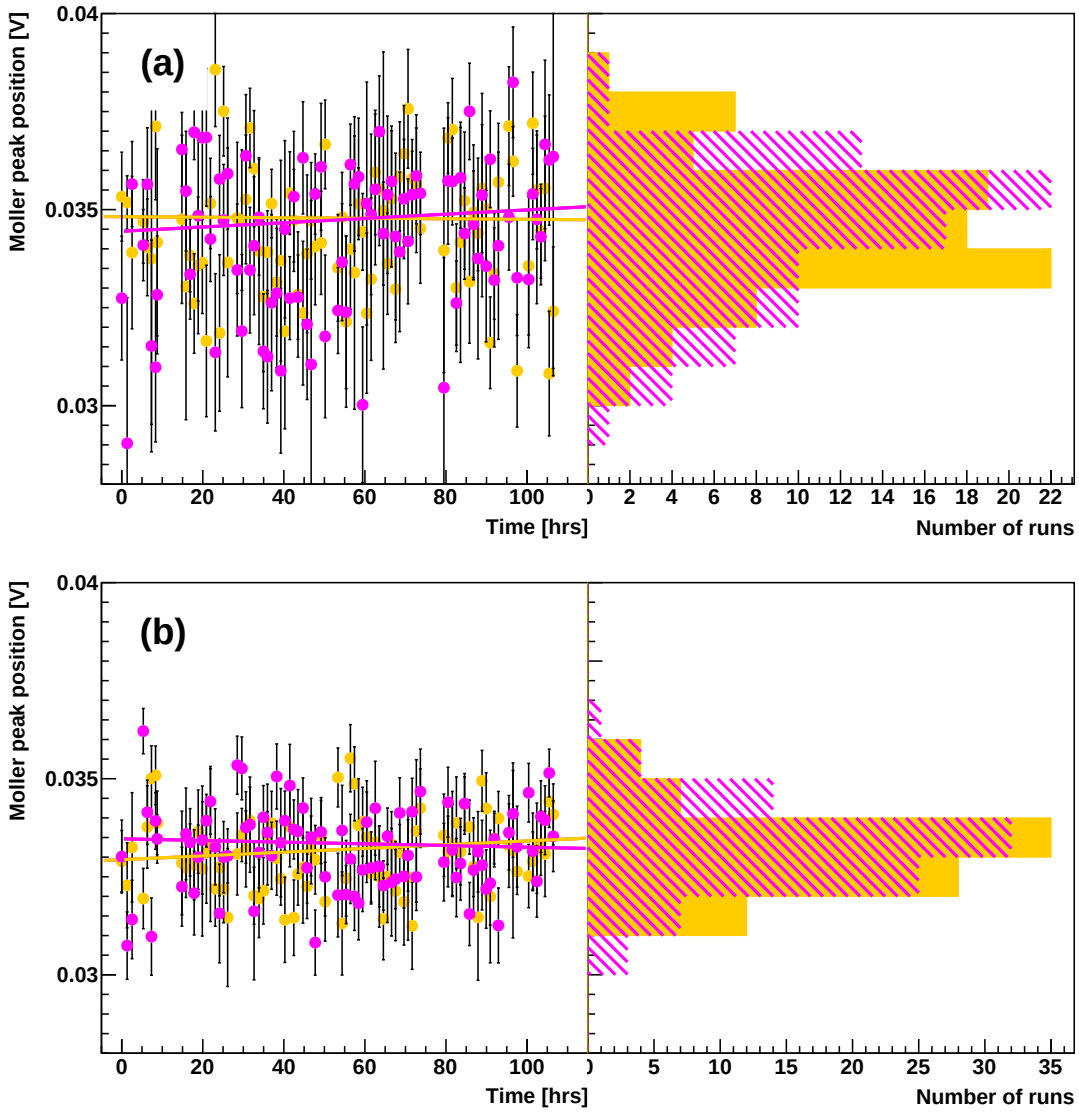

Figure 7.19: Dependence of the Møller peak position on time in the L (a) and R (b) polarimeter detectors. The lines represent the linear fit. Data for opposite beam polarizations are plotted with different colors.

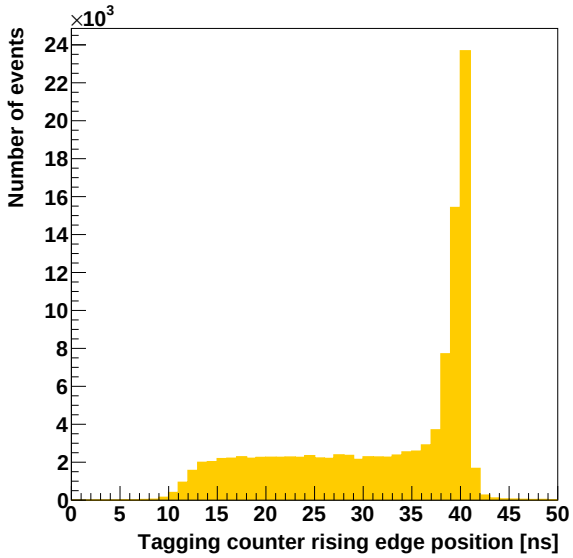

Figure 7.20: Histogram of the rising edge position in the tagging counter.

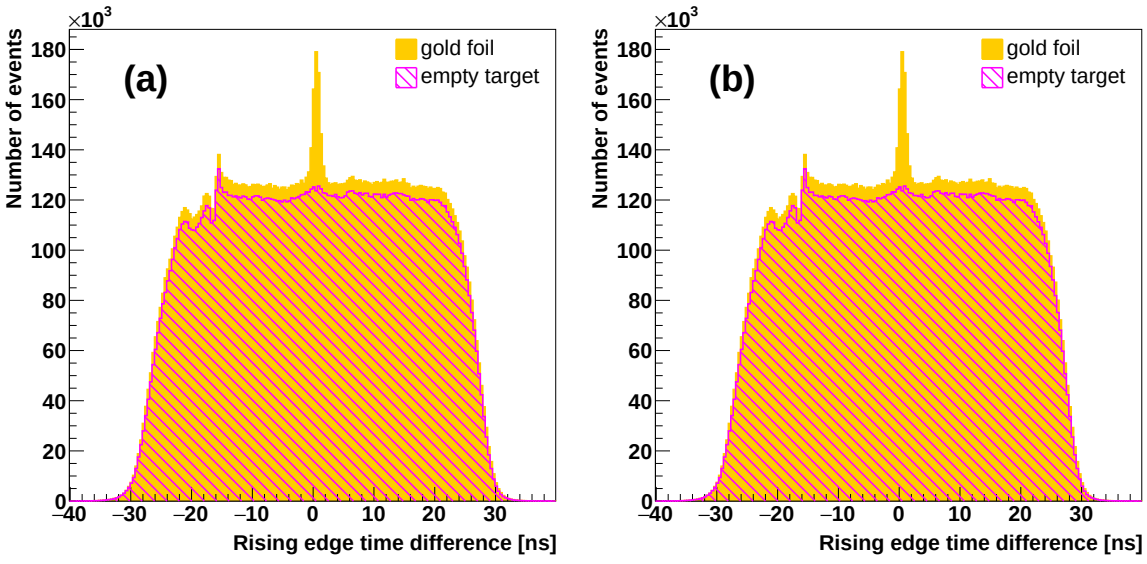

Figure 7.21: Histograms of the time distance between the rising edge position in the polarimeter and tagging counter, for runs with an empty target frame and with the gold target; (a) all events, (b) only single–peak events.

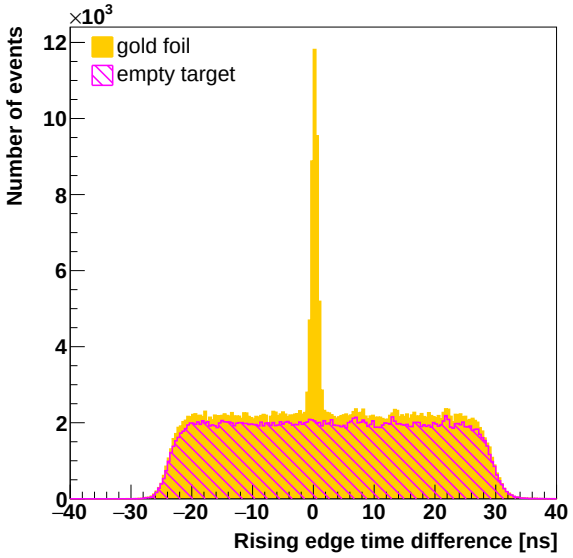

Figure 7.22: Histograms of the time distance between the signal rising edge position in the polarimeter and tagging counter, for events with the polarimeter-detector amplitude in the right half of the Møller peak and tagging counter amplitude in the full Møller peak, for runs with an empty target frame and with the gold target.

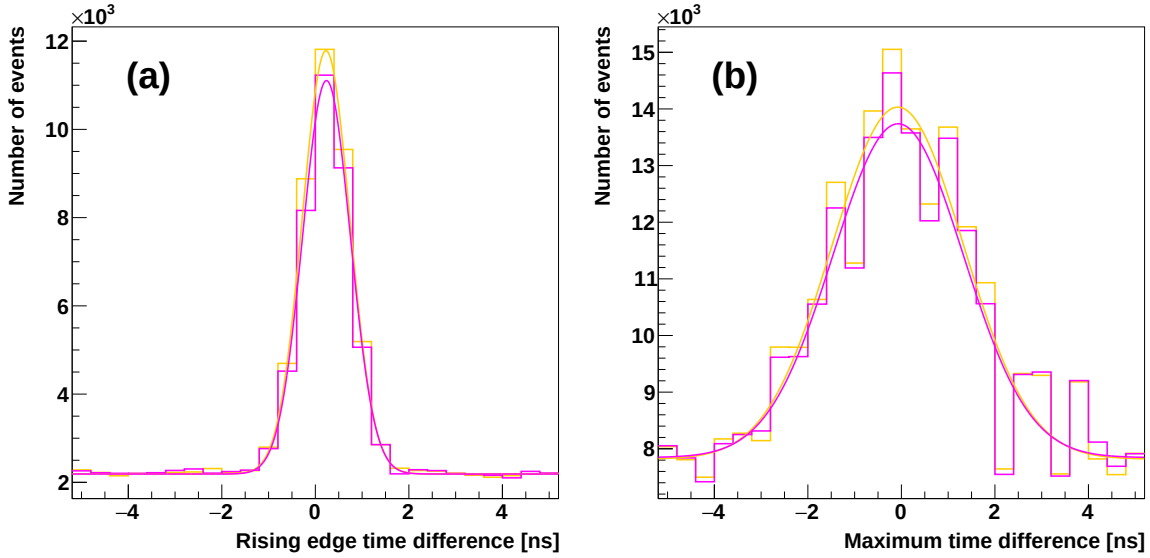

Figure 7.23: Central part of the histograms of the time distance between the signal position in the polarimeter and tagging counter, for events with the polarimeter-detector amplitude in the right half of the Møller peak and tagging counter amplitude in the full Møller peak, for runs with the gold target, shown with the fitted functions (see text); (a) time from rising edge, (b) time from signal maximum. Histograms for opposite beam polarizations are plotted with different colors.

Table 7.3: Results of the timing analysis in configuration A. The mean time distance between the rising edge position in the tagging counter and the polarimeter detector was determined from a Gaussian fit to the experimental distribution. The results were obtained with three different definitions of rising edge position, and the distribution widths σ are shown to demonstrate the accuracy of different analysis methods (see text for details).

detector	**analysis**	**mean**	σ
L	rising edge (50%)	0.20 ns	0.51 ns
L	rising edge (50%) interpolated	0.23 ns	0.51 ns
L	maximum	−0.03 ns	1.41 ns
R	rising edge (50%)	0.58 ns	0.51 ns
R	rising edge (50%) interpolated	0.55 ns	0.49 ns
R	maximum	0.52 ns	1.48 ns

board.

For comparison, the analysis was also performed by measuring the time difference between the signal maximum positions. The time difference distribution width in this case is about a factor of 3 larger than using the rising edge position, which shows that this method is much less precise. Maximum position is much more sensitive to noise and shape fluctuations, due to the fact that the signal derivative is zero in the maximum.

Electrons reflected back from the Møller dump are expected to be delayed by about 10 ns, which should be a measurable effect even with a limited timing precision. No such additional peak is visible in the spectrum, which suggests that the number of such events is much lower than the low–energy forward–scattered background from the beryllium target.

The empty–target runs can as well be fitted with the same function in order to verify if there is a statistically significant peak around zero time difference. The fit was performed with the peak position and width fixed according to the signal fit. The central parts of the time difference distributions for background events are shown with the fit results in Fig. 7.24. In three cases the resulting peak height was found in agreement with zero: (-46 ± 76) 1/ns for the L detector (one polarization) and (50 ± 64) 1/ns for R polarimeter detector (both polarizations). In the L detector, the result for the other polarization, (214 ± 77) 1/ns, deviates from zero by about 2.8 σ.

7.5. Calculation of the asymmetry

7.5.1. Beam

Data acquired with the beam trigger was used to determine the incident electron-beam polarization. A typical signal amplitude spectrum recorded in the Mott polarimeter (i.e., after beam Mott scattering both off the beryllium and gold targets), after dead time correction, before and after background (empty-target runs) subtraction, is shown in Fig. 7.25 for two opposite beam polarizations. The asymmetry arising due to the

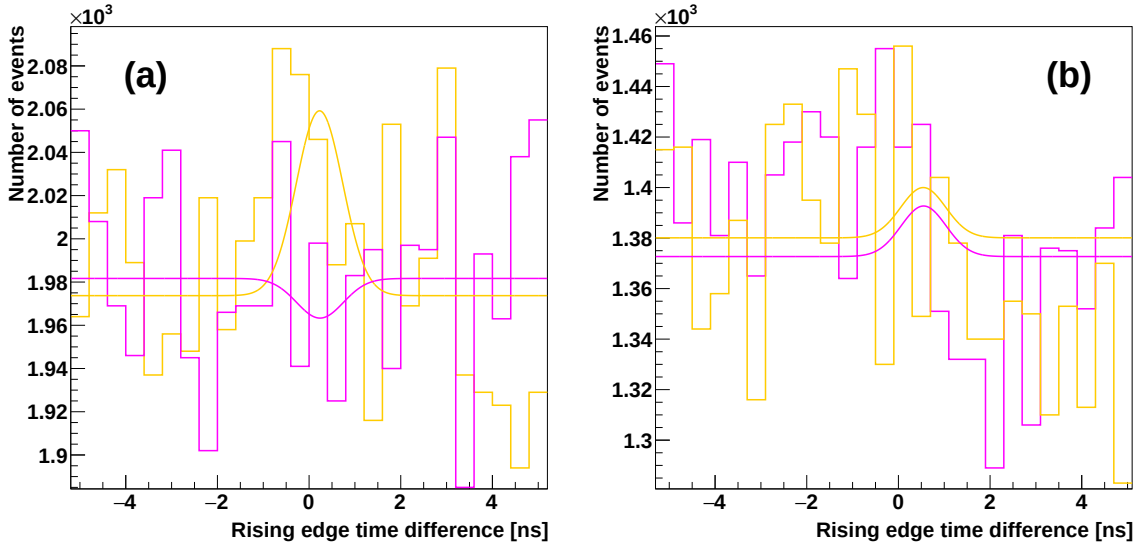

Figure 7.24: Central part of the histograms of the time distance between the signal rising edge position in the tagging counter and the L (a) or R (b) polarimeter detector, for events with the polarimeter-detector amplitude in the right half of the Møller peak and tagging counter amplitude in the full Møller peak, for empty target runs, shown with the fitted functions (see text). Histograms for opposite beam polarizations are plotted with different colors.

beam polarization is clearly visible. The half peak cuts are also marked in the drawing. A significant fraction of remaining internal, target-related background events, including Møller electrons, is also visible in the low-energy part of the spectrum shown in Fig. 7.25.

The beam asymmetries are listed in Tables 7.4 and 7.5, together with the fraction of background events passing the amplitude cuts, estimated using a gamma fit. In the final analysis, the asymmetries were obtained by counting events in the right half of the beam peak, where the signal-to-background ratio is sufficiently high that the subtraction of this remaining background is not necessary. According to an exponential fit to the background tail, the fraction of remaining background events in the data sample is approx. 1%.

If wider cuts are used, the asymmetry of the peak becomes important. Due to the asymmetry of the gamma distribution, a symmetric $\pm 2\ \sigma$ cut accepts a significantly larger part of the peak on the left hand side than on the right. Therefore, asymmetric cuts were applied in the full peak analysis, with a high–amplitude cut of $+2\ \sigma$ and a low–amplitude cut corresponding to the same value of the fitted gamma distribution as for the high–amplitude cut ($\Gamma(x_0 + 2\sigma)$).[1] The difference between the symmetric and asymmetric cuts is shown in Fig. 7.26.

The asymmetries obtained with full peak cuts are also shown in Tables 7.4 and 7.5 for comparison. The difference between full peak and half peak asymmetry val-

[1] Throughout this work the asymmetric signal-amplitude cut, with a low–amplitude cut corresponding to the same value of the fitted gamma distribution as for $+2\ \sigma$ high-amplitude cut, will be shortly referred to as the full peak amplitude cut.

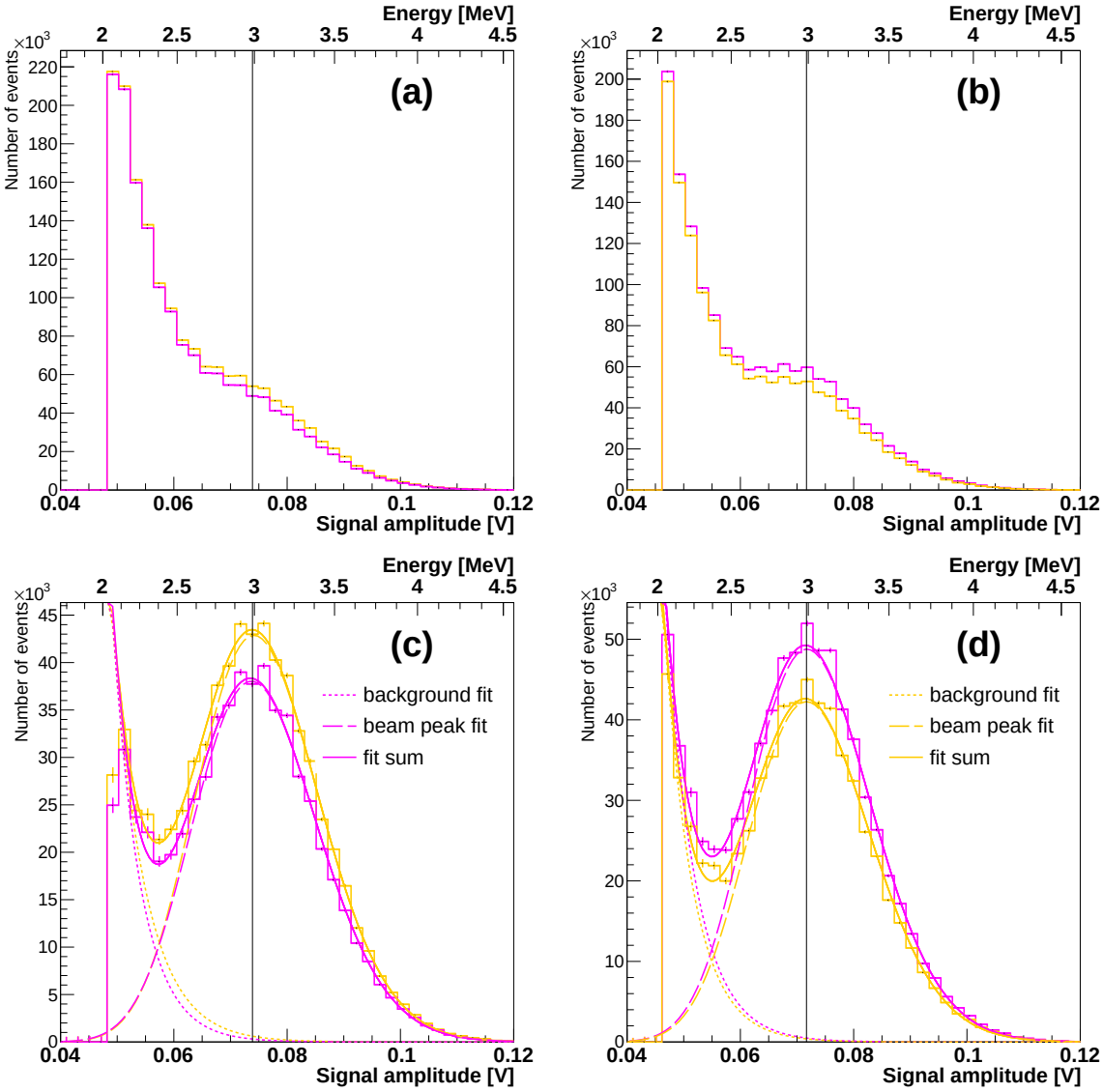

Figure 7.25: Signal amplitude spectrum, recorded in the polarimeter with the beam trigger, before (top) and after (bottom) empty-target background subtraction in the L (left) and R (right) polarimeter detector. The peak corresponds to beam electrons Mott-scattered off the beryllium and gold targets. The distributions are fitted with a sum of two gamma functions. The half peak low-amplitude cuts are marked with the black vertical lines. Histograms for opposite beam polarizations are plotted with different colors.

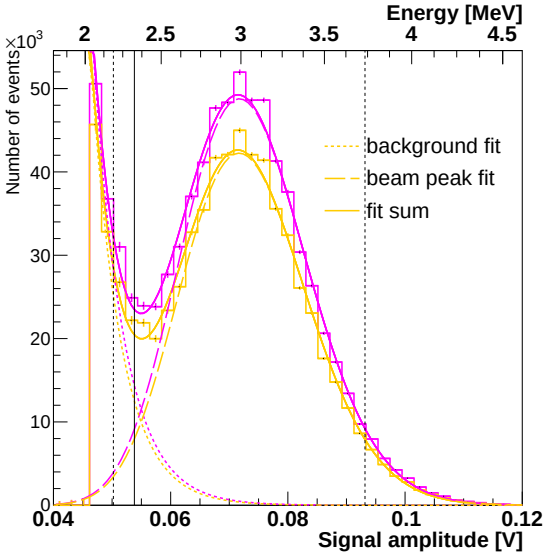

Figure 7.26: Signal amplitude spectrum after background subtraction in the polarimeter detector acquired with the beam trigger. The black vertical lines mark the part of the spectrum used to calculate the asymmetry in the full peak analysis, dotted lines: symmetric ± 2 σ cuts, solid line: asymmetric low-amplitude cut according to the fitted gamma distribution. Histograms for opposite beam polarizations are plotted with different colors.

ues is related to the different fraction of background events and different analyzing power, which is discussed in more detail below, and is taken into account in systematic uncertainty in Section 8.3.

The beam polarization measurement was repeated every day, and the individual results are in agreement within their statistical uncertainties, which can be seen in Fig. 7.27.

Background subtraction

The results with both the half peak and the full peak cuts must give the same beam polarization value if the analysis is performed correctly. The differrence between the half peak and full peak asymmetry can be partly explained by the fact that the full peak data contain more background events, as much as 20% in the R polarimeter detector.

In a perfect experiment, with 100% efficient event selection, the measured numbers of events would correspond to the beam electrons only, and the asymmetry could be written as

$$A_{beam} = \frac{N^+_{beam} - N^-_{beam}}{N^+_{beam} + N^-_{beam}}. \tag{7.3}$$

In reality, the measured numbers of events contain both the number of beam electrons and of the background events. Let us assume for simplicity that there is only one

Table 7.4: Results of the beam polarization measurements in configuration A (after empty-target background subtraction), obtained with two different low-amplitude cuts. Single-counter asymmetry values A^{beam} were obtained from Eq. (3.2), before and after dead time correction. The fraction of background events passing the selections was estimated from the fits to the amplitude spectra.

analysis	A^{beam} **without dead time correction**	A^{beam} **with dead time correction**	**% bgd events**
L half peak	0.0625 ± 0.0019	0.0695 ± 0.0022	0.4%
L full peak	0.0577 ± 0.0022	0.0642 ± 0.0029	5.4%
R half peak	0.0649 ± 0.0017	0.0750 ± 0.0021	0.4%
R full peak	0.0608 ± 0.0017	0.0731 ± 0.0024	5.0%

Table 7.5: Results of the beam polarization measurements in configuration B (after empty-target background subtraction), obtained with two different low-amplitude cuts. Single-counter asymmetry values A^{beam} were obtained from Eq. (3.2), before and after dead time correction. The fraction of background events passing the selections was estimated from the fits to the amplitude spectra.

analysis	A^{beam} **without dead time correction**	A^{beam} **with dead time correction**	**% bgd events**
L half peak	0.0454 ± 0.0017	0.0482 ± 0.0021	2.5%
L full peak	0.0404 ± 0.0013	0.0453 ± 0.0023	17%
R half peak	0.0461 ± 0.0015	0.0508 ± 0.0019	3%
R full peak	0.0360 ± 0.0012	0.0431 ± 0.0022	28%

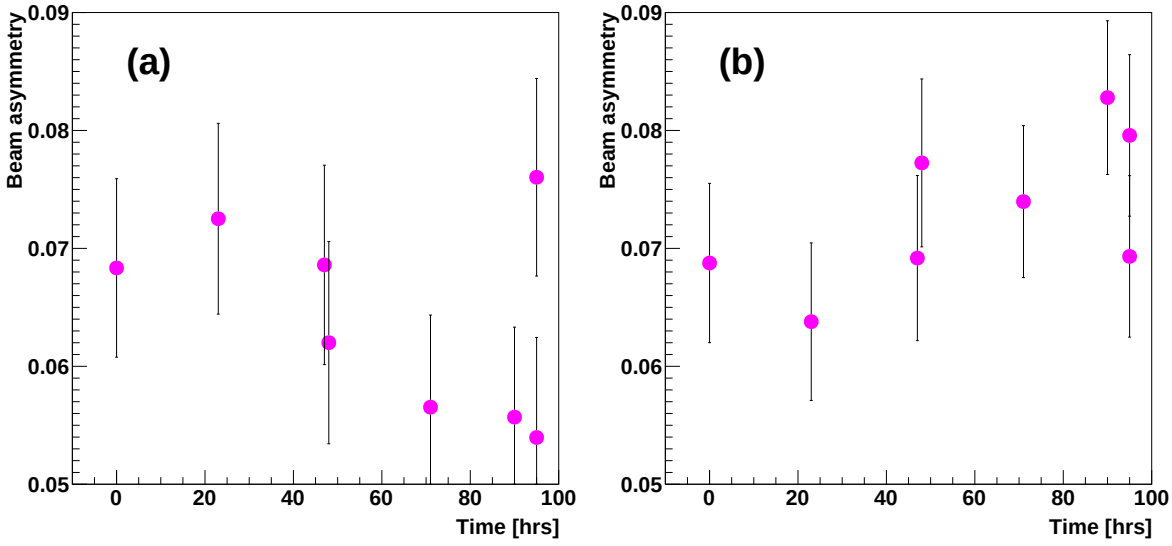

Figure 7.27: Time dependence of the asymmetry calculated for individual runs using events from the right half of the beam peak, in the L (a) and R (b) polarimeter detector.

source of background. In this case the total numbers of events are

$$N^+ = N^+_{beam} + N^+_{bgd} \tag{7.4a}$$

and

$$N^- = N^-_{beam} + N^-_{bgd}. \tag{7.4b}$$

The experimental asymmetry is determined from these two numbers according to

$$A_{exp} = \frac{N^+ - N^-}{N^+ + N^-} = \frac{N^+_{beam} + N^+_{bgd} - N^-_{beam} - N^-_{bgd}}{N^+ + N^-}. \tag{7.5}$$

The enumerator can be rewritten to separate the contribution from beam and background electrons:

$$A_{exp} = \frac{N^+_{beam} - N^-_{beam}}{N^+ + N^-} + \frac{N^+_{bgd} - N^-_{bgd}}{N^+ + N^-}. \tag{7.6}$$

Note that the denominator still contains the contributions from both types of events, thus in order to rewrite A_{exp} in terms of the original signal and background asymmetries one has to know the relative event rates of signal and background. They can be approximately determined from the fits to the signal amplitude spectrum.

Denoting the fraction of background events in the data sample by

$$x_{bgd} = \frac{N^+_{bgd} + N^-_{bgd}}{N^+ + N^-}, \tag{7.7a}$$

we find from Eqs. (7.4) that the fraction of beam events is

$$1 - x_{bgd} = \frac{N^+_{beam} + N^-_{beam}}{N^+ + N^-}. \tag{7.7b}$$

Now we can use Eqs. (7.7) to replace the total number of events $(N^+ + N^-)$ in the denominator of Eq. (7.6) with x_{bgd}:

$$A_{exp} = (1 - x_{bgd}) \frac{N^+_{beam} - N^-_{beam}}{N^+_{beam} + N^-_{beam}} + x_{bgd} \frac{N^+_{bgd} - N^-_{bgd}}{N^+_{bgd} + N^-_{bgd}}. \tag{7.8}$$

This way A_{exp} has been expressed in terms of the individual asymmetries of the two contributing types of events:

$$A_{exp} = (1 - x_{bgd})\, A_{beam} + x_{bgd} A_{bgd}. \tag{7.9}$$

According to Eq. (7.9), the measured asymmetry value is an average of the asymmetries describing the different types of events, each with a weight equal to the fraction of events belonging to that category. Therefore, if the background asymmetry is smaller (larger) that that of the signal, it decreases (increases) the measured asymmetry, which is illustrated in Fig. 7.28. In particular, if the background asymmetry is equal to zero, the measured value has to be divided by the fraction of signal events in the data sample $(1 - x_{bgd})$, in order to obtain the true asymmetry of the signal events.

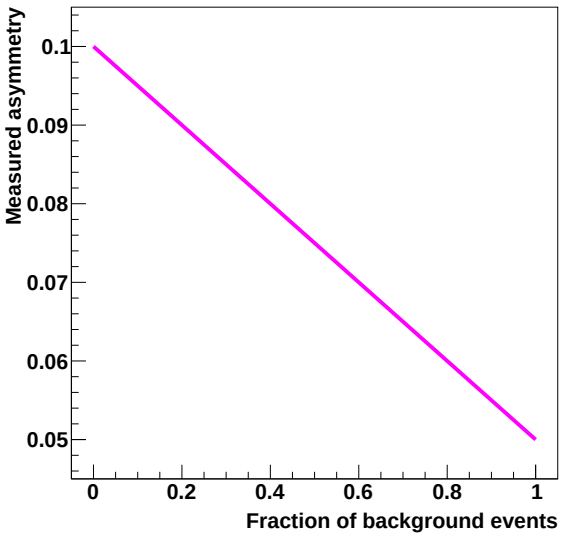

Figure 7.28: Dependence of the experimental asymmetry on the fraction of background events in the data sample x_{bgd}, for signal asymmetry $A_{beam} = 0.1$ and twice–lower background asymmetry $A_{bgd} = 0.05$.

The measured asymmetry values were corrected for the presence of background by subtracting the number of Møller and background events following from the fit combined with the asymmetry of background. The asymmetry was calculated independently for events in the beam peak and for events below the low–amplitude cut, where the rate of beam electrons is much lower than that of Møller electrons and background. The asymmetry was corrected by subtracting the number of background events estimated from background asymmetry and the weight obtained from the fit to the spectrum. The uncertainty of the corrected asymmetry is higher, since it is in fact a combination of two asymmetries with similar uncertainties.

The full dependence of the asymmetry on the low–amplitude cut in configuration B, before and after background subtraction, is shown in Figs. 7.29 and 7.30, respectively (the dependence was not as strong in configuration A). The subtraction of background removes the rapid decrease of the asymmetry in the left side of the plot (low cuts), while the right side (high cuts) is practically unchanged, since there is very little background in that part of the spectrum. The remaining dependence can be explained by the fact that the effective analyzing power as well depends on the low-amplitude cut; the differences between the results obtained with different cuts are included in the systematic uncertainty (cf. Section 8.3).

7.5.2. Møller

In order to record the Møller electrons in the polarimeter, a coincidence trigger of the tagging and one of the polarimeter detectors was used. As in the beam polarization measurement, the number of events recorded with an empty target frame was subtracted from the number of events recorded with the gold target foil.

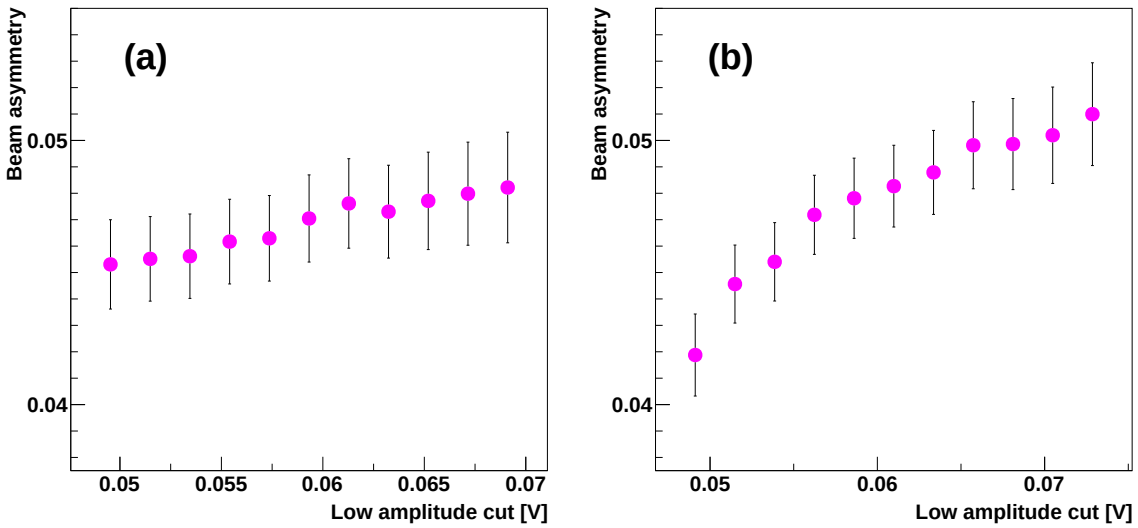

Figure 7.29: Dependence of the asymmetry in the L (a) and R (b) polarimeter detector on the low–amplitude cut.

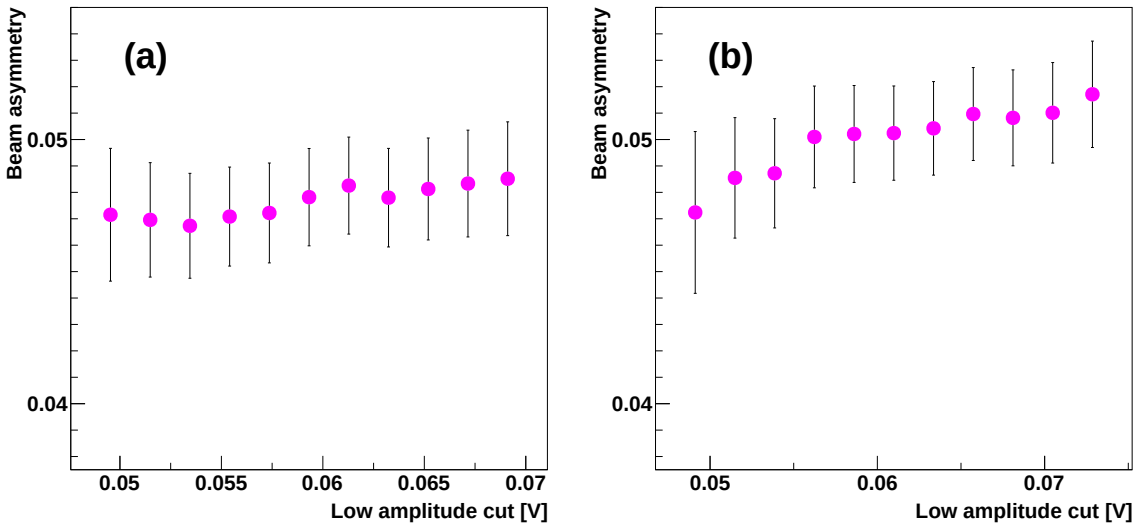

Figure 7.30: Dependence of the asymmetry in the L (a) and R (b) polarimeter detector on the low–amplitude cut, after low–energy background subtraction based on a fit to the spectrum.

Event selections

In addition to the shielding mentioned in Chapter 3, a further reduction of background was achieved by event selection based on two variables: (1) energy (signal amplitude) in the tagging detector and (2) arrival-time difference of the polarimeter and tagging detector signals.

Five different data selection approaches have been compared:

1. Raw data (no selections).

2. Tagging counter amplitude restricted to the 1.5 MeV peak.

3. Time difference in the $\pm 2\ \sigma$ range around the maximum.

4. Time difference in the $\pm 2\ \sigma$ range around the maximum, and the tagging counter amplitude in the 1.5 MeV peak.

5. Time difference in the $\pm 2\ \sigma$ range around the maximum, and the tagging counter amplitude in the 1.5 MeV peak, with background subtraction based on the interpolation of the time distribution.

The selection criteria and their effects are described below.

Amplitude selection

The tagging counter amplitude selection can be used to remove part of the background events present in the data collected with the Møller trigger, which produced a false coincidence with a beam electron in the tagging counter.

When data from all runs are combined, the 1.5 MeV peak is broadened compared to the peak width in an individual run (cf. Section 7.4.1). Therefore, the cuts were applied on a run–by–run basis, leading to a lower number of events, but also a lower fraction of background and therefore a lower statistical uncertainty, in comparison to a constant cut for all runs.

The signal amplitude spectrum after selections is shown in Fig. 7.31. Applying this selection decreases the fraction of background and beam events (estimated from fits to the spectrum) that are present in the Møller peak part of the spectrum, from which the asymmetry is calculated. As the fit to the background tail is getting unstable when background is removed from the data sample, all spectra with event selections were fitted with a fixed background shape, by rescaling the background obtained without selections.

Timing selection

The timing selection, discussed in Section 7.4.3, was used to remove the false coincidences of particles produced by two different beam electrons, present in the data collected with the Møller trigger due to the finite timing resolution of the coincidence logic.

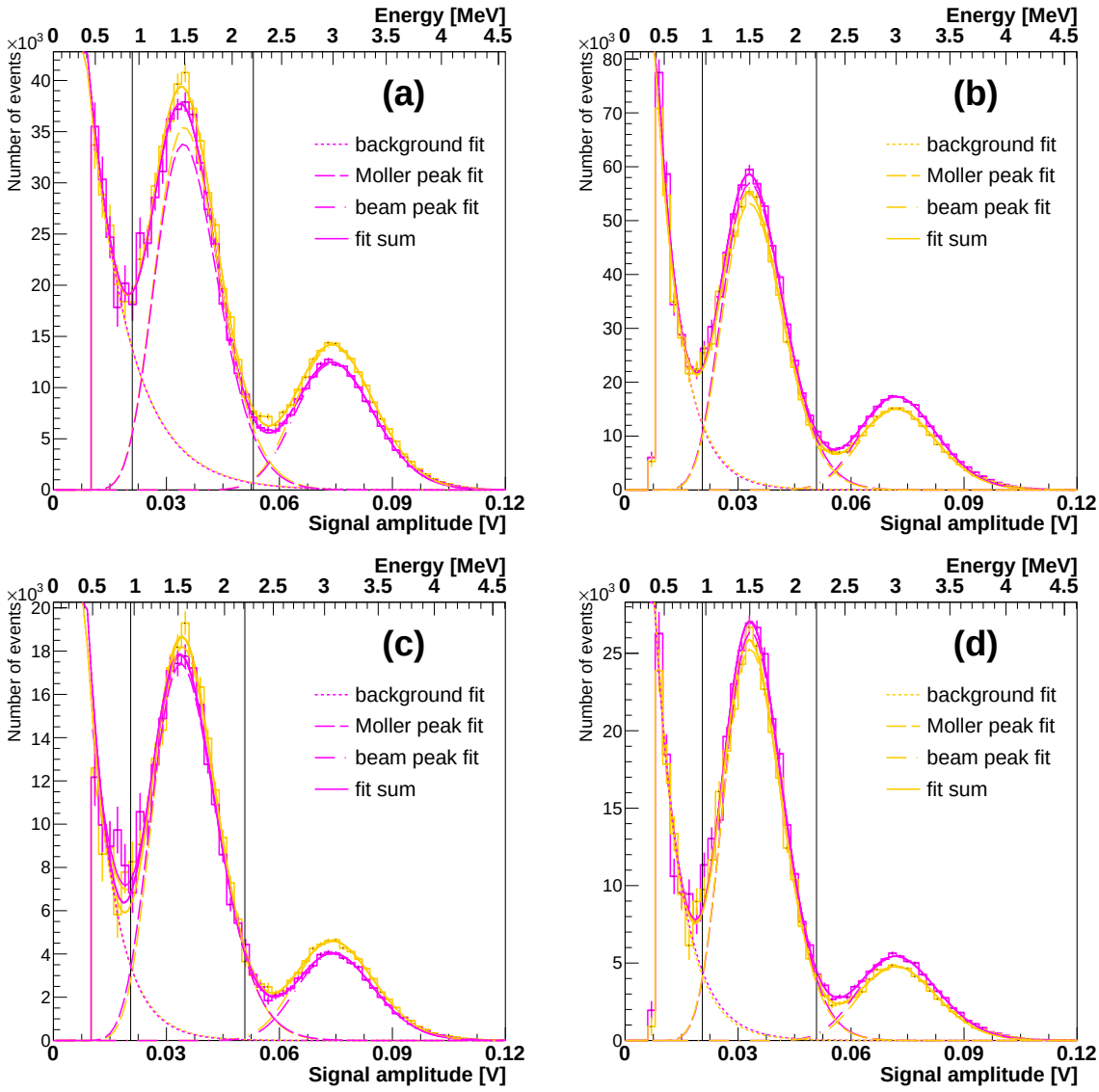

Figure 7.31: Signal amplitude spectrum, recorded in the L (left) and R (right) polarimeter detectors with the Møller (coincidence) trigger, after empty-target background subtraction, without (top) and with (bottom) full peak amplitude selection on the tagging counter data. The peak around 1.5 MeV corresponds to Møller electrons backscattered off the gold target and the peak at higher energies to doubly Mott-scattered beam electrons (false coincidences). Solid line – sum of an exponential and two gamma functions fitted to the spectrum; dashed line – gamma fit to the (Møller or beam) peak; dotted line – exponential fit to the background tail. The black vertical lines indicate the cuts applied to select the Møller scattering events. Histograms for opposite beam polarizations are plotted with different colors.

Table 7.6: Background level in the Møller polarization measurement in configuration A, for events with signal amplitude within the full Møller peak, after dead time correction. The number of background events recorded in both detectors was obtained from a fit to the distribution of time between the rising edge position in the tagging counter and the polarimeter detector (cf. Fig. 7.33). The fraction of target-induced background events was determined by comparing the background level before and after empty-target data subtraction.

detector	**total bgd**	**target bgd**	**% target bgd**
L UP	63890 ± 59	4014 ± 15	6.3%
L DN	64174 ± 59	3930 ± 15	6.1%
R UP	43884 ± 48	4829 ± 16	11%
R DN	44391 ± 48	5050 ± 16	11%

The signal amplitude spectrum after selections is shown in Fig. 7.32. The main observation is that the timing selection greatly reduces the amount of low–energy background and beam electrons producing false coincidences. This reduction is much more effective with timing selection than with the tagging counter amplitude selection (cf. Tables 7.7 and 7.8).

Thanks to the fact that with the timing selection the amount of low–energy background is very low also in the left half of the Møller peak, the asymmetry can be calculated using the data from the whole peak. In this case, again, the asymmetry of the peak has to be taken into account. The full peak cuts were calculated in the same way as for the beam peak in the beam polarization analysis.

Target-induced background

The time difference distributions of the events that pass the amplitude selections are shown in Fig. 7.33. A Gaussian peak, about 2 ns wide, corresponding to the coincidences of Møller electrons, is visible on top of background, whose distribution is uniform to a good approximation. The different level of background before and after empty–target data subtraction is also clearly visible.

The spectrum can be fitted with a sum of a constant and a Gaussian curve. The resulting background level can be used to estimate the number of background events passing the timing selection, according to the interpolation under the signal peak. The results are summarized in Table 7.6.

The ratio of the numbers of target induced background events recorded in the L and R polarimeter detector (0.80) is similar to the ratio of signal events (0.76), therefore, both effects can be explained with detector efficiency. Meanwhile, the amount of empty–target background is significantly lower in the R polarimeter detector, which seems to be caused by a lower amount of external background reaching this counter.

It is worth noting that the number of target induced background events from this analysis is significantly higher than the number obtained from the fit to the amplitude (energy) spectrum. According to the flat fit it accounts for 5.0% and 4.7% of events, compared to 3.8% and 1.5% according to the analysis presented in the previous section, in the L and R polarimeter detector, respectively. It can be explained by the false

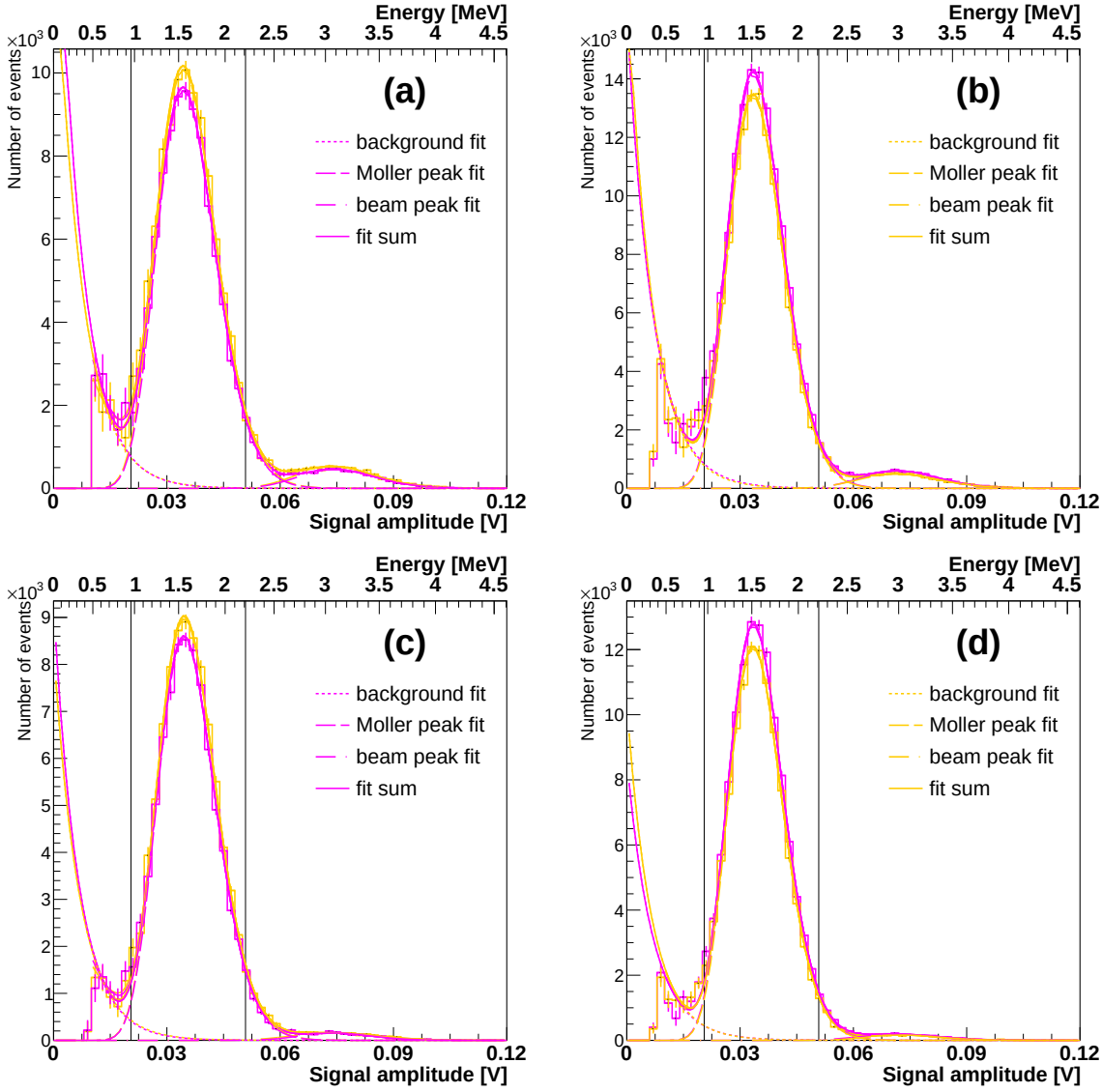

Figure 7.32: Signal amplitude spectrum, recorded in the L (left) and R (right) polarimeter detectors with the Møller (coincidence) trigger, after empty-target background subtraction, with the ± 2 σ timing selection, without (top) and with (bottom) full peak amplitude selection on the tagging counter data. The peak around 1.5 MeV corresponds to Møller electrons backscattered off the gold target and the peak at higher energies to doubly Mott-scattered beam electrons (false coincidences). Solid line – sum of an exponential and two gamma functions fitted to the spectrum; dashed line – gamma fit to the (Møller or beam) peak; dotted line – exponential fit to the background tail. The black vertical lines indicate the cuts applied to select the Møller scattering events. Histograms for opposite beam polarizations are plotted with different colors.

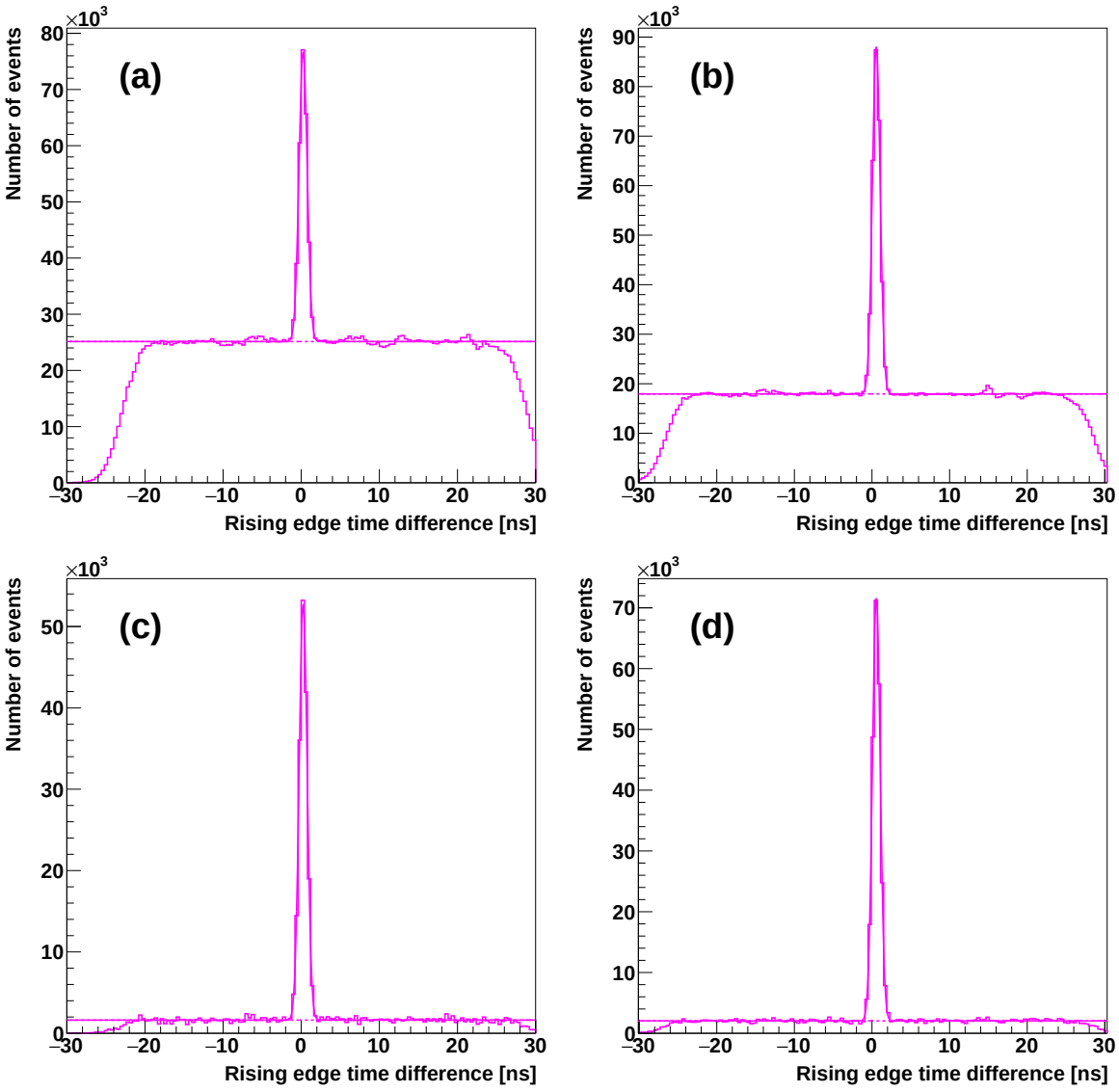

Figure 7.33: Histograms of the time distance between the rising edge position in the tagging counter and the L (left) or R (right) polarimeter detector, before (top) and after (bottom) empty–target background subtraction, for events with signal amplitude within the full Møller peak, after dead time correction. The distribution is fitted with a sum of a constant (background) and a Gaussian curve (signal), shown with a solid line. The background interpolation under the signal peak is marked with a dashed line.

coincidences of two Møller electrons (with approx. 1.5 MeV energy, thus passing the amplitude selections) produced by two different beam electrons.

Subtracting fitted background

An alternative method of determining the asymmetry follows from analyzing the time difference distributions shown in Fig. 7.33. The fitted uniform background can be subtracted from the number of events passing the selection criteria. In this method, the empty-target background subtraction is not necessary, since both sources of background (empty-target and target-induced events) are removed with a single fit.

The time distribution of background events is uniform, therefore, it can be fitted with a better precision than the exponential amplitude distribution. Since the random fluctuations of experimental data average out in the fit, the result is subject to a lower statistical uncertainty than the raw number of empty-target background events. This way, the uncertainty of the asymmetry is reduced.

Results

The results (the asymmetry, the number of events passing the selection, as well as the fraction of background and beam events present in the part of the spectrum selected for analysis) are summarized in Table 7.7 (after dead time correction). The same algorithms were used to analyze the data in configuration B; the results can be found in Table 7.8. In case of the analyses without timing selection, half-peak results are shown, since otherwise the subtraction of remaining background would be necessary for comparison. The results regarding the asymmetry are in agreement within the statistical uncertainties.

The amount of background remaining after subtracting the empty-target data is different in the L and R polarimeter detectors. This effect can be partly explained by the asymmetry of the experimental setup (different positions of the detectors, resulting in different background conditions). The difference is, however, much smaller if the event selections are applied.

A notable fact is that the asymmetry uncertainties obtained with the timing selection are comparable to those obtained without selections, despite the much lower number of events (thanks to the much lower amount of empty–target background passing the selection). The uncertainty of the number of events taking into account all effects (empty–target data subtraction and dead time correction) for analysis 1. on the L polarimeter-detector data is a factor of 5 higher than the square root of the number of events, while for analysis 5. this ratio is less than 2.

The results obtained with background interpolation are in agreement with the standard analysis using empty-target background subtraction with the same event selections. The slightly lower number of events shows that the fit removes some of the background remaining after event selection.

The Møller electrons asymmetry measured in individual runs can also be plotted as a function of time, and the results are in agreement within their statistical uncertainties, which can be seen in Fig. 7.34.

Table 7.7: Results of the Møller polarization measurements in configuration A (after dead time correction). The results were obtained with five different analysis methods (see text for details). Single-counter asymmetry values $A^{\text{Møller}}$ were obtained from Eq. (3.2). $N^{\text{Møller}}$ is the total number of events recorded in both detectors. The fraction of low-energy background and beam events passing the selections was estimated from the fits to the amplitude spectra.

selection (see text)	$A^{\textbf{Møller}}$ **(half peak)**	$N^{\text{Møller}}$	**% bgd events**	**% beam events**
1 L	0.0309 ± 0.0074	$(437.4 \pm 3.2)10^3$	8.1%	0.9%
2 L	0.0243 ± 0.0087	$(203.3 \pm 1.8)10^3$	5.8%	0.6%
3 L	0.0342 ± 0.0066	$(105.21 \pm 0.69)10^3$	2.4%	0.1%
4 L	0.0293 ± 0.0053	$(93.93 \pm 0.50)10^3$	1.5%	0.05%
5 L	0.0349 ± 0.0050	$(90.06 \pm 0.45)10^3$		
1 R	0.0360 ± 0.0045	$(602.6 \pm 2.7)10^3$	1.7%	0.4%
2 R	0.0303 ± 0.0055	$(278.0 \pm 1.5)10^3$	1.4%	0.3%
3 R	0.0312 ± 0.0046	$(139.96 \pm 0.64)10^3$	0.5%	0.08%
4 R	0.0337 ± 0.0040	$(125.93 \pm 0.51)10^3$	0.3%	0.02%
5 R	0.0345 ± 0.0040	$(120.74 \pm 0.48)10^3$		

selection (see text)	$A^{\textbf{Møller}}$ **(full peak)**	$N^{\text{Møller}}$	**% bgd events**	**% beam events**
4 L	0.0264 ± 0.0049	$(165.84 \pm 0.81)10^3$	3.8%	0.03%
5 L	0.0291 ± 0.0043	$(160.19 \pm 0.69)10^3$		
4 R	0.0317 ± 0.0035	$(219.51 \pm 0.77)10^3$	1.5%	0.01%
5 R	0.0309 ± 0.0033	$(210.12 \pm 0.69)10^3$		

Table 7.8: Results of the Møller polarization measurements in configuration B (after dead time correction). The results were obtained with two different analysis methods (see text for details). Single-counter asymmetry values $A^{\text{Møller}}$ were obtained from Eq. (3.2). $N^{\text{Møller}}$ is the total number of events recorded in both detectors. The fraction of low-energy background and beam events passing the selections was estimated from the fits to the amplitude spectra.

selection (see text)	$A^{\textbf{Møller}}$ **(half peak)**	$N^{\text{Møller}}$	**% bgd events**	**% beam events**
1 L	0.0238 ± 0.0047	$(387.6 \pm 1.8)10^3$	2.8%	1.5%
2 L	0.0233 ± 0.0055	$(189.0 \pm 1.0)10^3$	2.7%	1.0%
3 L	0.0201 ± 0.0046	$(107.02 \pm 0.49)10^3$	1.3%	0.3%
4 L	0.0204 ± 0.0042	$(98.66 \pm 0.41)10^3$	1.1%	0.6%
5 L	0.0208 ± 0.0042	$(95.58 \pm 0.40)10^3$		
1 R	0.0147 ± 0.0032	$(575.9 \pm 1.9)10^3$	4.1%	1.7%
2 R	0.0158 ± 0.0039	$(274.4 \pm 1.1)10^3$	2.1%	1.1%
3 R	0.0127 ± 0.0037	$(152.96 \pm 0.56)10^3$	0.6%	0.8%
4 R	0.0122 ± 0.0036	$(139.33 \pm 0.50)10^3$	0.3%	0.9%
5 R	0.0129 ± 0.0036	$(134.75 \pm 0.49)10^3$		

selection (see text)	$A^{\textbf{Møller}}$ **(full peak)**	$N^{\text{Møller}}$	**% bgd events**	**% beam events**
4 L	0.0189 ± 0.0037	$(171.42 \pm 0.63)10^3$	2.3%	0.4%
5 L	0.0193 ± 0.0035	$(166.44 \pm 0.57)10^3$		
4 R	0.0092 ± 0.0031	$(224.99 \pm 0.69)10^3$	1.1%	0.6%
5 R	0.0123 ± 0.0030	$(216.24 \pm 0.65)10^3$		

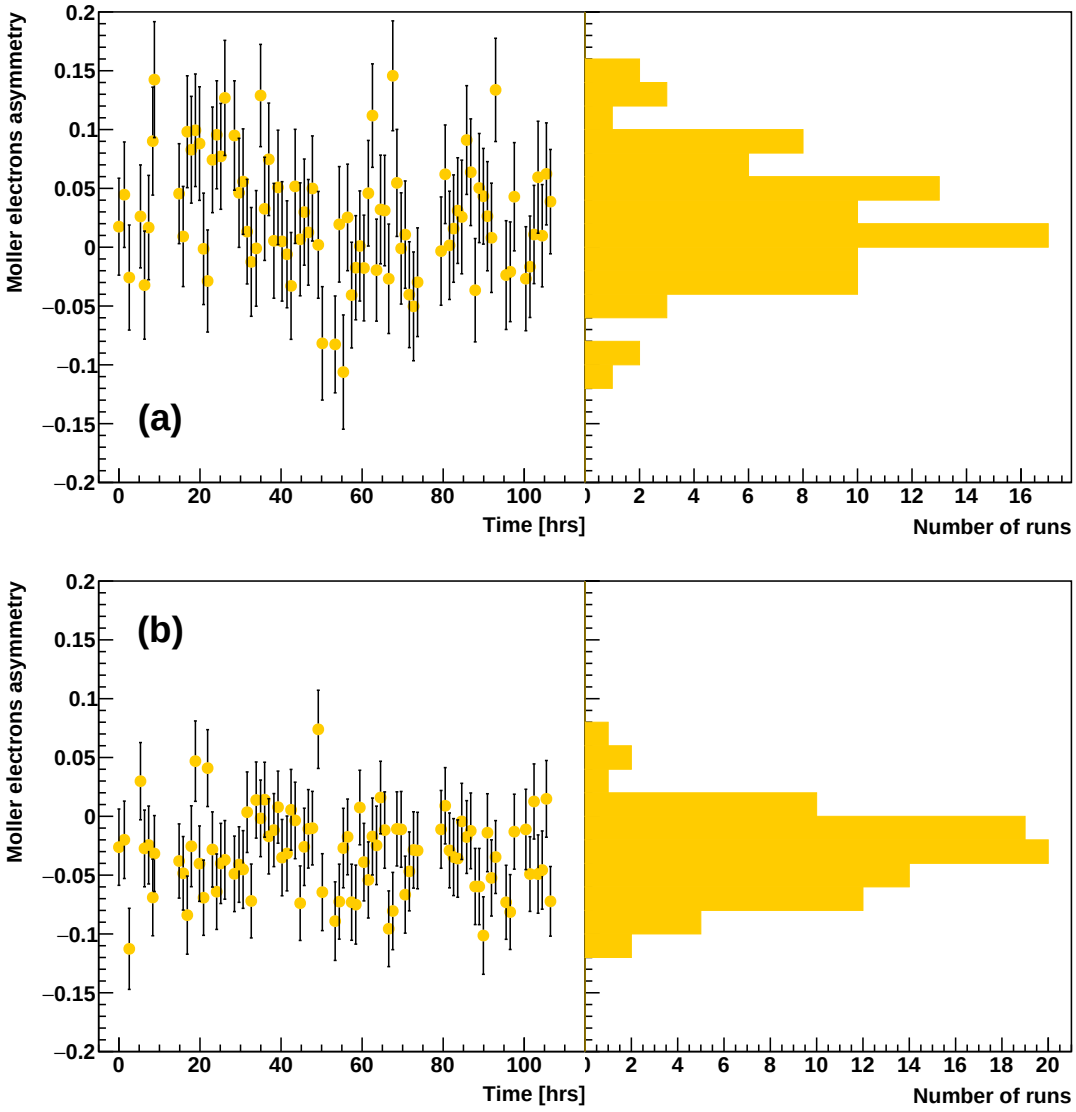

Figure 7.34: Time dependence of the asymmetry calculated for individual runs using events from the full Møller peak, in the L (a) and R (b) polarimeter detector.

Chapter 8

Analysis of uncertainties

The statistical and systematic uncertainties relevant for the measurement of polarization are discussed. Parts of this chapter were published in [31].

8.1. Statistical uncertainty

In case of the beam polarization measurement, the statistical uncertainty reflects mainly the number of recorded signal events. This is, however, not the case for Møller electrons. In this case, the signal-to-background ratio ranges from 1 to approx. 0.05 in different parts of the Møller peak, so in general, the statistical uncertainty follows mostly from the number of registered background events. Since the background spectrum is well described by an exponential distribution, the higher-energy part of the peak is subject to a much lower uncertainty than the low-energy tail of the Møller peak.

The dead time correction is subject to a significant statistical uncertainty as well, since it is based on the fits to the experimental time distributions, which was also included in the total statistical uncertainty. The contribution of the dead time correction to the asymmetry uncertainty is approx. 0.0006 with the beam trigger and 0.0003 with the Møller trigger (the statistical uncertainties of the single-counter asymmetry are of the order of 0.002 and 0.004 with the beam and Møller trigger, respectively).

8.2. Analyzing power

In view of the lack of experimental data on the effective Sherman function under the conditions corresponding to this experiment, it was obtained from a dedicated Monte Carlo simulation, initially used to optimize the parameters of the Mott polarimeter, including target thickness and scattering angle (cf. Chapter 5). The simulated values of the analyzing power used for data analysis were 0.0847 at 3 MeV and 0.0886 at 1.5 MeV. The effective Sherman function at beam energy could be determined experimentally, from the measured asymmetry and the independent measurement of the beam polarization. However, since the final result is to be obtained as the ratio of the polarizations before and after the scattering, it is favorable to use the values of the analyzing power obtained with the same method both at 1.5 MeV and 3 MeV. With

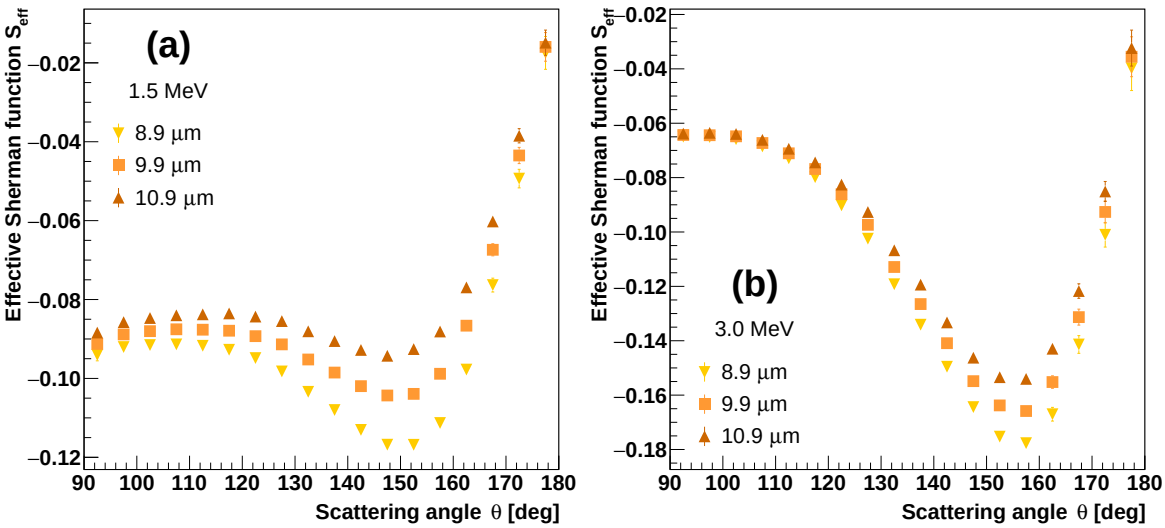

Figure 8.1: Dependence of the effective Sherman function on the electron scattering angle, obtained from the Monte Carlo simulation, for three target thicknesses, corresponding to the nominal target thickness and its extreme values used to estimate the uncertainty.

this approach the polarization ratio is less sensitive to systematic uncertainties of the Monte Carlo predictions, which partly cancel out.

In particular, the uncertainty of the target thickness might significantly affect the result of the absolute polarization measurement. At the same time, its influence on the polarization ratio should be much smaller. The gold target thickness uncertainty was estimated at 10%. The effective Sherman function values were calculated for the extreme values of 8.9 μm and 10.9 μm; their dependence on the electron scattering angle is shown in Fig. 8.1. The systematic uncertainties of the analyzing power related to the target thickness were estimated from the range of values obtained for different thicknesses as ± 0.0014 at 3 MeV and ± 0.0026 at 1.5 MeV.

The Monte Carlo simulation was validated by comparing its predictions to the experimental values from a few different polarimeters operating at energies between 100 keV and 14 MeV. The systematic uncertainties of the Monte Carlo predictions were estimated by analyzing the differences between the simulations and the values measured with the MAMI Mott polarimeter for energies from 1 to 3.5 MeV and several target thicknesses [50], cf. Chapter 5.

The total systematic uncertainties of the analyzing power, taking into account both effects, were estimated as ± 0.0034 at 3 MeV and ± 0.0063 at 1.5 MeV.

8.3. Dependence on applied cuts

The count-rate asymmetry was calculated for several values of the low-energy cuts applied to both Møller and beam spectra recorded in the polarimeter. The effective analyzing power was adjusted accordingly based on the Monte Carlo simulation results.

The energy loss of electrons in the gold target was also taken into account in the simulation. In order to calculate the effective Sherman function corresponding to the applied cuts, an effective Gaussian smearing, modeling the detector resolution measured experimentally at 1.5 and 3.0 MeV, was applied to the Monte Carlo-generated energy values.

The energy distributions before and after smearing are shown in Figs. 8.2. It is interesting to note that the average energy loss in scattering off the target is approx. 0.1 MeV, showing that the 9.9 μm gold target is relatively thick for electron energies of a few MeV.

Despite the limited detector resolution, events from the right half of the peak will have a larger average energy than those from the left half. The larger energy corresponds to a larger value of the effective Sherman function, since the energy loss is to a first approximation proportional to the distance travelled by the particle inside the target (leading to depolarization and multiple scattering). The effective Sherman function was calculated using events selected from the same part of the spectrum as in the data analysis. Several low-energy cuts were applied to the resulting energy spectra, yielding the effective Sherman function dependence on the low-amplitude cut shown in Fig. 8.3. A significant dependence is observed for the chosen target thickness of 9.9 μm. The difference between the full-peak value and that obtained with a half-peak cut can be of approx. 5% and further increase when even higher cuts are applied (cuts above the nominal beam energy value can be considered because of a finite energy resolution), which must be taken into account in the data analysis.

The dependence of the electron polarization on the low-amplitude cut is shown in Figs. 8.4 and 8.5 (the first data point corresponds to the full-peak cut and the last data point to the half-peak cut) for beam and Møller electrons, respectively. After the cut-dependent corrections, the results obtained with different low-amplitude cuts show no significant cut dependence, which confirms the consistency of the analysis.

The range of polarization values obtained with different cuts was used to estimate the systematic uncertainty of the result. The polarization uncertainty related to this effect was estimated as approx. ± 0.01.

Several timing cut and energy cut values in the tagging detector were considered, and the values resulting in the lowest uncertainty were used for the final result, while no significant dependence of the result on these selections was observed.

8.4. Target-related background

The background events can be divided in two classes: (*i*) empty-target background, which can be removed by subtracting the data acquired with an empty target frame and (*ii*) target-related background remaining after the subtraction.

The latter class of events consists of the low-energy background, whose spectrum can be described approximately as exponential, as well as Mott-scattered beam electrons, with energy around 3 MeV. The asymmetry of the low-energy background is much smaller than that of the signal, while the asymmetry for the beam electrons is higher than for Møller electrons. Therefore, the former type of events could decrease and the latter increase the measured asymmetry.

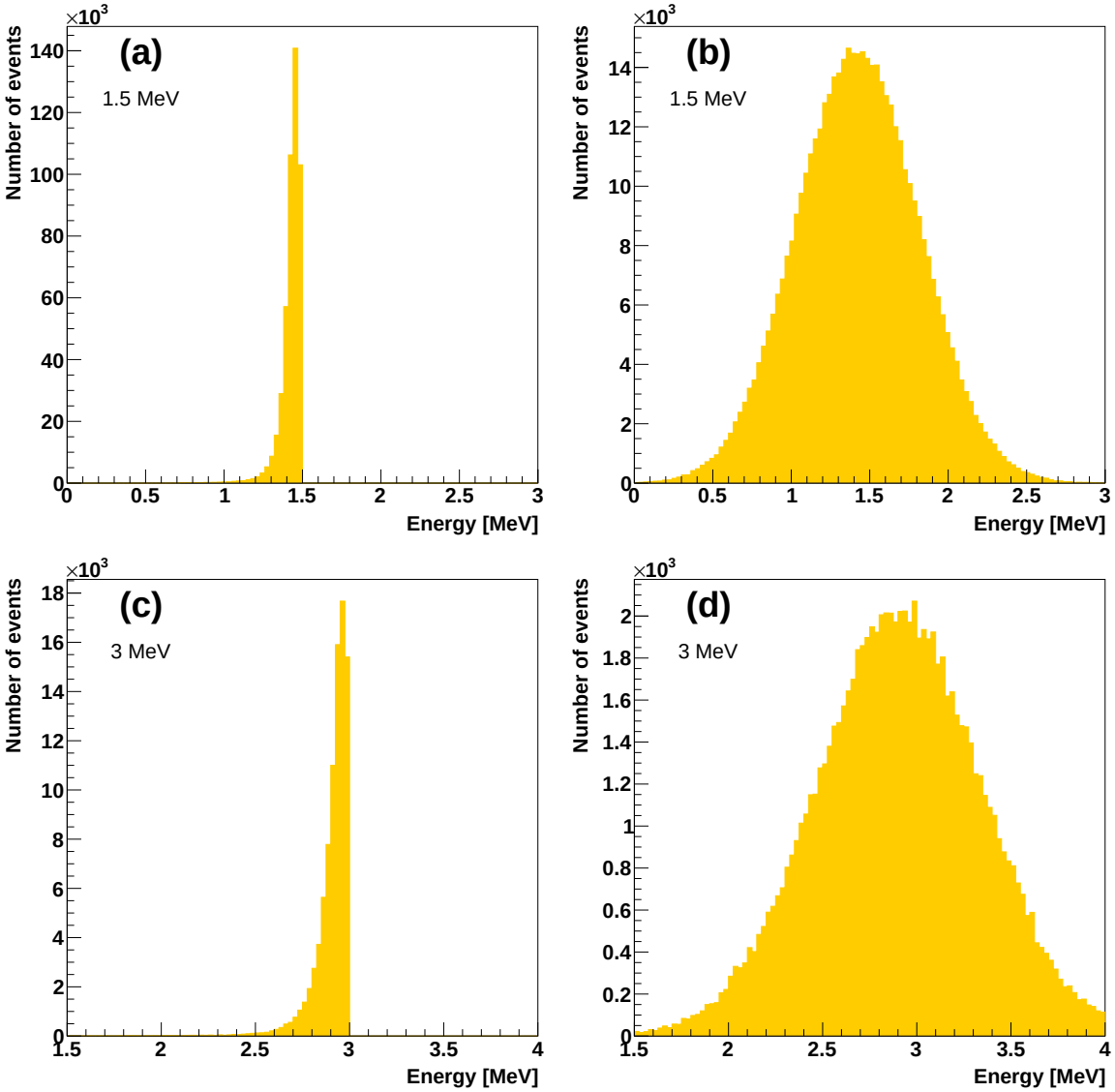

Figure 8.2: Simulated energy distribution after 1.5 MeV (top) and 3 MeV beam (bottom) scattering off a 9.9 μm gold target, before (left) and after smearing corresponding to the measured detector resolution (right).

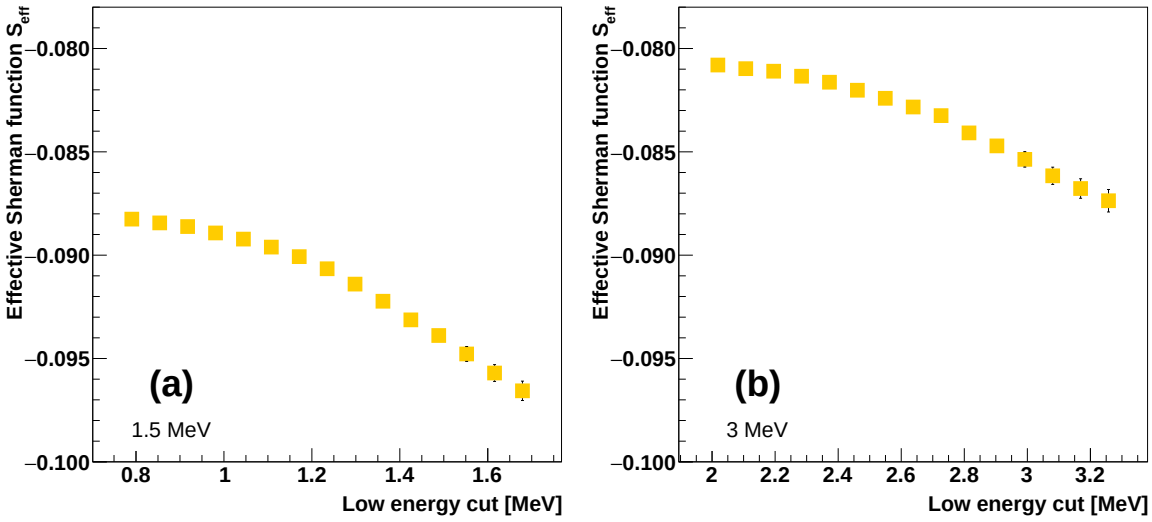

Figure 8.3: Dependence of the effective Sherman function S_{eff} on the low-energy cut for detectors placed at an angle of 120° with respect to the beam axis (scattering angle range $115° < \theta < 125°$), for two beam energies: 1.5 MeV (a) and 3.0 MeV (b). The detector resolution was modeled with a Gaussian peak fitted to the energy spectrum.

For the data collected with the beam trigger, the number of target-related background events was estimated from the fits to the spectrum, which are also shown in Fig. 7.25. For the data collected with the Møller trigger, the number of such events passing the selection criteria was calculated by interpolating the time difference distribution between the polarimeter and tagging detector signals. This method, independent of the background energy distribution, relies on the assumption that the time distribution of background events (false coincidences) is uniform. The validity of this approach was verified by establishing an upper limit on the existence of an additional background peak on top of the uniform distribution using the data collected with an empty target frame. No additional contribution was found within the statistical uncertainty.

8.5. Beam current stability

Another factor, which could affect the asymmetry measurement, is the stability of the beam current. The data were acquired in four-run sequences: the target in – target out – target out – target in. Histograms in Figs. 8.6 and 8.7, each made with data from one four-run sequence in configuration B, illustrate this effect. If the beam current was stable or changing linearly with time, the above order would ensure that the average event rate is unbiased in the signal as well as the background (empty target frame) data, see Fig. 8.6. In the contrary case there would be a wrong amount of background subtracted from the raw data (too much background is subtracted in Fig. 8.7 due to non-linear increase of the beam current).

The event rate, which is assumed to be proportional to the beam current, measured in 10 minute intervals, in configuration B, is plotted as a function of time in Fig. 8.8.

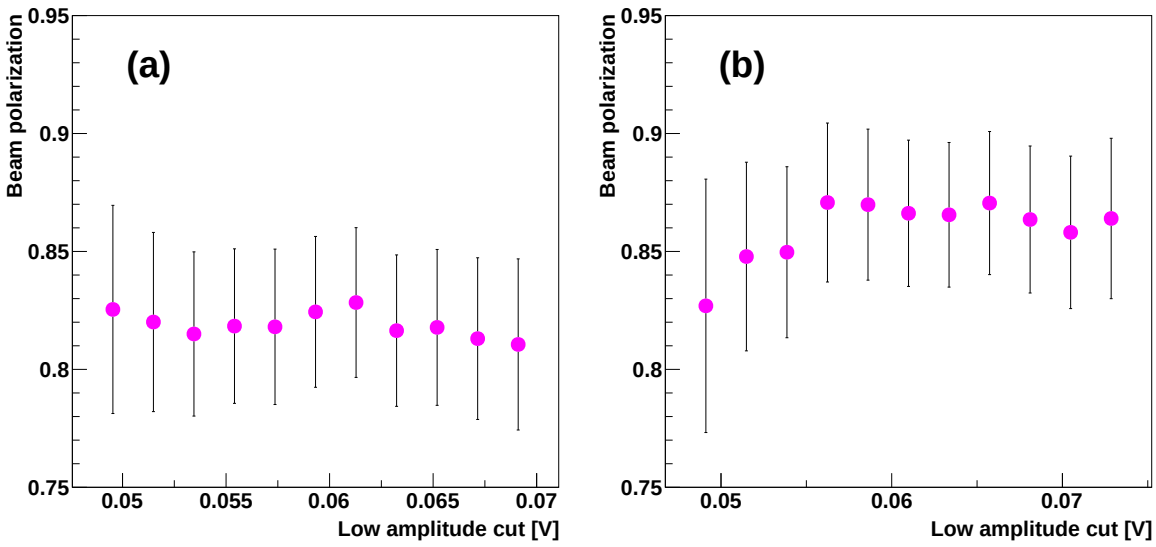

Figure 8.4: Dependence of the beam polarization measured with the L (a) and R (b) polarimeter detector on the low–amplitude cut, taking into account the effective Sherman function dependence on the low–energy cut as shown in Fig. 8.3.

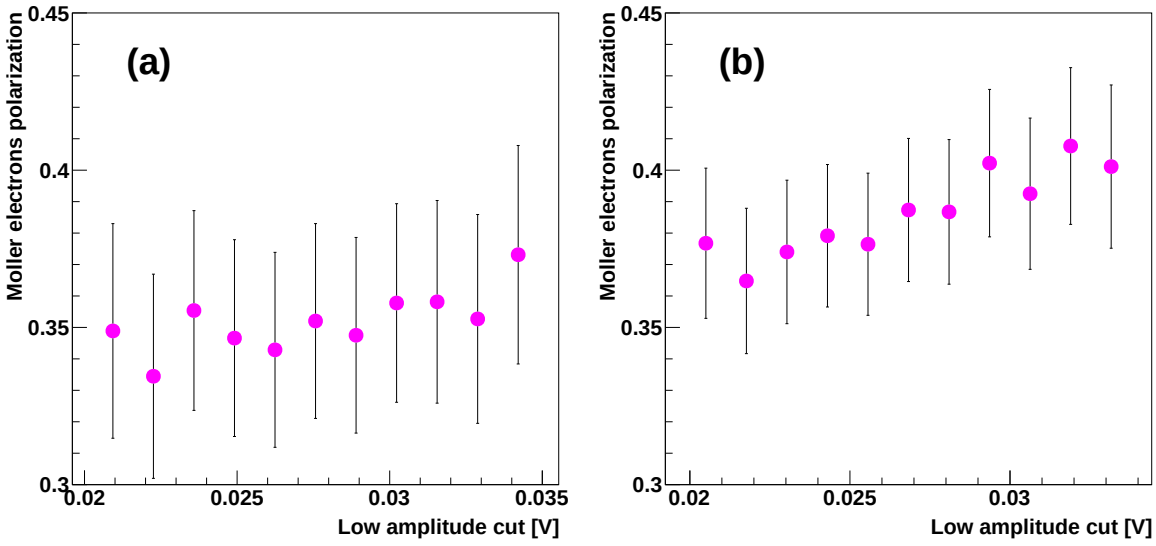

Figure 8.5: Dependence of the Møller electrons polarization measured with the L (a) and R (b) polarimeter detector on the low–amplitude cut, taking into account the effective Sherman function dependence on the low–energy cut as shown in Fig. 8.3.

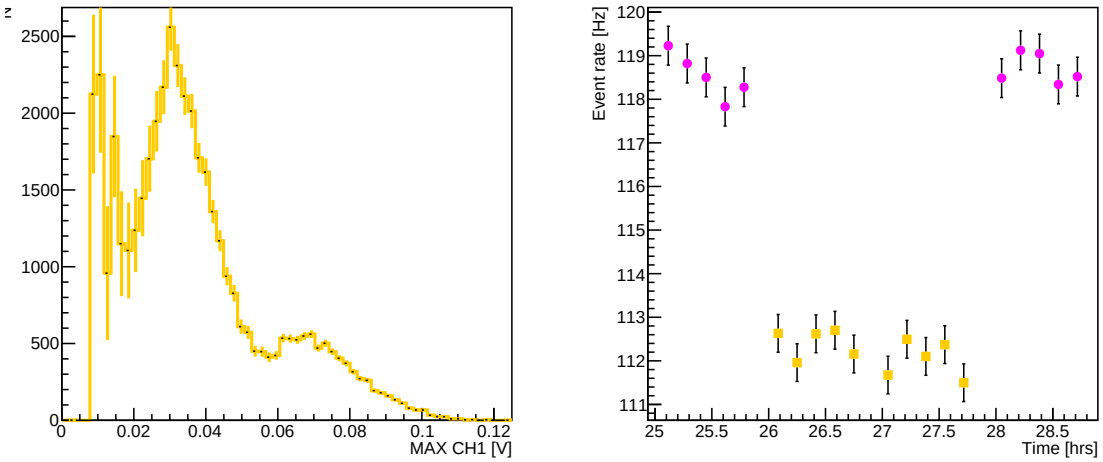

Figure 8.6: Left: signal amplitude spectrum in the polarimeter after background subtraction, made with data from 4 runs with stable beam current. Right: event rate dependence on time; magenta – runs with the gold target, yellow – empty target frame.

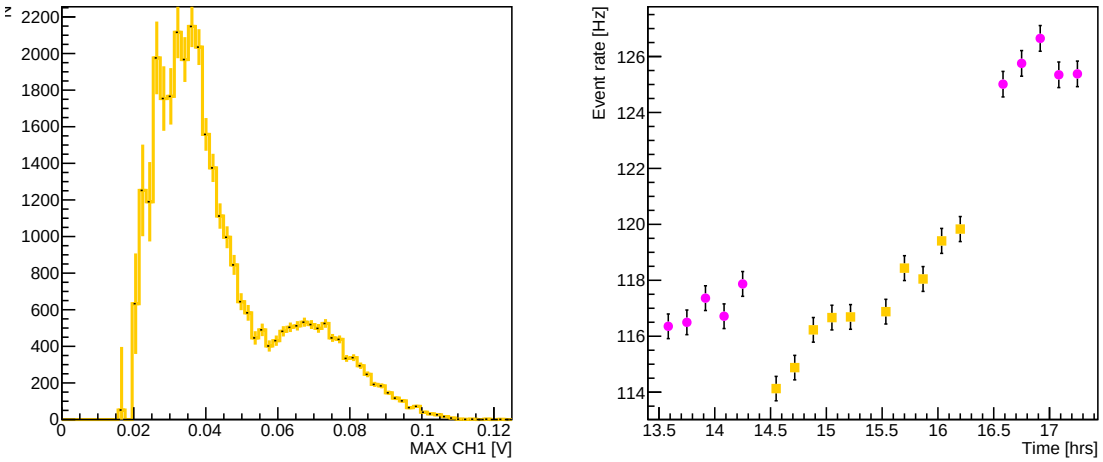

Figure 8.7: Left: signal amplitude spectrum in the polarimeter after background subtraction, made with data from 4 runs with beam current increasing non-linearly with time. Right: event rate dependence on time; magenta – runs with the gold target, yellow – empty target frame.

The beam current read out by the operator from the control display is also indicated with a red line. The black vertical lines mark the moments when the beam current was manually changed between runs. It can be seen that the current is changing quite significantly and that the changes are often non–monotonic.

The background (empty target frame) runs taken with a higher (lower) current than the signal runs, would result in an increased (decreased) asymmetry. The data were corrected by assigning each run a weight equal to the ratio of the average event rate (signal or background) during the whole data taking period to the average event rate during this run. The weights applied to each run in configuration B are shown in Fig. 8.9. The weight variation was in the range $\pm 10\%$, although the momentary variations of the beam current were larger (to some extent they average out during the run). The resulting asymmetry correction for the beam current instability is, however, negligible (order of 10^{-4}). The final asymmetry turns out to be insensitive to this effect as the random changes of the beam current average out to a large extent when data from all runs are combined.

During the data acquisition period in configuration A the run duration was reduced to 15 minutes (in comparison to 1 hour in configuration B) in order to further decrease the sensitivity to beam current changes.

8.6. Finite aperture of the collimators

The collimators between the Møller (beryllium) and Mott (gold) target accept events in the $\pm 1.5^\circ$ scattering angle range around the symmetric scattering angle of 26.75°. Due to the finite angular acceptance, Møller electrons reaching the polarimeter are not mono–energetic. Their energy range can be obtained for a given angular acceptance from a simple kinematical calculation; the result is shown in Fig. 8.10. It can be seen that the energy varies from 1.4 to 1.6 MeV for the scattering angles in the $\pm 1.5^\circ$ range around the symmetric scattering angle of 26.75°.

The theoretical Møller cross section dependence on the scattering angle is shown in Fig. 8.11. The variation of the cross section in the range of interest is approx. 7.9%. The histogram of the Monte Carlo-generated scattering angles is shown in Fig. 8.12. It can be seen that even though the distribution is slightly non–uniform, the mean scattering angle is practically the same as the nominal symmetric scattering angle (26.73° vs 26.75°).

8.7. Finite thickness of the Møller target

Møller scattering took place in a relatively thick target (100 μm), while the theoretical predictions refer to the scattering off an isolated electron. As a result of multiple scattering off atomic nuclei, the passage of electrons through the target material affects their state in two ways: it causes depolarization and alters the kinematics. The first effect was estimated with a Monte Carlo simulation taking into account the polarization transfer in Mott scattering; the depolarization in the passage of 3 MeV electrons through 100 μm of beryllium is negligible (below 0.1%) in the case of the electrons

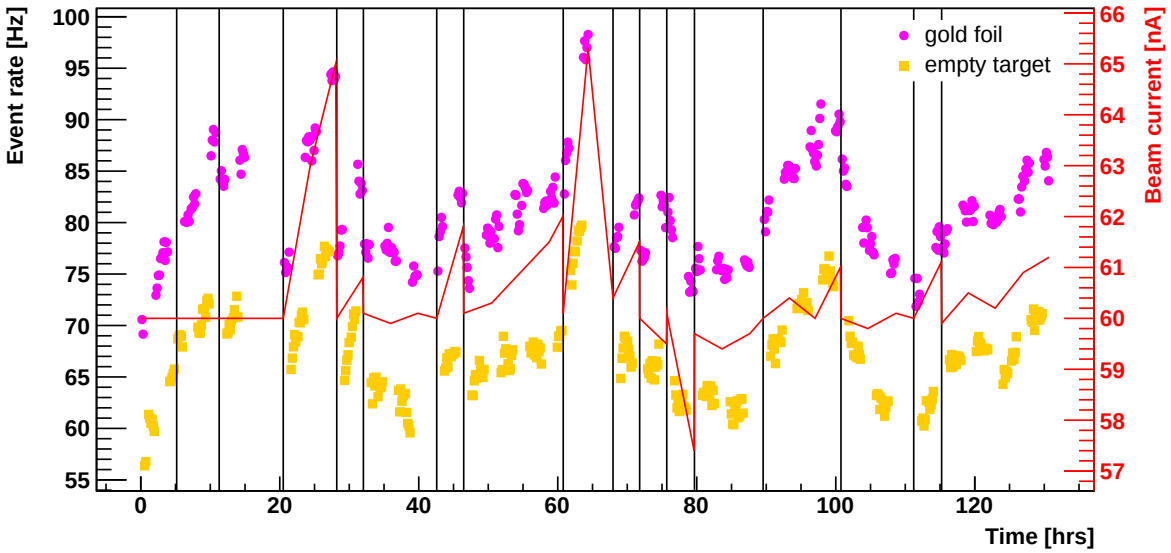

Figure 8.8: Points: event rate dependence on time; magenta – runs with the gold target, yellow – empty target frame. Red line: beam current. Black lines: moments of manual beam current changes.

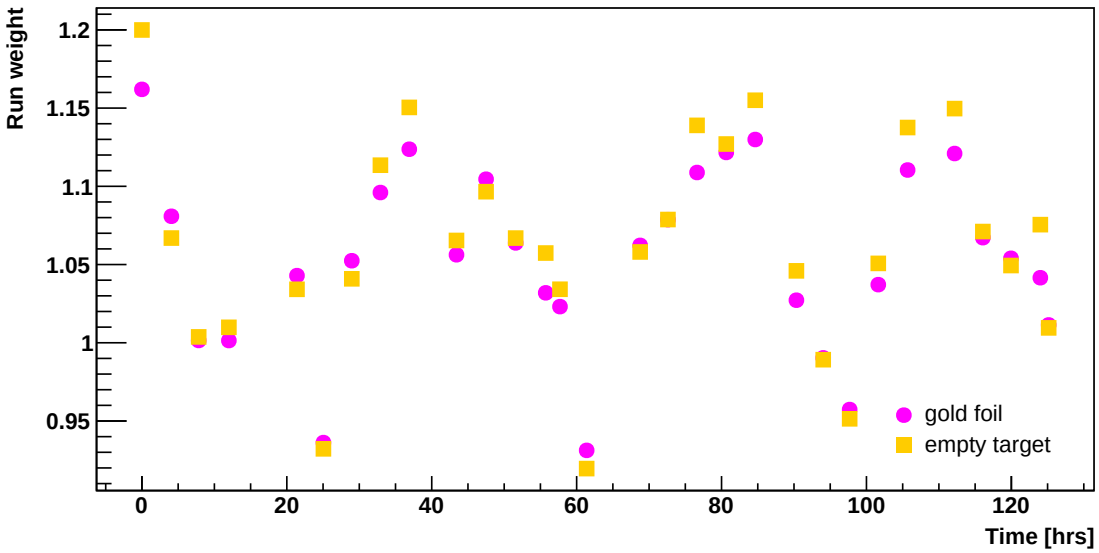

Figure 8.9: Run weights correcting the current instability; magenta – runs with the gold target, yellow – empty target frame.

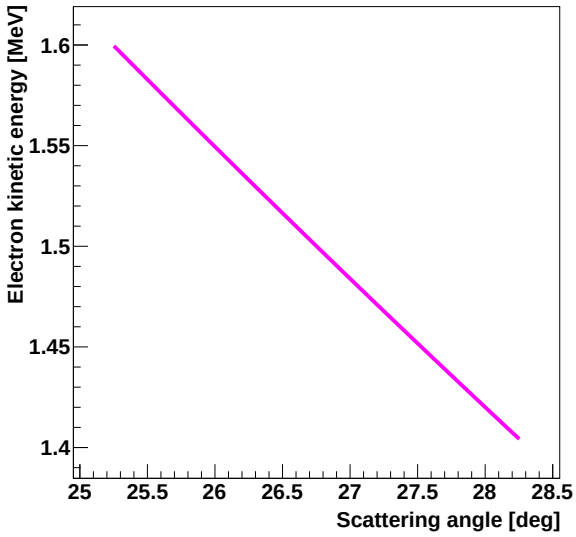

Figure 8.10: Theoretical dependence of the Møller electron kinetic energy on the scattering angle for a 3 MeV incident beam. The scattering angle range in the plot corresponds to the acceptance of the collimators.

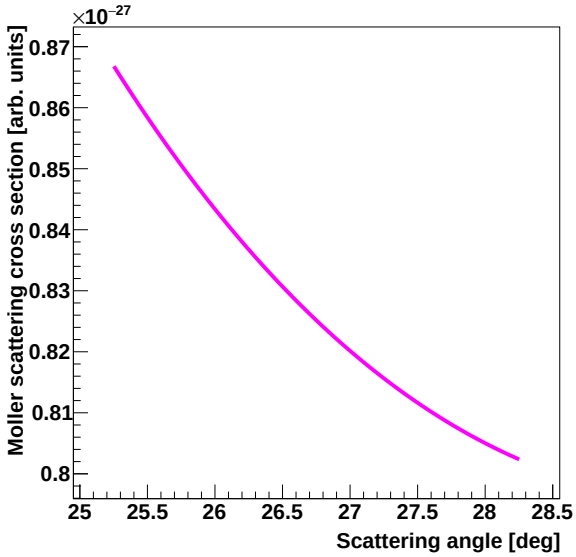

Figure 8.11: Theoretical dependence of the Møller scattering cross section on the scattering angle for a 3 MeV incident beam. The scattering angle range in the plot corresponds to the acceptance of the collimators.

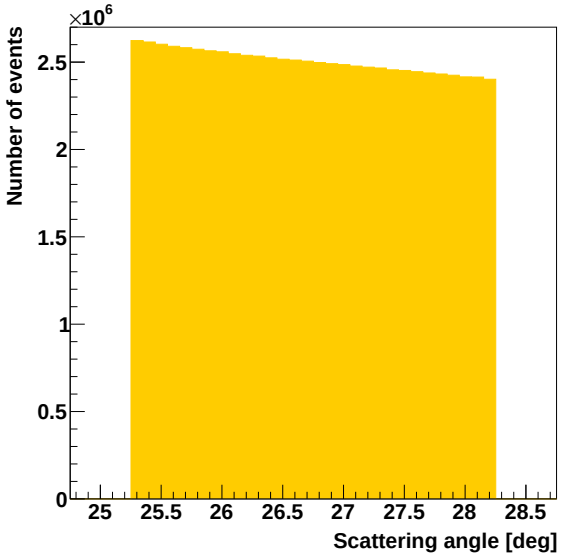

Figure 8.12: Histogram of the scattering angle sampled with the Møller scattering generator for a 3 MeV incident beam. The mean scattering angle is 26.73°, while the symmetric scattering angle is 26.75°.

that are scattered at small angles (see Section 6.3.3). The kinematic effect of multiple scattering is more significant, as it leads to the broadening of the energy (or angular) range of accepted Møller scattering events. However, since the polarization transfer dependence on the scattering angle is approximately linear, and the analyzing power almost constant in the considered energy range, the impact on the final experiment result was found to be negligible.

8.8. Beam position

The shift of the beam spot position with respect to the geometrical center of the beryllium target would affect the kinematic range of events accepted by the collimators. This effect is particularly important if the beam is off center in the Møller scattering plane. In this case, due to the scattering geometry, the average energy of Møller electrons is different from the design value of 1.5 MeV. The upper limit on this energy difference was estimated with a Monte Carlo simulation as 0.04 MeV for ±1 mm beam position shift in the Møller scattering plane (cf. Section 6.4.3). The change of the polarization transfer corresponding to this energy variation was determined from the theoretical predictions and amounts to approx. ±0.013.

8.9. Scattering off the collimators

If the beam was perfectly focused in the center of the beryllium target, it would be extremely unlikely for an electron, scattered outside of the nominal angular acceptance of the collimators, to scatter off the collimator surface and reach the polarimeter.

According to a Monte Carlo simulation, only about 0.1% of electrons reaching the Mott target would fall into that category. However, taking into account the real beam spot diameter of approx. 1.5 mm and beam position shift up to 1 mm, the simulated fraction of such events might be as high as 4.2% in the most pessimistic scenario. The systematic uncertainty related to this effect was estimated by assuming that the electrons scattered off the collimators are completely depolarized, which allowed us to calculate the upper limit on the asymmetry reduction. The upper limit on the contribution to the asymmetry is approx. -4.4% of the measured asymmetry value.

8.10. Alignment of the experimental setup

As the Mott polarimetry method is sensitive only to the polarization-vector component perpendicular to the scattering plane (according to Eq. (3.4)), there is a systematic uncertainty related to the possible rotation of the polarization vector with respect to the Mott scattering plane. Such rotation can be caused by two effects: rotation of the incoming-beam polarization and misalignment of the experimental setup (rotation of the Mott scattering plane with respect to the polarization vector).

According to the calculations, typical magnetic fields used to adjust the beam-spot position on the target lead to a rotation of the polarization vector much below 1 deg. The detector components were aligned with millimeter precision, which corresponds to a possible rotation of the Mott scattering plane of a similar order. Since the asymmetry is proportional to the cosine of the rotation angle, small rotations of the order of 1 deg are negligible compared to the other sources of uncertainty.

8.11. False asymmetries

Count-rate asymmetries calculated for the empty-target runs collected with the beam trigger were found to be 0.0044 ± 0.0029 and 0.0188 ± 0.0057, for configurations A and B, respectively. The empty-target background might have a nonzero asymmetry due to the fact that there is a small but nonzero analyzing power in electron scattering off the aluminum target frame.

Thanks to higher statistics, the empty-target asymmetry could be measured with a much better precision in the energy range corresponding to Møller electrons. The combined asymmetry, Eq. (3.3), obtained with the Møller trigger was 0.0002 ± 0.0005 in configuration A. Thanks to the fact that the beam polarization orientation was reversed periodically, it can be checked if the single-counter results, Eq. (3.2), which are more likely to be sensitive to false asymmetries, are also in agreement with zero. The single-counter asymmetry values were 0.0033 ± 0.0007 and 0.0037 ± 0.0008, for counter L and R, respectively, which indicates that there was a small false asymmetry in the experimental setup that cancels out when when data from two detectors are combined. A small change of the beam position in the direction perpendicular to the beam polarization direction is the most likely explanation of the observed asymmetry with respect to the beam-polarization reversal.

In configuration B, the empty-target asymmetry with the Møller trigger was $0.0059\pm$

0.0008, in perfect agreement with the single-counter asymmetry values of 0.0060 ± 0.0010 and 0.0059 ± 0.0012. The cancellation of false asymmetries might not take place in this configuration because the detectors were not placed opposite to each other. According to the Monte Carlo simulation, a 0.2 mm difference between the beam positions for opposite polarizations would produce an asymmetry in the intensity of the background electrons scattered off the collimators of approx. 0.0063 (i.e., of the same order as the experimental value). The corresponding asymmetry calculated for all electrons reaching the Mott target (most of which are not scattered off the collimators, cf. Section 8.9) would be, however, more than a factor of 5 lower. It is thus reasonable to assume that the false asymmetry in the signal data is approx. 1/5 of the measured empty-target asymmetry, which was included in the systematic uncertainty for configuration B. This can be considered as a conservative estimate, as the contribution of this false asymmetry should partly cancel out in the polarization ratio.

8.12. Radiative corrections

The magnitude of the radiative corrections to Mott scattering is expected to be increasing with energy [68] and might produce a significant contribution to the effective analyzing power with respect to the Monte Carlo-generated value. However, since the systematic uncertainty of the Monte Carlo predictions was estimated by comparing the simulated and measured values, this effect is already included in the uncertainty.

In the case of Møller scattering, the radiative corrections were estimated following the calculations of Tsai [69]. At 3 MeV, the correction to the cross section is below 1%; therefore, in our experimental conditions, this effect can be neglected compared to the other sources of uncertainty (the overall uncertainty of the effective Sherman function is 4% at 3 MeV and 7% at 1.5 MeV).

The relevant contributions to the polarization value uncertainties, which were included in the final results presented in this work, are summarized in Table 8.1.

Table 8.1: Summary of the individual uncertainties contributing to the total uncertainty of the beam polarization and the Møller electrons polarization in configuration A (values in configuration B are given in parentheses).

	beam polarization		**Møller electrons polarization**	
analyzing power[1]	0.034	(0.033)	0.024	(0.018)
cuts	0.010	(0.010)	0.010	(0.010)
beam position	—	(—)	0.013	(0.013)
scattering off the collimators[1]	0.019	(0.018)	0.007	(0.006)
false asymmetry[1]	—	(0.021)	—	(0.006)
total systematic	**0.040**	**(0.044)**	**0.030**	**(0.026)**
statistical	0.013	(0.017)	0.022	(0.026)
total	**0.042**	**(0.047)**	**0.037**	**(0.037)**

[1]Partly cancels out in the polarization ratio.

Chapter 9

Final results and conclusions

The final results regarding the polarization of beam and Møller electrons, the polarization transfer, and the experimental limits on the spin correlation function in Møller scattering, are summarized in this chapter. Most of these results were published in [31].

9.1. Determination of the final result

9.1.1. Beam polarization

The beam polarization values were calculated using Eqs. (3.3) and (3.4) from the measured numbers of events, assuming the Monte Carlo value of the effective Sherman function $S^{\text{beam}} = 0.0847 \pm 0.0034$. The results listed in Table 9.1 were obtained by counting events in the right half of the beam peak. According to the Monte Carlo simulation, the change of beam polarization in Mott scattering off beryllium at an angle of 26.75° is negligible (below 0.3%, cf. Section 6.3.3).

The beam polarization was independently measured at 3.5 MeV with the MAMI Mott polarimeter [50] operating directly on the beam; the results from both sources can be compared in order to verify the correctness of the measurement, as well as the accuracy of the Monte Carlo predictions for the analyzing power. The results from the MAMI polarimeter, 0.835 ± 0.020 and 0.806 ± 0.020, for the periods of data acquisition in configurations A and B, respectively, are in agreement within 1 σ with the results presented in Table 9.1. While still being consistent with statistical fluctuations, the slightly lower MAMI measurement results could also follow from the presence of the 2POL polarimeter installed directly behind the MAMI Mott polarimeter on the same beam extraction, which might cause additional background.

All beam polarization results presented above are also in agreement with the typical beam polarization values achieved at MAMI, which which are in the range from 80% to 85%.

9.1.2. Møller polarization

The mean polarization values of Møller electrons were calculated using Eqs. (3.3) and (3.4) from the measured numbers of events, assuming the Monte Carlo value of the effective Sherman function $S^{\text{Møller}} = 0.0886 \pm 0.0063$. The results listed in Table 9.2

Table 9.1: Results of the beam polarization measurements. N_L^{beam} and N_R^{beam} are the numbers of events (after background subtraction and dead time correction) recorded in the L and R detector, respectively. Single-counter asymmetry values A_L^{beam} and A_R^{beam} were obtained from Eq. (3.2) and the combined value A^{beam} from Eq. (3.3). The beam polarization P^{beam} was calculated from A^{beam} and the Monte Carlo value of the effective analyzing power.

	Configuration A	**Configuration** B
N_L^{beam}	$(586.9 \pm 1.3)10^3$	$(561.2 \pm 1.2)10^3$
N_R^{beam}	$(653.4 \pm 1.4)10^3$	$(671.9 \pm 1.3)10^3$
A_L^{beam}	0.0694 ± 0.0023	0.0482 ± 0.0021
A_R^{beam}	0.0748 ± 0.0021	0.0508 ± 0.0019
A^{beam}	0.0721 ± 0.0011	0.0495 ± 0.0010
P^{beam}	0.851 ± 0.042	0.826[1] ± 0.047

[1] In configuration B, the polarization, measured in the direction at an angle of 45° to the Møller scattering plane, was divided by cos(45°) to obtain the total beam polarization, which had an orientation perpendicular to the Møller scattering plane.

Table 9.2: Results of the Møller polarization measurements. $N_L^{\text{Møller}}$ and $N_R^{\text{Møller}}$ are the numbers of events (after background subtraction, dead time correction and event selection) recorded in the L and R detector, respectively. Single-counter asymmetry values $A_L^{\text{Møller}}$ and $A_R^{\text{Møller}}$ were obtained from Eq. (3.2) and the combined value $A^{\text{Møller}}$ from Eq. (3.3). The Møller electrons polarization $P^{\text{Møller}}$ was calculated from $A^{\text{Møller}}$ and the Monte Carlo value of the effective analyzing power.

	Configuration A	**Configuration** B
$N_L^{\text{Møller}}$	$(160.19 \pm 0.69)10^3$	$(166.48 \pm 0.57)10^3$
$N_R^{\text{Møller}}$	$(210.12 \pm 0.69)10^3$	$(227.63 \pm 0.70)10^3$
$A_L^{\text{Møller}}$	0.0291 ± 0.0043	0.0190 ± 0.0034
$A_R^{\text{Møller}}$	0.0309 ± 0.0033	0.0133 ± 0.0031
$A^{\text{Møller}}$	0.0300 ± 0.0019	0.0161 ± 0.0016
$P^{\text{Møller}}$	0.339 ± 0.037	0.258[2] ± 0.037

[2] In configuration B, the polarization, measured in the direction at an angle of 45° to the Møller scattering plane, was divided by cos(45°) to obtain the total Møller electrons polarization, which, according to the theoretical predictions, has an orientation perpendicular to the Møller scattering plane.

Table 9.3: Polarization transfer (length of the transverse polarization vector component in the final state of symmetric Møller scattering divided by the initial beam polarization). Experimental results are compared to the theoretical predictions [21].

	Configuration A	**Configuration** B
experiment	0.398 ± 0.046	0.312 ± 0.046
theory	0.399	0.382

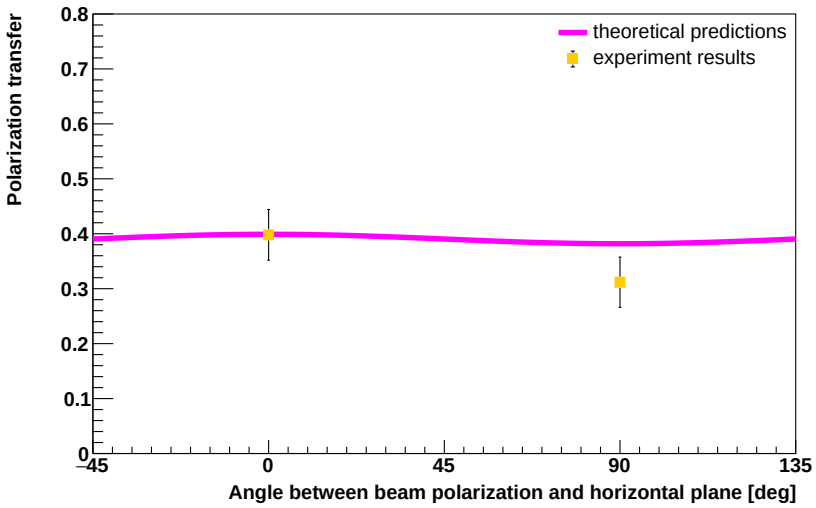

Figure 9.1: Polarization transfer (length of the transverse polarization vector component in the final state of symmetric Møller scattering divided by the initial beam polarization), plotted as a function of the angle between the beam polarization vector and the Møller scattering (horizontal) plane. Solid line – theoretical predictions [21], points – experimental data.

were obtained by counting events in the full Møller peak (using the cuts marked in Fig. 7.32).

9.1.3. Polarization transfer

When taking systematic uncertainties into account, the optimal approach to measure the polarization transfer is to define it as the ratio of electron polarizations before and after the scattering. This way, the impact of some systematic effects is partly suppressed (compared to an absolute polarization measurement), since their contributions to both polarization measurements are similar. This applies, in particular, to the systematic uncertainties of the Monte Carlo predictions and of the target thickness, which affect the effective Sherman function values at 1.5 and 3 MeV in a similar way.

In Table 9.3, the final polarization transfer measurement results, $P^{\text{Møller}}/P^{\text{beam}}$ (cf. Tables 9.1 and 9.2) are compared to the theoretical predictions [21] (predicted ratio of polarizations in the initial and final states of Møller scattering). The experimental values in both configurations were found to be in agreement with the theoretical predictions.

Table 9.4: Limits on the correlation function, Eq. (2.17), derived from the experimental results on the polarization transfer in Møller scattering presented in Table 9.3, compared to the theoretical predictions for the correlation function [21].

	Configuration A	**Configuration** B
experimental limit	$> -0.204 \pm 0.092$	$> -0.559 \pm 0.065$
relativistic prediction	0.025	-0.011
singlet state	-0.595	-0.797

In both experimental configurations, Møller scattering took place in the horizontal plane, and the beam polarization was either horizontal or vertical. It should allow us to verify the dependence of the polarization transfer on the angle between the beam polarization vector and the Møller scattering plane, as shown in Fig. 9.1. Unfortunately, the present experimental uncertainty is higher than the small expected amplitude of the angular dependence. Nevertheless, one can conclude that the experimental points are in agreement with the predicted theoretical dependence.

The experimental result regarding polarization transfer in Møller scattering can be also used to derive the experimental limit on the correlation function. The lower limit on the correlation function is compared to the theoretical predictions of relativistic quantum mechanics and predictions for the singlet state (nonrelativistic limit) in Table 9.4. It can be seen that the nonrelatvistic prediction is excluded by the experimental result at a level of above 4 σ in configuration A and above 3 σ in configuration B. The probabilities of obtaining such values, if the nonrelativistic theory holds, are of the order of 10^{-5} and 10^{-4} in configuration A and B, respectively. The combined probability of obtaining both results in independent measurements is of the order of 10^{-9}, which would correspond to a 6 σ deviation.

Both theoretical predictions are also plotted together with the theoretical and experimental limits in Fig. 9.2 illustrating the dependence of the correlation function on energy. It confirms that the 3 MeV beam energy is appropriate for distinguishing between the nonrelativistic and relativistic predictions with the present experimental uncertainty.

9.2. Summary and conclusions

Reviewed in these thesis were the theoretical predictions regarding polarization transfer from a polarized beam electron to the electrons after Møller scattering and quantum spin correlations between both electrons in the final state. An additional theoretical analysis showed that the correlation function is closely related to the polarization transfer. Namely, the average polarizations of two electrons in the final state, P_1 and P_2, and the correlation function C must fulfill the condition $-1 + \left|P_1(\vec{a}) + P_2(\vec{b})\right| \leq C(\vec{a},\vec{b}) \leq 1 - \left|P_1(\vec{a}) - P_2(\vec{b})\right|$.

A dedicated experimental setup for the measurement of polarization transfer in Møller scattering was designed and constructed. The Mott polarimetry method was used for the spin-projection measurement. The polarimeter was equipped with SiPM

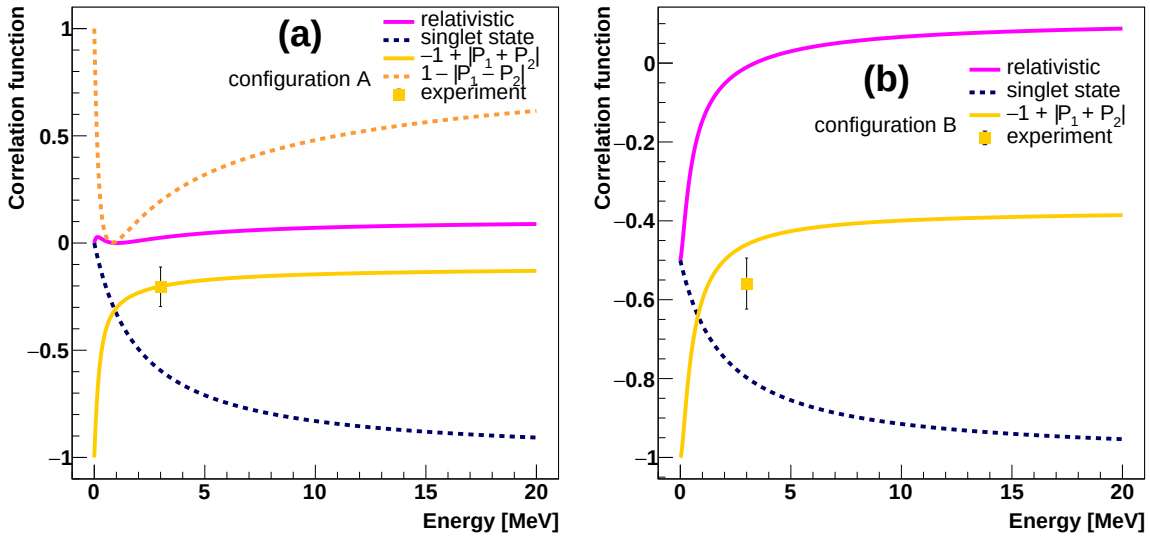

Figure 9.2: Dependence of the theoretical limits on the correlation function obtained from polarization transfer, Eq. (2.17), on beam energy (dashed lines) and experimental lower limits measured at 3 MeV (points), for a pair of electrons originating from Møller scattering with (a) the $\vec{a}$ and $\vec{b}$ vectors (on which the spins are projected) in the Møller scattering plane, (b) $\vec{a}$ and $\vec{b}$ vectors at angles equal to 45° to the Møller scattering plane. The theoretical predictions for the correlation function [20] and predictions for the singlet state (nonrelativistic limit) are shown for comparison (solid lines). The scattering is symmetric with respect to the beam direction.

detectors and a high sampling speed readout, necessary to distinguish signal (coincidence events) from background.

Monte Carlo simulation was used to demonstrate that the electrons detected in a Mott polarimeter may undergo several consecutive scattering events, thus the effective analyzing power cannot be calculated analytically. Therefore, a comprehensive optimization of a Mott-polarimetry measurement requires collecting a large amount of data, either from extensive experimental studies, or from a Monte Carlo simulation taking into account multiple Mott scattering in the passage of electrons through the target material.

A new model of Mott scattering for polarized electrons, which can be used with Geant4 instead of the default electron Coulomb scattering model, was developed [33]. The results of the Monte Carlo simulation agree with experimental values measured in wide ranges of energy and target thickness, which encourages the use of this code to obtain predictions for polarimetry in kinematical regions and conditions (energy, scattering angle, target material and thickness) where no measurements exist.

The effective Sherman function dependence on target thickness, as well as the optimal ranges of target thickness and scattering angle for the polarization transfer experiment were determined [34]. It was found that the target thickness values optimal from the statistics point of view are significantly greater than those typically used in MeV Mott polarimetry.

In the experiment, Møller electrons backscattered off a gold target were observed in the Mott polarimeter. Background events were efficiently suppressed based on the measured amplitude and time information and the remaining background could be subtracted with the use of empty-target data collected at the same time. It was confirmed that a standard Mott polarimeter is a suitable tool for measuring polarization with a divergent stream of Møller electrons despite the high-background environment.

The asymmetry of the polarimeter count rates arising from the beam polarization was measured. The beam polarization, as well as the mean polarization of the electrons in the final state of symmetric Møller scattering, was calculated assuming a Monte Carlo value of the analyzing power. The beam-polarization value was found in good agreement with an independent measurement with the MAMI Mott polarimeter, which confirmed the correct operation of the polarimeter.

The measured polarization transfer, defined as the ratio of polarizations before and after Møller scattering, was compared to the predictions of relativistic quantum mechanics [31]; up to our knowledge it was the first such measurement. The experiment was performed in two experimental configurations corresponding to two orientations of the beam polarization, and both results are in agreement with the theoretical predictions. Whether or not the small difference between the experimental and theoretical results for configuration B, of about 1.5 σ, reflects some real discrepancy can only be assessed in a measurement with increased precision.

The average polarization of electrons in the final state was used to calculate the experimental limits on the correlation function. It was shown that the results of the nonrelativistic calculations are excluded by the experimental result with high significance.

While the present measurement gives valuable insight into the polarization-related effects in relativistic Møller scattering (including the phenomenon of entanglement), the ultimate confirmation of the theory could only be achieved with a full spin-correlation experiment, based on a simultaneous measurement of the spin projections of both electrons in the final state. Such a measurement would be much more challenging; its feasibility, as well as possible improvements towards an optimized experimental setup, are discussed in Appendix A.

The possible violation of the CHSH inequality [72] with relativistic particles [21], which is a topic that gathered considerable attention [73, 74], is also discussed in Appendix A. Such a measurement would require a dedicated accelerator setup providing two polarized beams, but it is shown that the required beam polarization degree is technically attainable at present.

Bibliography

[1] A. Einstein, B. Podolsky, and N. Rosen, Phys. Rev. 47, 777 (1935).

[2] D. Bohm, *Quantum Theory*, Prentice-Hall, Inc., New York (1951).

[3] J. S. Bell, Physics 1, 195 (1964).

[4] A. Aspect, P. Grangier, and G. Roger, Phys. Rev. Lett. 49, 91 (1982).

[5] A. Aspect, J. Dalibard, and G. Roger, Phys. Rev. Lett. 49, 1804 (1982).

[6] P. Caban and J. Rembieliński, Phys. Rev. A 72, 012103 (2005).

[7] P. Caban and J. Rembieliński, Phys. Rev. A 74, 042103 (2006).

[8] P. Caban, J. Rembieliński, and M. Włodarczyk, Phys. Rev. A 77, 012103 (2008).

[9] P. Caban, J. Rembieliński, and M. Włodarczyk, Phys. Rev. A 79, 014102 (2009).

[10] P. Caban, J. Rembieliński, and M. Włodarczyk, Phys. Rev. A 83, 034101 (2011).

[11] P. Caban, J. Rembieliński, P. Witas, and M. Włodarczyk, Phys. Rev. A 83, 032115 (2011).

[12] P. Caban, Phys. Rev. A 77, 062101 (2008).

[13] M. Czachor, Phys. Rev. A 55, 72 (1997).

[14] H. Terashima and M. Ueda, Int. J. Quantum Information 1, 93 (2003).

[15] D. Ahn, H. J. Lee, Y. H. Moon, and S. W. Hwang, Phys. Rev. A 67, 012103 (2003).

[16] M. Lamehi–Rachti and W. Mittig, Phys. Rev. D 14, 2543 (1976).

[17] S. Hamieh et al., J. Phys. G 30, 481 (2004).

[18] H. Sakai et al., Phys. Rev. Lett. 97, 150405 (2006).

[19] P. Caban, J. Rembieliński, and M. Włodarczyk, Phys. Rev. A 88, 022119 (2013).

[20] P. Caban, J. Rembieliński, and M. Włodarczyk, Phys. Rev. A 88, 032116 (2013).

[21] M. Włodarczyk, P. Caban, J. Ciborowski, M. Drągowski, and J. Rembieliński, Phys. Rev. A 95, 022103 (2017).

[22] Ch. Møller, Ann. Phys. 406, 531 (1932).

[23] Ya. B. Zeldovich, J. Exp. Theor. Phys. 36, 964 (1959).

[24] P. L. Anthony et al., Phys. Rev. Lett. 95, 081601 (2005).

[25] J. Benesch et al., *The MOLLER Experiment: An Ultra-Precise Measurement of the Weak Mixing Angle Using Møller Scattering*, JLAB-PHY-14-1986 (2014).

[26] P. S. Cooper et al., Phys. Rev. Lett. 34, 1589 (1975).

[27] K. Aulenbacher, E. Chudakov, D. Gaskell, J. Grames, and K. D. Paschke, Int. J. Mod. Phys. E 27, 1830004 (2018).

[28] J. M. Grames et al., Phys. Rev. ST Accel. Beams 7, 042802 (2004).

[29] T. J. Gay and F. B. Dunning, Rev. Sci. Instrum. 63, 1635 (1992).

[30] K. Bodek et al., AIP Conf. Proc. 1563, 208 (2013).

[31] M. Drągowski et al., Phys. Rev. D 104, 092011 (2021).

[32] A. Jankowiak, Eur. Phys. J. A 28, s01, 149 (2006).

[33] M. Drągowski, M. Adamus, G. Weber, and M. Włodarczyk, Nucl. Instrum. Methods Phys. Res. B 488, 37 (2021).

[34] M. Drągowski, M. Adamus, V. Tioukine, and A. F. Żarnecki, Nucl. Instrum. Methods Phys. Res. B 535, 1 (2023).

[35] C. J. Powell, J. Electron Spectrosc. Relat. Phenom. 185, 1 (2012).

[36] D. Bote, F. Salvat, A. Jablonski, and C. J. Powell, At. Data Nucl. Data Tables 95, 871 (2009).

[37] R. Beigang, D. Schmidt, and P. J. West, J. Phys. Colloques 44, C7-229 (1983).

[38] J. D. Bjorken, S. Drell, *Relativistic Quantum Mechanics*, McGraw-Hill (1964).

[39] N. F. Mott, Proc. R. Soc. A 124, 425 (1929).

[40] J. Kessler, *Polarized Electrons. Second Edition*, Springer, Berlin (1985).

[41] N. Sherman, Phys. Rev. 103, 1601 (1956).

[42] F. Salvat, A. Jablonski, and C. J. Powell, Comput. Phys. Commun. 165, 157 (2005).

[43] A. Jablonski, F. Salvat, C.J. Powell, NIST Electron Elastic-Scattering Cross-Section Database, Version 3.1, Standard Reference Data Program Database 64, Available from: http://www.nist.gov/srd/nist64.cfm

[44] N.F. Mott, H.S.W. Massey, *The Theory of Atomic Collisions*, third edition, Oxford University Press, London (1965).

[45] B. Hahn, D.G. Ravenhall, R. Hofstadter, *Phys. Rev.* 101, 1131 (1956).

[46] J.P. Desclaux, *Comput. Phys. Commun.* 9, 31 (1975).

[47] Ch. Kittel, *Introduction to Solid State Physics*, fifth edition, John Wiley and Sons, New York (1976).

[48] G. D. Fletcher, T. J. Gay, and M. S. Lubell, Phys. Rev. A 34, 911 (1986).

[49] S. Agostinelli et al., Nucl. Inst. Meth. in Phys. Res. A 506, 250 (2003).

[50] V. Tioukine, K. Aulenbacher, and E. Riehn, Rev. Sci. Instrum. 82, 033303 (2011).

[51] ON Semiconductor, *Biasing and Readout of ON Semiconductor SiPM Sensors*, Application note AND9782/D Rev. 3, Semiconductor Components Industries, LLC (2019).

[52] ON Semiconductor, *ArrayJ Series. Silicon Photomultiplier (SiPM) High Fill-Factor Arrays*, ARRAYJ-SERIES/D Rev. 4, Semiconductor Components Industries, LLC (2018).

[53] ON Semiconductor, *J-Series SiPM Sensors*, MICROJ-SERIES/D Rev. 6, Semiconductor Components Industries, LLC (2018).

[54] S. Ritt, 2008 IEEE Nuclear Science Symposium Conference Record, 1512 (2008).

[55] S. Ritt, *DRS4 Evaluation Board User's Manual Rev. 5.1*, Paul Scherrer Institute (2016).

[56] Sung Hun Kim et al., IEEE Trans. Nucl. Sci. 62, 451 (2015).

[57] S. Qiao, A. Kakizaki, Rev. Sci. Instrum. 68, 4017 (1997).

[58] M.A. Khakoo et al., Phys. Rev. A 64, 052713 (2001).

[59] G. Weber et al., Nucl. Instr. Meth. Phys. Res. B 279, 155 (2012).

[60] M. Drągowski et al., Nucl. Instr. Meth. Phys. Res. B 389-390, 48 (2016).

[61] T. J. Gay et al., Rev. Sci. Instrum. 63, 114 (1992).

[62] H. Wegener, Z. Phys. 151, 252 (1958).

[63] L. Braicovich and B. De Michelis, Nuovo Cimento 58B, 269 (1968).

[64] J. Sromicki et al., Phys. Rev. Lett. 82, 57 (1999).

[65] M. Steigerwald, AIP Conf. Proc. 570, 935 (2001).

[66] J. M. Grames et al., Phys. Rev. C 102, 015501 (2020).

[67] T. Kohashi, M. Konoto, and K. Koike, Jpn. J. Appl. Phys. 45, 6468 (2006).

[68] X. Roca-Maza, EPL 120, 33002 (2017).

[69] Y. S. Tsai, Phys. Rev. 120, 269 (1960).

[70] M. Morhac et al., Nucl. Instr. Meth. Phys. Res. A 443, 108 (2000).

[71] T. Saito, *Experimental Test of Bell's Inequality via the* ^{1}*H(d,* ^{2}*He)n Reaction*, Doctoral dissertation, University of Tokio (2004).

[72] J. F. Clauser, M. A. Horne, A. Shimony and R. A. Holt, Phys. Rev. Lett. 23, 880 (1969).

[73] J. B. Araujo, B. Hiller, I. G. da Paz, M. M. Ferreira, Jr., M. Sampaio, and H. A. S. Costa, Phys. Rev. D 100, 105018 (2019).

[74] J. D. Fonseca, B. Hiller, J. B. Araujo, I. G. da Paz, and M. Sampaio, Phys. Rev. D 106, 056015 (2022).

[75] T. Nishitani et al., J. Appl. Phys. 97, 094907 (2005).

[76] Yu. A. Mamaev et al., Appl. Phys. Lett. 93, 081114 (2008).

[77] X. Jin et al., Appl. Phys. Lett. 105, 203509 (2014).

Appendix A

Measurement of spin correlations

A.1. Experimental setup

The proposed experimental setup for the measurement of spin correlations is very similar to the one used in the polarization transfer measurement, with the exception that both legs are equipped with identical Mott polarimeters. This way, the simultaneous measurement of the spin projections of both electrons is possible. There is no tagging counter in this configuration. Nevertheless, the signal events are still selected by a coincidence of two signals, one in each polarimeter.

Eq. (3.4) allows one to calculate the polarization of a single particle. However, in the spin-correlation experiment the joint probabilities of obtaining given spin projections of both particles have to be measured. They can be calculated from the two-detector count rates according to the matrix equation given by Saito [71]

$$\begin{pmatrix} P_{++} \\ P_{--} \\ P_{+-} \\ P_{-+} \end{pmatrix} = \frac{1}{4S_{\text{eff}}(\vec{a})S_{\text{eff}}(\vec{b})} \begin{pmatrix} c_{++} & c_{--} & -c_{+-} & -c_{-+} \\ c_{--} & c_{++} & -c_{-+} & -c_{+-} \\ -c_{+-} & -c_{-+} & c_{++} & c_{--} \\ -c_{-+} & -c_{+-} & c_{--} & c_{++} \end{pmatrix} \begin{pmatrix} \tilde{N}_{LL} \\ \tilde{N}_{RR} \\ \tilde{N}_{LR} \\ \tilde{N}_{RL} \end{pmatrix}, \tag{A.1}$$

where $\tilde{N}_{LL}$, $\tilde{N}_{RR}$, $\tilde{N}_{LR}$ and $\tilde{N}_{RL}$ are the normalized count rates of coincidences (e.g., $\tilde{N}_{LL} = N_{LL}/(N_{LL} + N_{RR} + N_{LR} + N_{RL})$, $S_{\text{eff}}(\vec{a})$ and $S_{\text{eff}}(\vec{b})$ denote the effective Sherman function for Mott scattering in the first and second polarimeter (measuring spin projections on directions $\vec{a}$ and $\vec{b}$, respectively), and the coefficients $c_{\pm\pm}$ are defined as

$$c_{\pm\pm} = (1 \pm S_{\text{eff}}(\vec{a}))(1 \pm S_{\text{eff}}(\vec{b})), \tag{A.2}$$

(e.g., $c_{-+} = (1 - S_{\text{eff}}(\vec{a}))(1 + S_{\text{eff}}(\vec{b}))$).

The matrix in Eq. (A.1) describes the most general case of arbitrary effective Sherman function values in both polarimeters. When both polarimeters are identical, which is the case in the proposed experiment design, the effective Sherman function takes, on average, the same value in both polarimeters. In this case $c_{+-} = c_{-+}$ and Eq. (A.1)

can be rewritten in a simpler form,

$$\begin{pmatrix} P_{++} \\ P_{--} \\ P_{+-} \\ P_{-+} \end{pmatrix} = \frac{1}{4S_{\text{eff}}^2} \begin{pmatrix} (1+S_{\text{eff}})^2 & (1-S_{\text{eff}})^2 & -(1-S_{\text{eff}}^2) & -(1-S_{\text{eff}}^2) \\ (1-S_{\text{eff}})^2 & (1+S_{\text{eff}})^2 & -(1-S_{\text{eff}}^2) & -(1-S_{\text{eff}}^2) \\ -(1-S_{\text{eff}}^2) & -(1-S_{\text{eff}}^2) & (1+S_{\text{eff}})^2 & (1-S_{\text{eff}})^2 \\ -(1-S_{\text{eff}}^2) & -(1-S_{\text{eff}}^2) & (1-S_{\text{eff}})^2 & (1+S_{\text{eff}})^2 \end{pmatrix} \begin{pmatrix} \tilde{N}_{LL} \\ \tilde{N}_{RR} \\ \tilde{N}_{LR} \\ \tilde{N}_{RL} \end{pmatrix}. \tag{A.3}$$

One finds by simple algebraic transformations of Eq. (A.3) that the probability of obtaining the same spin projections of both electrons is

$$P_{++} + P_{--} = \frac{1}{2S_{\text{eff}}^2} \left((1+S_{\text{eff}}^2)(\tilde{N}_{LL} + \tilde{N}_{RR}) - (1-S_{\text{eff}}^2)(\tilde{N}_{LR} + \tilde{N}_{RL}) \right), \tag{A.4}$$

and the probability of obtaining opposite spin projections of both electrons is

$$P_{+-} + P_{-+} = \frac{1}{2S_{\text{eff}}^2} \left((1+S_{\text{eff}}^2)(\tilde{N}_{LR} + \tilde{N}_{RL}) - (1-S_{\text{eff}}^2)(\tilde{N}_{LL} + \tilde{N}_{RR}) \right). \tag{A.5}$$

It can be seen that, thanks to the symmetry of the experimental arrangement, the correlation function $C = P_{++} + P_{--} - (P_{+-} + P_{-+})$, calculated from Eqs. (A.4) and (A.5), takes a trivial form

$$C = \frac{1}{S_{\text{eff}}^2} (\tilde{N}_{LL} - \tilde{N}_{LR} - \tilde{N}_{RL} + \tilde{N}_{RR}). \tag{A.6}$$

The first-choice scenario for the spin correlation experiment would correspond to configuration A, with horizontal spin-projection directions of both electrons. The direct realization of configuration B, with pairs of detectors at an angle of 45° to the Møller scattering plane, as shown in Fig. A.1(a), would be less suitable due to the high level of background in the detectors located close to the beam pipe.

The problem with background in configuration B can be worked around to some extent, taking advantage of the additional symmetry of configuration B, which was used in the polarization transfer experiment to place the detectors farther away from the beam. Taking into account the normalization condition (sum of probabilities is equal to 1), not all probabilities have to be known in order to calculate the correlation function. In can be written in the following equivalent form:

$$C = 2(P_{++} + P_{--}) - 1 = 1 - 2(P_{+-} + P_{-+}), \tag{A.7}$$

and in terms of count rates

$$C = \frac{1}{S_{\text{eff}}^2} \left(2(\tilde{N}_{LL} + \tilde{N}_{RR}) - 1 \right) = \frac{1}{S_{\text{eff}}^2} \left(1 - 2(\tilde{N}_{LR} + \tilde{N}_{RL}) \right). \tag{A.8}$$

Therefore, in principle it is sufficient to measure the count rates of two coincidences instead of four. However, the count rates must be normalized, thus the total number of counts in four detectors (four coincidences) has to be known, for example from the measurement in configuration A.

The two-polarimeter configuration with detector locations subject to the lowest level of background is shown in Fig. A.2. The $N_{\lambda\rho}$ coincidence in Fig. A.2 is the same

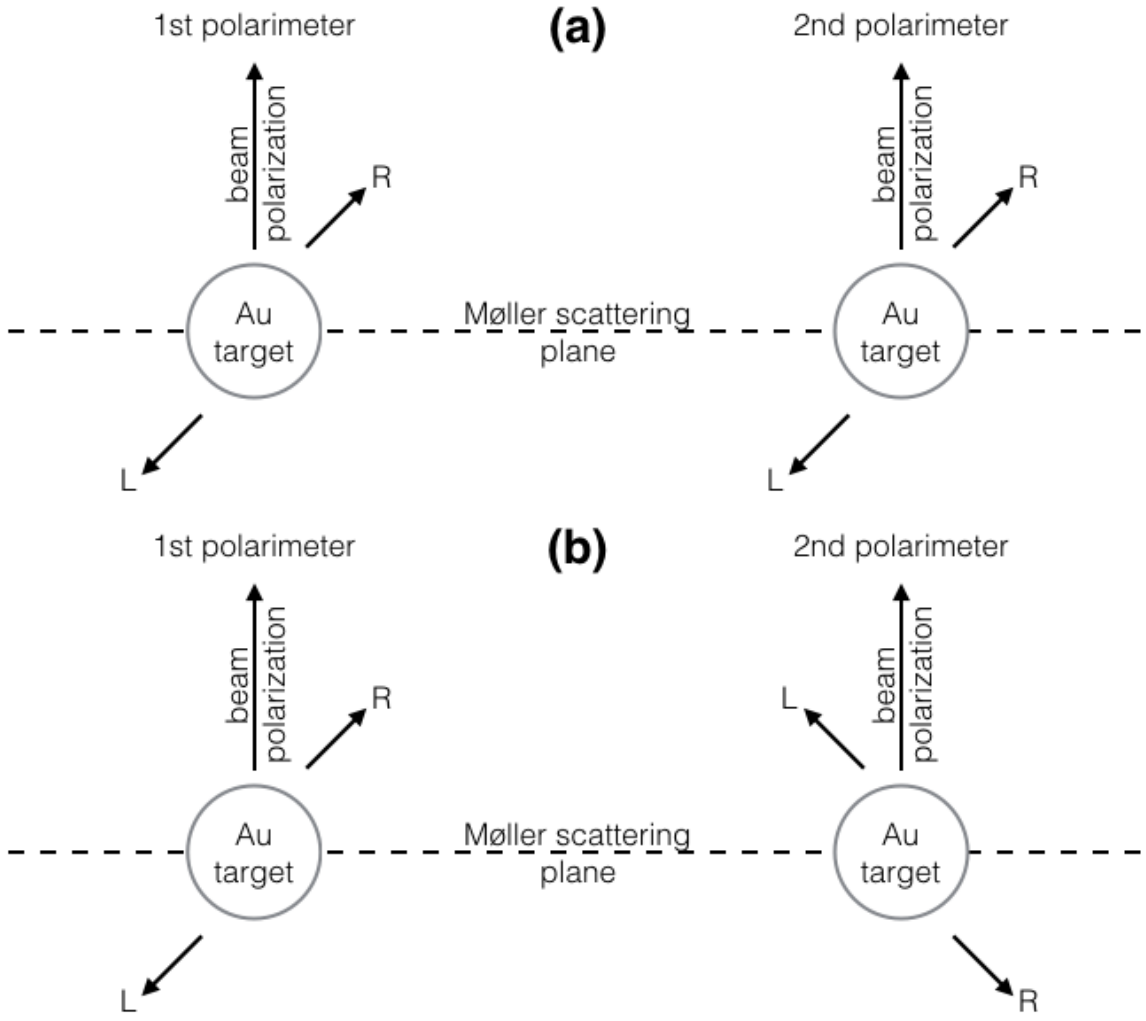

Figure A.1: Schematic illustration of the spin-correlation experiment (cross sections of both polarimeters in the gold-targets planes, perpendicular to the directions of the Møller-electrons streams) in configuration B (45° angle between the Møller and Mott scattering planes). L and R denote the locations of the detectors in the Mott polarimeters, with both spin-projection directions at an angle of 45° to the Møller scattering plane (default arrangement of the detectors) (a), spin-projection directions at 45° and 135° to the Møller scattering plane (b).

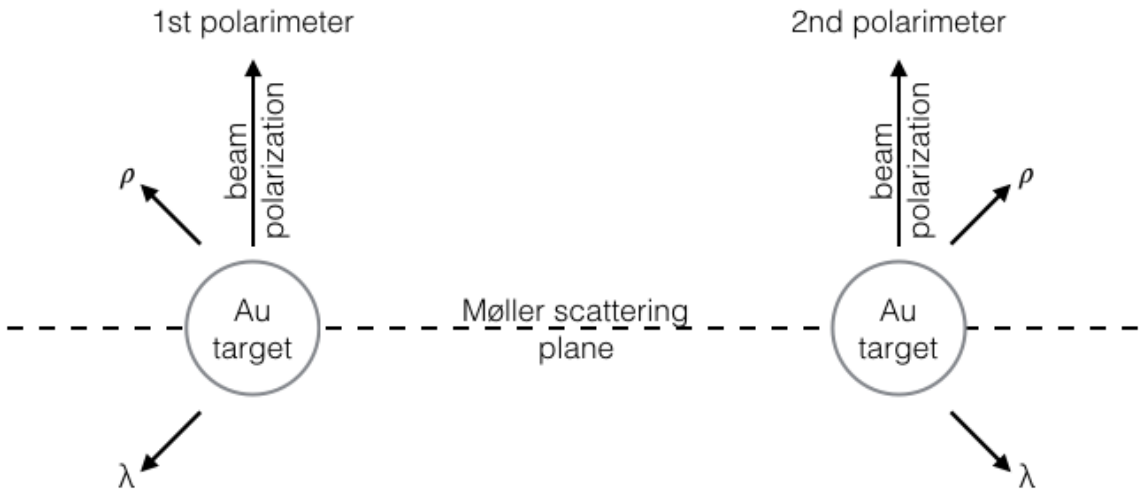

Figure A.2: Schematic illustration of the spin-correlation experiment (cross sections of both polarimeters in the gold-targets planes, perpendicular to the directions of the Møller-electrons streams) in configuration B with detector locations, denoted by λ and ρ, minimizing external background.

as the N_{LR} coincidence in the default configuration shown in Fig. A.1(a). Similarly, the $N_{\lambda\lambda}$ number in the layout shown in Fig. A.2 is the same as N_{LR} in the configuration shown in Fig. A.1(b) (i.e., with the first spin projection direction at an angle of 45° and the second spin projection direction at 135° to the Møller scattering plane).

The other two coincidences, which can be measured in the experiment illustrated in Fig. A.2, $N_{\rho\lambda}$ and $N_{\rho\rho}$, correspond to the N_{RL} numbers with both spin projection directions at 315° and with the first spin projection direction at 315° and the second spin projection direction at 225° to the Møller scattering plane, respectively. Thanks to the symmetry, the P_{-+} probabilities are equal in the default arrangements of the $\vec{a}$ and $\vec{b}$ vectors shown in Fig. A.1 and in the configuration mirrored with respect to the Møller scattering plane (45° corresponds to 315° and 135° corresponds to 225° angle between the spin projection direction and the Møller scattering plane). P_{-+} in all four configurations is shown in Fig. A.3. Therefore, the detector layout proposed in Fig. A.2 not only allows one to reduce the background, but also to measure the spin correlation function for two configurations of the $\vec{a}$ and $\vec{b}$ vectors simultaneously,

$$C(45°, 45°) = C(315°, 315°) = \frac{1}{S_{\text{eff}}^2}\left(1 - 2(\tilde{N}_{\lambda\rho} + \tilde{N}_{\rho\lambda})\right), \tag{A.9a}$$

$$C(45°, 135°) = C(315°, 225°) = \frac{1}{S_{\text{eff}}^2}\left(1 - 2(\tilde{N}_{\lambda\lambda} + \tilde{N}_{\rho\rho})\right), \tag{A.9b}$$

where $C(\alpha, \beta)$ denotes the spin correlation function for the angles α and β between the Møller scattering plane and the $\vec{a}$ and $\vec{b}$ vectors, respectively.

The proposed experimental setup for the spin correlation experiment is shown schematically in Fig. A.4. The correlation function is measured simultaneously in three configurations. In configuration A all four count rates are measured. At the same time two count rates corresponding to opposite spin projections of both electrons

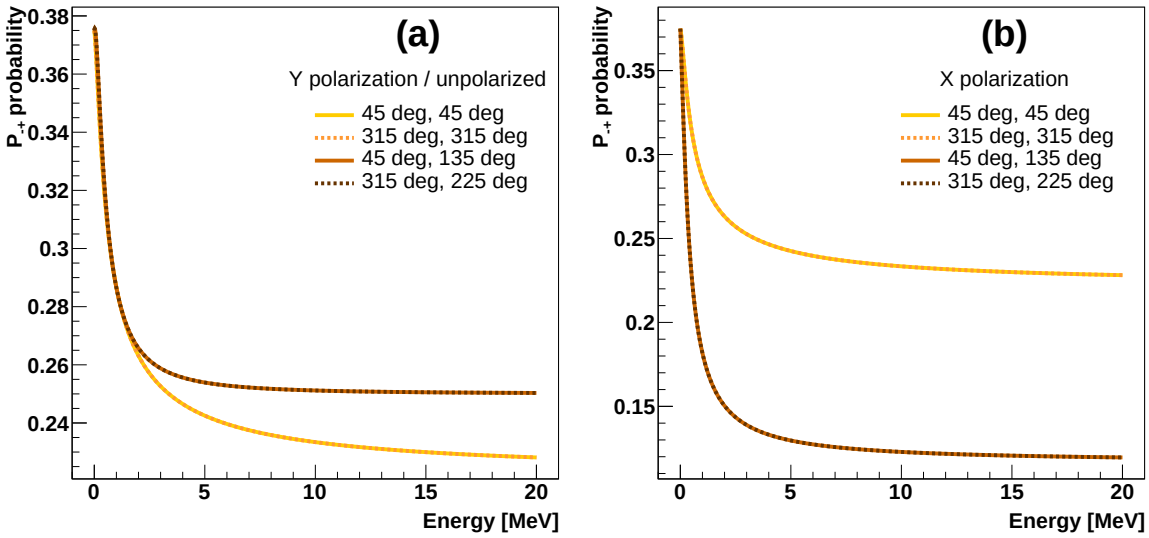

Figure A.3: Dependence of the P_{-+} probability on beam energy for a pair of electrons originating from Møller scattering (theoretical predictions [20]), for four sets of orientations of the $\vec{a}$ and $\vec{b}$ vectors (on which the spins are projected), with (a) unpolarized beam / beam polarization perpendicular to the Møller scattering plane, (b) beam transversely polarized in 85% in the Møller scattering plane. The scattering is symmetric with respect to the beam direction.

are measured in each of the two variants of configuration B, and the total number of counts in configuration A is used for normalization, allowing us to calculate the spin correlation function value under the assumption that the symmetry predicted by the theory holds.

A.2. Predictions for correlation experiments

A.2.1. Signal rate

In the polarization transfer measurement described in Chapter 7, data in configuration A were collected with the coincidence trigger for 42.85 hours. During this time 414 030 Møller scattering events were recorded in both detectors (within $\pm 2\,\sigma$ energy and timing cuts) at the average beam current of 60 nA, which corresponds to the event rate

$$f_{\text{exp}} = 161 \text{ evt/h/nA}. \tag{A.10}$$

The joint interaction (Møller and one Mott scattering) probability corresponding to this event rate is

$$p_{\text{exp}} = 7.2 \cdot 10^{-12} \tag{A.11}$$

taking into account that 1 nA $= 2.25 \cdot 10^{13}$ e$^-$/h.

According to the Monte Carlo simulation, as presented in Section 6.3.2, the total probability of Møller scattering off a 100 μm beryllium target into the $\pm 1.5°$ range

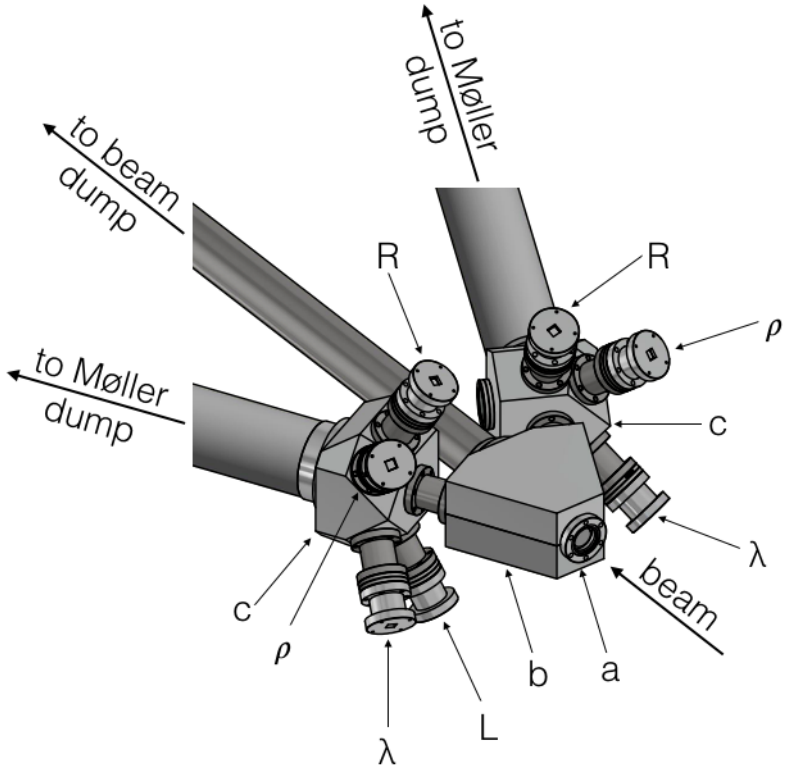

Figure A.4: Drawing of the experimental setup for the spin correlation measurement; a – Møller (Be) target, b – Møller scattering chamber, c – Mott scattering chambers, L, R, λ, and ρ – detectors in the Mott polarimeters. The shielding and the full length of the dump pipes are not shown.

around the symmetric scattering angle is

$$p_{\text{Møller}} = 1.6 \cdot 10^{-7}. \tag{A.12}$$

According to the Monte Carlo simulation performed with the polarized electron Mott scattering model (cross section from ELSEPA) the probability of subsequent backscattering off the 9.9 μm gold target into the 115° – 125° scattering angle range is

$$p_{\text{Mott}} = 1.9 \cdot 10^{-4}. \tag{A.13}$$

The Monte Carlo joint probability of both interactions is therefore $p_{\text{Møller}}\, p_{\text{Mott}} = 3.0 \cdot 10^{-11}$.

In order to be compared to the experimental value, the Monte Carlo probability has to be corrected for the loss of events due to pile-up removal and the timing and amplitude selections, which reject some of the signal events in the tails of the distributions (three times 2 σ cuts). The resulting value is $2.2 \cdot 10^{-11}$. The experimental probability, lower by a factor of 3, can be considered in agreement with the Monte Carlo predictions, taking into account finite detector efficiencies.

The simulated probabilities can be used to estimate the event rates in the correlation experiment. The interaction probability in the correlation experiment (i.e., Møller and

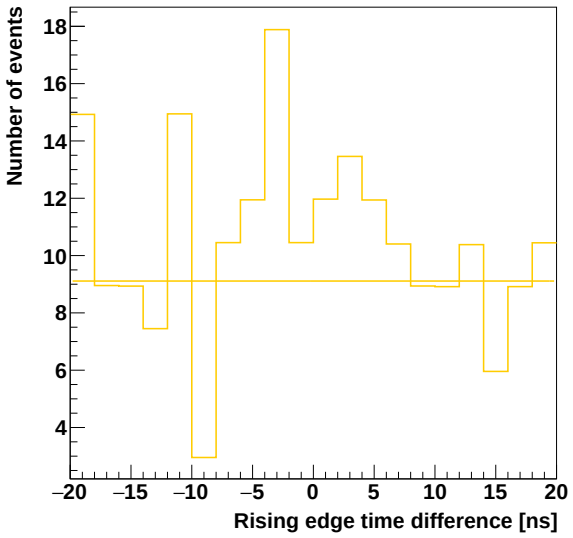

Figure A.5: Histogram of the time distance between the rising edge position in two polarimeter detectors, for events with both signal amplitudes in the Møller peak $\pm 2\ \sigma$, for runs with Au target, after dead time correction, shown with the fitted constant.

two Mott scatterings) is equal to

$$p_{\text{Møller}}\, p_{\text{Mott}}^2 = 5.8 \cdot 10^{-15}. \tag{A.14}$$

The total expected event rate is 0.13 evt/h/nA, which corresponds to

$$f_{\text{coinc}} = 0.032 \text{ evt/h/nA} \tag{A.15}$$

for each of the four coincidences.

A.2.2. Background rate

Data were collected for 7.76 hours with the coincidence trigger of both detectors in the Mott polarimeter, recording the false coincidences, which constitute background in the correlation experiment. During this time 270 false coincidence events were recorded, at the average beam current of 20 nA.

The number of events passing the $\pm 2\ \sigma$ energy and timing cuts is 9.1±0.7 (estimated from the fit to the timing distribution shown in Fig. A.5). The corresponding event rate is 1.2 evt/h at 20nA. The predicted signal to background ratio at 20 nA is about 1:2. Since the false coincidence rate is proportional to the square of the beam current, the rate at 1 nA is lower by a factor of 400:

$$f_{\text{bgd}} = 0.003 \text{ evt/h/nA}^2, \tag{A.16}$$

for each pair of counters.

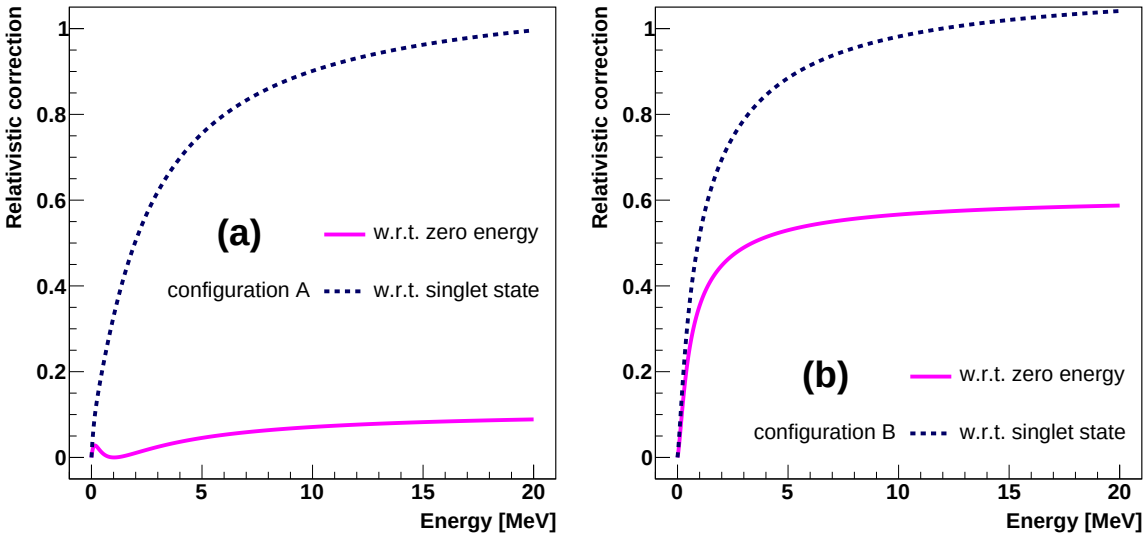

Figure A.6: Dependence of the relativistic correction to the correlation function on beam energy for a pair of electrons originating from Møller scattering (theoretical predictions [20]) with (a) the $\vec{a}$ and $\vec{b}$ vectors (on which the spins are projected) in the Møller scattering plane, (b) $\vec{a}$ and $\vec{b}$ vectors at angles equal to 45° to the Møller scattering plane. The scattering is symmetric with respect to the beam direction.

A.2.3. Correlation measurement

The absolute values of the correlation function are small in the range of relativistic energies. At 3 MeV they are approx. 0.025 and -0.011, in configuration A and B, respectively. Nevertheless, it can be seen in Fig. A.6, that the difference between the value at 3 MeV and the lowest value of the relativistic correlation function, which in both configurations is obtained in the zero-energy limit, is approx. 0.49 in the latter configuration of the $\vec{a}$ and $\vec{b}$ vectors.

Additionally, the $\vec{a}$ and $\vec{b}$ vectors, which are always perpendicular to electron momenta, depend on beam energy, since the symmetric scattering angle changes with beam energy. As a result, the singlet state prediction decreases with beam energy to values lower than the zero-energy limit, increasing the difference between the nonrelativistic and relativistic predictions. Therefore, the difference between the nonrelativistic and relativistic value for a given configuration of the $\vec{a}$ and $\vec{b}$ vectors (the relativistic correction) is even larger, as shown in Fig. A.6. At 3 MeV, the differences between the relativistic value and singlet state prediction are approx. 0.62 and 0.79, in configuration A and B, respectively.

The relative uncertainty of the number of signal events is

$$\frac{\Delta N}{N} = \frac{\sqrt{f_{\mathrm{bgd}} I^2 t + f_{\mathrm{coinc}} I t}}{f_{\mathrm{coinc}} I t} = \frac{\sqrt{f_{\mathrm{bgd}}}}{f_{\mathrm{coinc}}\sqrt{t}} \sqrt{1 + \frac{f_{\mathrm{coinc}}}{f_{\mathrm{bgd}} I}}. \tag{A.17}$$

Since the background contribution to the relative uncertainty is independent of the beam current, it is optimal to run with the highest beam current possible. In such

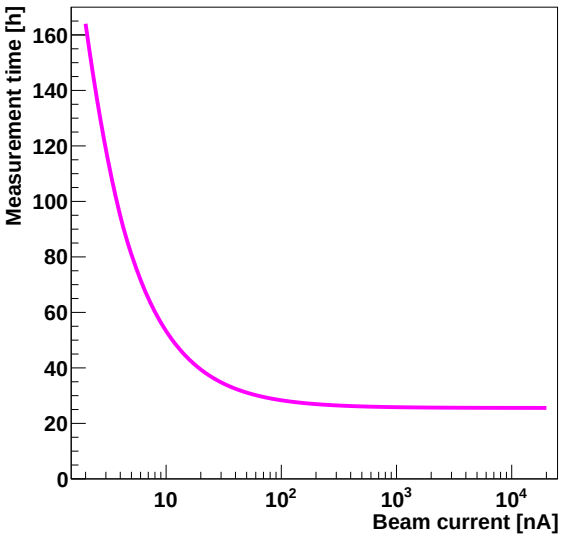

Figure A.7: Measurement time necessary to record a statistically significant number of coincidences, plotted as a function of the beam current.

case the I^2 term dominates and the uncertainty is determined mostly by the number of background events:

$$\frac{\Delta N}{N} \approx \frac{\sqrt{f_{\mathrm{bgd}}}}{f_{\mathrm{coinc}}\sqrt{t}}. \tag{A.18}$$

The relevance of this approximation is verified with plots of the measurement time corresponding to a given uncertainty as a function of the beam current in the 2 nA – 20 μA range available at MAMI, shown in Fig. A.7. It can be seen that the approximation is sufficiently accurate for beam currents above approx. 100 nA.

The signal and background event rates are shown in Fig. A.8 as a function of the beam current. In summary, even though the signal to background ratio might be favorable for very low beam currents, the event rates are extremely low. It is better from the statistics point of view to run at a higher beam current even though the signal to background ratio is much worse.

The uncertainty of the measured correlation function is

$$\Delta C = \frac{2}{S_{\mathrm{eff}}^2} \frac{\sqrt{(N_{LR}+N_{RL})^2(\Delta N_{LL}^2+\Delta N_{RR}^2)+(N_{LL}+N_{RR})^2(\Delta N_{LR}^2+\Delta N_{RL}^2)}}{(N_{LL}+N_{LR}+N_{RL}+N_{RR})^2}, \tag{A.19}$$

where ΔN with appropriate indices are the uncertainties of the numbers of recorded coincidences. Note that given the small value of analyzing power, the individual count rates of all coincidences and their uncertainties take approximately the same values. Under this assumption one obtains the approximate formula

$$\Delta C \approx \frac{1}{2S_{\mathrm{eff}}^2} \frac{\Delta N}{N}. \tag{A.20}$$

Let us assume that the uncertainty is determined only by the number of background

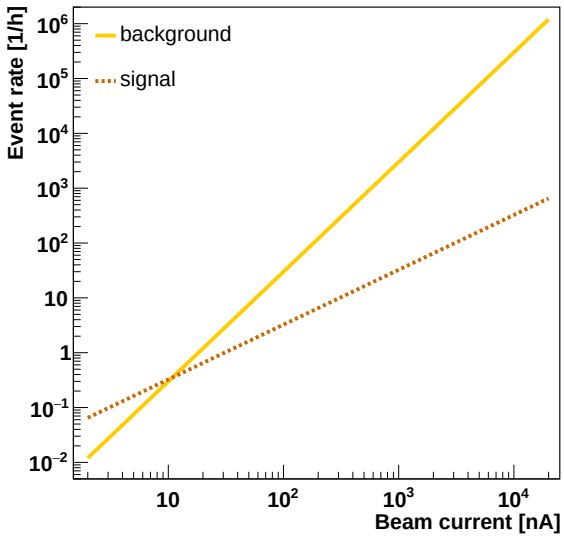

Figure A.8: Signal and background event rates plotted as a function of the beam current.

events. Using Eq. (A.18) one obtains

$$\Delta C \approx \frac{1}{2S_{\text{eff}}^2} \frac{\sqrt{f_{\text{bgd}}}}{f_{\text{coinc}}\sqrt{t}}. \tag{A.21}$$

The time needed to measure the correlation function with a given precision is

$$t = \frac{f_{\text{bgd}}}{f_{\text{coinc}}^2} \frac{1}{4\Delta C^2 S_{\text{eff}}^4}. \tag{A.22}$$

For example, taking into account the effective Sherman function value at 1.5 MeV of about 0.0886, the time needed to observe the relativistic correction to the correlation function of the order of 0.5 at a 3 σ level is approx. $4.1 \cdot 10^5$ h. The experiment would take 51 years assuming that the beam is available for an average 28 days per month. Such measurement is, therefore, totally impossible even with an accelerator available for the exclusive use of the experiment.

One can also use the above equations to determine the background rate corresponding to a given measurement time and precision. In order to calculate the highest background rate allowing to measure the correlation function with a given precision during a given beam time, one has to solve the following equation

$$\Delta C \approx \frac{1}{2S_{\text{eff}}^2} \frac{\sqrt{xI^2 + f_{\text{false}}I^2 + f_{\text{coinc}}I}}{f_{\text{coinc}}I\sqrt{t}}, \tag{A.23}$$

where x is the unknown background rate, and f_{false} is the rate of false coincidences of two Møller electrons originating from two different beam electrons, which cannot be distinguished from the signal events within the timing resolution $\Delta t = 2$ ns. Note that in case of a measurement with a lower level of background, the approximation of

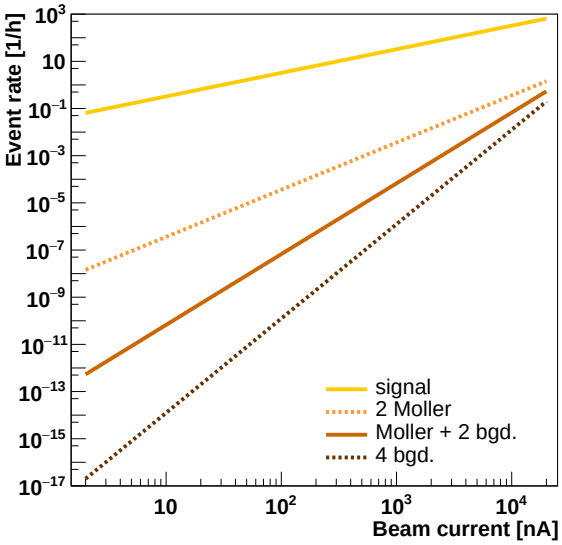

Figure A.9: Event rates for the measurement with tracking plotted as a function of the beam current for the signal and background: coincidence of four background signals (4 bgd.), one Møller and two background (Møller + 2 bgd.) and two Møller electrons (2 Møller).

Eq. (A.18) is no longer valid, so the exact uncertainty of the number of counts was used. The rate of false coincidences is

$$f_{\text{false}} = f_{\text{exp}}^2 \Delta t = 1.4 \cdot 10^{-8} \text{ evt/h/nA}^2, \tag{A.24}$$

and the solution is

$$x = \frac{1}{I^2}\left(4\Delta C^2 S_{\text{eff}}^4 f_{\text{coinc}}^2 I^2 t - f_{\text{false}} I^2 - f_{\text{coinc}} I\right). \tag{A.25}$$

For example, the highest background rate allowing to observe the relativistic correction of the order of 0.5 at a 3 σ level, during one year of beam time, at the beam current $I = 1$ μA, is

$$x = 2.6 \cdot 10^{-5} \text{ evt/h/nA}^2, \tag{A.26}$$

which, compared to the measured background rate of 0.003 evt/h/nA^2, is lower by 2 orders of magnitude.

A.2.4. Measurement with tracking

Such a substantial reduction of background cannot be achieved with simple modification of shielding and geometry. A reasonable solution is to use additional tracking detectors in the polarimeter arms, in coincidence with the main scintillation counters. In such a case the theoretical probability of a four–detector background coincidence is negligible ($f_{\text{bgd}}^2 \Delta t \approx 10^{-17}$ evt/h/nA^4). The probability of registering one Møller electron (which passes through the tracking detector) in coincidence with two background electrons in the other arm is higher, but still negligible ($f_{\text{exp}} f_{\text{bgd}} \Delta t \approx 10^{-13}$ evt/h/nA^3).

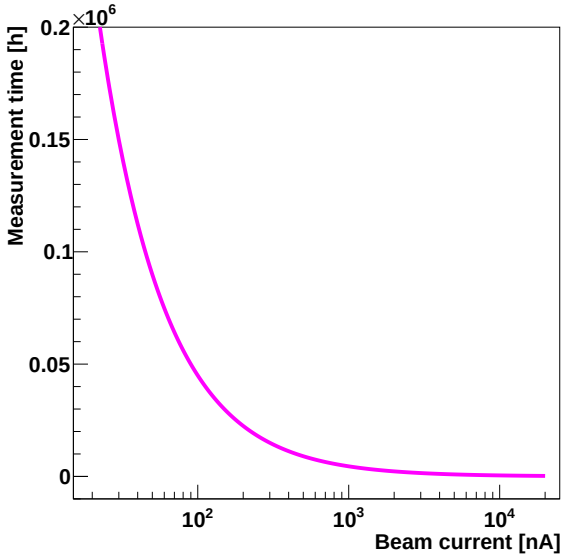

Figure A.10: Measurement time necessary to observe a relativistic correction equal to 0.5, assuming no external background, plotted as a function of the beam current.

In this case the false coincidences of two Møller electrons are the largest component of background (the rate is the same as without tracking, $f_{\rm exp}^2 \Delta t \approx 10^{-8}$ evt/h/nA^2), as shown in Fig. A.9.

The theoretical signal to background ratio at 1 μA is about 2000. In the absence of external background, the time needed to measure the correlation function with a given precision is

$$t \approx \frac{1}{4\Delta C^2 S_{\rm eff}^4} \frac{f_{\rm bgd}^2 \Delta t I^4 + f_{\rm exp} f_{\rm bgd} \Delta t I^3 + f_{\rm exp}^2 \Delta t I^2 + f_{\rm coinc} I}{f_{\rm coinc}^2 I^2}. \qquad \text{(A.27)}$$

It can be seen in Fig. A.10 that in the low–background situation it is desirable to use the highest beam current possible. However, even though the probability of a coincidence of two or more electrons is very low, the single–counter rates are high, leading to the overlapping signals observed in the experiment. The pile–up probability (i.e., the probability that for a given signal there is another one within an approximately 20 ns time window) should be linearly proportional to the beam current, therefore, it can be extrapolated from the fraction of pile–up events observed in the polarization transfer experiment, as shown in Fig. A.11. The result is about 10% at 20 μA and 0.5% at 1 μA. Note that in principle the event should be rejected from analysis if there is an overlapping signal in any of the four detectors taking part in the coincidence, therefore, it does not seem possible to perform the measurement with the beam current higher than a few μA.

In the absence of external background, the time necessary to observe the relativistic correction of the order of 0.5 at a 3 σ level, at the beam current $I = 1$ μA, is approx. 187 days. However, the rate of background events in which a single beam electron produces signal in two detectors is unknown and cannot be reliably determined without an experimental test.

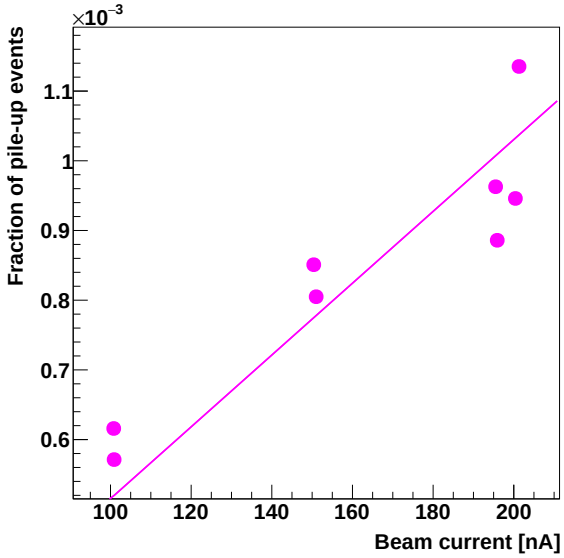

Figure A.11: Fraction of pile–up events recorded in the polarimeter detector with the beam trigger, plotted as a function of the beam current.

A.3. Violation of Bell-type inequalities

The Bell-type inequality used commonly in the case of spin-1/2 fermions is the CHSH inequality [72],

$$\left|C(\vec{a},\vec{b}) + C(\vec{c},\vec{b}) + C(\vec{c},\vec{d}) - C(\vec{a},\vec{d})\right| < 2, \tag{A.28}$$

which requires the correlation experiments to be performed with four different pairs of spin-projection directions, described by $\vec{a}$, $\vec{b}$, $\vec{c}$, and $\vec{d}$ vectors. A typical arrangement of the spin projection directions in all four experiments is shown schematically in Fig. A.12.

The left hand side of the CHSH inequality is plotted as a function of beam energy in Fig. A.13(a) in the case of an electron beam scattered off a target. In the simplest case of scattering off an unpolarized target, plotted quantity approaches zero with increasing energy. The typical polarization of the target electrons achieved experimentally is equal to approx. 8%. Also in this case, the correlation function is small enough to fulfill the above inequality for electrons of relativistic energies. However, in the case when both interacting electrons are highly polarized, it is possible to find configurations in which the CHSH inequality is not conserved; as an example, a hypothetical case of 90% target polarization was analyzed.

While the preparation of a highly polarized target does not seem technically feasible at present, an experiment with two polarized beams is possible. The left hand side of the CHSH inequality for two colliding beams of equal energy and polarization is plotted as a function of beam energy in Fig. A.13(b). With 85% beam polarization, the left hand side of inequality (A.28) is slightly below 2. With 90% polarization, a significant violation of the inequality is observed both for the polarized target and for colliding beams. Such a measurement is not unrealistic, since polarization degrees as high as 92% were reported by several authors using special photocathode materials [75–77].

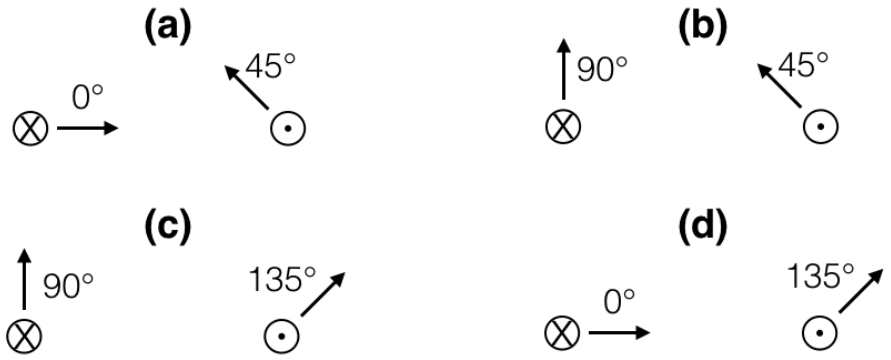

Figure A.12: Spin-projection measurement directions in four experiments necessary in order to evaluate the CHSH inequality, (a) $C(\vec{a},\vec{b})$, (b) $C(\vec{c},\vec{b})$, (c) $C(\vec{c},\vec{d})$, (d) $C(\vec{a},\vec{d})$. The angles between the vectors on which the spin is projected and the Møller scattering plane take values: $0°(\vec{a})$, $45°(\vec{b})$, $90°(\vec{c})$ and $135°(\vec{d})$. Note that the angles in the drawing are measured counter-clockwise for the electron on the left hand side, and clockwise for the electron on the right hand side, since the momenta of both electrons are perpendicular to the drawing but have opposite directions.

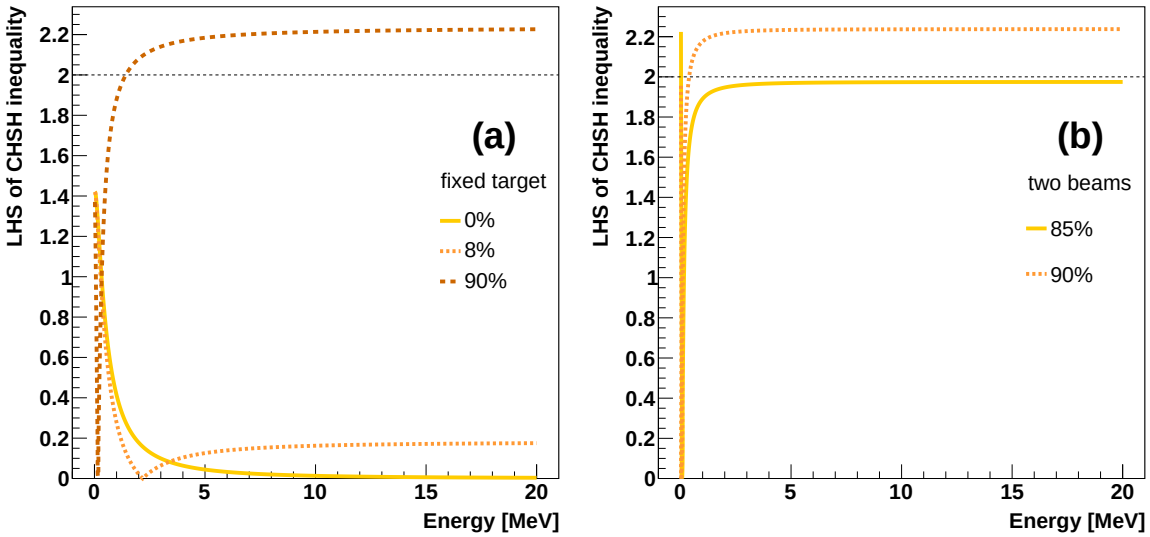

Figure A.13: Dependence of the left hand side of the CHSH inequality on beam energy for a pair of electrons originating from symmetric Møller scattering (theoretical predictions [20]) for (a) a stationary target, for three degrees of target polarization: unpolarized, 8% and 90% polarization (beam electron polarized in 85%), (b) two polarized beams of equal energies and opposite momentum directions (85% and 90% polarization of both beams). In both cases the electrons are polarized in the same direction, perpendicular to momentum, and in the Møller scattering plane. The angles between the vectors on which the spin is projected and the Møller scattering plane take values: $0°(\vec{a})$, $45°(\vec{b})$, $90°(\vec{c})$ and $135°(\vec{d})$, cf. Fig. A.12.

The experiment with colliding beams would also have significant advantages over fixed target measurements. Since the electrons scattered perpendicular to the beam directions would be detected, there would be no geometrical limitations to the positioning of the counters. Thanks to the large angle and lack of the target, a significantly lower background level can be expected as well.

Appendix B

Drawings of the experimental setup

The cross section of the experimental setup in the Møller scattering (horizontal) plane is shown in Fig. B.1. The details of the collimators are shown in Fig. B.2. The Mott scattering chambers and their cross section are shown in Figs. B.3 and B.4 in configurations A and B, respectively. The details of the target ladder and frames are shown in Fig. B.5. The vertical cross section of the experimental setup, along a signal-electron trajectory, is shown in Fig. B.6. The details of the lead shielding of the detectors are shown in Fig. B.7. The arrangement of the detector assembly (scintillator, lightguide and SiPM) is shown in Fig. B.8.

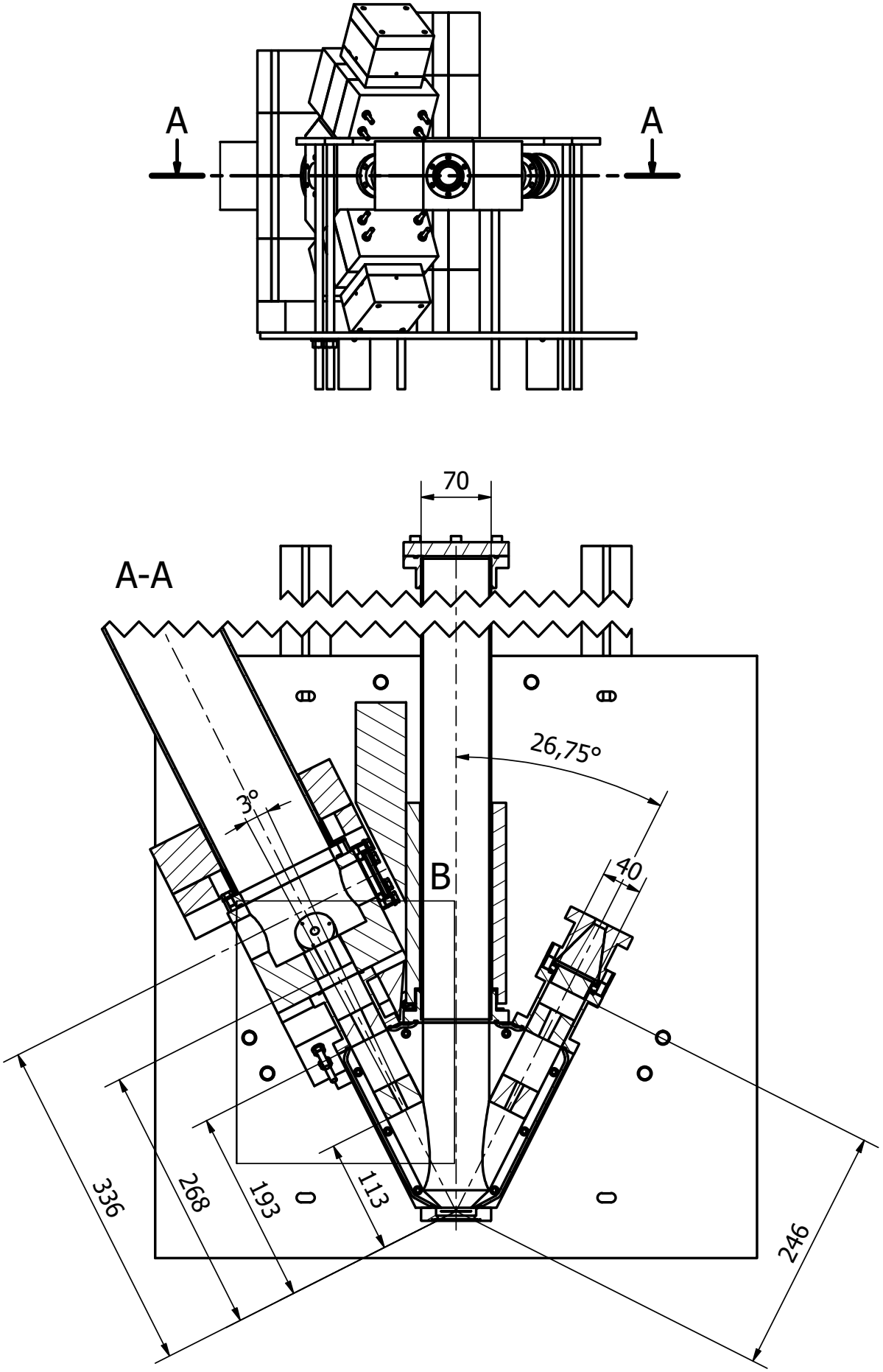

Figure B.1: Cross section of the polarization transfer experiment in the Møller scattering plane.

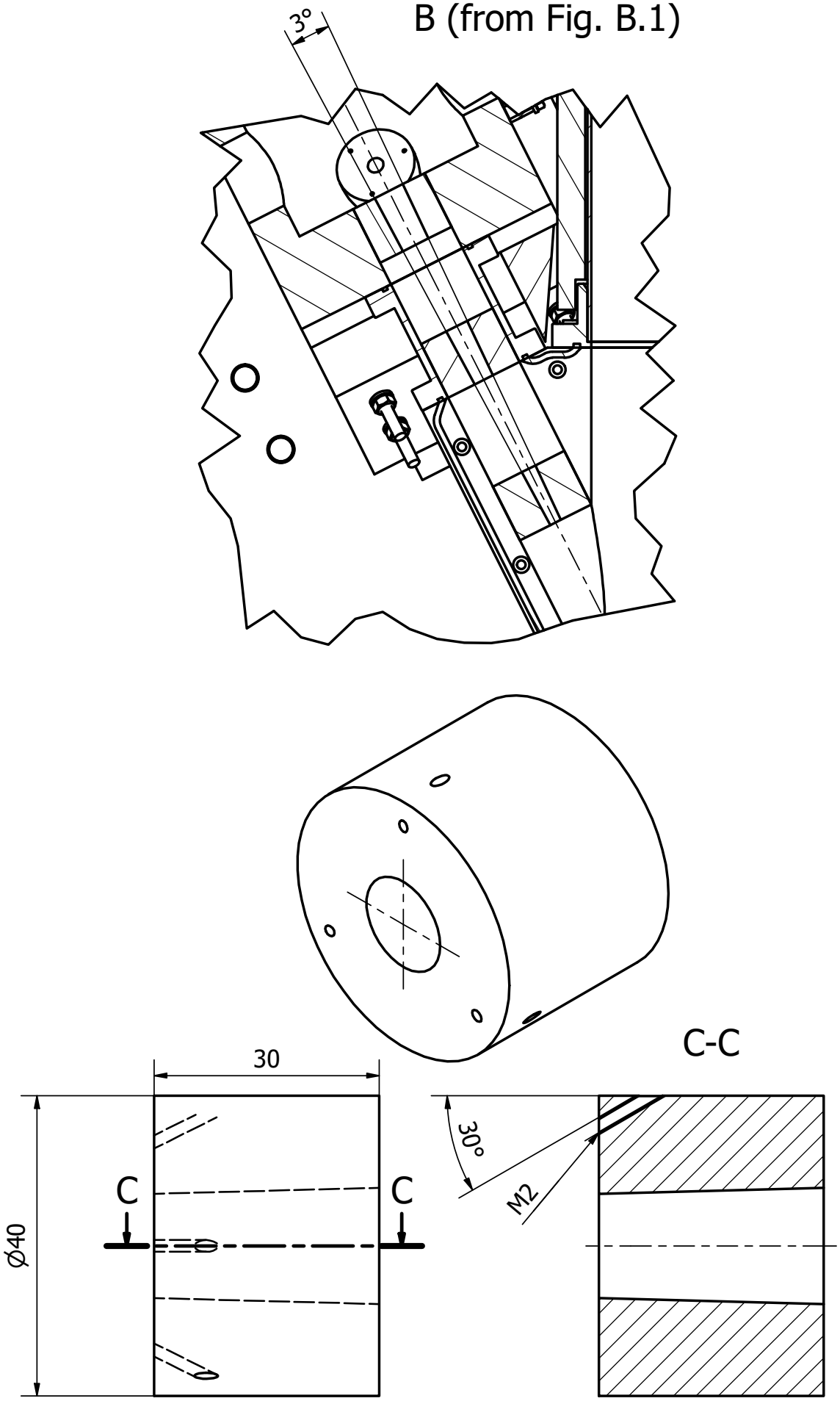

Figure B.2: Collimators in the Møller scattering chamber.

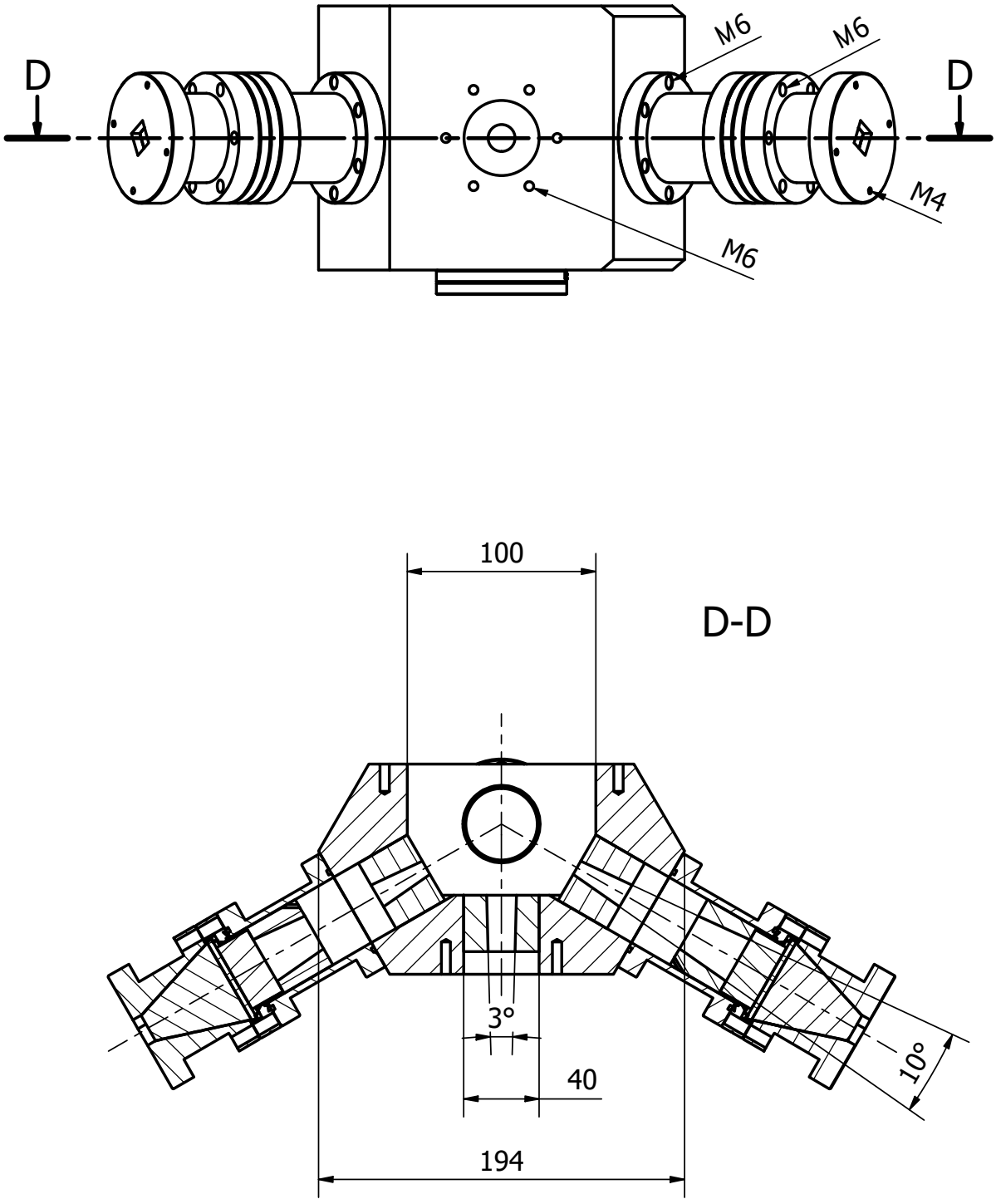

Figure B.3: Drawings of the Mott scattering chamber in configuration A.

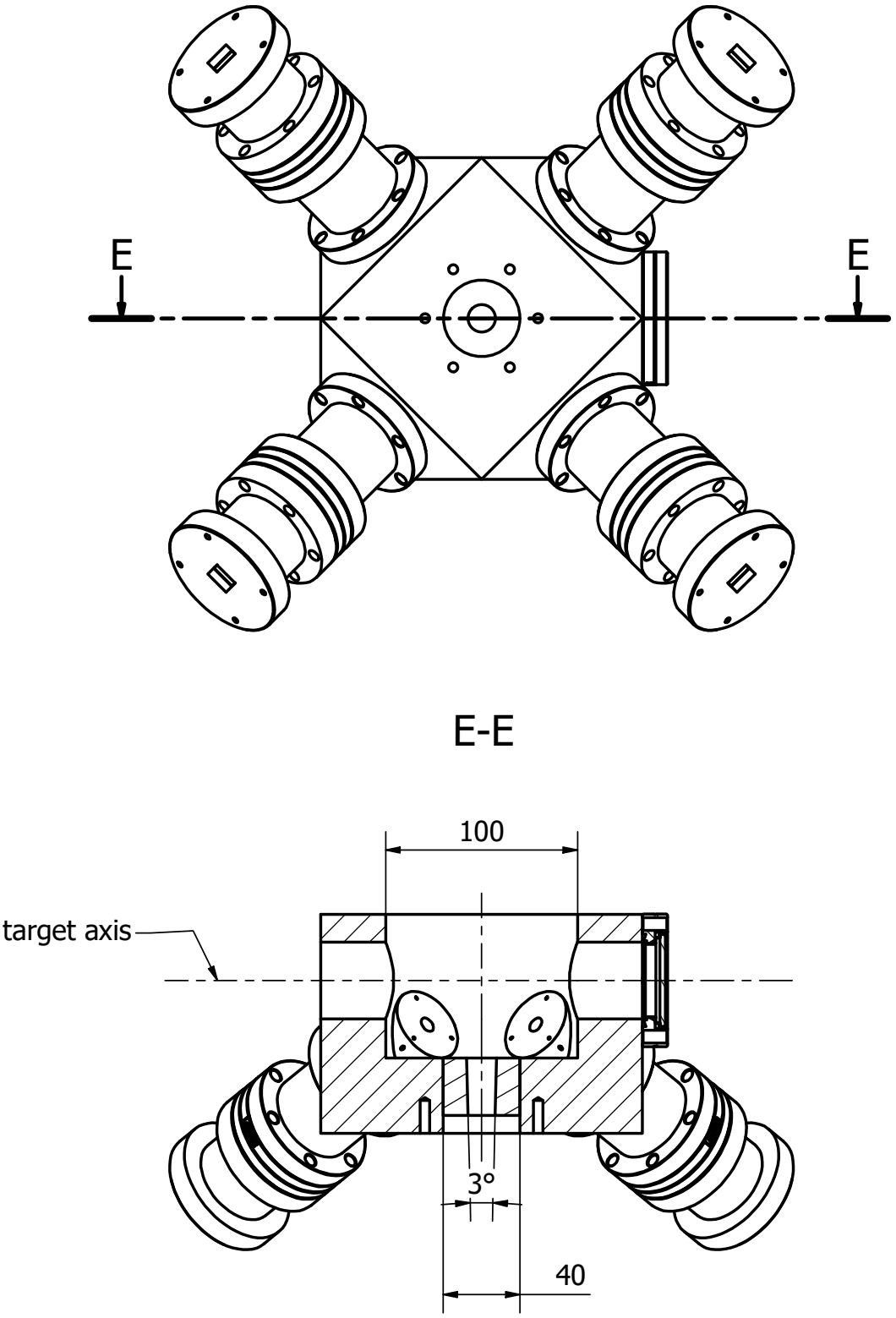

Figure B.4: Drawings of the Mott scattering chamber in configuration B.

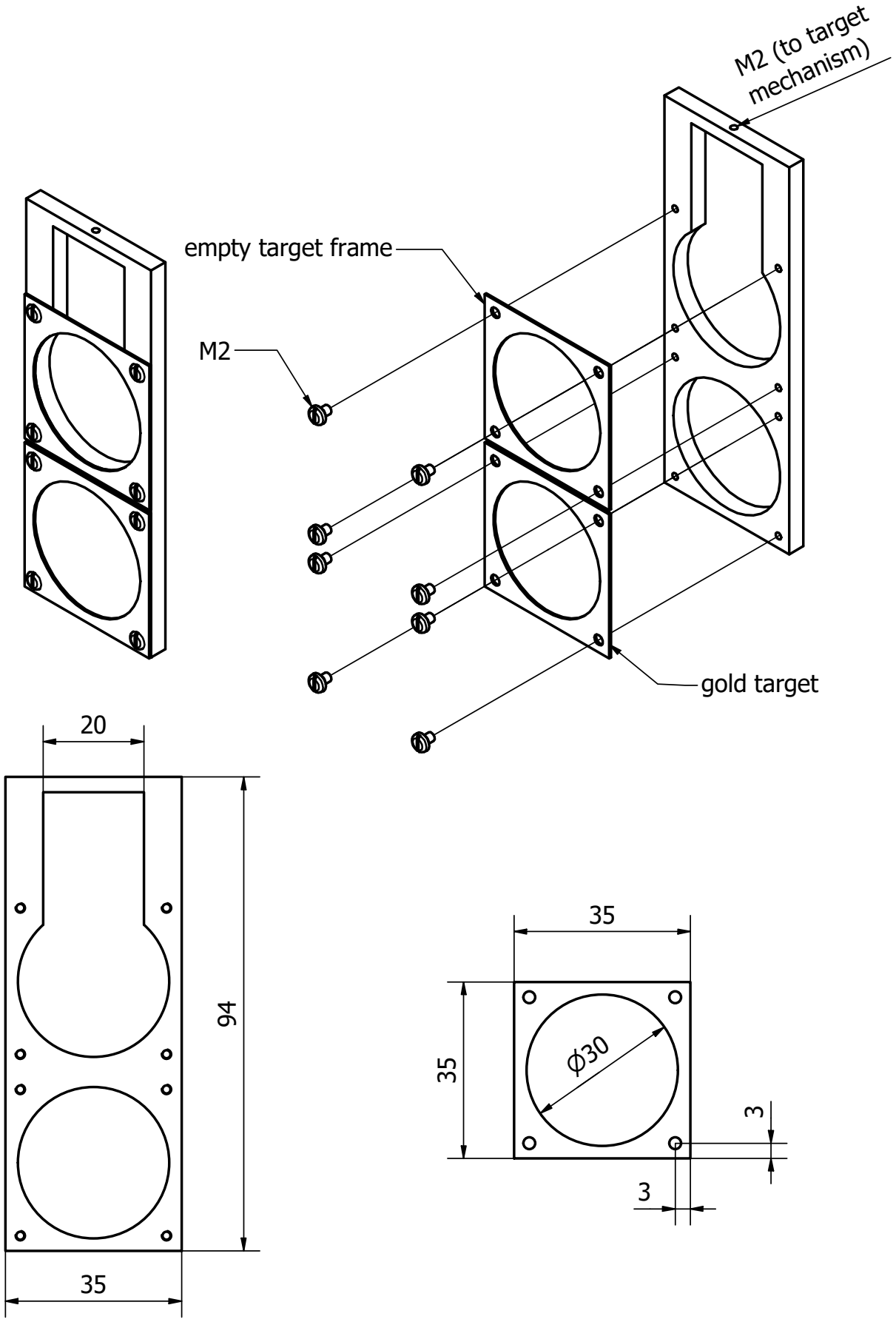

Figure B.5: Target ladder in the Mott polarimeter.

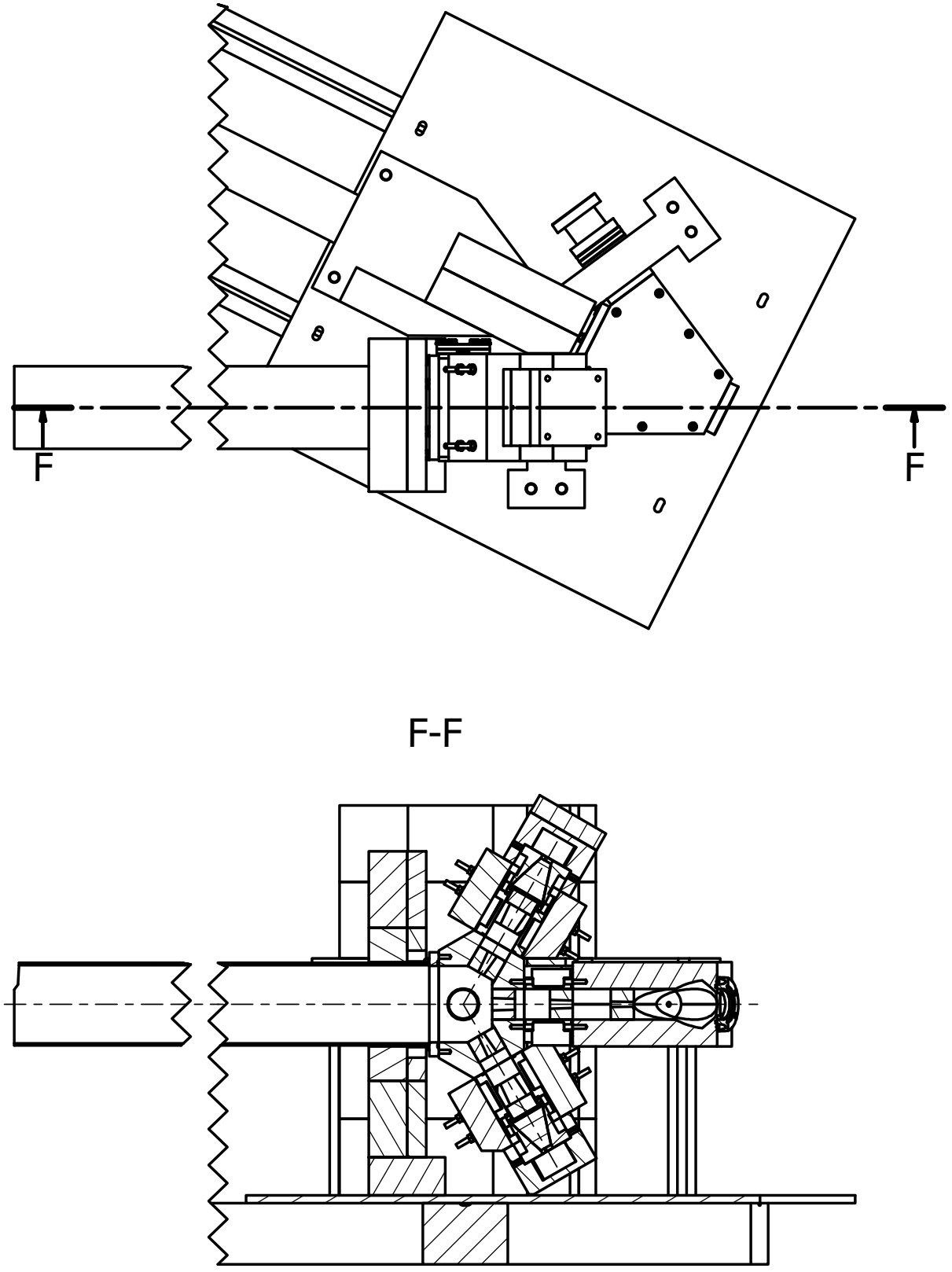

Figure B.6: Cross section of the polarization transfer experiment along a signal-electron trajectory.

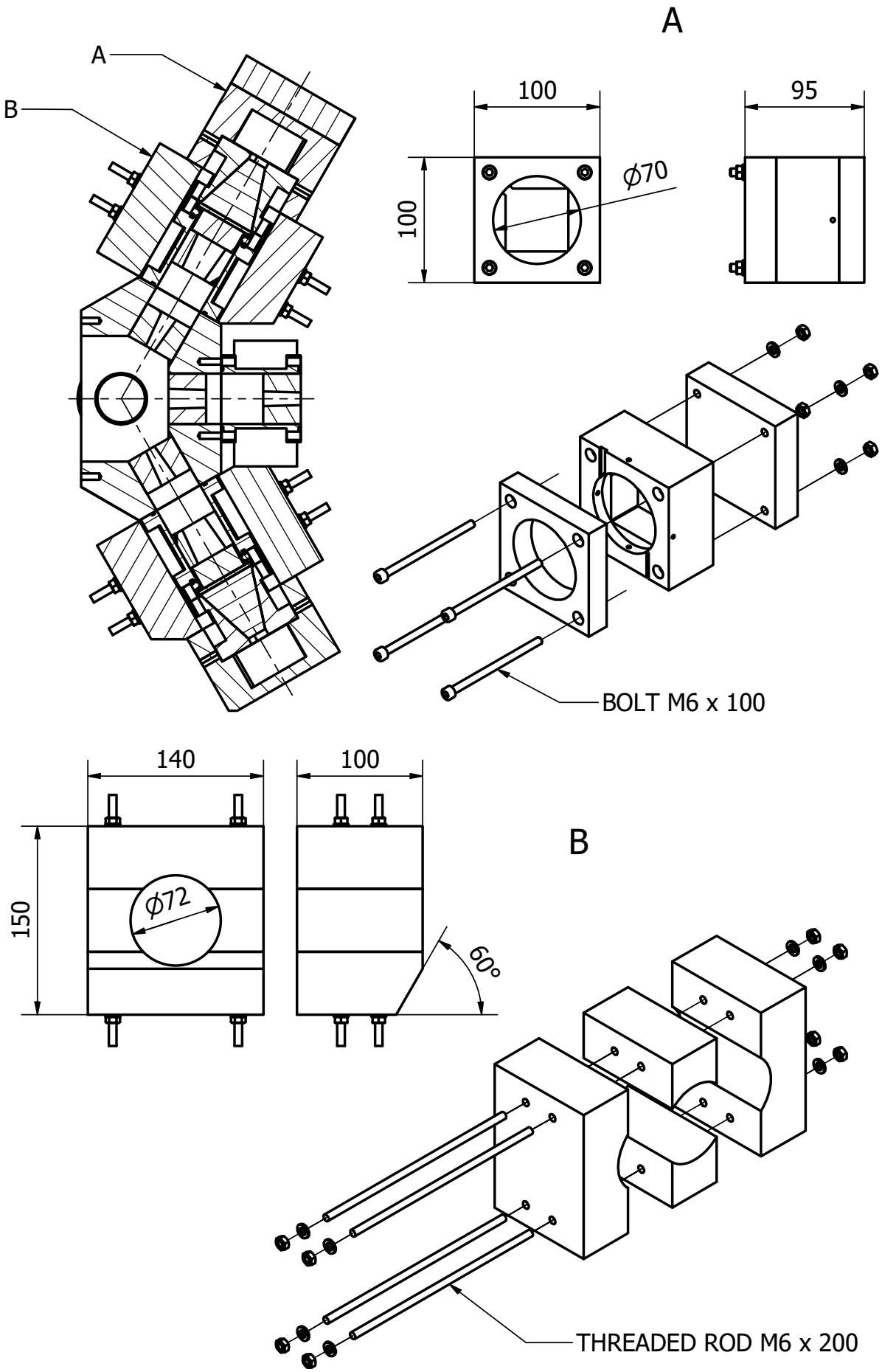

Figure B.7: Lead shielding of the Mott-polarimeter detectors.

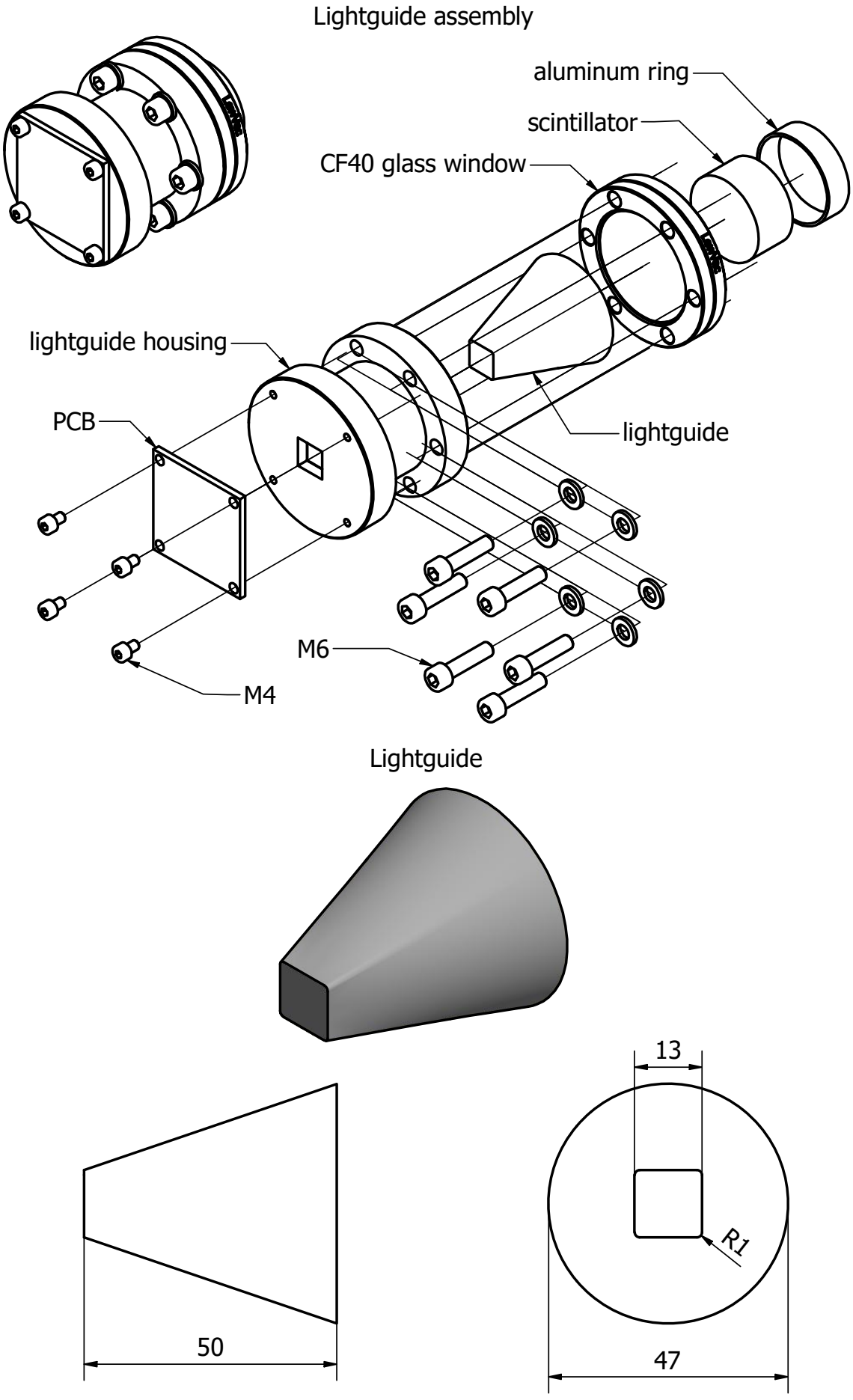

Figure B.8: Drawings of the lightguide assembly.